2016

Design and fabrication of solid nitrogen cooled MgB2 based persistent magnet for MRI application

Dipakkumar J. Patel
University of Wollongong

UNIVERSITY
OF WOLLONGONG
AUSTRALIA

Design and Fabrication of Solid Nitrogen Cooled MgB_2 based Persistent Magnet for MRI Application

A thesis submitted for fulfilment of the requirements for the award of the degree

DOCTOR of PHILOSOPHY

From the

UNIVERSITY OF WOLLONGONG

By

Dipakkumar J. Patel, B.Sc., M.Sc.

Institute for Superconducting and Electronic Materials

Australian Institute for Innovative Materials

Faculty of Engineering and Information Sciences

School of Mechanical, Materials and Mechatronics Engineering

University of Wollongong, NSW, Australia

August 9, 2016

Certificate of Originality

This is to certify that the work presented in this thesis was carried out by the candidate in the laboratories of the Institute for Superconducting and Electronics Materials (ISEM), at the University of Wollongong, NSW, Australia, and has not been submitted for a degree to any other academic institution for higher education.

Dipakkumar J. Patel

August 9, 2016

To my Family

Acknowledgements

It is a pleasure to express my sincere gratitude to my principal supervisor, Prof. Jung Ho Kim, for believing in me and providing me with the opportunity to work with him. His continuous academic guidance, support, encouragement, and careful reading and correction of my manuscripts, have helped me to complete this thesis.

I would like to thank Prof. S. X. Dou for promptly replying my email regarding an open Ph.D. position in Institute for Superconducting and Electronic Materials (ISEM) back in 2012 and for forwarding my CV to my principal supervisor Prof. Jung Ho Kim. Since then, his continuous support and encouragement have helped me tremendously to finish my Ph.D. study on time.

I would like to thank my co-supervisor Dr. Md Shahriar Al Hossain for providing me with 360° support when and where needed. He has always been ready to discuss experimental results, giving useful suggestions and ideas, financial support for experiments, and most importantly, moral support throughout my thesis work. I also would like to thank my co-supervisor Dr. Khay Wai See for his continuous support and technical help with crucial data acquisition systems for most of my experiments.

This thesis work has been conducted under the Future Fellowship project (no. FT110100170) of Prof. Jung Ho Kim from the Australian Research Council. A partial funding for this thesis work has been received from Australian Research Council DECRA project (no. DE130101247) of Dr. Md Shahriar Al Hossain, University of Wollongong and Australian Institute for Innovative Materials internal grant, the Korea Basic Science Institute grants C36222, and C36948, JSPS KAKENHI grant number 26709021, Hyper Tech Research Inc., and Deanship of Scientific Research at King Saud University research group project number RGP-VPP-290.

I would like to thank Dr. Mitchell Nancarrow and Dr. Tony Romeo for help with the SEM in the Electron Microscopy Centre of the University of Wollongong. I would also like to thank Dr. Tania Silver for correcting the English in my manuscripts and thesis.

My sincere thanks to Dr. Zongqing Ma for providing quick feedback on my manuscripts, Dr. Xun Xu and Dr. Germanas Peleckis for providing technical and administrative support, A/Prof. Z. Cheng, Prof. A. Pan, and Dr. K. Konstantinov for allowing me to use their laboratories, Mr. Robert Morgan, Mr. Paul Hammersley, and Mr. Mathew Davies for providing vital timely mechanical workshop support and liquid helium supply on time for experiments, Mr. John Wilton for electrical workshop support, Mr. Paul Scully, Mrs. Narelle Badger, and Mrs. Crystal Mahfouz for administrative support, and Mrs. Joanne George and Dr. Candace Gabelish for procurement and safety related support.

I would like to express my sincere thanks to our collaborators, Dr. Seyong Choi and his colleagues Dr. Seoungjunk Kim, and Mr. Jonggi Hong from the Korean Basic Science Institute, Korea, and Mr. Mike Tomsic, Mr. Matt Rindfleisch, and Mr. David Doll of Hyper Tech Research Inc., USA, for their technical as well as financial support. I would also like to thank Mr. Vinod Kaila, and Mr. Anand Makasana of Aditya High Vacuum Pvt. Ltd., Ahmedabad, India for fabricating solid nitrogen cooling system. I also would like to thank Prof. Mike Sumption, and Dr. John Voccio of the Ohio State University, USA, and the Massachusetts Institute of Technology, USA, respectively, for their valuable suggestions. I also would like to thanks, Prof. Subrata Pradhan of Institute for Plasma Research, India, Prof. Ekrem Yanmaz of Gelisim University, Turkey, Prof. Mohammed Shahabuddin of King Saud University, Saudi Arabia, and Dr. Minoru Maeda of Nihon University, Japan for co-authoring manuscripts.

A big thanks to my colleagues from the Institute for Plasma Research (IPR), India, the magnet division head and mission leader of SST-1, Prof. Subrata Pradhan, and the directors (Prof. D. Bora (current), Prof. P. K. Kaw (former)) for granting me leave to pursue higher study, Dr. Aashoo Sharma and Mr. Upendra Prasad for taking care of my work and showing their willingness to relieve me for my Ph.D. study. Sincere thanks should also go to my other colleagues and close friends Dr. Vipul Tanna, Mr. Kalpesh Doshi, Mr. Pankaj Varmora, Mr. Pragnesh Dhorajiya, Mrs. Ananya Kundu, Mr. Piyush Raj, Mr. Yohan Khristi, Mr. Arun Panchal, Mr. Azad Makwana, Mr. Dinesh Patel, Mr. Ashok Patel, Ms. Priyavandana Rathod, Mr. Vinod

Kaila, Mr. Surendrasinh Jadeja, and Mr. Jagdish Vihola for their support. I also would like to thanks to an administration staff of IPR, Mr. Harish Khanduri, Mr. Anuj Harvey, Mr. Hitesh Mehta, Mrs. Falguni Shah, Mr. Hitesh Suthar, and Mr. H. K. Sharma, who made my work easy when I was in IPR as well as here at ISEM.

I would also like to thank my colleagues Mr. Wenbin Qiu, Mr. Hyunseock Jie, Mr. Hiroki Kobayashi, Mr. Shaon Barua, Dr. Ashkan Motaman, Mr. Sujith Kalluri, Mr. Chandrasekar Subramaniyam, and Mr. Sudipta Pramanik for their support and encouragement in good and bad times throughout this thesis work.

Many thanks to the IEEE Council on Superconductivity for providing me with a very valuable registration fee waiver and a travel stipend to attend the Applied Superconductivity Conference – 2014 in the USA and Magnet Technology Conference – 24 in South Korea. I would also like to thank the UOW Global Challenge Program for providing me with a Global Challenge travel scholarship to attend Magnet Technology Conference - 24 in South Korea.

My family, especially my wife Mrs. Dipti Patel, deserve special thanks for taking care of me and keeping me healthy through my Ph.D. study, taking care of my son, Master Devyansh Patel, and most importantly, sacrificing her career for my professional career development. Because of her constant support, for which I owe her hearty thanks, I never felt disadvantaged at any stage of this thesis work. I would also like to thank my parents, Mr. Jayantibhai Patel and Mrs. Karunaben Patel, and my parents-in-law, Mr. Ramdas Patel and Mrs. Ushaben Patel, for their support.

Finally, I would like to thank all those people who helped me directly or indirectly for successful completion of this thesis. Although this work was solely done by me, without the support of countless people at the different stages of the work, I would probably not have been able to complete this thesis

Abstract

Physicians and surgeons rely critically on magnetic resonance imaging (MRI) scans to diagnose and treat critical injuries and medical conditions. In an MRI system, high, stable (<0.1 ppm h^{-1}), and uniform (≤10 ppm in 50 cm diameter of spherical volume) magnetic fields are required for obtaining high-resolution images of the human body. The unique possibilities for the operation of superconducting magnets (i.e., persistent-mode) make them ideal for MRI application. Thus, in the majority of commercially available MRI systems, superconducting persistent magnets based on niobium titanium (NbTi) have been used. These magnets, which are cooled in an expensive liquid helium (LHe) bath at 4.2 K, cannot currently be avoided. Thus, the high operation costs of MRI systems obstruct their extensive use in developing and underdeveloped countries.

To fulfill the above requirements, magnesium diboride (MgB_2), which was found to be superconducting in 2001, is considered as a promising candidate for LHe-free operation in MRI due to its relatively low material and fabrication costs compared to high-temperature superconductors (HTS). Owing to these benefits, there have been many recent reports on technology development for MgB_2 based MRI magnet systems. In fact, *PARAmed* has already commercialized LHe-free MRI systems, called “open sky MRI”. These MRIs are not operated in a persistent mode, however, due to difficulties in making superconducting joints using MgB_2 conductors. In general, MRI magnets are operated in the persistent mode to retain magnetic field stability throughout the spherical imaging volume, to keep the long-term drift rate of the magnetic field under 0.1 ppm h^{-1}, and to maintain overall stable operation. Moreover, it has been reported that the heat capacity of MgB_2 magnets can be significantly enhanced by cooling them using solid nitrogen (SN_2) with a cryocooler. The high heat capacity of SN_2 can enable a magnet to operate for a certain time period in the absence of the cooling source (i.e., cryocooler), which is suitable for areas where power failure is common.

In this thesis, the design, fabrication, and validation of an SN_2 cooled MgB_2 based persistent magnet for MRI application were conducted. All the necessary

technologies, such as the SN_2 cooling system, the MgB_2 solenoid coil fabrication, and validation, and the superconducting joining processes for the MgB_2 wires that were needed for the development of the SN_2 cooled MgB_2 based persistent magnet were studied and methodically developed. During this thesis work, some existing problems were effectively solved, and a new key technology (i.e., the superconducting joining process) was developed. As a result, the first MgB_2 based persistent magnet was demonstrated in an SN_2 environment which meets the technical requirements for MRI application.

Several SN_2 cooling systems have been reported for HTS applications, whereas only one SN_2 cooling system was reported for an MgB_2 magnet before this thesis work. As per the literature, SN_2 and the other cooling systems developed before this thesis work encountered several problems, such as poor uniformity of the SN_2, a thermal contact problem between the SN_2 and a magnet in the event of repeated thermal disturbances, high heat load, possible leaks in joints between dissimilar materials at cryogenic temperatures, and a thermal contact problem between a cryocooler and the SN_2 chamber. In fact, solutions of some of the above problems have been reported in the literature. Therefore, firstly, to test the MgB_2 based persistent magnet in the SN_2 environment, optimal design analysis and validation of the SN_2 cooling system with enhanced temperature uniformity in its SN_2 chamber were conducted. The cooling system was designed using stainless steel (SS), except for the radiation shield, to avoid joints between dissimilar materials and prevent leaks at cryogenic temperatures. Due to the low thermal conductivity of the SS, however, it produced a temperature gradient across the SN_2 chamber. To minimize such temperature gradients, a unique approach using a copper (Cu) flange on the SN_2 chamber was developed and experimentally validated. In addition to these considerations, to validate the SN_2 cooling system, an MgB_2 based solenoid coil was fabricated and tested.

Apart from the cooling system, high-performance superconducting joints are equally important for realizing MgB_2 based persistent-mode magnets for MRI application. Therefore, I proposed a concept and fabricated superconducting joints using unreacted *in situ* undoped monofilament MgB_2 wires, which yielded reliable

performance in the operating temperature range of 4.2 K to 25 K. MgB_2-MgB_2 joints in magnets, are known to lead to fading of localized electrical, thermal, and mechanical properties. To overcome these problems, the ends of the two wires were inserted into a pellet press, which was then filled with a mixture of unreacted magnesium and boron powders, followed by heat-treatment. The critical current capacity (I_c) and joint resistance were precisely evaluated by the standard four-probe method in open-circuit and field-decay measurements in a closed-loop, respectively. These joints demonstrated up to 66% of the current-carrying capacity of the unjoined wire at 20 K, 2 T and joint resistance of 1.4 x 10^{-12} Ω at 4.2 K in self-field.

Furthermore, according to the literature, it is well known that the high-field performance of *in situ* MgB_2 can be significantly improved by carbon (C)-doping. Thus, it is desirable to use C-doped MgB_2 conductor where high in-field performance is required. Nevertheless, most of the high-performance joint results were reported for *in situ* MgB_2 conductors without C-dopant for low-field operation. It was reported that the critical current, I_c, of an unreacted *in situ* undoped monofilament wire joint was >230 A at 10 K. On the other hand, when using an unreacted *in situ* C-doped monofilament wire under the same experimental conditions, the I_c of the joint was only 16 A at 10 K. Thus, a new approach to a superconducting joining process for unreacted *in situ* C-doped MgB_2 wires was developed. By controlling the pressure inside the joint, successful retention of the current carrying capacity in the joint of up to 72% compared to a wire without a joint was obtained. The closed-circuit resistance of the closed-loop coil was less than 1.8 x 10^{-13} Ω at 16.7 ± 4.7 K, as measured by the field-decay measurement method.

Although the concept of SN_2 cooling for MgB_2 based persistent magnets for MRI application was proposed a decade ago, researchers were not able to demonstrate persistent-mode operation of an MgB_2 based magnet in an SN_2 environment. Thus, to demonstrate the first MgB_2 based persistent magnet in the SN_2 environment, an MgB_2 based solenoid coil was fabricated with a persistent-current switch (PCS). The coil was wound on an SS former in a single layer (22 turns), with an inner diameter (I.D.) of 109 mm and height of 20 mm, without any insulation. The two ends of the coil were then joined to make a PCS to obtain the persistent-current

mode. After a heat-treatment, the whole magnet was installed in the SN_2 chamber. During persistent mode operation of the magnet at ~100 A, the resultant total circuit resistance was estimated to be $<7.4 \times 10^{-14}$ Ω at 19.5 K ± 1.5 K, which meets the technical requirement for MRI application.

Prior to this thesis work, there was only one report on the testing of an MgB_2 magnet in SN_2. The assembled magnet was prematurely quenched, however, at currents ranging from 79 A to 88 A, even though the individual coil could carry 100 A current. Apart from this, this thesis work only reported persistent-mode operation of the MgB_2 coil in SN_2 with current close to 100 A. Therefore, finally, the high current operation of an MgB_2 solenoid coil was achieved in an SN_2 environment above 25 K. For this purpose, an MgB_2 solenoid coil constructed from multifilament *in situ* wire was fabricated via the 'wind and react' method. The coil was wound on a Cu former (I.D. of 130 mm, O.D. of 135.2 mm, and height of 15 mm) with two layers and 23 turns. The coil was able to successfully carry a 200 A current at 28 K in an SN_2 environment.

Table of Contents

List of Figures

List of Tables

Lists of Nomenclature

Abbreviations

AC	Alternating current
Ag	Silver
Al	Aluminium
Ar	Argon
ACMS	Australia china material science conference
ASC	Applied superconductivity conference
B	Boron
BSE	Backscattered electron
BCS	Bardeen, Cooper, and Schriefer
CH_4	Methane
C_8H_{10}	p-dimethylbenzene
$C_4H_6O_5$	Malic acid
CICC	Cable-in-conduit conductor
Cu	Copper
CV	Curriculum vitae
CHPD	Cold high-pressure densification
CIP	Cold isostatic pressure
CT	X-ray computed tomography
CTFF	Continuous tube forming and filling
DI-BSCCO	Drastically innovative-bismuth strontium calcium copper oxide
DECRA	Discovery early career researcher award
DC	Direct current
DSV	Diameter of spherical volume
EDS	Energy-dispersive X-ray spectroscopy
EPE	Expanded polyethylene
Fe	Iron

GL	Ginzburg-Landau factor
GM	Grifford-McMahon
Hg	Mercury
HT	Heat-treatment
HTS	High-temperature superconductor
HIP	Hot isostatic pressure
I.D.	Inner diameter
ISM	Induction/synchronous motor
IMD	Internal magnesium diffusion
LIMD	Local internal magnesium diffusion
LHe, He	Liquid helium, helium
LNe, Ne	Liquid neon, neon
LN_2, N_2	Liquid nitrogen, nitrogen
LH_2, H_2	Liquid hydrogen, hydrogen
LCR	Inductance, capacitance, resistance
MWCNT	Multiwall carbon nanotubes
MLI	Multilayer insulation
MgB_2	Magnesium diboride
Mg	Magnesium
MRI	Magnetic resonance imaging
MT	Magnet technology conference
Nb	Niobium
Ni	Nickle
NbTi	Niobium titanium
Nb_3Sn	Niobium tin
NMR	Nuclear magnetic resonance
O_2	Oxygen
O.D.	Outer diameter
Ph.D.	Doctor of philosophy
PCS	Persistent current switch
PIT	Powder-in-tube
RT	Room temperature

SEM	Scanning electron microscope or microscopy
SFCL	Superconducting fault current limiter
SS	Stainless steel
SST - 1	Steady state superconducting tokamak
SMES	Superconducting magnetic energy storage
SN_2	Solid nitrogen
SmBCO	Samarium bismuth copper oxide
TC, TS	Transitional conductor, Temperature sensor
Ti	Titanium
VSM	Vibration sample magnetometer
VTI	Variable temperature insert
YBCO	Yttrium barium copper oxide
XRD	X-ray diffraction
Zn	Zinc
3D	Three-dimensional

Greek Letters

$\boldsymbol{\varepsilon, \varepsilon_{irr}}$	Effective total emissivity, strain, irreversible strain
$\boldsymbol{\varepsilon_H}$	Emissivity of a hot body
$\boldsymbol{\varepsilon_L}$	Emissivity of a cold body
ξ	Coherence length
$\boldsymbol{\lambda_L}$	London penetration depth
$\boldsymbol{\sigma}$	Stefan-Boltzmann Constant, 5.67×10^{-8} W m^{-2} K^{-4}
$\boldsymbol{\mu, \mu_0}$	Magnetic permeability of a material (or magnetic moment), magnetic permeability of free space (1.26×10^{-6} H m^{-1})
$\boldsymbol{\sigma_{irr}}$	Irreversible tensile stress
$\boldsymbol{\rho}$	DC electric resistivity, material density
γ	Gyromagnetic or magnetogyric ratio
$\boldsymbol{\tau_{sd}}$	Diffusion time
$\boldsymbol{\delta_{sd}}$	Diffusion distance
$\boldsymbol{\rho C_e}$	Effective specific heat

ΔQ_s	External supplied energy
ΔT	Temperature difference

Symbols

A	Area of a cold body or cross-sectional area of a conductor
a, a_1	Radius of the filament or inner radius of a coil, inner radius of a coil
b, a_2	Outer diameter of a coil
B, B_c	Magnetic flux density (T), critical magnetic flux density (T)
B_{c2}	Upper critical field
B_0	Initial magnetic field
C, C	Attachment factor, carbon
C_p	Specific heat
D	Inner diameter of a cylinder
D_{th}	Thermal diffusivity
D_0	Outer diameter of a cylinder
d	Outer diameter of a flange
e	Charge of an electron
E	Weld joint factor
E_c	Critical electric field
E_y	Modulus of elasticity
FS	Design factor
F_{he}	Elastic buckling stress
F_{ic}	Predicted buckling stress
H, H_c	Enthalpy or magnetic field strength (A m^{-1}), critical magnetic field strength (A m^{-1})
H_{irr}	Irreversibility field
I	Current
I_c, i_c	Critical current
i_0, I_{op}	Initial current, operating current
J	Average overall current density
J_c, J_e	Critical current density, engineering current density

K, k	Thermal conductivity
L, l	Length of a conductor/cylinder, inductance or mean free path
M, m	Isotopic mass, mass of an electron
N	Number of multilayer insulation layers or number of turns
n	n-index or n-value
n_{se}	Density of the superconducting electrons
P	Internal design pressure
P_a	Allowable external pressure
P_{rgc}	Pressure inside a system (vacuum)
R	DC resistance
T_c	Critical temperature
Q	Conduction heat load
Q_{rad}	Radiation heat load
Q_{rgc}	Residual gas conduction heat load
R_0	Radius of a cylinder
S_{ho}, S	Allowable stress
S_y	Minimum yield strength
V, V_c	Voltage, critical voltage
T_H	High-temperature
T_L	Low-temperature
t	Thickness of a cylinder/flange, time
T_0	Operating temperature

Organisations

ARC	Australian Research Council
AIIM	Australian Institute of Innovative Materials
ASME	American Society of Mechanical Engineers
ASTM	American Society for Testing and Materials
AMS	American Magnetics Inc.
EMC	Electron Microscopy Centre
ISEM	Institute for Superconducting and Electronic Materials

HTR	Hyper Tech Research Inc.
IEEE	Institute of Electrical and Electronic Engineers
JSPS	Japanese Society for the Promotion of Science
KBSI	Korean Basic Science Institute
MIT	Massachusetts Institute of Technology
NASA	National Aeronautical Space Organisation
UOW	University of Wollongong
UNSW	University of New South Wales

Chapter 1

1. Introduction

1.1. Background of the Thesis Research Project

Magnetic resonance imaging (MRI) is a key diagnostic tool for diagnosing some critical injuries and diseases. By 2010, there were about 30,000 MRI systems installed worldwide [1], and about 3000 systems are being installed every year [2]. This number is increasing more than 6% per year [1, 2]. Around the world, half a million scans are estimated to be conducted each day [1]. By 2017, the MRI scanner market is anticipated to be $7.4 billion [1].

The superconducting magnet is the key component of the MRI system. They are used in the MRI for producing a strong and highly stable (<0.1 ppm h^{-1}) magnetic field required for a better image quality [3]. The majority of current MRIs (which use superconducting magnets) are using niobium titanium (NbTi, critical temperature (T_c) - 9.8 K) or niobium tin (Nb_3Sn, T_c – 18.2 K) based superconducting magnets, and are operated in expensive liquid helium (LHe) baths at 4.2 K [4, 5]. In general, an MRI machine requires 2000 - 3000 L LHe to cool down its superconducting magnet and refill the LHe reservoir [2]. In the case of any problem (quench – superconductor go in the normal state) in the MRI magnet, a huge amount of LHe gets evaporated, and often, the refilling cost is from $50,000 to $90,000 around the world [1]. Furthermore, it is expected that the requirement for LHe for MRI systems may exceed its supply by 2017 [1]. In addition, the currently installed MRI machines around the world are merely serving slightly above 10% of humanity [5], so that there is clear need to serve more of humanity in the developing world. Due to these compelling reasons, there is now an unavoidable demand for the development of LHe-free, and somewhat less expensive, MRI systems [1].

In 2001, magnesium diboride (MgB_2) was observed to be superconducting with T_c of 39 K [2, 6]. MgB_2 conductor is considered as a promising candidate for the development of an LHe-free MRI system. MgB_2 is a good possible replacement candidate for NbTi for certain MRI machines due to its relatively low material and fabrication costs (compared to high-temperature superconductors (HTS)), with the

possibility of operation in the temperature range from 10 – 25 K, promising current carrying capacity below 5 T, 20 K, and availability in long piece length conductor [3-7].

The superconducting magnets can produce a very strong magnetic field in a small volume compared to any normal conductor, such as copper or aluminium based magnets, with significantly lower power consumption. Nevertheless, superconducting magnets come with relatively more complexity and cost in terms of their cooling. Cooling is a must requirement for any superconducting magnet to operate. From the development of the first superconducting MRI magnet in 1962, up to the mid-1990s, all superconducting magnets had been cool down by LHe [7]. After the discovery of HTS materials with T_c above liquid nitrogen (LN_2) temperature in 1986, LN_2 also started to be used for HTS magnet cooling. The price difference between LHe and LN_2 is almost 10 times, and thus, HTS magnets are much cheaper to operate. Nevertheless, the cost of HTS conductor is almost 20 to 40 times higher compared to NbTi [5]. Like HTS and Nb_3Sn magnets, MgB_2 magnets can also be operated in an LHe-free environment using cryocoolers. The magnet fabrication complexity and cost for Nb_3Sn magnets is less suitable for clinical MRI application. Currently, the cost of the typical MgB_2 conductor is up to $ 4.5/m, which is expected to be reduced in the near future [8]. Thus, MgB_2 conductor undoubtedly could offer better economy in term of conductor cost compared to HTS for LHe-free MRI magnet development. Furthermore, MRI magnet is preferably operated in a persistent-mode, which is currently difficult with HTS compared to MgB_2.

A cryocooler can be used to cool down such a practical superconducting magnet to the operation temperature without any cryogen, although the thermal stability of the magnet is often compromised in this route [9]. Thus, it is desirable to use some cryogen to enhance the thermal stability of the superconducting magnet [10].

To enhance the thermal stability of an overall MgB_2 based MRI magnet system, an inexpensive and lightweight cryogen, solid nitrogen (SN_2), is also being considered as a potential option with a cryocooler [11-14]. The high heat capacity of SN_2 can also keep the MgB_2 magnet at its operation temperature, even if the

cryocooler is turned off for short maintenance purposes or due to temporary power failure [15, 16].

This thesis, therefore, presents the original research and development work done for the '***Demonstration of Solid Nitrogen Cooled MgB_2 Based Persistent magnet for MRI Application'***. The following section of Chapter 1 includes a brief introduction to superconductivity.

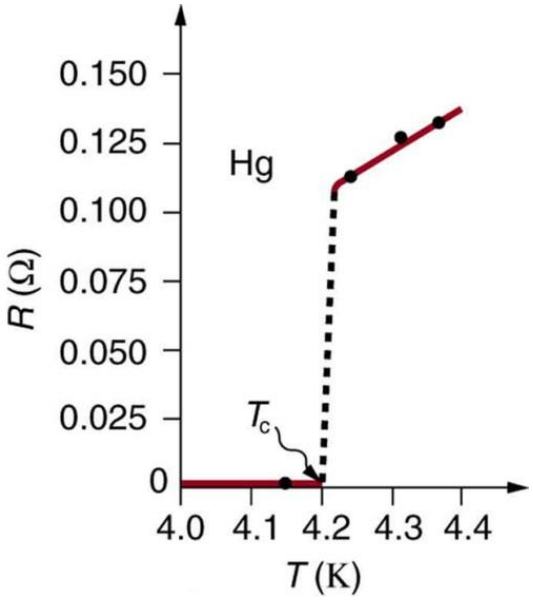

Figure 1-1. Superconducting transition in mercury (Hg) at 4.2 K [17].

1.2. Superconductivity: A Brief Introduction

1.2.1. Superconductivity and its Critical Surface

The dc electrical resistivity of some materials vanishes down to absolute zero below a certain temperature. In 1911, Kamerlingh Onnes in Leiden observed this phenomenon in mercury (Hg) at 4.2 K (see figure 1-1) [18], three years after he first liquefied helium. He named this phenomenon **superconductivity**. The temperature when electrical resistivity vanishes is called the **critical temperature (T_c)** of the material in question. Apart from T_c, the **critical current density (J_c)** and the **critical magnetic field (H_c)** form a critical surface, under which, superconductivity can exist in a particular material as shown in figure 1-2. Above this critical surface, a superconducting material remains in the normal state. Furthermore, it was observed that $H_c(T)$ can be well approximated by a parabolic law as per [19]:

$$H_c(T) \approx H_c(0)[1 - t^2] \quad (1.1)$$

where $t = T/T_c$.

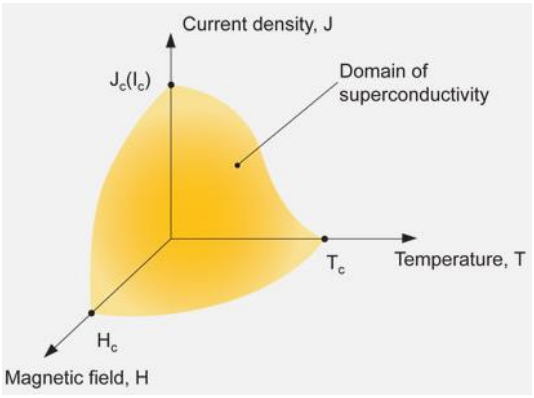

Figure 1-2. The critical surface of a superconductor [20].

1.2.2. Meissner Effect

Apart from the zero dc electrical resistivity of superconducting materials below T_c, superconducting materials exhibit another unique characteristic. In 1933, Meissner and Ochsenfeld observed that in a superconducting state, a weak magnetic field (B, $B = \mu H$, where μ is the magnetic permeability of a material) is expelled from the interior of the bulk superconductor, irrespective of the path used to apply the magnetic field, i.e., $B = 0$ inside the superconductor, as shown by figure 1-3 [21].

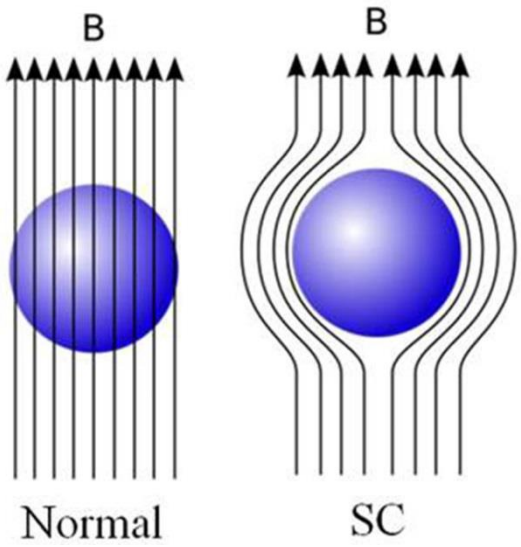

Figure 1-3. Diagram of the Meissner effect [22].

This characteristic of the superconductor is called the **Meissner effect.** This perfect diamagnetism property of a superconductor is more fundamental than the zero dc electrical resistivity (ρ), i.e., ρ = 0 because perfect diamagnetism automatically requires a conductor to be a perfect electrical conductor. The surface supercurrent is primarily responsible for the Meissner effect.

1.2.3. London Penetration Depth (λ_L) and Coherence Length (ξ)

Detailed experiments on field expulsion suggest that when a bulk superconductor placed in an external magnetic field, it cannot produce a perfect surface current which keeps all magnetic fields away from its interior. Some magnetic field always penetrates to certain distance into the bulk superconductor. In 1935, London observed that, while exhibiting the Meissner effect, there was a supercurrent flow within a penetration depth at the surface of the superconductor [23]. London symbolised this ***penetration depth*** as

$$\lambda_L = \sqrt{\frac{m}{\mu_0 e^2 n_{se}}} \tag{1.1}$$

where m and e are the mass and charge of an electron, respectively, and n_{se} is the density of the superconducting electrons.

According to the London theory, within λ_L the magnetic field exponentially decreases with the increasing distance from the edge of the superconducting specimen. The temperature dependence of the $\lambda(T)$ can be approximated by

$$\lambda(T) \approx \lambda(0)[1 - t^4]^{-1/2} \tag{1.2}$$

where $t = T/T_c$.

It was experimentally observed that the λ determined experimentally was somewhat larger thanλ_L. In 1955, A. B. Pippard successfully solved this discrepancy by introducing the concept of the **coherence length (ξ_0)** by proposing a nonlocal generalization of the London theory [24]. In the nonlocal electrodynamics of the normal metal, the ξ_0 plays a role similar to the mean free path, l. The coherence length ξ in the presence of scattering was assuming to be related to that of pure material ξ_0 by

$$\frac{1}{\xi} = \frac{1}{\xi_0} + \frac{1}{l} \tag{1.3}$$

Inside a superconductor, the density of the superconducting electrons changes gradually over a distance ξ. Therefore, there is no sharp boundary between superconducting and normal areas within a superconductor. In the core of a superconducting region, $\boldsymbol{\xi}$ has a constant value, whereas it gradually decreases on moving inside a normal region and is zero at the centre of a normal region as shown in figure 1-4.

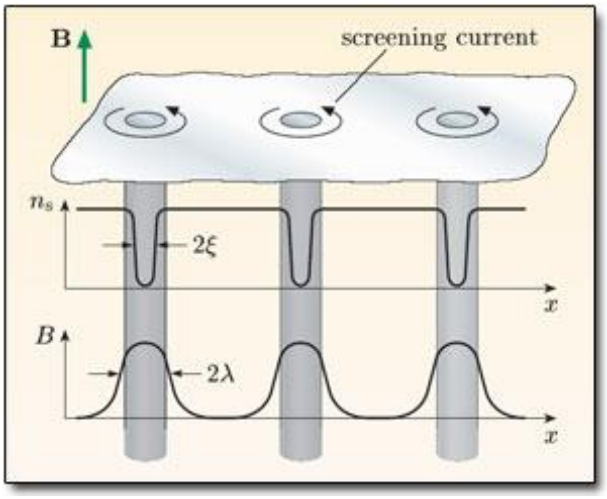

Figure 1-4. The density of superconducting electrons, coherence length, and penetration depth inside a superconductor [25].

According to the theory of Ginsburg, Landau, Abrikosov, and Gorkov on classifying types of superconductors, a superconductor is type I if $\xi > \sqrt{2}\,\lambda$, and type II if $\xi < \sqrt{2}\,\lambda$. The ratio $\kappa = \frac{\lambda}{\xi}$ is called the ***Ginsburg-Landau (GL)*** parameter.

1.2.4. Types I and II Superconductors

The first time superconductivity was discovered in Hg. After that various other materials such as lead and indium were also found to be superconducting. These materials are classified as ***type I superconductors*** or ***soft superconductors*** because of their low H_c value, typically less than ~0.1 T. Thus, these materials are not suitable for constructing a magnet. ***Type II superconductors*** or ***hard superconductors*** have two H_c values. Like a *type I superconductor*, up to the lower critical field, H_{c1}, a *type II superconductor* completely expels magnetic field from its interior, whereas above H_{c1} up to the upper critical field, H_{c2}, partial penetration of

the magnetic field occurs (figure 1-5). This state is called the ***mixed* or *vortex state.*** Typically, the H_{c2} value may be 100 times greater than the H_{c1} [26]. Thus, type II superconductors are suitable for magnet construction.

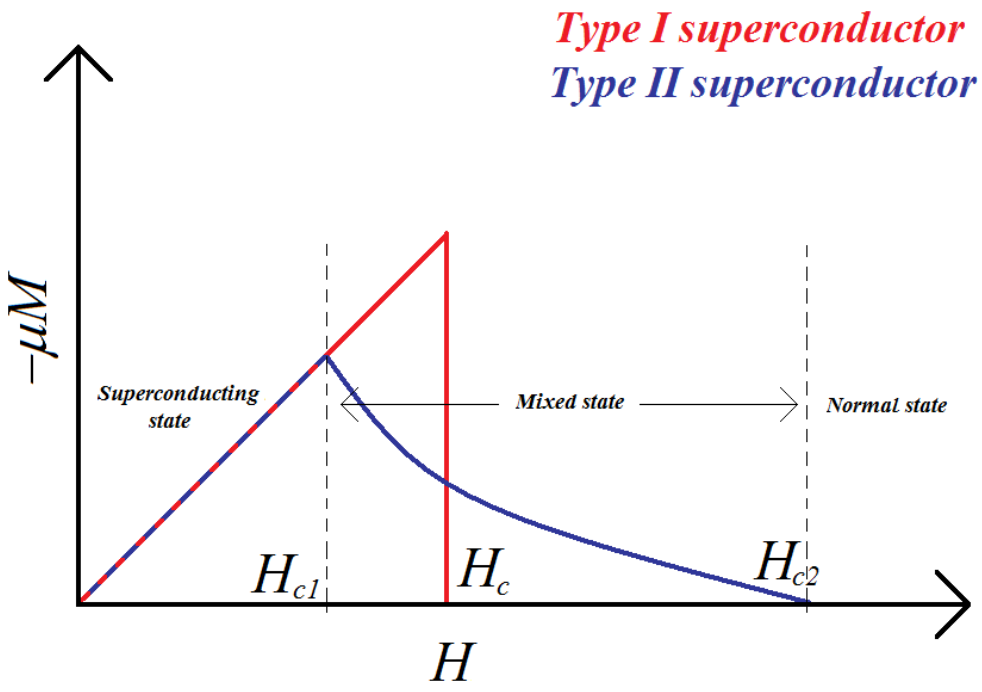

Figure 1-5. Superconducting and mixed states of type I and II superconductors [27].

1.2.5. Mixed or Vortex State

In the mixed or vortex state, many quantized flux vortices, called **fluxons,** are present in a superconducting sea. These fluxons increase in number with an increasing magnetic field, as shown in figure 1-6 until H_{c2} is reached, and then the superconductivity of a superconducting material collapses.

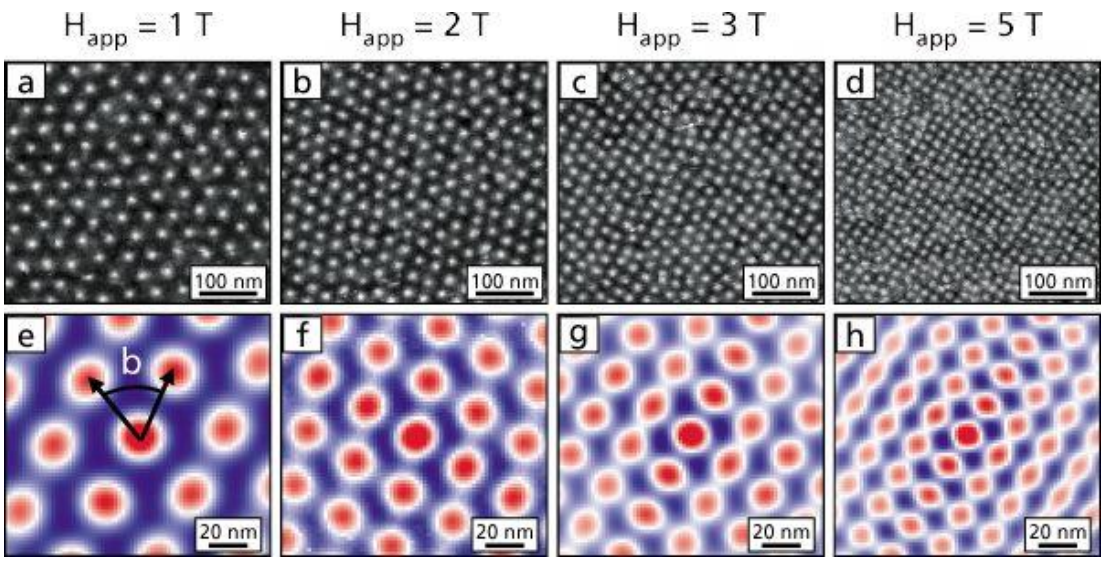

Figure 1-6. Fluxons in superconducting materials. Red in (e), and white in (a) are normal regions; blue in (e), and black in (a) are superconducting regions; white rings in (e) represent the superconducting screening current [28].

Each of these fluxons is a tube of radius $\lambda(T)$, in which a superconducting screening current circulates around a non-superconducting region $\xi(T)$, carrying quantized magnetic field $\phi_0 = \frac{h}{2e} = 2 \times 10^{-15}$ Wb [29], as shown in figures 1-4 and 1-6.

1.2.6. Isotope Effect

Apart from the properties of superconductors discussed above, the T_c of a superconductor also varies with isotopic mass. This means that the transition temperature changes smoothly when two different isotopes of the same element are mixed together. In mercury, when the average atomic mass changes from 199.5 to 203.4 atomic mass units (amu), the T_c changes from 4.185 to 4.146 K [33]. Equation (1.4) may be used to fit the experimental results within each series of isotopes

$$M^{\alpha} T_c = constant \tag{1.4}$$

where M is the isotopic mass and α is an experimental constant.

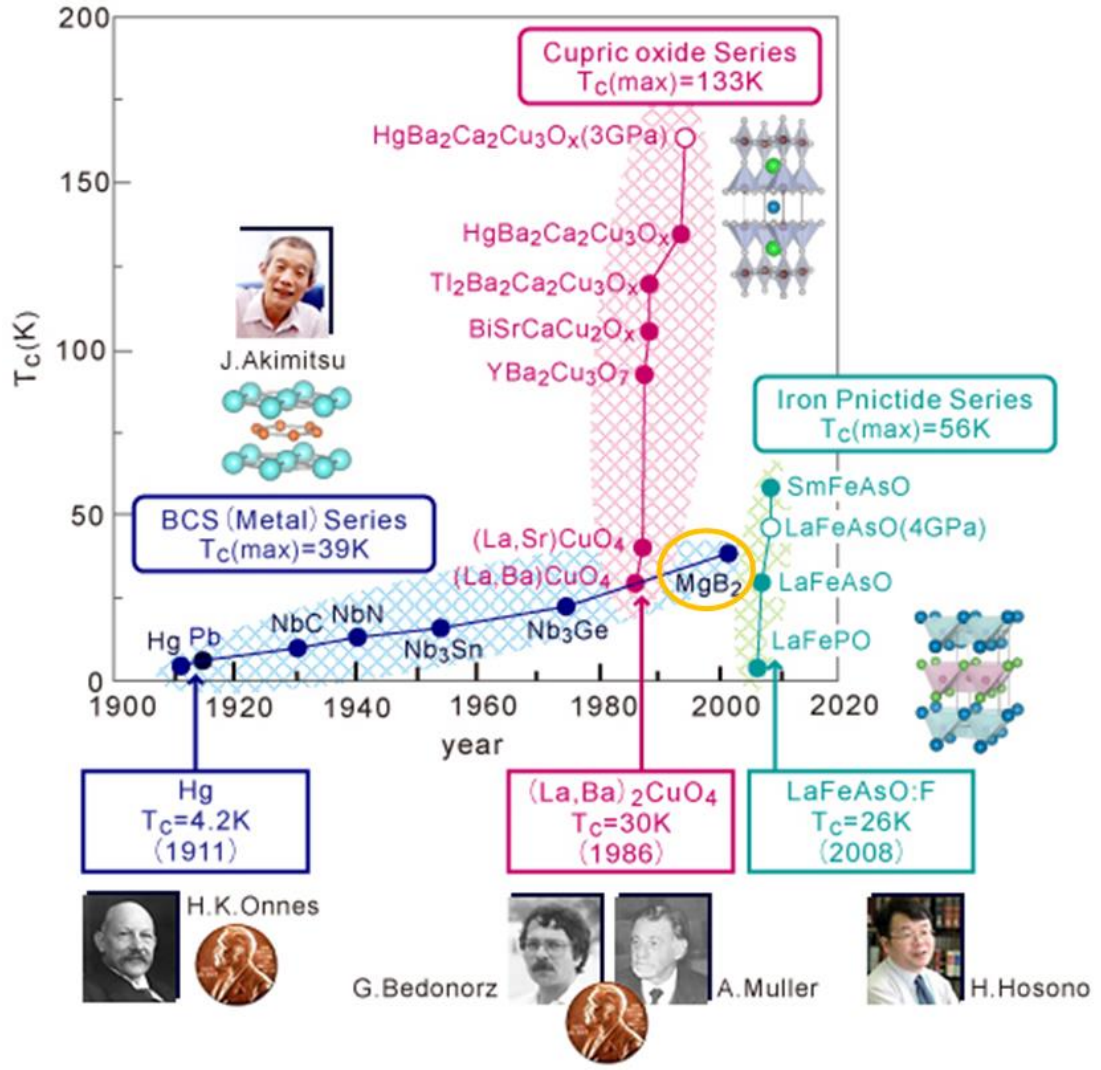

Figure 1-7. The trend of the development of superconductors [30].

The superconducting state of a material is an ordered state of the conduction electrons. In the ordered state, loosely associated pairs of electrons are formed. Bardeen, Cooper, and Schriefer (BCS) explained the nature and origin of the ordering in superconductors via **BCS theory** [31, 32].

Figure 1-7 shows the trend in the development of superconducting materials since superconductivity was first observed in Hg in 1911 at 4.2 K, whereas table 1-1 shows the selected superconductors and their particular critical parameters values. Among the listed superconductors, as aforementioned, type I superconductors are not used for magnet construction, whereas the type II superconductors are used for magnet construction.

Table 1-1. Selected type I and type II superconductors and their T_c and $\mu_0 H_{c2}$ (B_{c2})* [9].

Type I	T_c**(K)**	$\mu_0 H_c$* **(T)**	**Type II**	T_c**(K)**	$\mu_0 H_{c2}$* **(T)**
Ti (metals)	0.39	0.0100	Nb (metal)	9.5	0.2*
Zr	0.55	0.0047	NbTi (alloy)	9.8	10.5**
Zn	0.85	0.0054	NbN (metalloid)	16.8	15.3**
Al	1.18	0.0105	**MgB_2**	**39**	**35-60**#
In	3.41	0.0281	Nb_3Sn(Compound)	18.2	24.5**
Sn	3.72	0.0305	Nb_3Al	18.7	31.0**
Hg	4.15	0.0411	Nb_3Ge	23.2	35.0**
V	5.38	0.1403	$YBa_2Cu_3O_{7-x}$(oxides)	93	150*
Pb	7.19	0.0803	$Bi_2Sr_2Ca_{n-1}Cu_nO_{2n+4}$$	85-110	>100*

* O K, estimated
** 4.2 K, estimated
# 4.2 K, estimated (35 T (⊥), 60 T (||))
$ n = 2, Bi2212; n=3, Bi2223

As of now, among all the listed superconductors in table 1-1, NbTi has been the main superconductor used for a commercial magnet fabrication. Due to the difficulty in magnet fabrication and the high strain sensitivity, Nb_3Sn is mostly used for high-field magnet applications. Due to their brittle nature and the high cost of the HTSs such as yttrium barium copper oxide (YBCO) or bismuth strontium calcium copper oxide (BSCCO), they have only been used for certain applications, for example, current leads or an insert magnet, etc. MgB_2, which was found to be superconducting in 2001, has been developed very quickly and won its place in the commercial market [6]. Due to its possible LHe-free operation combined with high T_c of 39 K and relatively cheaper fabrication cost compared to HTS, MgB_2 has special appeal for commercial applications. This superconductor's application in MRI is the main topic of research in the present thesis.

1.3. References

[1] Wang Z, Van Oort J M and Zou M X 2012 Development of superconducting magnet for high-field MR systems in China *Physica C* **482** 80-6

[2] Lvovsky Y, Stautner E W and Zhang T 2013 Novel technologies and configurations of superconducting magnets for MRI *Supercond. Sci. Technol.* **26** 093001

[3] Patel D, Md Shahriar Al H, Khay Wai S, Qiu W, Kobayashi H, Zongqing M, Seong Jun K, Hong J, Jin Yong P, Choi S, Maeda M, Shahabuddin M, Rindfleisch M, Tomsic M, Dou S X and Kim J H 2016 Evaluation of persistent-mode operation in a superconducting MgB_2 coil in solid nitrogen *Supercond. Sci. Technol.* **29** 4LT02-9

[4] Cosmus T C and Parizh M 2011 Advances in whole-body MRI magnets *IEEE Trans. Appl. Supercond.* **21** 2104-9

[5] Jiayin L 2012 Monofilament MgB_2 wire for MRI magnets. (Master's thesis, Massachusetts Institute of Technology)

[6] Nagamatsu J, Nakagawa N, Muranaka T, Zenitani Y and Akimitsu J 2001 Superconductivity at 39 K in magnesium diboride *Nature* **410** 63-4

[7] Patel D, Hossain M S A, Motaman A, Barua S, Shahabuddin M and Kim J H 2014 Rational design of MgB_2 conductors toward practical applications *Cryogenics* **63** 160-5

[8] Kara D C 2013 Production of a viable product in magnetic resonance imaging using MgB_2. (Master's Thesis, Case Western Reserve University)

[9] Iwasa Y 2009 *Case studies in superconducting magnets, design and operation issues* (New York: Springer)

[10] Wilson M N 1983 *Superconducting magnets* (Oxford University Press)

[11] Iwasa Y, Bascuñán J, Hahn S and Park D K 2012 Solid-cryogen cooling technique for superconducting magnets of NMR and MRI *Phys. Proc.* **36** 1348-53

[12] Bascuñán J, Hahn S, Ahn M and Iwasa Y 2010 Construction and test of a 500 MHz/200 mm RT bore solid cryogen cooled Nb_3Sn MRI magnet *AIP Confer. Proc.* **1218** 523-30

[13] Yao W, Bascuñán J, Kim W S, Hahn S, Lee H and Iwasa Y 2008 A solid nitrogen cooled MgB_2 "demonstration" coil for MRI applications *IEEE Trans. Appl. Supercond.* **18** 912-5

[14] Iwasa Y 2006 HTS and NMR/MRI magnets: Unique features, opportunities, and challenges *Physica C* **445-448** 1088-94

[15] Hales P, Jones H, Milward S and Harrison S 2005 Investigation into the use of solid nitrogen to create a "Thermal Battery" for cooling a portable high-temperature superconducting magnet *Cryogenics* **45** 109-15

[16] Haid B, Lee H, Iwasa Y, Oh S S, Ha H S, Kwon Y K and Ryu K S 2001 Stand-alone solid nitrogen cooled "permanent" high-temperature superconducting magnet system *IEEE Trans. Appl. Supercond.* **11** 2244-7

[17] http://infofavour.blogspot.com/2016/01/short-note-on-superconductivity-and.html

[18] Onnes H K 1911 The resistance of pure mercury at helium temperatures *Comm. Phys. Lab. Univ. Leiden* **12** 120

[19] Onnes H K 1913 *Comm. Phys. Lab. Univ. Leiden* **29** 133b

[20] www.see.ed.ac.uk
[21] Meissner W and Ochsenfeld R 1933 *Naturwissenschaften* **21** 787
[22] http://en.wikipedia.org/wiki/Meissner_effect
[23] London F a H 1935 *Proc. Roy. Soc. (London) A149* 71
[24] Pippard A B 1953 *Proc. Roy. Soc. (London)* 547
[25] http://www.open.edu/
[26] Kittel C 2005 *Introduction to solid state physics* (Hoboken, NJ: Wiley)
[27] http://commons.wikimedia.org/
[28] http://physics.nist.gov/
[29] Abrikosov A A 2004 Nobel Lecture: Type-II superconductors and the vortex lattice *Reviews of Modern Physics* **76** 975-9
[30] www.supera.titech.ac.jp
[31] Bardeen J, Cooper L N and Schrieffer J R 1957 Theory of superconductivity *Phys. Rev.* **108** 1175-204
[32] Bardeen J, Cooper L N and Schrieffer J R 1957 Microscopic theory of superconductivity *Phys. Rev.* **106** 162-4
[33] Reynolds C A, Serin B and Nesbitt L B 1951 The isotope effect in superconductivity. I. mercury *Phys. Rev.* **84** 691-694

Chapter 2

2. Literature Review

This thesis work has been carried out under a project entitled 'Design and fabrication of solid nitrogen (SN_2) cooled magnesium diboride (MgB_2) based persistent magnet for magnetic resonance imaging (MRI) application'. The ultimate aim of this thesis project was to carry out research and development to demonstrate a laboratory scale MgB_2 based persistent magnet in SN_2, which meets the operation requirements for an MRI magnet. Thus, this Literature Review was carried out based on the context of the project.

The first section of the Literature Review briefly discusses MRI, its hardware, why is a superconducting magnet used as the main magnet in the 1.5 T MRI, and why does MgB_2 have good potential for application in future MRI. The second section discusses MgB_2 material, MgB_2 conductor fabrication processes, performance, mechanical properties, and MgB_2 applications. The third section discusses the cooling system, including how SN_2 can be a good potential option as a cryogen in MRI, and the fourth section discusses persistent (superconducting) joining processes for MgB_2 conductors, including the suitability of monofilament MgB_2 conductor for persistent magnet fabrication for MRI, unlike NbTi.

2.1. Magnetic Resonance Imaging (MRI)

Magnetic resonance imaging is known as an **MRI**, which essentially uses the principle of nuclear magnetic resonance **(NMR)**. It has been a powerful tool for the entire medical sector ever since the first human MRI scan was conducted on July 3, 1977 [1, 2]. Before this, an Armenian-American professor and medical practitioner, Raymond Vahan Damadian, reported in *Science* how tumours and normal tissues can be distinguished *in vivo* by NMR [3]. MRI has been used for various patient diagnostics before, after, or during medical treatments or surgical procedures. It is better, compared to an X-ray computed tomography (CT) scan because it does not require any exposure to a radiation [4].

2.1.1. Nuclear Spin and the Gyromagnetic Ratio

To produce an image of an object in MRI, the property of **nuclear spin** of certain atomic nuclei within the object is utilized. As per modern quantum mechanics, certain atomic nuclei possess the property of spin. The spinning process of an atomic nucleus about its rotation axis produces a tiny magnetic field in the direction of its principal rotation axis. The sum of all these tiny magnetic fields from the nuclei within the object is called the magnetic moment, represented by μ. In order to visualize a magnetic moment, consider a proton rotating about its axis. Many positive charges are distributed on proton spheres and are also each rotating about an axis of a proton. Due to the rotation of positive particles, a current of positive charges is generated in a tangential direction. This current generates a small magnetic field in the transverse direction, which is the magnetic moment of that nucleus. Similarly, when electron rotates in an orbit, it also generates a small magnetic field parallel to the rotation axis.

Table 2-1. Gyromagnetic ratios of some nuclei.

Nucleus	**H^{1}**	**C^{13}**	**F^{19}**	**N^{23}**	**P^{31}**
$\gamma/2\pi\left(\frac{\mathrm{MHz}}{\mathrm{T}}\right)$	42.58	10.71	40.08	11.27	17.25

As each of these elementary particles has a mass and radial rotation or angular velocity, thus, atomic nuclei also have the property of angular momentum. In general, an object with angular moment has a tendency to conserve its angular motion until and unless some external force is applied. Thus, for the nucleus, when a perpendicular external field is applied on it, instead of 'tip over', it deflects to a circular motion about the magnetic field, which is called the **precession** of the atomic nucleus. This precession has a certain angular frequency w_0. The w_o of the specific nucleus is linearly proportional to the applied external magnetic field (B_0), and the **gyromagnetic or magnetogyric ratio** γ of that nucleus. This result in the famous **Larmor frequency,** [5, 6] relationship $w_0 = \gamma \cdot B_0$. The gyromagnetic ratio for various nuclei is given in table 2-1 [7]. In MRI, hydrogen nuclei are used to obtain images due to their abundance in the body with its high water content and their high gyromagnetic ratio.

2.1.2. Principle of MRI Imaging

In the early days, NMR was used for spectroscopic analysis before Lauterbur (1973) had the idea of using it as an imaging tool [8]. Images of any living body can be taken in an MRI machine. In this thesis, however, we will only use word human MRI imaging. To take an image of a body part, the human body is placed in the MRI machine. Thus, when hydrogen nuclei in the body's water are placed in a strong magnetic field generated by the large homogeneous magnet called the **main magnet** in the MRI machine, some migrate to a higher energy level (antiparallel to the applied field) and some to a lower energy level (parallel to the applied field). The energy difference between the two levels is linearly proportional to the strength of the applied magnetic field; this phenomenon is called the **Zeeman Effect.** In thermal equilibrium, the number of nuclei in the higher energy level is slightly less than that of the lower energy level. Thus, based on the principle of superposition, the net magnetization direction of the hydrogen nuclei is parallel to the applied field, as shown in figure 2-1 [9]. Furthermore, if the field strength is increased, the number of nuclei in the lower energy level can be increased compared to the high energy level [9]. Thus, strong initial magnetization can yield a better signal for imaging. This is the reason why a high central magnetic field is often preferred in MRI.

The second step in the imaging process is to put a very short pulse of the gradient field on the imaging volume by utilizing **gradient coils** to precisely vary the magnetic field at the known location. Thus, we can take an image of a certain location of the body part. At this stage, the precession frequency of the nuclei at the specific location is known. In the next step, to produce precession in the hydrogen nuclei, another pulse of the magnetic field is applied using **radio frequency (RF) coils** which match the Larmor frequency of the nuclei**,** so that the nuclei are tipped over by 90° from their initial direction and start precession until thermal equilibrium restores them to their initial alignment direction. The decay in the precession is called **free induction decay (FID)**. The FID produces an RF signal, which is acquired using an **RF receiver** coil. These FID data are ultimately utilized to produce an image of the body part. For obtaining a 2D image of the body part, however, several short pulses of the gradient and RF coils are applied on the human body part with some other complex techniques, and FID data are acquired in *k*-space,

which is eventually Fourier transformed into real two-dimensional (2D) space as shown in figure 2-2 [10, 11]. This is how the image is obtained in MRI using the NMR principle.

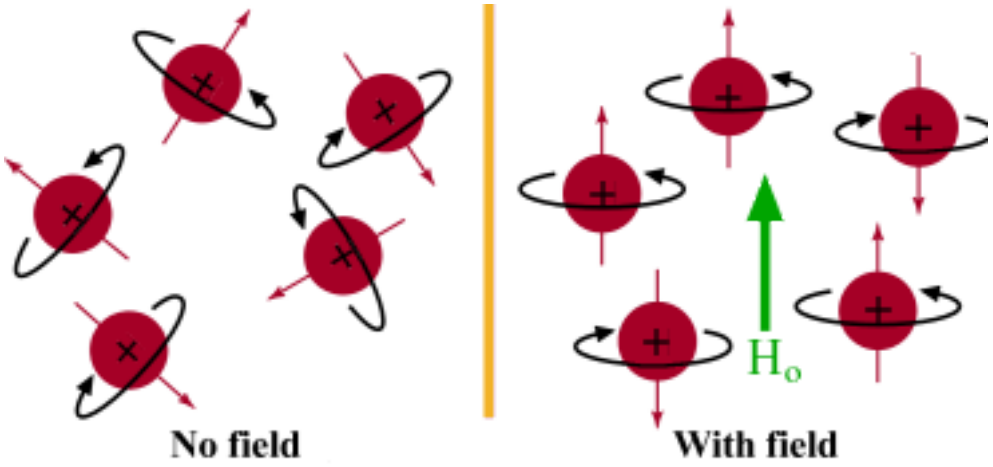

Figure 2-1. Alignment of hydrogen nuclei alignment in a magnetic field [12].

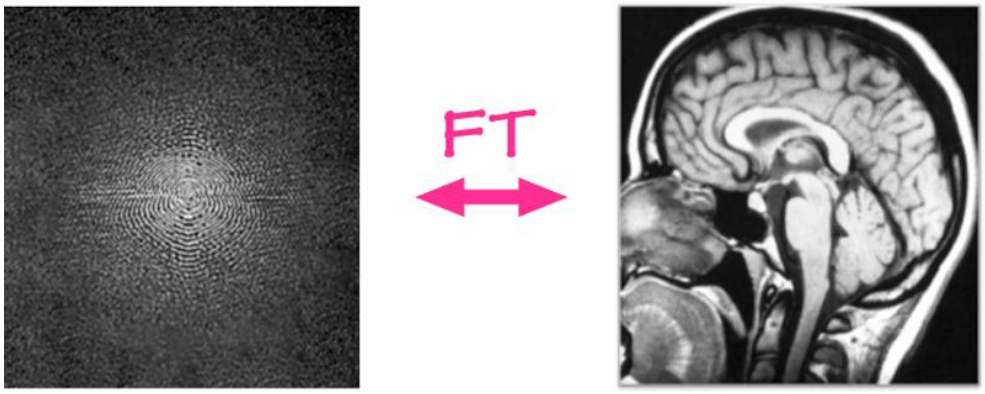

Figure 2-2. *k*-space data transformed into the image using Fourier transformation [10].

2.1.3. MRI Hardware – The Main Magnet

The main hardware in the MRI system is the main magnet, a set of gradient coils, the RF transmitter, the RF receiver, the housing, and a computer for performing various operations for image formation. A cutaway image of an MRI scanner is shown in figure 2-3, whereas a detailed inner view of an MRI is shown in figure 2-4. As can be seen in figure 2-4, the gradient and RF coils are placed on the inner side of the main magnet. The design, fabrication, and demonstration of the laboratory scale superconducting main magnet, which can be utilized for making

more advanced working MRI magnets, are the aims of this thesis. Thus, the discussion is limited to the main magnet of the MRI. A detailed discussion of the other magnets or coils is beyond the scope of this thesis.

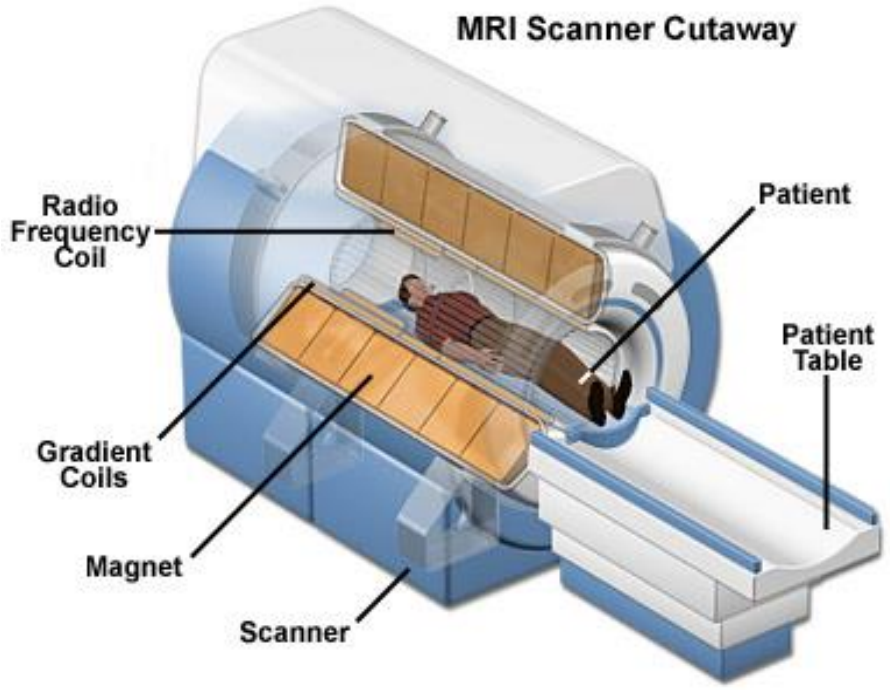

Figure 2-3. Cutaway of MRI scanner [13]

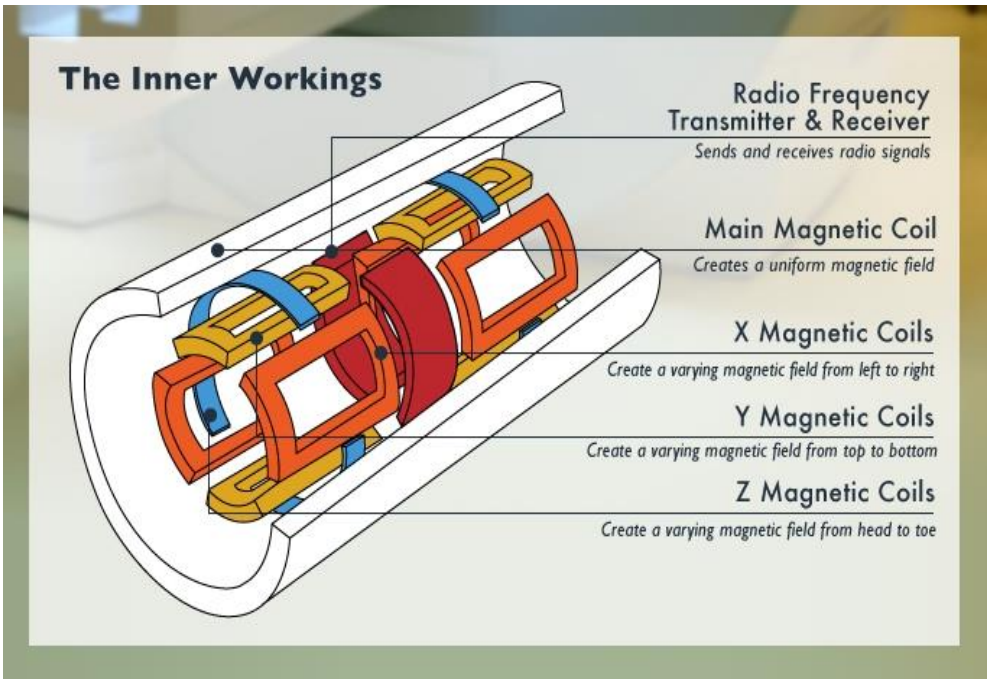

Figure 2-4. Detailed inner view of MRI scanner [14]

Before the advancement of high field superconducting magnets for MRI application, copper (Cu) based electromagnets or permanent magnets were used for the main magnet. Of course, the superconducting magnets are much more expensive to buy and operate compared to low field electromagnets or permanent magnets, but superconducting magnets nevertheless offer several advantages over low field magnets.

2.1.4. Why is a Superconducting Magnet Used as the Main Magnet in the 1.5 T MRI?

Before discussing superconducting magnet application in the MRI, it would be most important to first discuss why a high field (i.e., 1.5 T) magnet is used in MRI? There are several advantages to using a high field 1.5 T magnet in the MRI. Some of the key advantages are higher signal-to-noise ratio, better detection of calcifications and haemorrhage, better detection of gadolinium enhancement, etc., [15]. Often, MRI scans are done in life-threatening conditions, so it is very important that the MRI scan gives as much as information to surgeon or physician to enable wise decisions on the health condition, which could save the life of a patient. Hence, the advantages of using a high field MRI magnet become much more compelling.

It is not economical for clinical application to produce 1.5 T high fields using a Cu-based magnet for several reasons. Some of the reasons are: (i) due to the inherent resistance of the Cu conductor, power consumption for 1.5 T productions would be too high to afford for everyday use, (ii) for producing a high magnetic field, more current naturally needs to be passed through the conductor. Thus, either the conductor needs to be bigger or the number of turns needs to higher. Both eventually lead to large magnet size. In addition to this, to dissipate the heat generated by a resistive Cu magnet, a large cooling reservoir would be required. This could further increase the size of the overall magnet, which is certainly not suitable for hospital settings. Nevertheless, high field homogeneity cannot be achieved in Cu-based magnets in MRI. Therefore, the Cu magnet is certainly not suitable for use in MRI for high field production. The permanent magnets are quickly eliminated from the race because they cannot produce a 1.5 T field.

Therefore, the only option is to use a superconducting main magnet to produce a 1.5 T or higher field. The superconducting magnet can produce a 1.5 T

field with a reasonable magnet size because a superconductor can carry much higher current than a Cu conductor without any resistance. Furthermore, the superconducting magnet can be operated in persistent-mode, which can provide very good field homogeneity, as well as stability, in the magnetic field compared to the resistive Cu magnet. In addition to the previously discussed three key advantages, high field homogeneity is the fourth advantage to using the superconducting magnet in MRI. High field homogeneity directly improves the image quality, as well as offering the option of using certain pulse sequences that cannot be used with a resistive Cu magnet [9, 11, 15]. This is how the high fabrication and operation cost of superconducting magnet is justified compared with the Cu magnet for 1.5 T MRI. Apart from these considerations, for any technology to take its place in the market, in particular when huge cost is involved, it often has to undergo massive scrutiny before it is widely accepted. Likewise, the superconducting magnet application in MRI would have been gone through this. Therefore, a superconducting magnet is used in the MRI application.

2.1.5. Why does MgB_2 have Good Potential for Application in Future MRI?

Superconducting magnets are used in MRI systems with field strength >0.6 T despite the cost, and the problems in designing, fabrication, and complexity of installation [16]. MgB_2 based 0.5 T 'open sky MRI' systems are also available on the market [17]. Different types of superconducting conductors have been used for making commercial MRI main magnets, including niobium titanium (NbTi), niobium tin (Nb_3Sn), and MgB_2. The majority of current 1.5 T MRI systems use NbTi magnets. In an MRI system, high, stable (<0.1 ppm h^{-1}), and uniform (≤10 ppm in 50 cm diameter of spherical volume (DSV)) magnetic fields are required for obtaining high-resolution images of the human body [18]. Only superconducting magnets operated in persistent-mode can offer stable magnetic field <0.1 ppm h^{-1}. Thus, superconducting magnets are an indispensable part of modern MRI systems. The MRI magnets are cooled by an expensive liquid helium (LHe) bath at 4.2 K. The cost of the magnet fabrication, cryostat fabrication, and LHe make the overall system expensive. In addition to that, a superconducting to normal transition, called

'quench' of the magnet, can result in an evaporation of LHe. Refilling with LHe makes the MRI system even more expensive from the operation point of view.

Soaring LHe prices and possible shortages have increased the demand for LHe-free MRI magnets more than ever [19]. Thus, if an MRI magnet can be fabricated using a superconductor which can be operated without LHe, it will be certainly beneficial. In this direction, current NbTi conductor cannot possibly be used for MRI without LHe. If the operation temperature is to be kept at 15-20 K, Nb_3Sn is also not suitable, as its critical temperature is close to 18 K. Thus, the only option is to use high-temperature superconductors such as bismuth strontium calcium copper oxide (BSCCO), rare earth barium copper oxide (REBCO), or MgB_2. Still, in terms of cost, MgB_2 is much better compared to BSCCO or REBCO [18, 19]. Recent detailed market research and cost comparisons of different MgB_2 and NbTi based MRI systems suggest that for underdeveloped or developing countries, an MgB_2 based extremity MRI system would be certainly a viable option for commercialization [20].

In addition, NbTi based MRI magnets are operated in LHe temperature at 4.2 K, whereas their superconducting critical temperature, T_c, is 9.8 K, which leaves only about a 2 K temperature margin [21]. Due to very small temperature margin, current NbTi MRI magnets often have a problem of premature quench. On the other hand, if an MgB_2 MRI magnet is operated at 20 K, it leaves a big temperature margin because of its high T_c of 39 K. Thus, an MgB_2 magnet has a good chance to operate in quench free manner [18], which is certainly beneficial for the protection of the magnet. These are the reasons why MgB_2 has a good potential for application in MRI in the future. These facts are being recognised by the research community and industry, so there are many recent reports, including this thesis, on the efforts toward the development of MgB_2-conductor-based MRI magnet technology [20, 22-33]. Some work was published before this thesis work was started and some published during this thesis work. In fact, *PARAmed* has already commercialized LHe-free MgB_2 based MRI systems, called "open sky MRI" [17].

2.1.6. Summary

In this section of the Literature Review on the MRI, the principle of MRI imaging, MRI hardware, the application of superconducting magnets in MRI, and the key features of MgB_2 for potential application in future MRI have been discussed. The literature clearly suggests that MgB_2 has a very good potential for application in MRI, although, as all technologies require time to be matured, MgB_2 may also need some time and effort before it can take an important place in the commercial market. Thus, this thesis work adds some key technology development toward those efforts. The following section discusses MgB_2 material and current status of its development within the scope of the thesis in further detail.

2.2. Magnesium Diboride (MgB_2)

Magnesium diboride (MgB_2) was synthesized back in the 1950s, but its superconducting properties were first observed by J. Akimitsu group in 2001 [34]. It is a binary compound made up of two elements: magnesium (Mg) and boron (B) [35]. The cost of MgB_2 is lower than for the other high-temperature superconducting (HTS) materials such bismuth strontium calcium copper oxide (BSCCO) and rare-earth element barium copper oxide (REBCO) [18, 36]. The reasons are that the HTS materials are made up of rare earth elements that are expensive compared to the precursors of MgB_2, other materials used for making HTS are more expensive than for MgB_2, and the fabrication process for making HTS is much more complicated than for MgB_2 [37].

2.2.1. Crystal Structure and Basic Properties of MgB_2

MgB_2 has a simple hexagonal crystal structure as shown in Figure 2-5 with space group p6/mmm. The lattice parameters of pure MgB_2 are a = 3.084 Å and c = 3.524 Å, and the interatomic distance is B-B intra-layer 1.780 Å, Mg-Mg intra-layer 3.084 Å, Mg-Mg interlayer 3.524 Å and Mg-B 2.5 Å [35]. The boron atoms are arranged in a honeycomb structure whereas; the Mg atoms are located at the pores of the hexagons. The inter-plane B-B distance is almost double the in-plane B-B distance. The Mg and B layers form ionic bonds by sharing valence electrons with each other. The 2D covalent σ bonds are responsible for holding the B atoms in a

plane, whereas the three-dimensional (3D) metallic π bonds exist between the layers [38]. It is supposed that the B layers are responsible for the superconductivity in MgB_2 [39]. MgB_2 follow conventional Bardeen-Cooper-Schrieffer (BCS) superconductivity [40]. This was apparent when the boron isotope B^{11} was used in the place of B^{10}, and ~ -1 K shift in T_c was observed [41]. The grain size in typical polycrystalline MgB_2 material is from 10 nm - 10 μm [42]. The anisotropy of MgB_2 is from 1.5-5, which is lower than for HTS, which eliminates the need for texturing as for the HTS [43]. The coherence length (ξ) of MgB_2 is ~4 - 5 nm and the penetration depth λ is 100-140 nm, with the Ginzburg-Landau (GL) factor $\kappa = \lambda/\xi$, where ξ is the coherence length, ≈26 at absolute zero [44]. MgB_2 has two superconducting energy gaps $\Delta_1(\sigma) \approx 5$ - 7 meV and $\Delta_2(\pi) \approx 1.5$ - 3 meV [45].

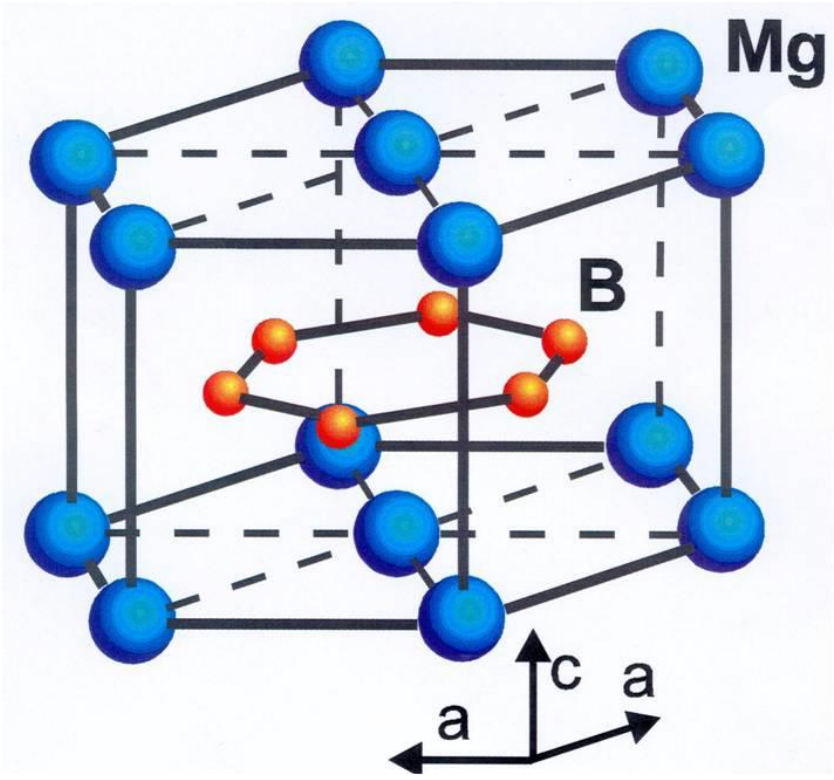

Figure 2-5. Crystal structure of MgB_2 [46].

Pure MgB_2 has a very narrow transition width of less than 1 K with the onset critical temperature ($T_{c\text{-onset}}$) of 39-40 K [34]. Various isovalent and aliovalent atoms with different radii have been substituted to increase T_c, but except for zinc (Zn) (T_c increase of 1 K), all other substitutions decrease T_c. The normal state resistivity ($\rho(T_c)$) of MgB_2 is ~0.4 μΩ cm, which is much lower than for all commercial

superconductors, with a high residual resistivity ratio (RRR) of ~20 [47]. The depairing current density of MgB_2 is ~10^7 A cm^{-2} which is only one order lower than for HTS [48]. Pure MgB_2 conductor achieves a transport critical current density (J_c) on the order of 10^6 A cm^{-2} at 4.2 K in self-field, but ~3.8 x 10^4 A cm^{-2} in 6 T [49]. Pure MgB_2 has a low lower critical field, H_{c1} (0), of 50 mT, an upper critical field, H_{c2}, of 15-20 T, and an irreversibility field (H_{irr}) of 6 - 12 T at 4.2 K [50]. Silicon carbide (SiC) doped MgB_2 wires showed H_{c2} of about 33 T, which is greater than for Nb_3Sn [51].

2.2.2. MgB_2 Suitability for Magnet Fabrication

The magnet-grade conductors are those conductors which meet the rigorous requirements for magnet construction and widespread commercial availability. More than 10,000 superconducting materials so far have been discovered [52]. Out of those, only about 100 materials meet the requirement of having a T_c greater than 4.2 K (usable temperature) and B_{c2} >10 T. When a conductor can tolerate the required magnetic field without a large transport current, the third requirement is that the conductor should carry enough of a current to be practically viable compared to the Cu conductor, that is, the critical current density (J_c) of the conductor should be greater than 1 GA m^{-2} [52]. Finally, it should be possible to fabricate wire or tape using that superconducting material. At this point, only ~10 superconducting materials survive for practical magnet grade application, and MgB_2 is one of the conductors which satisfy all these requirements.

2.2.3. Fabrication of MgB_2 Conductors for Magnet Application

MgB_2 triggered a great deal of interest in the research community soon after the discovery of its superconductivity in 2001 [34], due to the possibility of its operation in cryogen-free, SN_2, or mixed cooling environments. The simple crystal structure, high critical temperature, high J_c, large coherence length, and transparency of grain boundaries to the current flow of MgB_2, make it special [35]. These properties of MgB_2 offer the further promise of some key large-scale applications [53]. As can be seen in figure 2-6, the MgB_2 conductor can open up a new domain of applications for superconducting direct current (DC) magnets, especially below 5 T and 20 K. During the past 15 years, MgB_2 has been fabricated in various forms,

including single crystals, bulk, thin films, tapes, and wires [54-63]. In particular, enormous efforts have been directed towards the improvement of J_c and the understanding of MgB_2 materials [37, 64-66]. The J_c values for MgB_2 have been reported to be as high as 40,000 A cm^{-2} at 10 T and 4.2 K, and 40,000 A cm^{-2} at 5 T and 20 K [67]. This gives proof that the performance of MgB_2 conductors can compete with and even exceed that of the conventional low-temperature superconductor (LTS) NbTi. The J_c of pristine MgB_2 drops rapidly, however, with increasing external magnetic field due to its low upper critical field (B_{c2}) and weak pinning strength. To take advantage of its higher T_c of 39 K, enhancement of B_{c2} and improvement of in-field performance are of primary importance. Attempts to enhance the B_{c2} and flux pinning have been made by using a number of techniques, including additives, substitution, and various mechanical processing techniques [59, 65, 68, 69].

Currently, long-length MgB_2 conductors are commercially available with high J_c and high engineering critical current density (J_e). After the discovery of MgB_2 material, in 2005, kilometre-scale long-length conductors were starting to be produced by Columbus Superconductors using an ***ex situ*** powder-in-tube (PIT) technique [24], and after that, Hyper Tech Research Inc. (HTR) started to produce long length MgB_2 conductors using the ***in situ*** continuous tube forming and filling (CTFF) process [70].

Different types of MgB_2 conductor fabrication techniques have been used, such as PIT technique (*in situ* and *ex situ*), CTFF, internal magnesium diffusion (IMD), and local internal magnesium diffusion (LIMD). Together with these, cold high-pressure densification (CHPD), cold isostatic pressure (CIP), and hot isostatic pressure (HIP) during conductor fabrication have also been applied on the laboratory scale, and improvement in the conductor performance has been noticed. Nevertheless, these techniques are not being used for commercial wire production so far. The commercially used wire fabrication techniques are discussed below. The *in situ* processed MgB_2 conductors have been used for this thesis work.

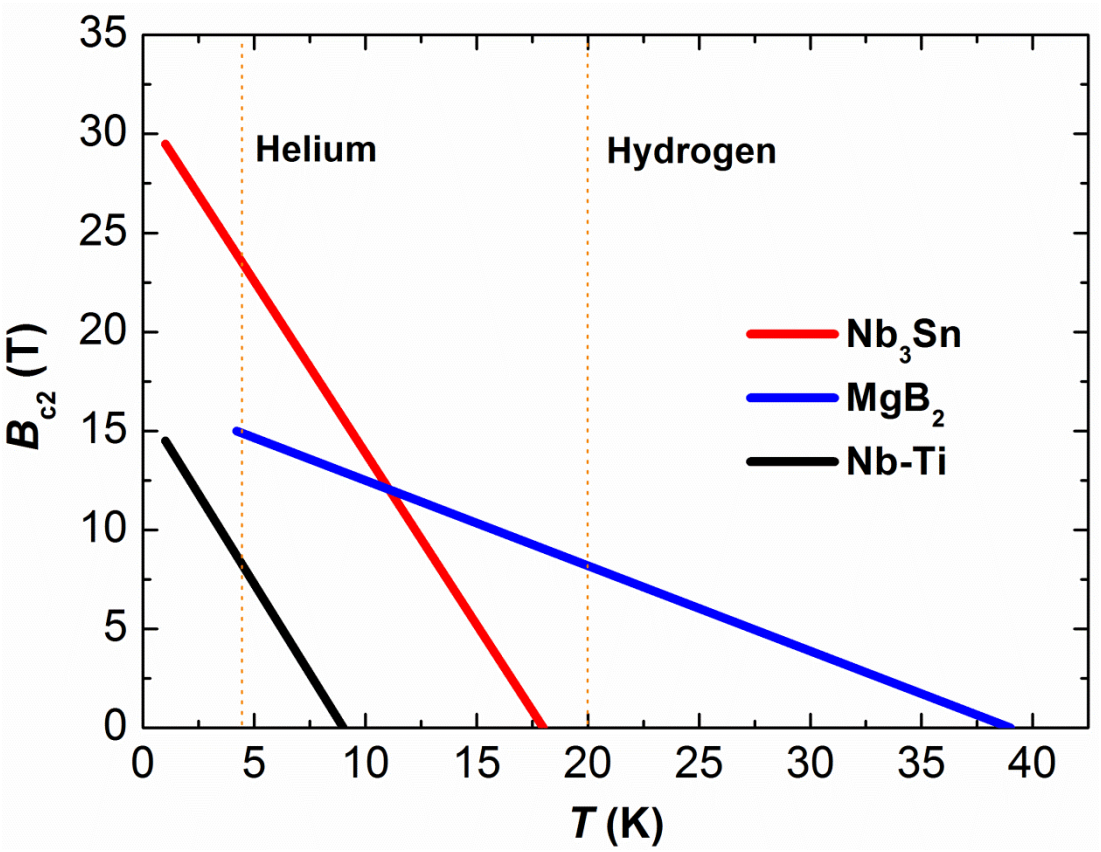

Figure 2-6. Comparison of B_{c2} of low-temperature superconductors (NbTi and Nb_3Sn) and MgB_2 [71].

2.2.3.1. Powder-In-Tube (PIT) Technique (*in situ* and *ex situ*)

The powder-in-tube (PIT) technique is a well-known method for producing long-length superconductors, due to its simplicity [39, 57]. The fabrication steps in PIT wire fabrication are shown in figure 2-7. In this method, a suitable metal tube is filled with the precursor powder, and the tube is drawn or rolled into a wire or tape, followed by heat-treatment. Usually, a heat-treatment temperature of 600 - 950 °C is used with a variety of heating schedules to form well connected MgB_2 filaments. There are two variants of the PIT method, an *in situ* and an *ex situ*. In an *in situ* method, stoichiometric Mg and B are used to fill a suitable metallic tube, such as Cu, niobium (Nb), silver (Ag), nickel (Ni), titanium (Ti), iron (Fe), stainless steel (SS), Cu-Ni, Monel, etc. In an *ex situ* method, already formed MgB_2 powder is used. For improving J_c, however, further suitable heat-treatment (900-1000 °C) is also applied in the *ex situ* case [72]. Due to a possible reaction of Mg with sheath materials such

as Ag, Cu, and Ni below 825 °C, and Fe and Ta at 900 °C, Nb is often used as a barrier between the sheath and the MgB_2 core in an *in situ* process [73]. The requirement for Nb makes an *in situ* processed conductor quite expensive; therefore, the search for another inexpensive barrier material is indispensable.

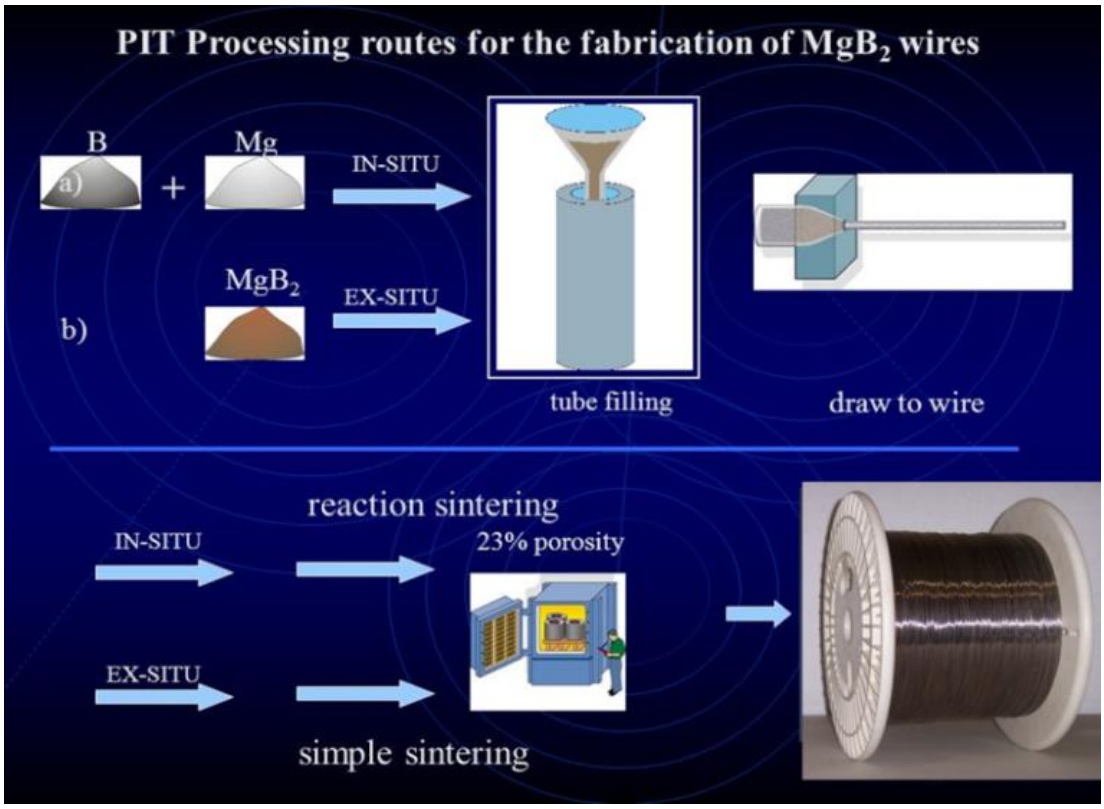

Figure 2-7. The fabrication steps for PIT MgB_2 wire [74].

The *In situ* method has several advantages over the *ex situ* method such as low-temperature reaction processes and easy nanoparticle doping to enhance J_c [58]. On the other hand, the *ex situ* method is more suitable for long lengths, a high packing factor, and complex multifilamentary conductor geometry [58]. The *in situ* reaction yields strong intergrain coupling with a low packing factor, whereas the *ex situ* process yields tightly packed grains, although their intergrain coupling is much weaker [75]. At present, many research groups are actively involved in enhancement of the connectivity of grains in *ex situ* processed conductors [75-78]. Some of the *ex situ* processed tapes show J_c values of ~10^4 A cm^{-2} at 20 K in self-field [79]. In the case of *ex situ* conductors, heat-treatment normally improves the J_c, but it is still lower compared to *in situ* due to relatively poor intergrain coupling [80-83]. Kario *et*

al obtained J_c of 3.5×10^4 A cm^{-2} at 9 T and 4.2 K in *ex situ* MgB_2 with 5% C addition [84].

2.2.3.2. Continuous Tube Forming and Filling (CTFF)

Figure 2-8 contains a schematic illustration of the continuous tube forming and filling (CTFF) process, a technique for the fabrication of MgB_2 conductors. This technique was developed by Hyper Tech Research Inc. (HTR) to prepare long-length MgB_2 wires [53, 70]. In this process, a continuous metal strip (Nb, Fe, etc.) is used as the inner barrier. As this metal ribbon enters and moves through the tube shaping dies, they gradually form it into a 'U' shape. After the composite powder (magnesium (Mg) and boron (B)) is inserted, the closing dies gradually close off the tube. After the tube has been closed, it passes through subsequent dies to reduce the diameter to a fine wire (i.e., 0.832 mm).

So far, HTR has 10 years of manufacturing development experience on various MgB_2 composite conductors. These conductors have been designed by keeping manufacturability in mind. The processing steps are designed to be commercially viable. HTR regularly manufactures composites in lengths over 10 km [85]. Even though long lengths are no limitation, wire quality over lengths >10 km is still not consistent, either due to issues with the manufacturing process or with the starting material [29, 70, 85, 86]. The strands are mainly made from *in situ* powders, with Nb or Fe barriers, a Cu stabilizer, and a Cu- Ni outer sheath (called "Monel"), and there are different filament numbers from 7 to 61 in the final multi-filamentary conductor. Heat-treatment is typically in the 700°C range for 20 to 40 minutes. For reacting and winding the wire, S-glass braid is normally coated on the surface of the conductor as an insulator. Recently, HTR has been working on increasing the filling factor to 30%, which would increase the critical current (I_c) towards practical applications.

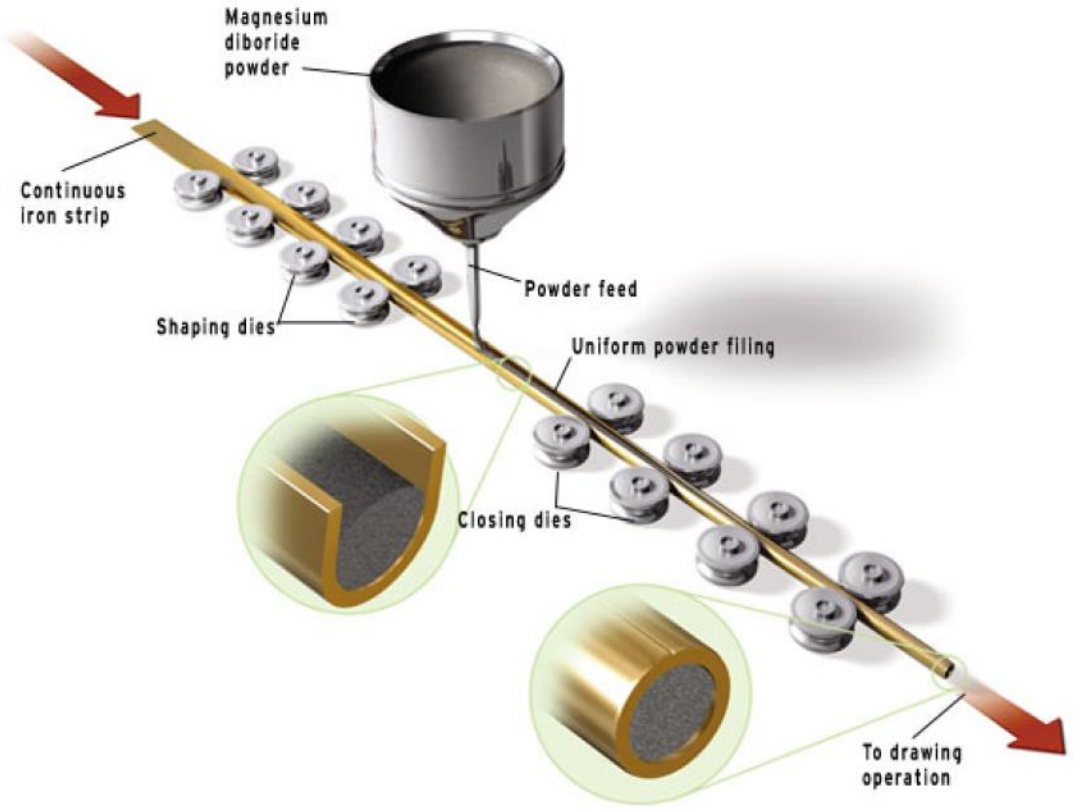

Figure 2-8. Schematic illustration of the continuous tube forming and filling (CTFF) [71].

The monofilament wire, multifilament round '18 + 1 Nb/Cu/Monel' wire, and a multifilament rectangular shaped conductor currently offered by HTR are shown in figure 2-9(a), (b), and (c), respectively. Typical J_c and J_e measurements for standard multifilament MgB_2 conductor manufactured by HTR indicate J_c values of 9×10^4 A cm^{-2} at 4.2 K and 5 T; and 2.1×10^5 A cm^{-2} at 20 K and 1 T [18, 59]. These numbers give critical current (I_c) of 80 and 200 A with a 15% MgB_2 filling factor in the multifilament strands; which produce J_e of 1.4×10^4 and 3.2×10^4 A cm^{-2}, respectively [18]. In this project, some wires made by HTR have been used.

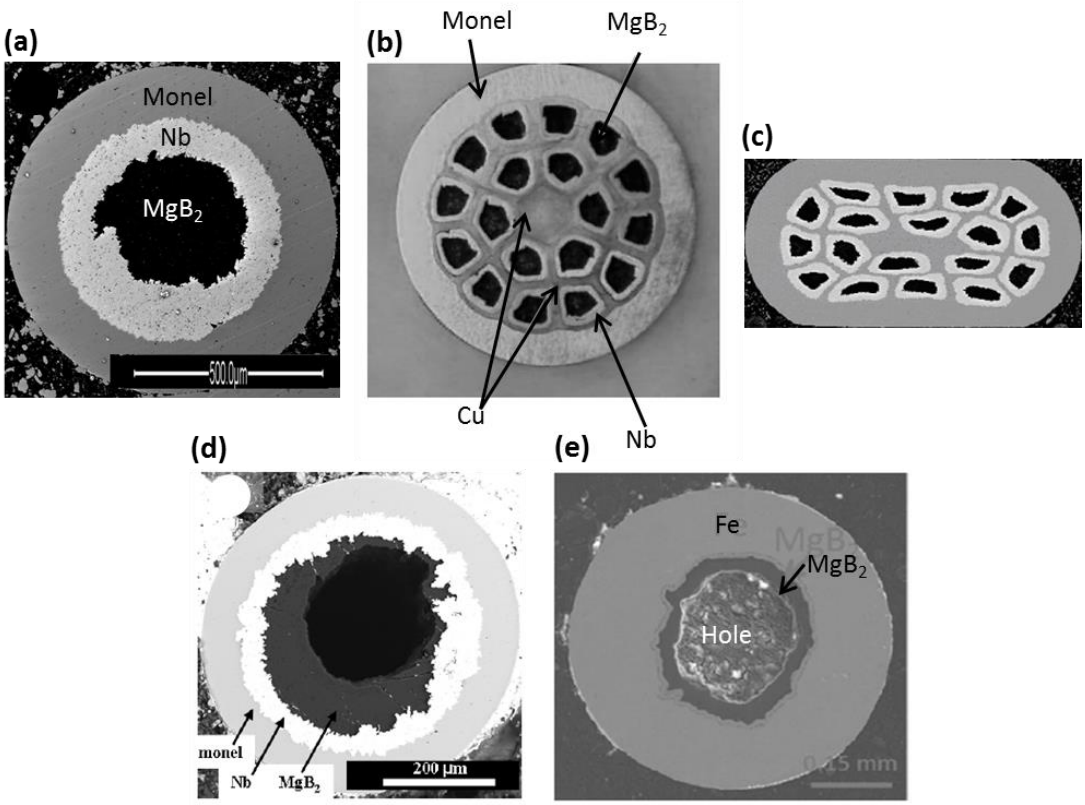

Figure 2-9. MgB_2 wire prepared in various configurations: Hyper Tech (a) monofilament, (b) '18 + 1' round multifilament, and (c) 18-filament rectangular. Reproduced with permission of Hyper Tech Research Inc., (d) internal magnesium diffusion (IMD) processed sample of Li *et al* with full MgB_2 reaction layer [87], (e) IMD processed sample which showed the highest J_c ever for MgB_2 wire of Ye *et al* [88].

2.2.3.3. Internal Magnesium Diffusion (IMD)

The IMD technique is a variant of the *in situ* PIT technique for MgB_2 conductor fabrication. Giunchi *et al* proposed this technique; in fact, initially it was called reactive liquid Mg infiltration [89, 90]. In IMD, a Mg rod is embedded axially in a B-filled tube, and the process continues with a drawing followed by heat-treatment, as shown in figure 2-10 [91-93]. Compared to the conventional *in situ* PIT process, which yields a system of randomly connected MgB_2 fibres associated with copious porosity, an IMD process can produce a dense MgB_2 layered structure with excellent longitudinal and transverse connectivity [94].

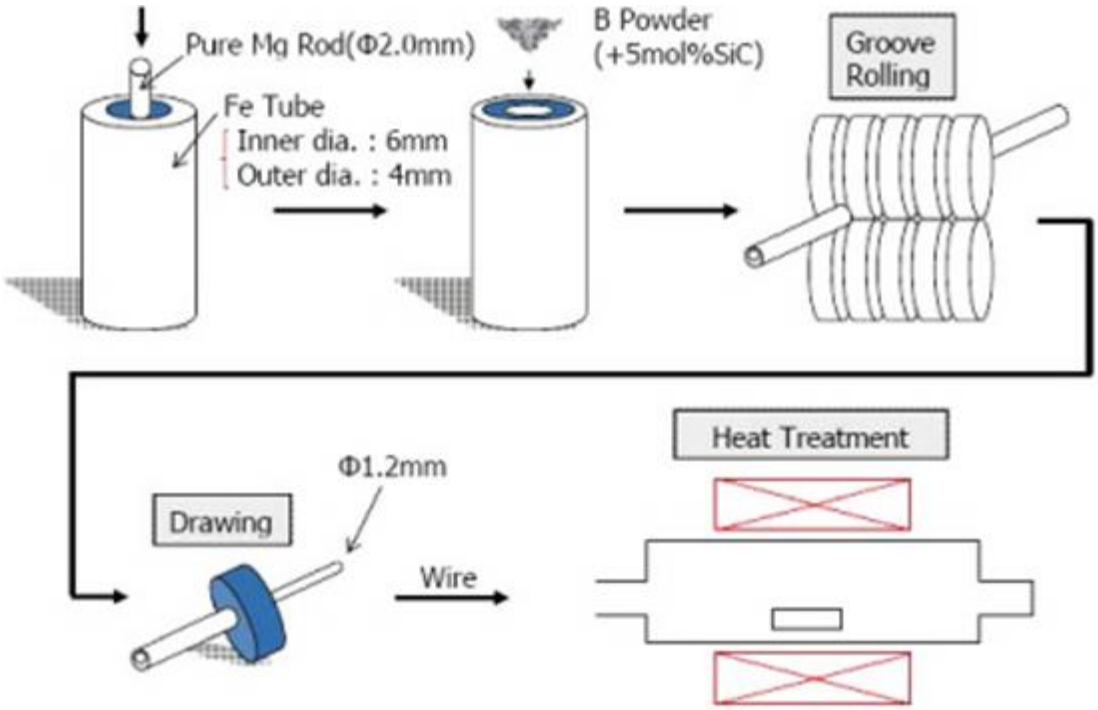

Figure 2-10. Schematic illustration of IMD [92].

Kumakura *et al* attained a high J_c of 1.1 x 10^5 A cm^{-2} at 4.2 K and 10 T in various SiC-doped mono and multifilament MgB_2 wires using the IMD process [95]. Subsequently, Ye *et al* reported J_e of 3.7 x 10^3 A cm^{-2} at 4.2 K and 10 T by doping their B-precursor for IMD processed wires with both SiC and a liquid aromatic hydrocarbon [96]. Li *et al* also prepared a series of monofilament wires using 10 – 100 nm amorphous B that was doped with 2 mol% C by adding methane (CH_4) to the process gases [97-99]. They obtained the best layer J_c value of 1.07 x 10^5 A cm^{-2} at 10 T and 4.2 K, and the best J_e value of 1.67 x 10^4 A cm^{-2} at 4.2 K and 10 T [87]. One of their IMD processed monofilament conductors with a full MgB_2 reaction layer is shown in figure 2-9(d). 37-filament IMD-processed MgB_2 wires were fabricated by Ye *et al* [100]. These wires showed a better J_c value of 7.6 x 10^4 A cm^{-2} at 4.2 K and 10 T compared to wires with a smaller number of filaments (1 and 7 filaments) fabricated under the same conditions [100]. Very recently, the unprecedented performance of MgB_2 wire compared to its competitor NbTi was reported by Ye *et al* [88]. They fabricated high-performance MgB_2 superconducting wires using IMD, in conjunction with p-dimethylbenzene (C_8H_{10}) pre-treatment of the C-coated B powder with nanometre-sized particles, and the resultant Fe-sheathed

conductor is shown in Figure 2-9(e). Due to diffusion of Mg to B sites, a hole was created in the centre of the conductor. The resulting wires exhibited the highest ever J_c of 1.2 x 10^5 A cm^{-2} at 4.2 K and 10 T, and J_e of about 1 x 10^4 A cm^{-2}. Not only at 4.2 K but also at 10 K, the J_c values for the wires fabricated in this study were, in fact, higher than for NbTi wires at 4.2 K in the magnetic field at which the measurement was carried out. At 20 K and 5 T, the J_c and J_e were about 7.6 x 10^5 A cm^{-2} and 5.3 x 10^3 A cm^{-2}, respectively, which are the highest values reported for MgB_2 wires to date [88].

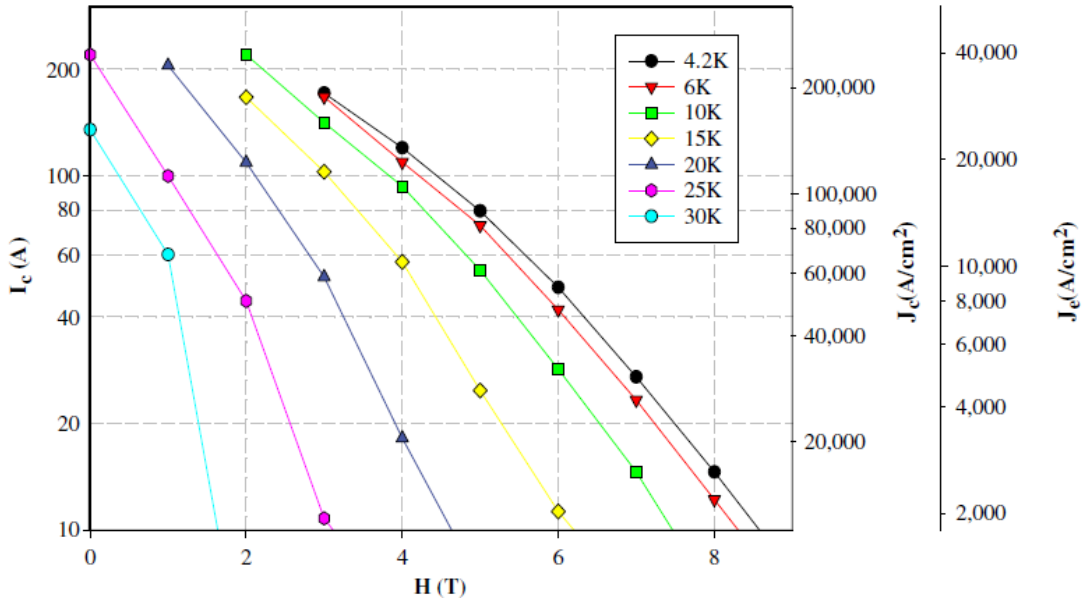

Figure 2-11. I_c, J_c, and J_e properties of commercial multifilament wires produced by HTR [53].

2.2.3.4. Local Internal Magnesium Diffusion (LIMD)

The IMD-processed wires have shown the best performance so far. Recently, Kim *et al* proposed an economical way of producing high-performance MgB_2 wires using coarse Mg powder [101]. Maeda *et al* named this process local internal Mg diffusion (LIMD) because, in this method, bigger particle size Mg (~150 μm) diffuses to B sites and forms highly dense MgB_2 locally [102]. Moreover, ductile Mg coarse powders are elongated during cold-working, leading to an alignment of voids and enhanced grain connectivity; as a result, superconducting

wires with improved performance can be fabricated [71, 101]. In this method, the *in situ* PIT technique is used for producing long length MgB_2 conductors.

Kim *et al* fabricated various samples using coarse Mg with inexpensive C-encapsulated crystalline B, using different heat-treatment conditions [101]. They achieved their best J_c value of 2.7 x 10^4 A cm^{-2} at 4.2 K and 10 T, which is comparable to the best result reported for wires made from expensive amorphous B combined with a C-dopant, such as SiC or malic acid ($C_4H_6O_5$) [101, 103]. Recently, Maeda *et al* reported J_c of 1 x 10^4 A cm^{-2} at 4.2 K and 8 T, using LIMD assisted by CHPD, with inexpensive crystalline B and large-size Mg as the precursors [102].

The current carrying capacities of any MgB_2 conductor depend on its overall fabrication process. Figure 2-11 shows the selected properties (I_c, J_c, and J_e) of commercial multifilament MgB_2 wires produced by HTR. As can be seen in the figure, in the low field region, typically below 2 T and 20 K (MRI magnet operation regime) the I_c, J_c, and J_e are >100 A, >1.5 x 10^5 A cm^{-2}, and >1.8 x 10^4 A cm^{-2}, respectively. In this thesis work, *in situ* processed MgB_2 wire has been used. Thus, the discussion will be limited to *in situ* processed MgB_2 wire only.

2.2.4. Conductor Performance and Boron Powder

The *in sit*u method has been used successfully to make MgB_2 wires and tapes [53]. In most cases, both high purity crystalline or amorphous B powder and small size Mg are used to make the MgB_2 conductor [103]. If this wire is to be applied in an industrial application, however, the costs of the raw materials will be significantly increased, and this needs to be taken into serious consideration [102]. The material cost could be decreased significantly by using low-grade precursors. High purity (98-99%) amorphous B powder is about ten times more expensive than low purity (95-97%) crystalline B powder [102]. Figure 2-12 shows a comparison of J_c in MgB_2 monofilament wires made from different B powders with amorphous and crystalline phases. Crystalline B is known to have the β-rhombohedral structure, which is quite stable, even after high-temperature heat-treatment [101]. Thus, it is hard for crystalline B to fully react with Mg powder to form MgB_2. A relatively long heat-treatment time or high heat-treatment temperature is obviously required. High-

performance MgB_2 conductor, at the moment, is fabricated using amorphous B. As can be seen in figure 2-12, J_c of the wire made from amorphous B (>98%) showed better performance under high magnetic field. In contrast, J_c values for the wire made from crystalline B powder were quite poor under high magnetic field. For example, the J_c was estimated to be below 1000 A cm^{-2} at 10 T and 4.2 K for monofilament MgB_2 wire with crystalline B.

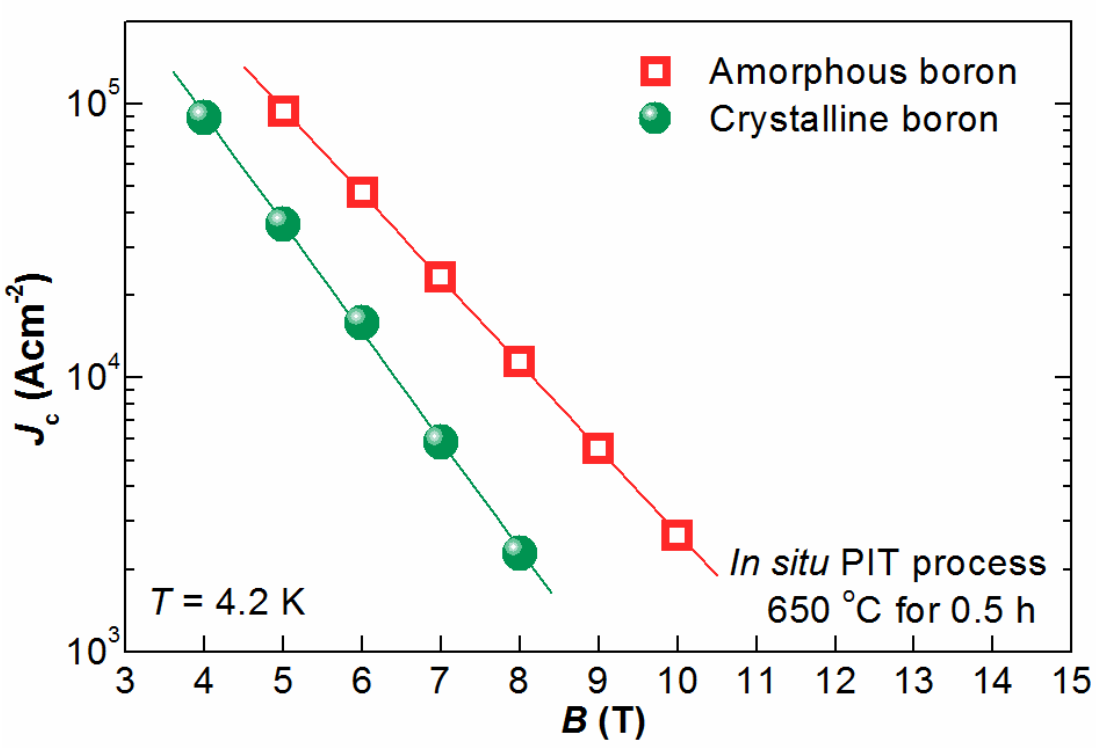

Figure 2-12. Comparison of J_c at 4.2 K for MgB_2 wires made from crystalline and amorphous nano-boron [71].

The J_c of a wire made from an amorphous B may well cross over that of wires made from crystalline B, in the low-field region. This suggests that a wire made from crystalline B may be better compared to amorphous B for a magnet system which operates in the 1- 2 T range for the greater economy [102]. Together with B powder, the conductor fabrication process with chemical doping and mechanical deformation for performance enhancement in the specific application region should be chosen for producing cost effective conductors.

2.2.5. Stress and Strain Effect

The stress and strain tolerance of any superconductor are an important property for its application in a magnet winding because a certain winding tension on a conductor has to be imposed for a compact and tight magnet winding. This stress produces a finite strain on a conductor. Furthermore, during magnet charging, there is also compressive and hoop stress on the conductor [52]. With respect to stress and strain in a conductor, the J_c behaviour of the conductor often changes. The sheath material, geometry, and a number of filaments in the conductor play key roles in the J_c vs. strain behaviour of MgB_2 conductor [104, 105].

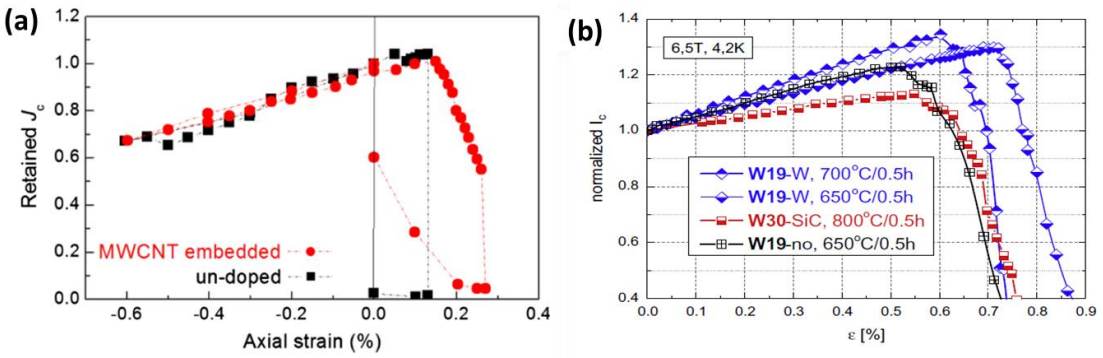

Figure 2-13. (a) Normalized J_c vs. axial strain (%) plot of monofilament undoped and multiwall carbon nanotube (MWCNT) doped MgB_2 wire [104], (b) normalized I_c vs. strain (ε) plot of multifilament undoped, silicon carbide (SiC) doped, and tungsten (W) doped square wire [105].

Figure 2-13 shows the normalized J_c (I_c) vs. strain effect of mono- and multifilament round wire and square wire, respectively. As can be clearly seen in figure 2-13(a), J_c decreases with compressive strain because an MgB_2 filament is already pre-compressed by the matrix material, so further compression leads to additional compressive strain in the filament, and J_c decreases. On the other hand, under an axial strain, the J_c value increases up to the point of irreversible strain (ε_{irr}). This is due to release of the pre-compressive strain. The irreversible tensile strain limit for monofilament undoped wire is 0.16% (figure 2-13(a)), whereas for, the multifilament wire, it is 0.5% (figure 2-13(b)). This means that a multifilament wire can tolerate high axial strain, which is better for magnet application. As can be seen in figure 2-13(a) and (b), certain additional doping further enhances ε_{irr}. Along

with highε_{irr}, MgB_2 has high irreversible tensile stress (σ_{irr}) from 250-800 MPa [106].

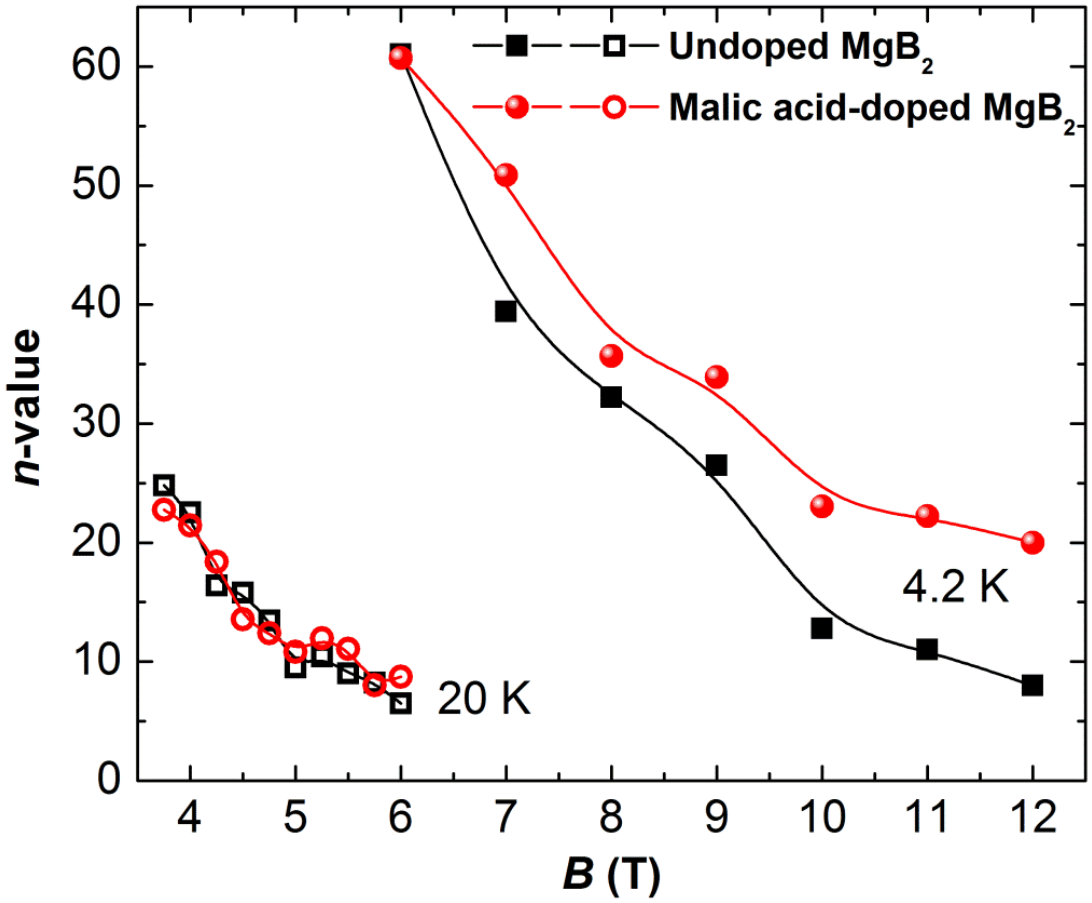

Figure 2-14. Magnetic field dependence of *n*-value for undoped and malic acid treated MgB_2 conductors at 4.2 and 20 K [71].

2.2.6. Index (*n*) Value

The voltage-current characteristic is commonly known to yield a critical index for optimization of the design of superconductors for applications [107, 108]. In particular, a power-law is commonly used for calculating and modelling the nonlinear transition of a superconductor and can be expressed by

$$V = V_c \left(\frac{I}{I_c}\right)^n \tag{2.1}$$

where V is the voltage, V_c is the critical voltage (in case of MgB_2, 1 μV cm^{-1}), I is the transport current, I_c is the critical current, and n is the *n*-value (or *n*-index), which is

calculated in the range of 0.1-1 μV cm^{-1}. Even if superconductor magnets operate under DC conditions, resistive dissipation, which mainly occurs due to index and joint resistances, must be minimized to achieve stable operating conditions [52]. Compared with LTS, HTS show a smoother transition from the superconducting state to the normal state with increasing transport current, with the result that their voltage rise due to a low *n*-value cannot be negligible below the critical current [108]. Therefore, HTS magnets must operate at a lower operating current than their I_c to reduce the index dissipation [52].

The typical *n*-value for persistent magnet-grade conductors is required to be greater than 50 [52]. The index resistance, however, due to low *n*-values <30, makes it unviable to operate an MgB_2-based magnet in persistent-mode with a decay rate <0.01 ppm h^{-1}, even if all the joints are superconducting [52]. Therefore, the *n*-value of a conductor is a parameter that plays an important role in the prediction of its decay properties. For a magnet operated in persistent current mode, the current decay, i, behavior can be expressed by [108]

$$i = \left\{\left({i_0}^{1-n} + \frac{E_c.l}{R.{i_c}^n}\right)e^{(n-1)\frac{R}{L}t} - \frac{E_c.l}{R.{i_c}^n}\right\}^{\frac{1}{1-n}} \tag{2.2}$$

where R is the joint resistance, n is the *n*-value, L is the inductance of the magnet, and l is the total length of the magnet conductor. In addition, E_c is the critical electric field, i_c is the critical current, and i_0 is the initial current. As shown in equation (2.2), the current decay strongly depends on the *n*-value and the joint resistance. When a conductor with a high *n*-value is used as a magnet material, the resistance component due to the *n*-value can be effectively reduced. It is well known that a high quality sample shows a high *n*-value. It is thus essential to fabricate MgB_2 conductor with a highly uniform microstructure, in order to reduce dissipation for magnet applications in persistent-mode operation [108]. Figure 2-14 shows the magnetic field dependence of the *n*-value for undoped and malic acid treated MgB_2 conductors at 4.2 and 20 K. As can be seen in the figure, the *n*-values at 20 K are estimated to be less than 30, so they need to be further increased.

As discussed in [52] with reference to the particular MRI magnet, for keeping the long-term drift rate of the magnetic field below 0.01 ppm h^{-1}, if the *n* value of the

conductor used in that magnet winding is 20, the operating current (I_{op}) of the magnet should be 56% of I_c; if the n value is 30 and 50, I_{op} should be 68% and 79% of I_c, respectively. This is strongly dependent on the inductance of the magnet, however.

2.2.7. MgB_2 Applications

The largest commercial market for superconducting wires is MRI magnets, because, for better image quality, the high field strength is indispensable [7]. An MgB_2 superconductor has the potential to have a great impact on this industry [109]. The impact greatly depends on the price and performance of the conductor at a given temperature and background magnetic field. The first commercial MgB_2-based MRI scanner was produced by Paramed (Genova, Italy) with a magnet fabricated by ASG Superconductors [23]. The tape geometry was used in this project for the MgB_2 conductor [24]. The option of SN_2 as a cryogen due to its high heat capacity is being strongly considered for future MgB_2 based MRI magnet systems [27, 110-112]. The technological challenge of developing the required persistent joints for MgB_2 to be used in MRI needs to be solved completely, however. Due to the difficulties in making consistent persistent joints for multifilament MgB_2 conductor [26, 113], the option of using monofilament conductor is now being considered [25].

Superconducting fault current limiters (SFCL) have been investigated and developed over the past two decades. The key benefits are a negligible influence on the electrical network under normal operating conditions, practically instantaneous limitation, and automatic response without an external trigger [53]. Together with other properties, its sharp transition from superconducting to normal state makes MgB_2 ideal for resistive-type FCL. In the temperature range from 20 - 30 K, however, MgB_2 is a suitable candidate for low-cost inductive FCL coils, too. A low AC loss MgB_2 conductor is an important factor for this application. There have been several reports aimed at the development of an MgB_2-based FCL [114-118].

With low short-circuit current together with small size and weight, the superconducting transformer can be utilized as an energy saving component in power distribution. The current-limiting capabilities of the superconductor can be used to reduce the interrupting ratings of circuit breakers and in some cases, allow the use of mesh networks for a tightly coupled power system [119]. Recently, a 12.5 kVA

MgB_2-based superconducting transformer was designed and tested by Hascicek *et al* [120]. The standard multifilament "18 + 1 Nb/Cu/Monel" MgB_2 conductor made by HTR was used in this work [59, 119].

Superconducting motors and generators have several potential advantages compared to conventional ones. They can be power-dense, lightweight, small, highly efficient, and reliable [119]. In the near future, fuel cell vehicles with hydrogen storage tanks are expected to be developed as next-generation cars [121]. With very low power consumption, a high-temperature superconducting induction/synchronous motor (HTS-ISM) has been proposed to drive a pump for circulation and transfer of liquid hydrogen (LH_2) [122]. An HTS-ISM with a squirrel-cage-type rotor winding composed of MgB_2 wires has been fabricated and tested in both LHe and LH_2 [123-125]. A stator winding using MgB_2 for a fully superconducting motor has been fabricated and tested recently by Kajikawa *et al* [126], which provides evidence for the potential application of MgB_2 in motors. Racetrack coils using MgB_2 for a cryogenic rotor in an LH_2 cooled superconducting generator have been developed for NASA by HTR [59].

MgB_2 has a good chance of being employed as a magnet conductor for high energy physics applications, for example, particle accelerators [127]. An engineering current density of at least 1.2 X 10^5 A cm^{-2} at 4 K in the field of 12-16 T needs to be achieved in the MgB_2 conductor for high energy physics applications [128]. Moreover, Tajima *et al* studied MgB_2 thin films for application in RF structures for particle accelerator [129]. Steadily improving its properties should enable MgB_2 to be used in the windings of undulator magnet installations and replacement of wiggler magnets in accelerator applications, as well as for light-source bending magnets and solenoids for a muon collider [119].

Adiabatic demagnetization refrigerators may be the cooling choice for future NASA instruments operating in space that features detectors operating well below 1 K [130]. A salt pill is used as a paramagnetic material, and these devices produce cooling by manipulating the entropy of this material. The thermal switch between the pill and a heat sink is opened and closed by ramping the magnetic field up and down. The heat is then pumped up a chain of stages, each at successively higher temperatures, and each stage requiring a superconducting magnet. Currently, NbTi

and Nb_3Sn are used at 4 K and 10 K, respectively, for the magnet conductor, whereas NASA is considering MgB_2 as a magnet for operation at 15 K [119]. For getting entry into this application, however, MgB_2 may have to fulfil stringent requirements of conductor size in the range of 0.075 – 0.200 mm with an I_c in the range of 3 – 30 A in 3 – 4 T magnetic field at 15 K [119].

Since the 1970s, magnetic separation has been increasingly used for the purification of liquids, such as heavy-metal-ion removal from laboratory wastewater, purification of kaolin clay in the paper coating industry, waste recycling in the steel industry, and recycling of glass grinding sludge in cathode-ray-tube polishing factories [131]. Zhu *et al* have developed a NbTi based 5.5 T magnetic separator [132]. The bore sizes of these magnets are in the range of 1- 2 m; hence, they require considerable lengths of the conductor. MgB_2 can offer potential low-cost wire with conduction cooled operation in the 10 – 25 K range.

Superconducting magnetic energy storage (SMES) and magnetic levitation trains require the storage of energy in fairly large coils. Due to the higher volume of superconductor, over time, MgB_2 as a relatively cheaper conductor can offer cost effectiveness for this application. The typical field requirement in both applications is in the range of 2 – 5 T. Continuous demand for energy and high public traffic, especially in metropolitan cities of the developing world will lead to significant development of both these devices. MgB_2 may have to achieve better performance at 10 – 25 K operation, however, to suit this application. A 100 MJ SMES system with advanced superconducting power conditioning using MgB_2 has been conceptualized by Naoki *et al* [133], whereas several theoretical studies on MgB_2 in this application have been reported [134-137]. Most recently, Ye *et al* reported that the record high critical current density of 7.6 x 10^5 A cm^{-2} at 20 K and 5 T for MgB_2 conductor produced by the internal Mg diffusion process can open a window for application in magnetic levitation trains [88].

2.2.8. Summary

This section of the Literature Review has presented the crystal structure and material properties of MgB_2, its suitability for magnet application, the MgB_2 conductor fabrication process, MgB_2 conductor performance and the boron powder

effect on the cost of the conductor, the stress and strain effect, the very important parameter, the '*n value*', for persistent-mode operation, and lastly MgB_2 applications. In the last 15 years, MgB_2 material and conductor production have been advanced significantly. At this stage, MgB_2 is certainly ready for practical application. In terms of the conductor fabrication stage, however, somewhat more production is required to make it cost competitive with existing NbTi conductor. The next section of the Literature Review discusses cryogenic cooling.

2.3. Cryogenic Cooling

As mentioned above, a superconducting material only shows superconducting behaviour below a certain temperature. This means that each superconductor has to be cooled down to a certain cryogenic temperature.

2.3.1. Cooling Options for Superconducting Magnets

Until 1990, all superconducting magnets were cooled down by LHe and were thus classed as **'wet magnets'**. After the discovery of HTS materials in 1986 and the commercialization of the HTS conductors with advances in cryocooler technology, the development of LHe-free operation has meant that '**dry magnets'** with no cryogen (LTS and HTS) have started to be developed [138, 139]. The dry magnet system is less cumbersome to design and fabricate, provided that the magnet generates virtually no dissipation on its own, e.g., AC losses, under normal operating conditions [52]. There are five cryogenic cooling methods that are considered for cooling any magnet system [52].

2.3.1.1. Bath-Cooled Cryostable

Magnet systems built in the early 1980s were the bath-cooled cryostable system. In this type of cooling system, each turn of a magnet is in contact with the liquid cryogen.

2.3.1.2. Bath-Cooled Adiabatic

In this type of magnet system, the winding pack is very dense and there is no direct contact of each individual turn with the cryogen, rather, the entire magnet is

cooled through its outer surface, and the rest of the winding pack is cooled by conduction. These types of magnet systems are conducive to high performance.

2.3.1.3. Force-Cooled Cryostable

In this type of magnet system, the conductors are made up of cable-in-conduit conductor (CICC), and the liquid cryogen passes through it. This type of cooling system is mainly used in large-scale applications.

2.3.1.4. Force-Cooled Quasi-stable

In this type of magnet system, the cryogen passes through the passage inside the magnet winding pack, but the cryogen does not make contact with each individual turn.

2.3.1.5. Cryocooled

In this type of magnet system, the magnet is directly connected with a cryocooler, and the cooling within a winding pack is done by conduction.

2.3.2. Liquid Cryogens

Up until the 1990s, LHe was the main cryogen that was used for most superconducting magnets. Since the discovery of the HTS materials, however, many other cryogens are also being considered as cooling sources, depending on their boiling point temperature at atmospheric pressure. There are six usable liquid cryogens, oxygen (O_2, 90.18 K); argon (Ar, 87.28 K); nitrogen (N_2, 77.36 K); neon (Ne, 27.09 K); hydrogen (H_2, 20.39 K); and helium (He, 4.22 K). In this regime, however, LHe, and LN_2 are mostly used for magnet cooling purposes.

2.3.3. Solid Cryogens

The main purpose of designing a wet magnet, or magnet with a certain cryogen, is to provide high heat capacity to a cold mass, that is, thermal stability. The large enthalpy density of LHe in a wet magnet at 4.2 K is 2.6 J cm^{-3}, which is about ~10,000 times higher than the Cu enthalpy density of ~0.0003 J cm^{-3} in the absence of any cryogen [52]. Thus, it is always beneficial to use cryogen for cooling a superconducting magnet.

2.3.4. Why could Solid Nitrogen be a Potential Option for the MgB_2 MRI?

As mentioned earlier, the unique possibilities for the operation of superconducting magnets (i.e., persistent-mode) make them ideal for MRI with a central field strength >0.6 T [36]. Thus, in the majority of commercially available MRI systems, superconducting persistent magnets based on NbTi have been used [18]. These magnets, which are cooled in an LHe bath at 4.2 K, cannot currently be avoided. Thus, the high operation costs of MRI systems are obstructing their extensive use in developing and underdeveloped countries [20].

To fulfil the above requirements, the MgB_2 magnet, which can be operated in an LHe-free manner, is considered to be one of the potential candidates for next-generation MRI application [23, 29]. The MgB_2 based MRI magnet is considered for operation at temperatures of 15-20 K to obtain the optimal benefits of its superconducting properties and cost of cooling [28, 30, 110]. In fact, in this temperature range, a cryocooler can readily give very good cooling capacity to cool a magnet. In a dry magnet, however, the thermal stability of MgB_2 can be somewhat compromised. Thus, it is always favourable to use some cryogen for cooling purposes.

Therefore, it has been reported that the heat capacity of MgB_2 magnets can be significantly enhanced by cooling them by using SN_2 with a cryocooler [140]. As can be seen in figure 2-15, SN_2 has a high heat capacity compared with other solid cryogens. Solid neon is ruled out of the choice because it is about 200 times more expensive than SN_2 on a volume basis [52, 141]. It is well known that the high heat capacity of SN_2 can enable a magnet to operate for a certain time period in the absence of a cooling source (i.e., cryocooler) [27], which are suitable for areas where power failure is common.

Thus, there are three major benefits to using SN_2 as a cryogen: (i) enhanced thermal stability against premature quenches due to the higher heat capacity, (ii) the simpler system dynamics, and (iii) the possibility of operation of the magnet in the absence of the cooling source, i.e. cryocooler [142]. These are the reasons why solid nitrogen could be a potential option for the MgB_2 MRI.

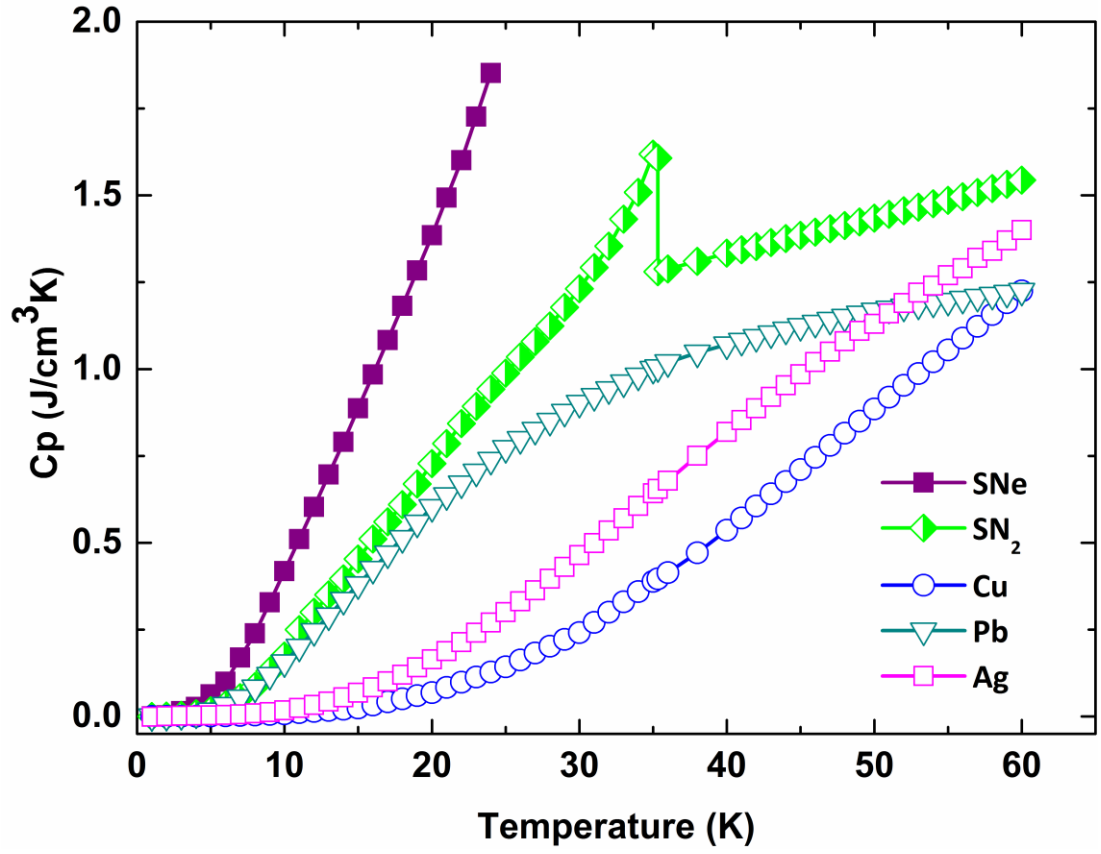

Figure 2-15. Heat capacity vs. temperature plots of various solid cryogens and other substances [5, 16].

2.3.4.1. Formation of Solid Nitrogen

The formation of SN_2 is usually conducted using LN_2 in two ways. The LN_2 is vacuum pumped, and due to the reduction in the vapour pressure of LN_2, LN_2 slowly starts to reduce its temperature. At a temperature of ~63 K, LN_2 changes it phase and goes into the SN_2 phase. Instead of vacuum pumping, the temperature of LN_2 can also be reduced by a cryocooler down to 63 K. In this way, SN_2 can also be formed.

Nakamura *et al* observed that the thermal contact between magnet and cryogen would be poor if the formation of SN_2 was done by vacuum pumping [143]. Hence, the reduction in the temperature is better done by conduction cooling using a cryocooler. In this thesis work, SN_2 was formed by conduction cooling using a two stage Gifford-McMahon (GM) cryocooler.

2.3.4.2. Solid Nitrogen Cooling Systems

The first cooling system using SN_2 was designed and tested by Haid *et al* for a magnet composed of six double pancake coils of BSCCO-2223/Ag composite tape [144]. The cold container was housed in a single-walled cryostat. The estimated heat load on the cold container was 400 mW. The cold container, cryostat, and tubes were composed of Cu, Al, and SS, respectively. They were able to operate this system down to 20 K. Isogami *et al* conducted a study on the thermal behaviour of an SN_2 impregnated magnet system under transient heating [145]. They reported that the magnet stability was significantly enhanced in the SN_2 environment. Haid *et al* demonstrated that by using SN_2 as a heat capacitor, the warming time of the system from 20 K to 40 K could be more than 1 day [146]. Nakamura *et al* observed that the thermal stability of the HTS tape was drastically improved in SN_2 when it was formed by conduction cooling [143]. In 2004, Bascuñán *et al* tested the first MgB_2 based racetrack coil in the SN_2 environment at 10 K [147]. Subsequently, Bascuñán *et al* presented a status report on their 0.6 T/650 mm, room temperature (RT) bore, SN_2 cooled MgB_2 demonstration coil for an MRI [140]. They used a two-stage GM cryocooler and cooled down their magnet to 10 K. Yao *et al* reported an SN_2 cooled MgB_2 demonstration coil for MRI application [27]. Due to poor thermal contact between the SN_2 'can' and the 2^{nd} stage of the cryocooler, they were only able to cool down their magnet to 14 K. Song *et al* designed and tested a cooling system using SN_2 for an HTS SFCL [148]. They also used a two-stage GM cryocooler and were only able to cool their SFCL down to 30 K because the heat load on their cooling chamber was higher, about 6.4 W. First, Bascuñán *et al* cooled their Nb_3Sn magnet down to 4.2 K using mixed cryogen cooling, both SN_2 and LHe [149]. Subsequently, Kim *et al* designed and tested their mixed cryogen cooling system using SN_2 and LNe for SMES [150]. They used a two-stage GM cryocooler that had a cooling capacity of 35 W and 0.8 W at 41 K and 4.2 K, respectively. Due to the considerable high heat load on the system, about 17.582 W, they were only able to cool down their system to 20 K. Recently, Pradhan *et al* reported that they had found leaks at a low-temperature in the dissimilar material joining between SS and Cu in their toroidal field coils during operation of the Steady State Superconducting Tokamak (SST – 1) [151]. Hence, in order to avoid any dissimilar material joining,

in this thesis work, the entire cooling system was designed and fabricated using SS, except for the radiation shield, to avoid any low-temperature leaks and keep residual gas conduction at a minimum by keeping best vacuum possible.

2.3.4.3. Thermal Diffusion, Transient Heating, and Thermal Dry-Out in SN_2

Thermal diffusion is the property of a solid material that indicates how fast a material can diffuse heat. The **Thermal diffusivity** D_{th} ($m^2\ s^{-1}$) strongly depends on the material density (ρ), thermal conductivity (κ), and specific heat (C_p) by the following relation [52]:

$$D_{th} = \frac{\kappa}{\varrho . C_p} \tag{2.3}$$

The time required, $\tau_{sd,}$ for any heat pulse applied to one location to reach another location at a distance, $\delta_{sd,}$ is given by [52]:

$$\tau_{sd} = \frac{1}{D_{th}}\left(\frac{\delta_{sd}}{\pi}\right) \tag{2.4}$$

Table 2-2 lists the approximate values of the D_{th} and τ_{sd} for δ_{sd} = 10 mm of SN_2, and Cu utilizing $\rho\,(T)$, $\kappa\,(T)$, and $C_p\ (T)$ data from [152-154]. As can be seen from the table, compared to Cu, the thermal diffusivity of SN_2 is much lower at 20 K, which indicates that SN_2 is not a good heat diffuser. Furthermore, the time required for heat diffusion of Cu is much lower compared to SN_2 at 20 K. Thus, in order to utilize reasonable thermal diffusivity and a reasonable diffusion time for SN_2, it is advisable to operate an MgB_2 magnet around 15 K instead of 20 K. As the heat capacity of SN_2 is very high, however, it would be acceptable for SN_2 to absorb heat very slowly compared to the heat diffusion time required to keep the temperature uniform around magnet. Thus, SN_2 is better for use in the persistent-mode magnet where there is no or very low heat production.

Table 2-2. Approximate values of the D_{th} and τ_{sd} for δ_{sd} = 10 mm of SN_2 and 10 mm of Cu [52].

T (K)	D_{th} [mm^2 s^{-1}]		τ_{sd} [s] for δ_{sd} = 10 mm	
	SN_2	Cu	SN_2	Cu
5	157	0.36 x 10^6	0.06	27 x 10^{-6}
10	70	0.17 x 10^6	0.14	60 x 10^{-6}
20	0.58	0.29 x 10^5	17	0.3 x 10^{-3}
30	0.22	8000	46	1.3 x 10^{-3}

As the thermal diffusion distance is the square root of the thermal diffusion time according to $\delta_{sd} \propto \sqrt{\tau_{sd}}$ (from equation 2.4), in the event of **transient heating**, only a very small thickness around the magnet will be able to absorb heat, which is a disadvantage of SN_2. Thus, SN_2 might not be suitable for a magnet which often quenches.

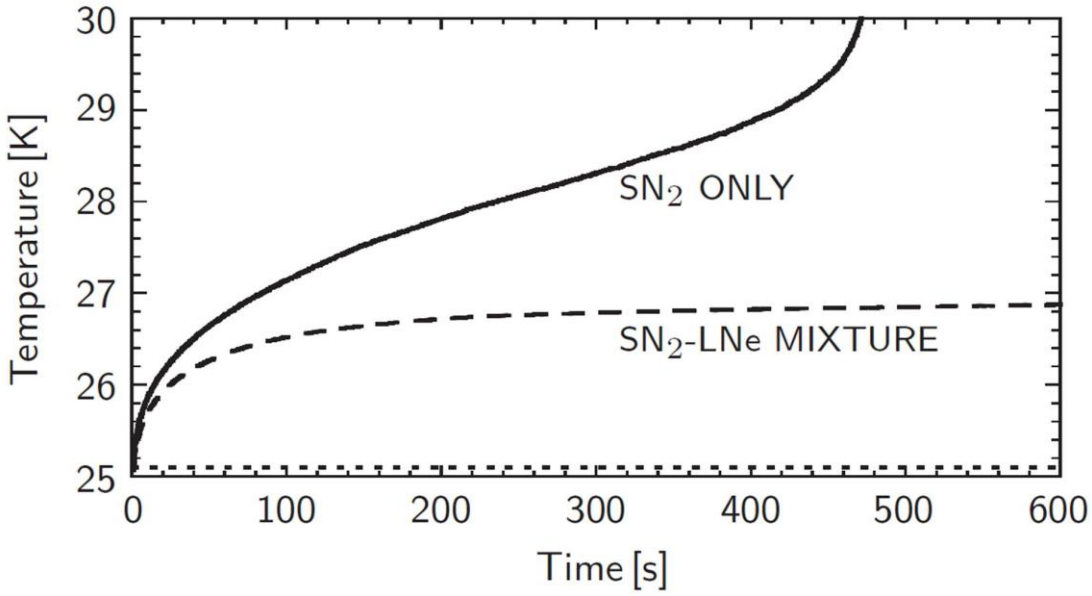

Figure 2-16. Temperature vs. time curves for an HTS strip under disturbance of over-current. The solid line indicates only SN_2, the dashed line indicates a mixture of SN_2-LN_e, and the dotted line indicates the initial temperature of 25.1 K [52, 143, 155, 156].

Furthermore, the cooling system using only SN_2 has a potential thermal contact problem from repeated thermal disturbances, such as a local heating or an over-current, called **thermal dry-out phenomena** [150]. In the event of thermal dry-out, the magnet slowly lost contact from the solid cryogen. Thus, the temperature rises more rapidly, as shown in figure 2-16, when quench occurs. Essentially, a thin

vapour layer at the interface is responsible for this temperature rise. The Kyoto group proposed that a small amount of the liquid cryogen can solve the problem of dry-out [52, 143, 155, 156].

2.3.4.4. Mixed Cooling

Recently, Song *et al* reported the use of mixed cryogens such as $SN_2 - LN_2$, SN_2 – LNe (22 K – 24.6 K), and solid Ar – LN_2 [157]. Operation with a mixed cryogen normally begins once SN_2 is formed in the cooling chamber, and then another suitable cryogen in gas form (~1% of total volume) is slowly injected into the system. The gas changes its phase and is transformed to a liquid, so the solid and liquid cryogens remain in the cooling chamber in mixed form. Of course, in the mixed cooling mode, operation temperature range is narrowed down to the liquid phase temperature range of the liquid cryogen. Thus, we also designed our SN_2 cooling system such that mixed cooling operation can be performed if required.

2.3.5. Summary

This section of the Literature Review discusses various cryogenic cooling options: liquid cryogens, solid cryogens, SN_2, why SN_2 could be a potential option for the MgB_2 MRI, formation of SN_2, SN_2 cooling systems developed to date, thermal diffusion of SN_2, transient heating, and thermal dry-out in SN_2 and its solution via adopting the mixed cooling option. The Literature Review suggests that due to the high heat capacity of SN_2, it can be a very good heat capacity enhancer for the overall magnet system. In particular, when the magnet is operated in the persistent-mode, SN_2 can provide very good thermal stability against small disturbances, which can avoid any premature quenches. However, SN_2 seems to be less suitable for applications where quenching occurs often, due to its low thermal diffusivity. The following section discusses MgB_2 superconducting (persistent) joints and persistent-mode magnet development for MRI application.

2.4. MgB_2 Superconducting Joint and Persistent-Mode Magnet Development for MRI Application

MRI is one of the largest practical applications of superconductors for the welfare of humanity [156]. As mentioned in the previous section, the superconducting magnet not only can produce very strong magnetic fields using a minimum coil winding volume but can also provide very stable magnetic fields as well. In general, if we use a direct current (DC) power supply to charge superconducting magnet, due to the very small alternating current (AC) ripples in the DC current and their fluctuation, it is very difficult to achieve a very uniform (≤10 ppm in 50 cm diameter of spherical volume (DSV)) magnetic field [18]. Furthermore, continuous current feeding can be costly for everyday operation, and it can also produce joule heating in the LHe cryostat, which eventually can evaporate LHe. To avoid these problems, the superconducting magnet in the MRI is operated in the persistent-mode (current flow in a closed-loop) [18, 19, 52]. Therefore, for obtaining high-resolution images of the human body in the MRI, high, ultra-stable (<0.1 ppm h^{-1}), and uniform magnetic fields can be produced.

To obtain **persistent-mode**, the two ends of the magnet are short-circuited after initial charging of the magnet using a **superconducting joint** having joint resistance (R) on the order of 10^{-12}-10^{-14} Ω or less [158]. Usually, the magnet used in the MRI has a very high inductance (L), and thus, under these operating conditions, the current decay is negligibly small due to the very high decay time constant ($\tau = L/R$), on the order of tens of thousands of years in some cases [159]. Hence, in the persistent-mode, a very stable (guaranteed <0.1 ppm h^{-1}) magnetic field can be achieved.

The superconducting joints are indispensable parts of the persistent magnet that are needed to achieve persistent-mode operation to confine the supercurrent in the closed-loop. Usually, the MRI magnet is made in a modular fashion (see figure 2-17) because of (i) limitations in the length of a single wire, (ii) limitations in controlling the field geometry, (iii) technical limitations on the size of the coil, and (iv) limitations on the ability to arrange the coil such that a very uniform and strong magnetic field (see figure 2-18) can be produced [158, 160].

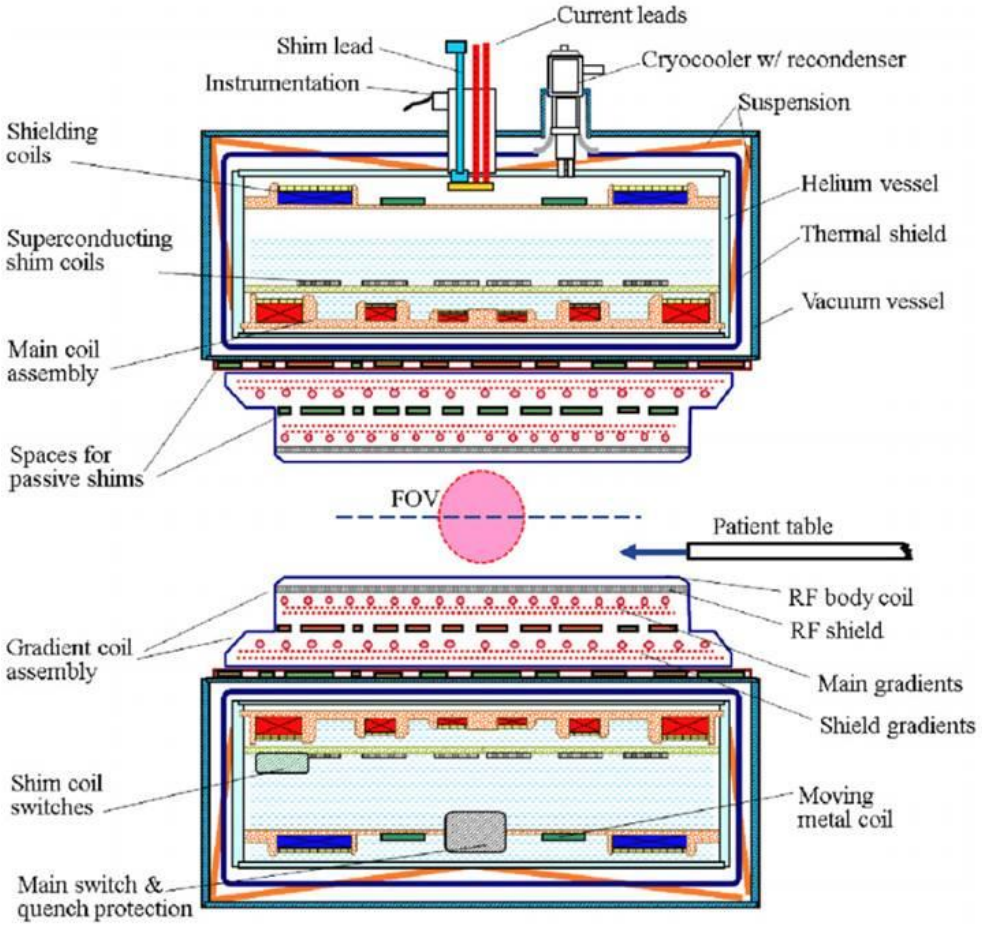

Figure 2-17. Cross-sectional schematic illustration of the components of a traditional MRI scanner (multi-coil design) [18].

In a typical MRI main magnet design, up to eight coils are used (see figures 2-17 and 2-18) to produce a homogeneous magnetic field in a 50 cm DSV [18, 36]. In figure 2-18, the curved lines represent uniformity of 10, 100, 1000, 10,000, and 100,000 ppm. All these modules of the coil are connected in series using superconducting joints in a certain configuration. The ends of the first and last coil are connected using a **persistent current switch (PCS)** as shown in figure 2-19.

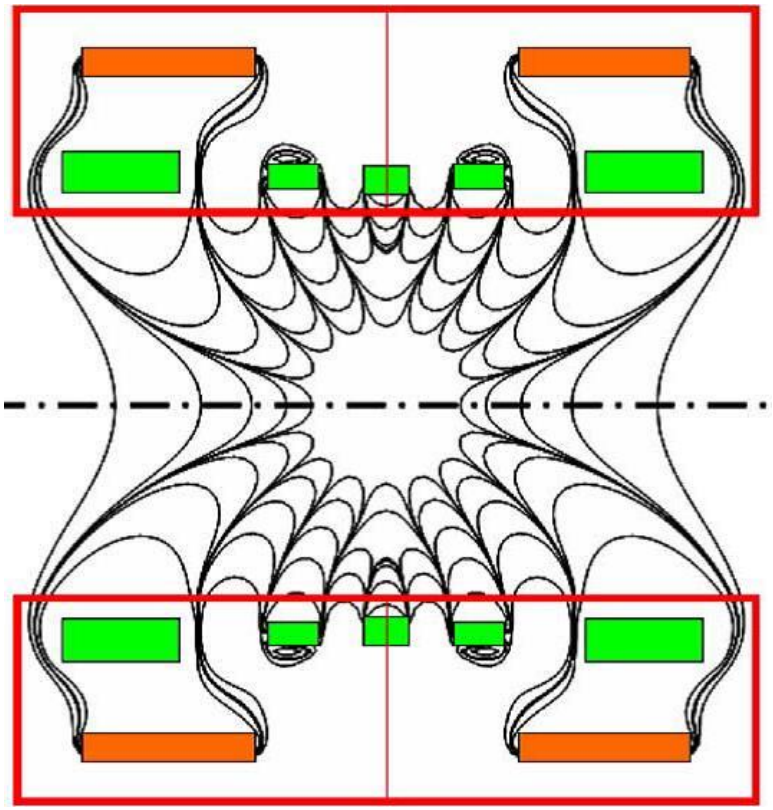

Figure 2-18. Actively shielded cylindrical MRI magnet configuration. The curved lines represent 10, 100, 1000, 10,000 and 100,000 ppm uniformity [36].

Usually, the PCS is fabricated from a superconducting conductor that has a high resistivity matrix [52]. For making a PCS, a small solenoid coil is wound non-inductively. Then, the two ends of the coil are connected with the two ends of the magnet using superconducting joints. Thus, as shown in figure 2-19(a), the small solenoid coil and the two superconducting joints form the PCS. Furthermore, to drive the small solenoid coil in the normal state for coil charging, an electrical heater is also co-wound on the solenoid coil. For charging the magnet, current leads are connected on the either sides of the solenoid coil of the PCS using normal solder joints. The current lead connections could be varied, however, depending on the design of the overall MRI magnet.

To charge the MRI magnet, first, the heater of the PCS is switched on to raise the resistance of the PCS to greater than the total circuit resistance of the MRI magnet. The temperature of the PCS while charging the magnet is greater than T_c of the conductor used for fabricating the small solenoid. Then, due to the low circuit

resistance of the magnet, when current is passed, current passes through the main magnet, as shown in figure 2-19 (a). During charging of the coil, <1% of leakage current passes through the PCS [52]. A carefully designed PCS can further lower the leakage current, however. Usually, it takes a day or two to charge a typical MRI magnet. Once the magnet reaches its nominal current, the heater of the PCS is switched-off. Thus, the current follows the superconducting path from the PCS. Under these conditions, as shown in figure 2-19(b), the current starts to flow in the closed-loop. Finally, the current leads are de-energized, and the power supply is turned off. Hence, due to the very small circuit resistance and high inductance of the coil, the current attenuation is almost negligibly small. This operation is called **persistent operation**.

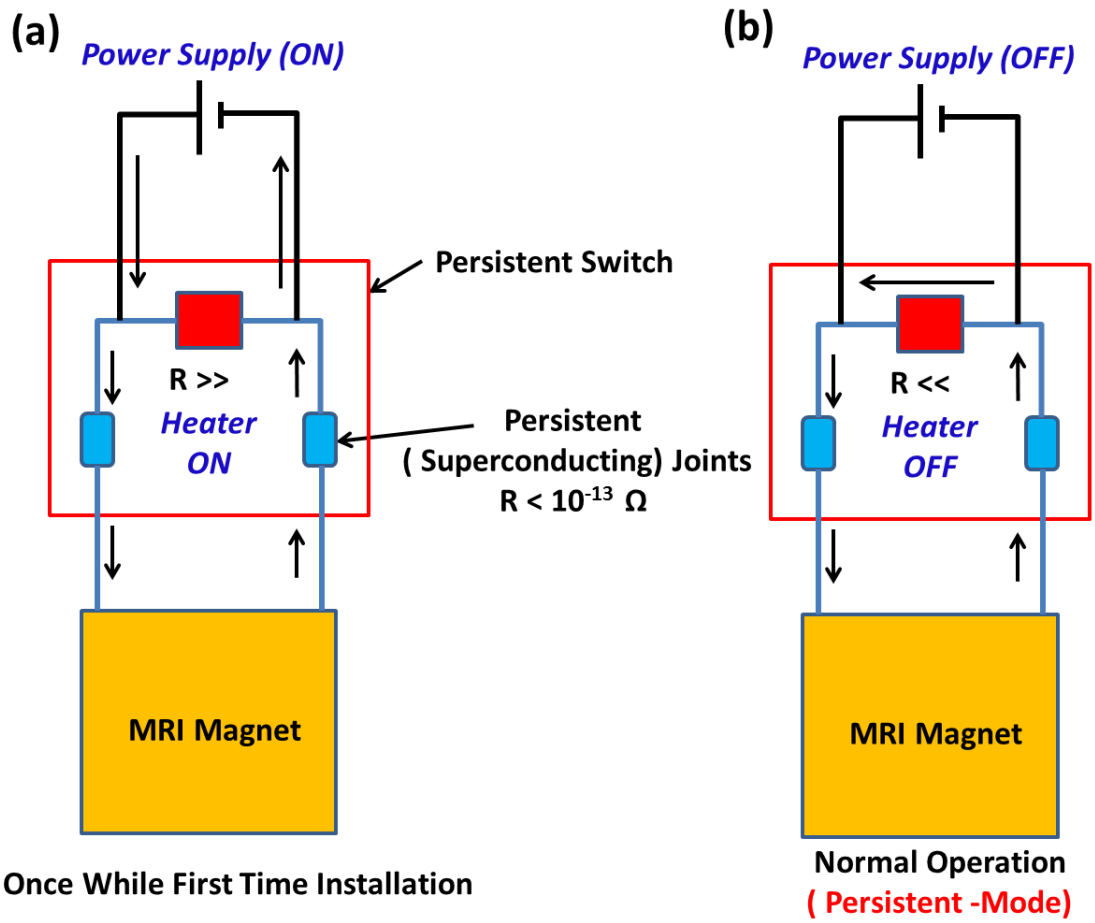

Figure 2-19. Schematic illustration of the persistent-mode operation: (a) during first time installation and magnet charging, (b) when the magnet is kept in the persistent-mode. The MRI magnet is composed of a set of individual coils and is internally connected by superconducting joints in a series.

The 'open sky MRI' has already been commercialized using MgB_2 conductor [17]. These MRIs, however, are operated in a driven mode due to difficulties in making reliable superconducting joints for MgB_2 conductors. As has been discussed, MRI magnets are required to run in persistent-mode operation to obtain high-quality images [18, 36]. Therefore, to operate an MgB_2 based MRI magnet in the persistent-mode, the superconducting joints between two MgB_2 conductors are as critical as the other key components. Therefore, for wide applicability of MgB_2 in MRI, more work was needed to be done on the joining process prior to starting this thesis work.

Thus, in this section of the Literature Review, the available literature on the joining of MgB_2 conductors and the development of MgB_2 based persistent magnets is reviewed. Section 1 describes the joining methods reported so far for MgB_2 conductors.

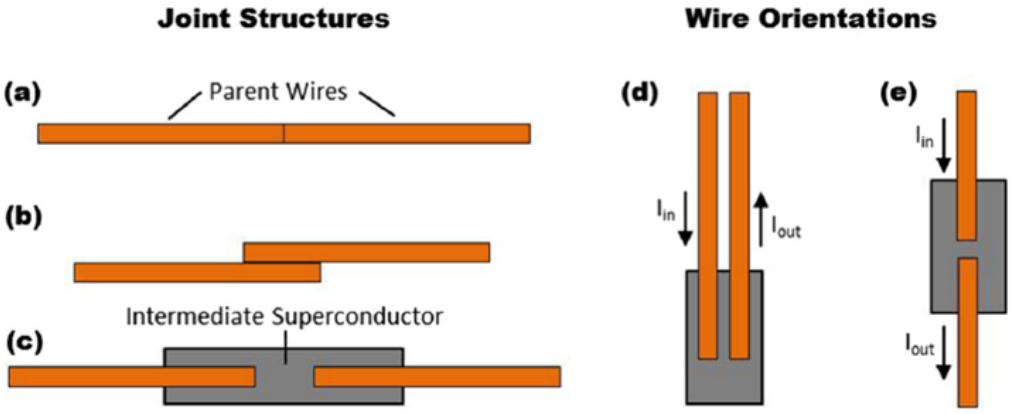

Figure 2-20. Common MgB_2 joint structures and wire orientations. (a) butt joint, (b) lap joint, (c) indirect joint, (d) termination joint, (e) continuous joint [158].

2.4.1. MgB_2 Superconducting Joining Methods and Architectures

For continuous performance improvement and increasing the feasibility of fabricating superconducting joints between MgB_2 conductors, joint fabrication methods and architectures have been continuously improved [158]. Different research groups have proposed different methods for fabricating superconducting joints, starting before this thesis work. Most of the published works (papers and patents) used the common joint structures shown in figure 2-20. For a specific joint structure, the direction of the current is trivial. If any joining process can provide

good superconducting performance and if it fits with the other requirements of the geometry, it can be used for the application. The following subsections discuss the joining methods reported so far in detail.

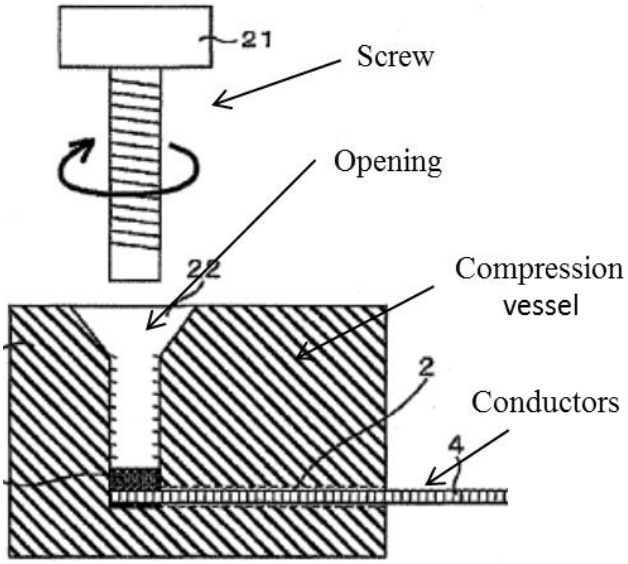

Figure 2-21. Schematic diagram of the joint cross-section of Ichiki *et al* [161].

2.4.1.1. Hitachi Ltd.

The first superconducting joint results using MgB_2 wire were reported by Takahashi *et al* of Hitachi Ltd. [162]; they made a joint between MgB_2 and NbTi, and tested it at 4.2 K. A pictorial representation of this joining process has not been reported so far, but it is expected that the recent patent filed by Ichiki *et al* from Hitachi Ltd. would be the method that Takahashi *et al* might have used (see figure 2-21) [161]. Ichiki *et al* proposed several wire insertion configurations for making superconducting joints using MgB_2 conductors (see patent document) [161]. In this joining process, a compression vessel is used to hold two conductors in the suitable configuration. Two openings are kept, one for insertion of the wires and the other for filling with precursor powder between the two conductors for making the superconducting joint. Following the insertion of two conductors into the one opening, Mg + 2B powder is poured in at the other opening. The screw is used to press the powder in the compression vessel. Finally, heat-treatment is applied to form a superconducting connection between the two conductors.

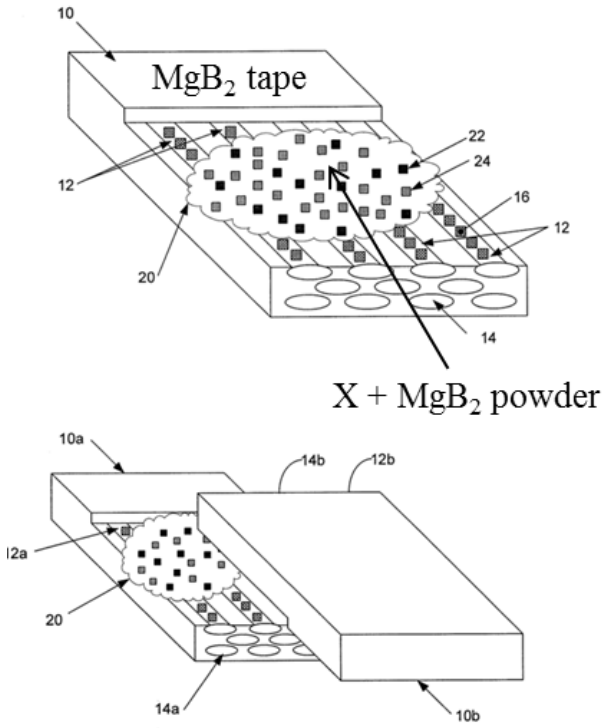

Figure 2-22. Schematic illustration of one of the joining steps of Nardelli *et al* [163].

2.4.1.2. ASG Superconductors, S.p.A.

The first MgB_2 to MgB_2 joint results were reported by Braccini *et al* [58], although in this publication, they didn't show any pictorial representation of the joining process. Later in 2009, however, Nardelli *et al* from ASG Superconductors, S.p.A., filed a patent on their joining process with several configurations [163]. A similar joining process was also reported by Li *et al* from the Chinese Academy of Sciences [164]. A schematic illustration of one of the joining steps in the ASG Superconductors, S.p.A patent is shown in figure 2-22. For fabricating a superconducting joint using this joining process, multifilament tapes are first mechanically polished from one end until the MgB_2 cores are exposed. Then two tapes are aligned using several different configurations (see patent document), and MgB_2 powder with third elements is used between the two tapes. Some enclosure is used to confine the powder between the two tapes while applying pressure. Then, the joint is heat-treated at a suitable temperature for making the superconducting connection between the two tapes.

2.4.1.3. Chinese Academy of Sciences

In 2008, Li *et al* from the Chinese Academy of Sciences reported a joining process for MgB_2 mono- or multifilament tape and wire [164]. The joining process for MgB_2 tape is shown in figure 2-23. In this method, in the first step as shown in figure 2-23(a), the sheath material at the joint location is peeled off using mechanical polishing. This is achieved by starting the polishing on one side of rectangular tape until the filaments are exposed. Depending on the polishing feasibility, 5-10 mm of the sheath is removed. In the second step, as shown in figure 2-23(b), after removing the sheath, keeping Mg and B powder in the stoichiometric ratio of MgB_2 in between the two conductors, they are aligned such that the locations where the sheath has been removed face each other. In the third step, as shown in figure 2-23(c), both conductors brought tightly together, and the joint is enclosed by thin Cu or Fe foil for protection and enhancing the mechanical strength. For further improving the density of MgB_2 at the joint location, ~0.6 GPa of compressive pressure is applied in a perpendicular direction to the joint location. Finally, in the fourth step, as shown in figure 2-23(d), the entire joint is heat-treated in Ar inert atmosphere at ~700 °C for about 1 hour. Figure 2-23(d) shows a model cross-sectional view of the joint after heat-treatment.

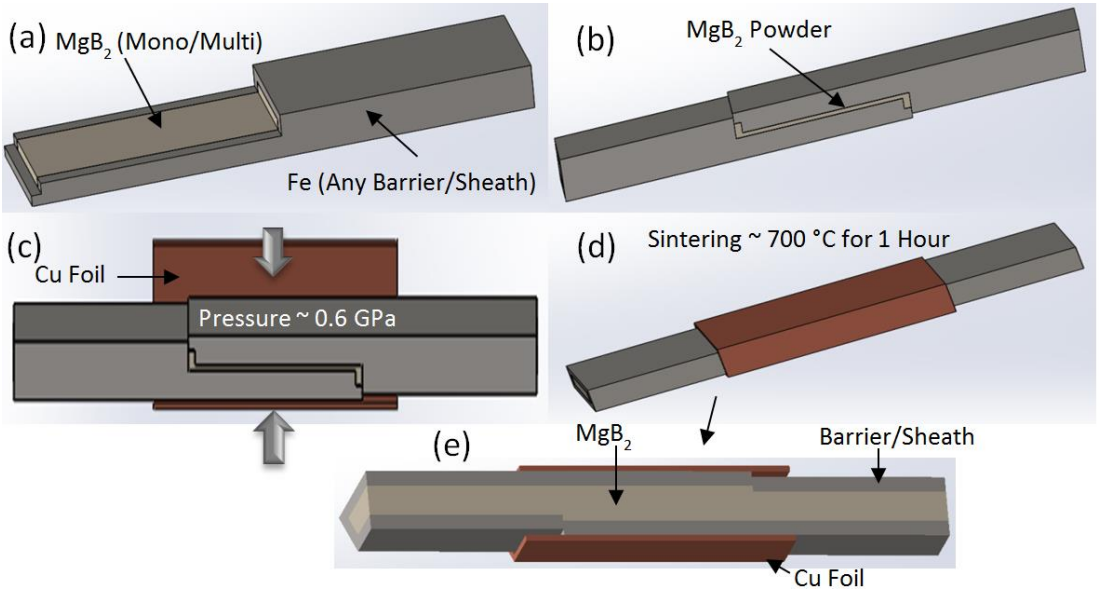

Figure 2-23. The joining process of Li *et al* for MgB_2 tape [164].

Later in 2010, Li *et al* also reported joining process for MgB_2 wire [165]. Their joining process is shown in figure 2-24. In this method, an MgB_2 wire with larger diameter compared to the diameter of the wires to be joined is used as a transitional conductor along with MgB_2 powder for creating a superconducting connection between the two connecting wires. In this method, in the first step, as shown in figure 2-24(a), part of the sheath material at the joint location is peeled off. Depending on the feasibility, about 5 mm of the sheath is removed. In the second step, as shown in figure 2-24(b), the transitional conductor (TC), MgB_2 wire with slight bigger diameter, is taken, and two appropriate holes are made on both ends. In the third step, as shown in figure 2-24(c), both conductors are inserted into the holes on either side of the TC, while keeping MgB_2 powder between the conductor and the TC. For improving the density and connection of the MgB_2 at a joint location, ~0.6 GPa of compressive pressure is applied in a perpendicular direction to the joint location. Finally, in the fourth step, as shown in figure 2-24(d), the entire joint is heat-treated in Ar inert atmosphere at ~700 °C for about 1 hour.

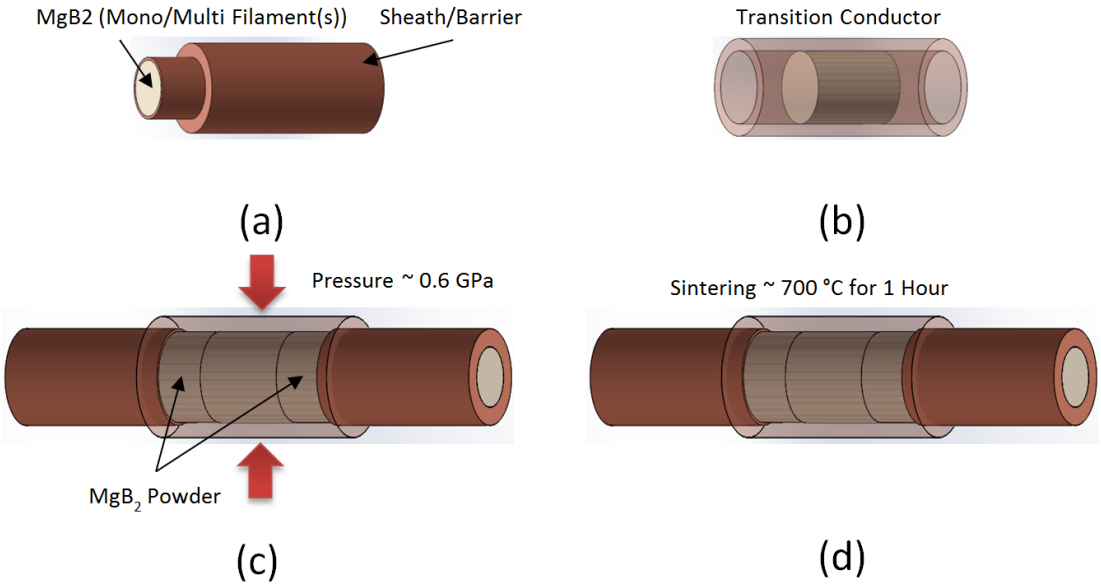

Figure 2-24. The joining process of Li *et al* for MgB_2 wire [165].

2.4.1.4. Massachusetts Institute of Technology

In 2008, the group headed by Yukikazu Iwasa at the Massachusetts Institute of Technology (MIT) also started a project on the development of an SN_2 cooled MgB_2 based persistent magnet for MRI application. Thus, several joining processes

(some improved versions) from his group have been reported over the past several years.

Joining process of Yao *et al*: One of the first joining processes from MIT was reported by Yao *et al* for MgB_2 wires [113]. Their joining process is shown in figure 2-25. When this method was first reported, 18 + 1 multifilament MgB_2 conductor was used [53]. As per this method, in the first step, the Cu and Monel array surrounding the MgB_2 filaments is etched by nitric acid. The length of the filaments is kept around 15 - 20 mm, and the etching time can be 1 - 2 h. In the second step, in order to get a fresh cross section of filaments, they are trimmed around 3-5 mm. In the third step, as shown in figure 2-25(a), an appropriately dimensioned SS billet is made, and the two etched wires are inserted into the billet with the filaments allowed to fan out in billet bore. After inserting wires into the billet, the area, as shown in figure 2-25(a), is pinched, so that sealing can be achieved. In the fourth step, as shown in figure 2-25(b), the MgB_2 powder is poured into the billet. In the fifth step, as shown in figure 2-25(c), an appropriately dimensioned SS rod is inserted into the billet and in the sixth step, as shown in figure 2-25(d), the rod is pressed into the billet to compact the MgB_2 powder at the joint location. In the seventh step, heat-treatment of joint is carried out with an appropriate heat-treatment schedule, as per [113].

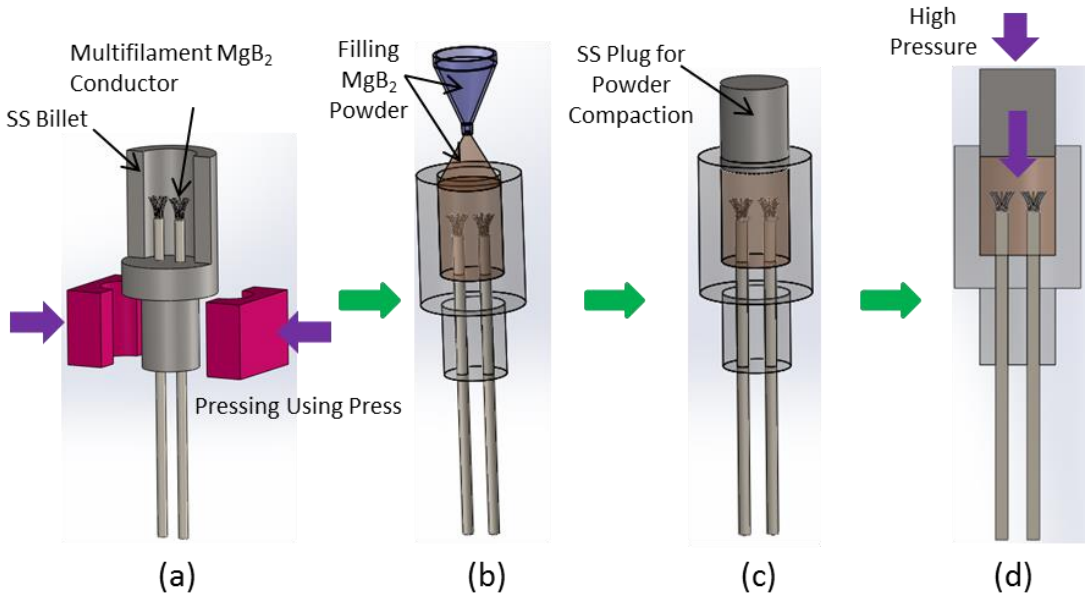

Figure 2-25. The joining process of W. Yao *et al* for wire [113].

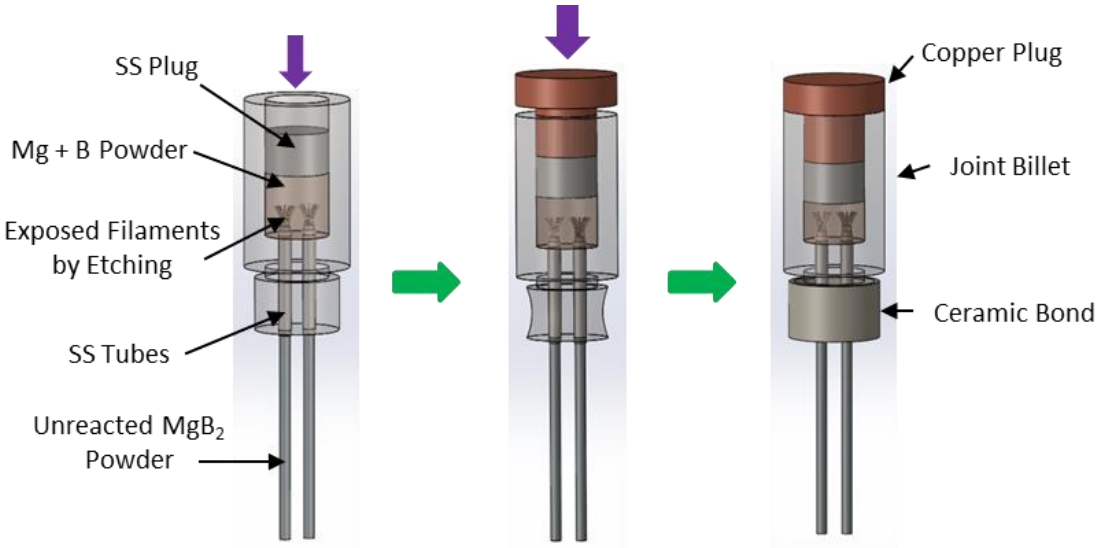

Figure 2-26. The joining process of D. K. Park *et al* for wire [11].

Joining process of D. K. Park *et al*: Later, the joining method of Yao *et al* was modified by D. K. Park *et al* for MgB_2 wire [26]. Their modified joining process is shown in figure 2-26.The differences in this process compared to Yao *et al* are that the SS plug is replaced by a Cu plug for pressing the MgB_2 powder within a specific pressure range from 0.6 GPa – 0.8 GPa and that a ceramic bond is used for better sealing at the insertion location of the conductor in the billet to avoid evaporation of volatile Mg during the heat-treatment. Furthermore, the specific heat-treatment schedule (~700 °C for 90 min) was used, which gave better results compared to the entire heat-treatment schedule used for various samples by Yao *et al*.

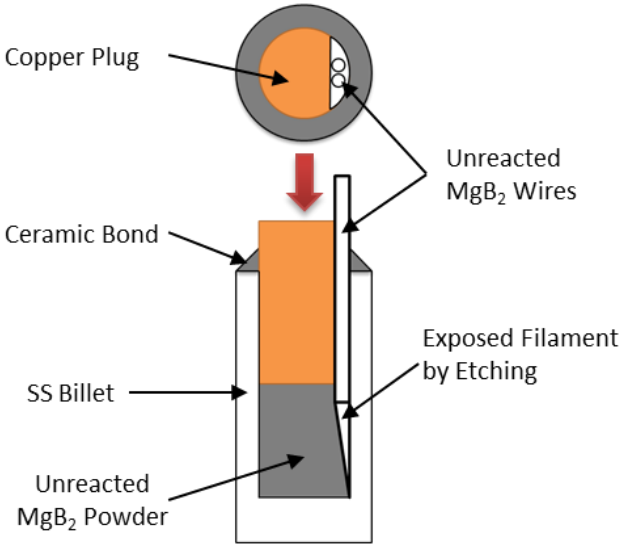

Figure 2-27. Schematic cross-sectional view of joint prepared by Ling *et al* for MgB_2 wire [25].

Joining process of Ling *et al*: Very recently, Ling *et al* reported a joining process for monofilament MgB_2 wire [25]. For this joining process, a patent application has also has been filed by Hahn *et al* [166]. A schematic cross-sectional view of the joint prepared by Ling *et al* is shown in figure 2-27. As per this method, in the first step, the Cu and Monel® surrounding the MgB_2 filament are etched by nitric acid. In the second step, the filaments are sheared at an acute angle to increase the contact area. In the third step, the two prepared wires are inserted into the billet and aligned such that the two surfaces cut at an acute angle face each other. In the fourth step, the billet is filled by MgB_2 powder without any pressure. In the fifth step, a Cu plug inserted and pressed to partially seal the top of the billet. In the sixth step, a paste made of a ceramic material is used to completely seal the top of the billet. Finally, in the seventh step, the joint is heat-treated at ~700 °C for 90 min. The schematic cross-section of a joint prepared by this method is shown in figure 2-27.

2.4.1.5. Bruker EAS GmbH

Along with MIT, Bruker EAS GmbH also patented several joining configurations for joining MgB_2 conductors [167]. A schematic illustration of one of the joining architectures of Bruker EAS GmbH is shown in figure 2-28. The overall fabrication process is similar to the MIT joining process with different orientations. Nevertheless, they have not reported any performance results so far.

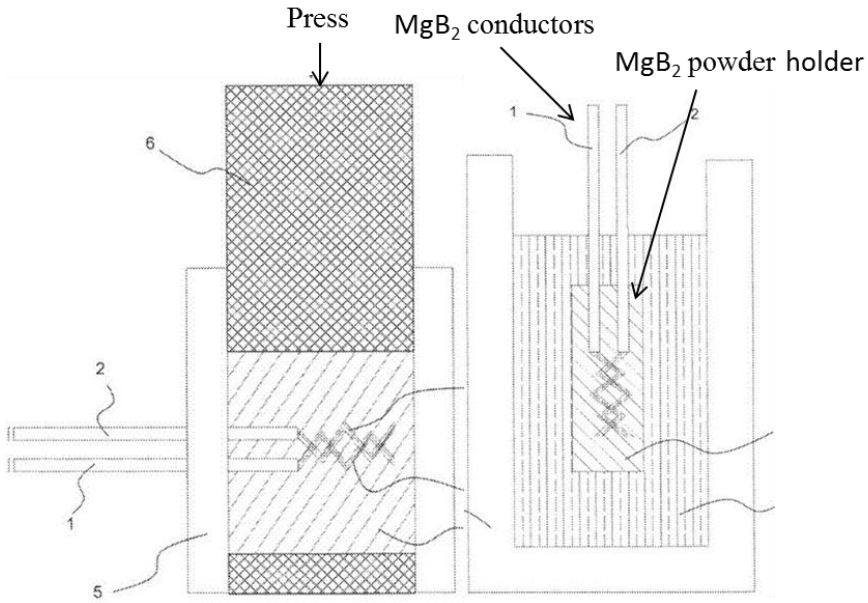

Figure 2-28. Schematic diagram of one of the joining architectures of Bruker EAS GmbH [167].

2.4.1.6. Hyper Tech Research Inc.

In 2010, Doll and Tomsic of Hyper Tech Research (HTR) Inc., also filed a patent on an MgB_2 wire joining process [168]. A 3D model of the joint and a schematic diagram of a cross-section of the joint are shown in figure 2-29. In this joining process, the joint foundation is used to give support to wires and hold the powder that is poured in between the two conductors. The wires are cut at an angle from the end and introduced into the joint foundation from the two sides, as shown in figure 2-29(a). The inserted wires are aligned as shown in figure 2-29(b). The Mg + 2B powder is poured in between the wires and pressed using a suitable plug, as shown in the figure. Finally, heat-treatment is carried out to form a superconducting connection between the two wires.

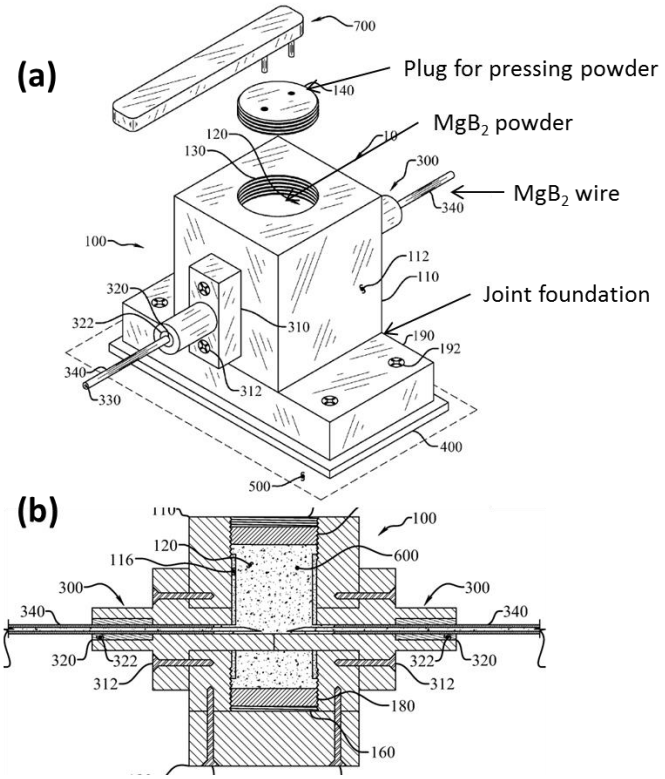

Figure 2-29. (a) 3D model, and (b) schematic cross-sectional view of Hyper Tech Research Inc. joint [168].

2.4.1.7. Siemens Corporate Technology

During the Applied Superconductivity Conference (ASC, 2014) in Charlotte, USA, Oomen *et al* of Siemens Corporate Technology presented a joining process for fully reacted *ex situ* tape [169]. The joint fabricated by Oomen *et al is* shown in figure 2-30.

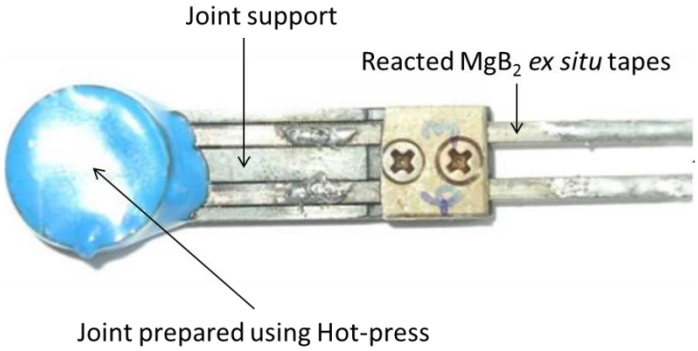

Figure 2-30. Joint fabricated by hot-pressing by Oomen *et al* [169].

For fabricating a joint by this process, the MgB_2 tape ends are first cut at a 10° angle, and then two tapes are aligned on the joint support (figure 2-30). The cut sections of both tapes are aligned such that they face away from the joint support, so that when the precursor powder is poured on top of both tape ends, the powder makes a direct connection with the filaments. The unreacted Mg + 2B powder is used to fill between the open faces of both tapes, and then the powder is pressed in a hot-press to form MgB_2.

Apart from above joining process by Siemens Corporate Technology, Lakrimi of Siemens PLC, Camberley also filed a patent on an MgB_2 joining process [170]. However, he has not reported any schematic illustrations or results for the joints.

2.4.1.8. Summary

The joining structures and orientations so far reported in the literature suggest that some of the joint structures were chosen because, during R & D phase of the joining process, they might have shown good performance. On the other hand, the purpose of the proposing different joining structures might have been merely due to the benefits of IP rights for long-term development. It has been observed, however, that more than just the structures of the joints, the execution of the joints plays a very important role. I also tried most of the structures myself (discussed in subsequent chapters), but unfortunately, most of them didn't give satisfactory results for *in situ* MgB_2 conductors. Hence, I developed a new approach for making superconducting joints, although it should be noted that my joint structure is similar to that of Bruker EAS GmbH [167].

2.4.2. Suitability of Monofilament MgB_2 Conductor for Magnet Winding, unlike NbTi

Soon after the discovery of NbTi and Nb_3Sn in early 1960, researchers initially fabricated monofilament conductors using these superconducting materials. Magnets fabricated using monofilament NbTi or Nb_3Sn, however, were quenched at much lower current than expected. Later, the cause of the quench in these magnets

was identified as due to the 'flux jumping' characteristics of monofilament NbTi and Nb_3Sn conductors [21, 52].

2.4.2.1. Flux Jumping

When a magnetic field is applied on a superconducting slab, it induces current in the opposite direction to screen the external magnetic field, as shown in figure 2-31(a). This induced current is similar to an eddy current, but it does not decay with time due to zero resistance inside the superconductor. When the external magnetic field is increased further, the screening current will flow with very high current density. Because this density is higher than J_c, the surface current will decay resistively until it reaches J_c, and the magnetic field will penetrate inside the superconductor as shown in figure 2-31(b). In this condition, current will be flowing on both faces of the slab in opposite directions at critical current density. A second magnetic field increment will produce a similar effect. After several increments, the magnetic field fully penetrates inside slab as shown in figure 2-31(b). Any further increase in the external magnetic field will fully penetrate the slab, but it will not make any changes to the screening current pattern. At this stage, all regions in the slab are either carrying critical current or none at all, and this is known as the **critical-state model** [171].

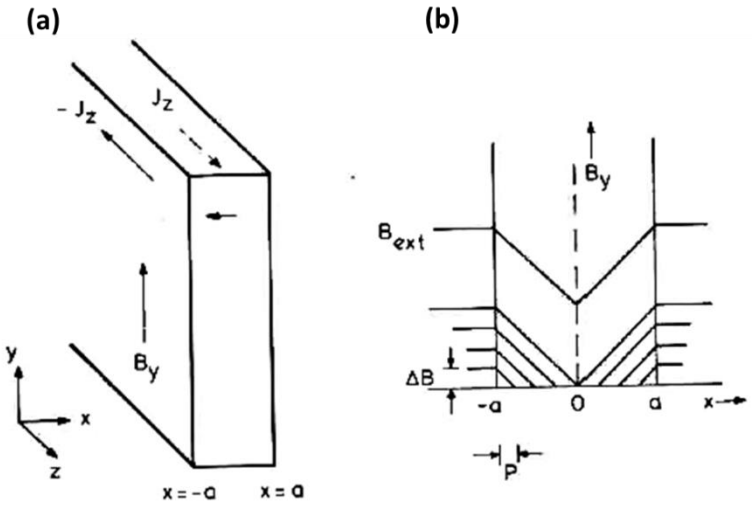

Figure 2-31. (a) Induction of the screening current due to parallel external magnetic field application, (b) pattern of reduction in the internal magnetic field with increasing external magnetic field due to a reduction in the screening current [171].

The flux jumping is associated with the fall in the critical current density of the superconductor due to the increased temperature from the heat generation due to flux motion within the superconductor. The interaction between these two inherent properties of superconductors may lead to the unstable critical-state and eventually results in flux jumping.

2.4.2.2. Nature of Flux Jumps

The nature of flux jumps can be understood more clearly by considering an imaginary experiment on the slab in figure 2-31(a) [171]. When a small heat pulse is applied to the slab, the temperature of the slab will rise, and the J_c will fall. This will lead to screening current decay to some extent, allowing the magnetic field to penetrate further into the slab. This flux motion will generate heat and raise the temperature of the slab even further. Thus, we can consider it as a feedback loop. Under these conditions, the feedback loop is positive, i.e. it will reinforce the original disturbance. Thus, if the disturbance is strong enough, it will cause an avalanche of heat generation and flux motion will occur – **a flux jump.**

2.4.2.3. Solution to Flux Jumping

In early 1960, when magnets fabricated from monofilamentary NbTi and Nb_3Sn wires were quenching at very much lower current than expected values, it was a very big setback for the magnet designers who were trying to further advance the development of superconducting magnet technology. Nevertheless, as soon as the cause of the premature quenching was understood as due to the flux jump characteristics of those monofilamentary conductors, successful cures for flux jumping were identified. Therefore, the best solutions to avoid flux jumping are to reduce flux motion caused by $-\Delta J_c$ (the so-called adiabatic stability of the superconductor) or to conduct away heat generated due to flux motion (dynamic stability). Both solutions require subdivision of the superconductor, i.e. reduction in the diameter of the superconductor (multifilamentary superconductor).

The criterion for flux jumping was developed using the adiabatic theory of flux jumping, in which the effective specific heat per unit volume of a superconductor is taken into account [52, 171].

$$\rho C_e = \frac{\Delta Q_s}{\Delta T} = \rho C - \frac{\mu_0 J_c^2 a^2}{3\rho C (T_c - T_0)} \tag{2.5}$$

where ρ is the density of the superconductor, ρC_e is the effective specific heat of the superconductor, ΔQ_s is the external supplied energy, ΔT is the temperature increase due to the external heat, C is the specific heat of the superconductor, μ_0 is the permeability of free space, J_c is the critical current density of the superconductor, a is the radius of the filament, T_c is the critical temperature of the superconductor, and T_0 is the operating temperature.

In the above equation (2.5), the last term represents the energy stored in the screening current, which eventually reduces the effective heat capacity of the superconductor. Thus, when the last term is equal to the heat capacity of the superconductor, the effective heat capacity goes to zero, and the smallest disturbance will cause a temperature rise in the superconductor, which leads to flux jumping.

Thus, the best solution to avoid flux jumps is to keep the last term in equation (2.5) well below the value of the heat capacity of the superconductor at a given operating temperature. As per Wilson, if we can keep the last term divided by the total heat capacity of the superconductor less than 1, flux jumps can be avoided, as per the following equation [171]:

$$\frac{\mu_0 J_c^2 a^2}{3\rho C (T_c - T_0)} < 1 \tag{2.6}$$

As it is assumed that no heat is being exchanged with the surroundings, the above criterion for flux jumping is called the **adiabatic criterion of the flux jump**. In the above equation, we can effectively control two variables, J_c and a, whereas other variable values are automatically decided by the operation conditions. In the case of NbTi and Nb_3Sn, however, they are already fixed which is very difficult to vary. In addition, if we use a superconducting conductor, we would like to pass as much as current as possible within the safe limit of the magnet, so it is not desirable to control J_c for flux jumping limitation purposes. We can effectively control the radius of the filament, however, to match the criterion. Therefore, we can write equation (2.6) in the following form:

$$a < \sqrt{\frac{3\rho C(T_c - T_0)}{\mu_0 J_c^2}} \quad (2.7)$$

2.4.2.4. Comparison of MgB_2 and NbTi Filament Size for Flux Jumping

Based on the criterion in equation 2.7 for flux jumping, MgB_2 and NbTi conductor are compared with respect to the minimum filament diameter requirement to avoid flux jumping. The comparison is shown in table 2-3.

Table 2-3. NbTi and MgB_2 parameters for evaluation of flux jump criterion.

Parameters	**NbTi**	**MgB_2**
J_c (A m^{-2})	1.5 x 10^9	1.14 x 10^9 (at 20 K)
ρ (kg m^{-3})	6.2 x 10^3	1.145 x 10^3 (3356)
C (J kg^{-1})	0.89	7.264 (at 20 K)
T_c (K)	6.5	34
a (mm) for satisfying criterion	0.116	0.456
a (mm) for safe operation (50% of criterion)	0.058	0.228
Diameter of filament with safe limit (mm)	0.116	0.456

In table 2-3, the NbTi parameters are taken from [171]. The MgB_2 current density is taken from [30] (75% of multifilament wire J_c at 20 K); the density is measured using *in-situ* monofilament wire 3356 [31]; the heat capacity value (0.0081 J cm^{-3} K^{-1} at 20 K) is taken from [52]; then, using the density, the specific heat is calculated; the T_c of the conductor is taken from the [30]; and the safe criterion value is taken from [171].

In the case of the *in-situ* monofilament MgB_2 conductor [31], the filament diameter is usually about 0.4 mm, which is below the safe limit for flux jumping in MgB_2. **The above table clearly indicates that it is possible to use MgB_2 in monofilament form at 20 K without flux jumping, whereas it is not possible to use NbTi in monofilament form.**

2.4.2.5. Experimental Evidence of the Absence of Flux Jumps in Monofilament MgB_2 Wire above 8 K, unlike NbTi at 4.2 K

To support the calculation, an experiment was carried out to test for flux jump behaviour in monofilament NbTi and MgB_2. Figure 2-32 shows the magnetization loop of monofilament NbTi wire at 4.2 K, as reported by Ling *et al*

[21, 25]. As can be seen in the figure, there are severe flux jumps in monofilament NbTi wire at 4.2 K. Thus, NbTi is not suitable for use in monofilament form.

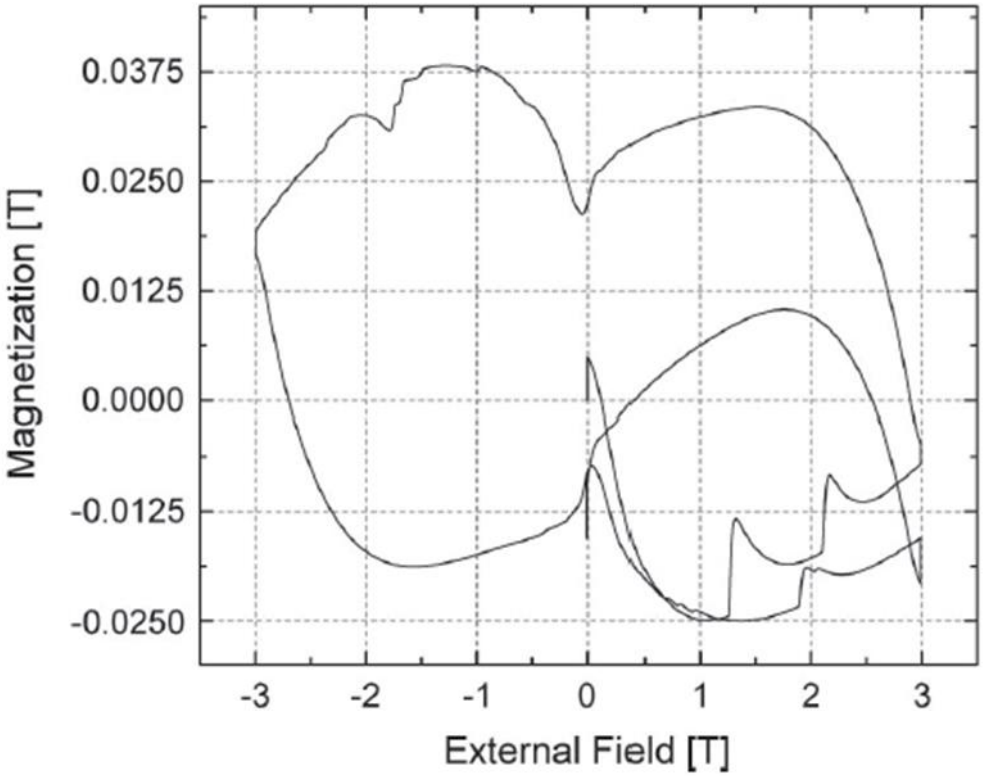

Figure 2-32. Magnetization vs. magnetic field traces of monofilament NbTi wire at 4.2 K [25].

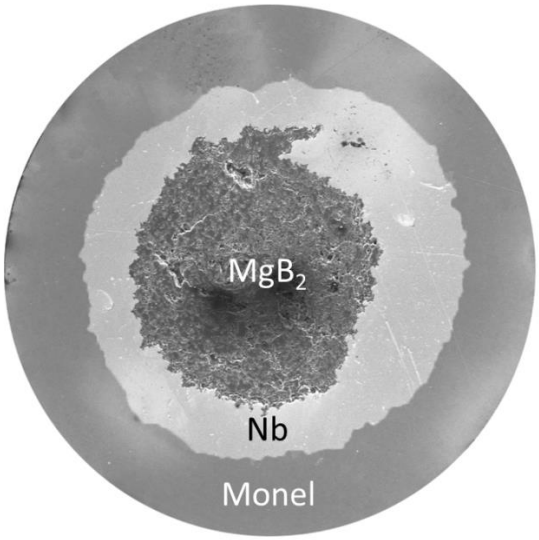

Figure 2-33. Cross-sectional SEM image of the monofilament MgB_2 wire used for flux jump characterization. The Monel sheath was etched away [172].

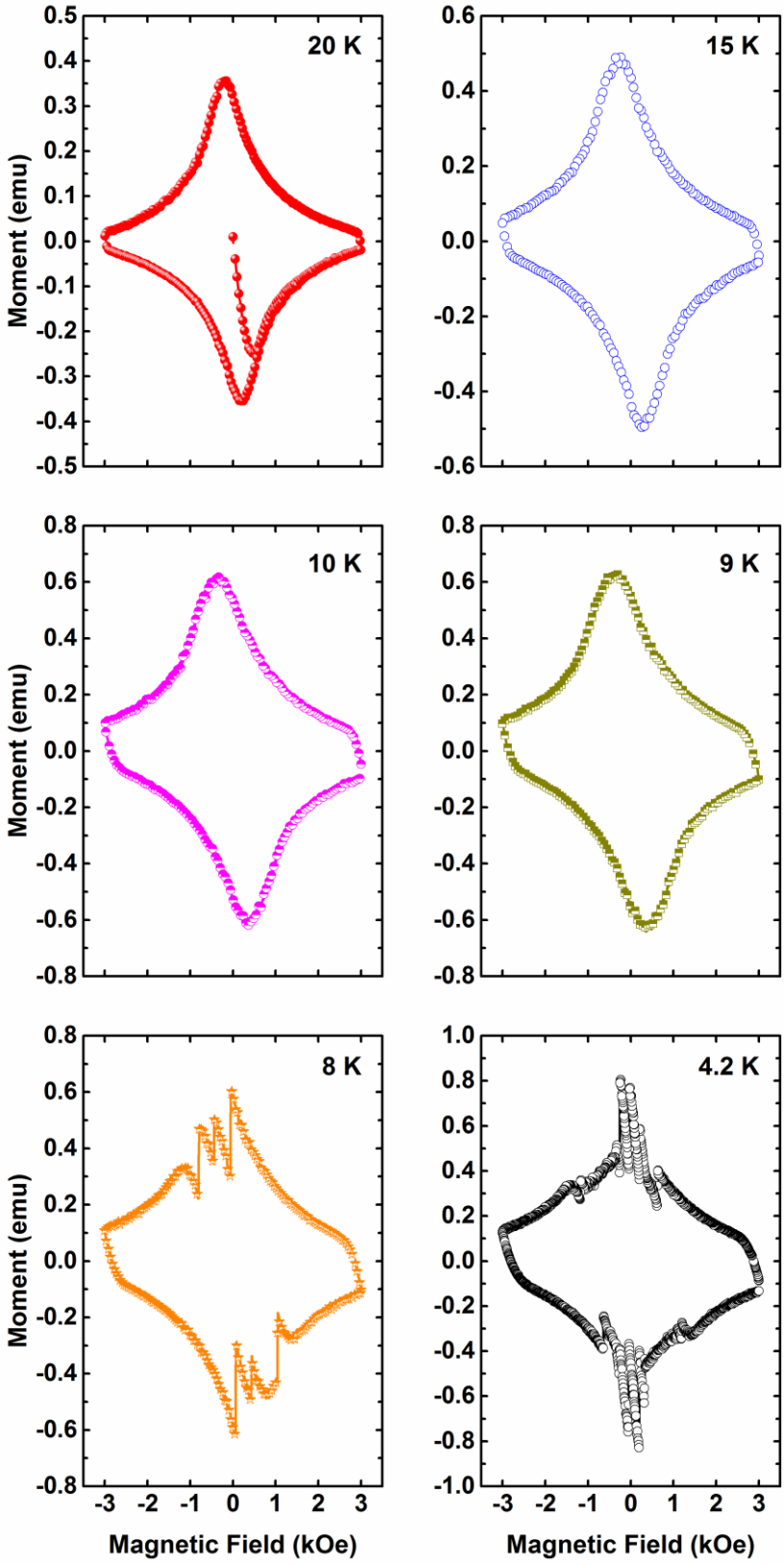

Figure 2-34. Moment vs. magnetic field (*B*) traces of the monofilament MgB_2 wire shown in figure 2-33 at different temperatures. The sweep rate of *B* was 150 Oe s^{-1}.

To evaluate the flux jump characteristics of the monofilament conductor, the monofilament *in-situ* conductor shown in figure 2-33 was used. The Monel sheath was etched away using nitric acid prior to installing the sample in the vibration sample magnetometer (VSM) for magnetization study. Figure 2-34 shows the moment vs. magnetic field traces of the wire at different temperatures. As can be seen in the figure, down to 9 K, there was no flux jumping. On the other hand, flux jumping was observed at 8 K. These flux jumps could be combined effects of both MgB_2 and Nb because the MgB_2 was surrounded by a Nb barrier. At 4.2 K, significant flux jumps were observed. These results indicate that monofilament MgB_2 conductor is suitable to use at temperatures above 10 K.

To theoretically estimate the ultimate result of flux jump, equation (2.7) can be rewritten in the form of equation (2.8) (using enthalpy of the superconductor) according to [21, 52]. Equation (2.7) indicates whether flux jumping will be initiated or not, but it does not tell whether flux jumping will proceed or not. Equation (2.8) indicates whether flux jumping will proceed or not. In equation (2.8), $H(T_c)$ and $H(T_0)$ are the enthalpy of the superconductor at the critical temperature and the operating temperature, respectively.

$$a < \sqrt{\frac{3[H\ (T_c) - H(T_0)]}{\mu_0 J_c^2}} \tag{2.8}$$

2.4.3. Voltage-Current Characteristics and Resistance Evaluation Methods for Superconducting Joints

Like superconducting conductors, voltage (*V*) vs. current (*I*) characteristics are observed in a superconducting joint when current is passed through it. The appearance of a *V* - *I* curve in a joint is due to its resistive loss mechanism. This loss mechanism is similar to what is observed in superconducting conductors [158].

Type-II superconductors possess three loss mechanisms. The first is the flux creeping process. In the flux creep, depinning of flux lines from the pinning centres occurs. This loss mechanism results in an exponential *V* - *I* characteristic at relatively low electric fields. This phenomenon is explained by the Kim-Anderson model [173].

The second is the flux-flow process. Flux flow in a material takes place when the Lorentz force on the flux lines exceeds the maximum pinning force. This process results in a linear $V - I$ characteristic at higher electric fields [174].

The above two loss mechanisms can also be found in homogeneous materials. In practice, however, it is not possible to make a truly homogenous material. Thus, some kinds of defects and inhomogeneity are always present in the material. Magnetic conductors are made up of mono- or multifilament strands surrounded by a low resistivity matrix material. Thus, when current is passed beyond the capacity of the conductor, flux flow takes place along with current redistribution among the filaments (the third loss mechanism) through the resistive matrix, which produces Ohmic dissipation [175]. The current redistribution process is expected to be responsible for the non-linear characteristics of the $V - I$ curve [176]. The power law is used to fit the non-linear characteristics of the $V - I$ curve in superconductors as follows:

$$V \propto I^n \tag{2.9}$$

where the *n*-value is related to the Gaussian-like distribution of critical current over the tested superconductor length [158]. The high inhomogeneity of the superconducting material is often associated with a low *n*-value or broad transition [177].

The measurement of the joint resistance of a persistent joint is equally important for evaluating the quality of a joint at different temperatures and external magnetic fields as the successful joining process. Typically, for application in MRI, a persistent joint resistance $<10^{-12}\ \Omega$ is generally considered as acceptable. Such low resistance is very difficult to measure by currently available low-level voltage measurement instruments. Hence, a specific joint resistance measurement technique needs to be used after initial evaluation of the joint by the standard four-probe method.

2.4.3.1. Four-Probe Measurement Method

The four probe measurement method is well known as a way to obtain the $V - I$ characteristic of a superconductor and it is widely used by researchers for

measuring low-level voltages [178]. In this method, current is passed from separate leads, and corresponding voltages are measured with separate leads to form the $V - I$ curve. From this curve, using the 1 μV cm^{-1} criterion (for MgB_2), the I_c value is calculated. By means of Ohm's law, the resistance can also be calculated. Due to the extremely low current flow for measurement of voltage in the leads, the effect of the inherent resistance of the leads can be completely avoided, and a clean signal can be measured. Whereas in two-probe measurements, current and voltage are measured by the same leads, and the resistance of leads add into the measurement output, which is not favourable for very low-level resistance measurements.

With commercially available voltmeters, ~10^{-9} V can be measured with the required accuracy. In fact, picovolt meters are also commercially available, but for precise measurements of voltage levels in this range, the experimental environment should be completely noise-free (from different noises that can affect electrical voltage measurements). When the varying magnetic field is involved in the environment, however, it becomes difficult to measure a few pico-ohms of resistance with the required accuracy. Nevertheless, with a highly engineered electronic resistance measurement system, a few pico-ohms can be measured. For measurements of resistance <10^{-12} Ω, the field-decay measurement technique needs to be used.

In general, the current carrying capacity and joint resistance are first measured by the four probe method down to the maximum feasible limit depending on the available low-level resistance measurement system at a particular temperature and magnetic field. If the results are favourable and up to expectation, the field-decay measurement technique is used for further accurately measuring the joint resistance.

2.4.3.2. Field-Decay Measurement Method

In the early days, when persistent joints were made between NbTi – NbTi, due to the undeveloped state of low resistance measurement instruments, it was not possible to measure a joint resistance in the range of even a few nano-ohms with the required accuracy. Hence, Iwasa devised a joint evaluation method called **field-decay measurement** for measuring joint resistance down to an extremely low level [179]. Using this method for the first time, he measured joint resistance in the range

of 10^{-13} Ω. Now, with improved low voltage measurement instruments and Hall sensors, this method can measure extremely low levels of resistance, too. When this method was first proposed by Iwasa, first, a search coil was used for measuring the voltage induced while current was flowing through a persistent magnet or single-/multi-turn coil. However, as high-quality hall sensors are commercially available, instead of search coil, now hall sensors are used for measuring magnetic field produced by current flowing in the persistent magnet.

In order to measure joint resistance, the current decay formula of an *L*- *R* circuit as shown below is used:

$$B = B_0 \, e^{-\left(\frac{R}{L}\right) t} \tag{2.10}$$

where *B* is the final magnetic field, B_0 is the initial magnetic field, *L* is the inductance of the closed-loop coil, and *t* is the decay time in seconds.

For measuring joint resistance by this method, a single-/multi-turn coil with a joint is made, and the inductance is calculated or measured. A Hall sensor is placed at an appropriate location of the coil with the joint. The coil is charged with an external power supply, or current is induced in the closed-loop coil.

The charging process for the coil using an external power supply has already been discussed at the beginning of section 2.4.

For inducing current in the closed-loop coil, the closed-loop coil is placed in the bore of another coil, where changing magnetic field can be produced. Typically, a magnetic field is set at 1 to 2 T as the background magnetic field. The closed-loop coil is cooled down below its superconducting transition temperature. Then, the background magnetic field is decreased linearly. Due to the changing magnetic field, current is induced in the coil with the joint.

Over a period of time, the current in the closed-loop coil decays, depending on the joint resistance and the *n*-value of the conductor [31, 52]. The decay in the current is observed over some period of time by recording the magnetic field of the coil. Finally, using equation (2.10), the total circuit resistance is calculated. In this circuit resistance, the influence of the joint resistance is significant. Thus, circuit resistance is often attributed to joint resistance.

In persistent-mode after initial charging of the coil, the current decays somewhat faster than would be expected from its actual characteristics in the beginning. Nevertheless, after some time, current decay follows the trend based on equation (2.10). The rapid decay in the initial period is due to the **settling phenomenon,** and it influences the field decay measurement results.

2.4.3.3. The Settling Phenomenon in a Persistent-Mode Magnet and its Effects on the Field-Decay Measurement Results

When a persistent magnet is charged with current, the initial current distribution within the superconductor is nonhomogeneous. Thus, over a period of time, current is redistributed into an individual filament through the resistive matrix. This induces some decay in the current prior to achieving perfect homogeneity of the current distribution in the conductor. This phenomenon is called the **settling phenomenon** [158].

The settling time is short when the initial charging current is close to the I_c of the conductor because the flux has fully penetrated the entire conductor cross-section. In most persistent-mode magnets, however, the charging current is well below the I_c of the conductor, and thus, the settling effect is dominant in this situation [158]. Nevertheless, when current is induced using a changing magnetic field, the induced current is close to the I_c of the conductor. In this situation, the settling time is short. A detail discussion on the settling phenomenon was reported by Brittle *et al* [158].

2.4.4. Performance of a Joint between MgB_2 Conductors

A performance evaluation of the currently reported superconducting joint results indicates that the overall performance of a superconducting joint greatly depends on the conductor used for fabricating the joint, that means the conductor used for winding the magnet. The first MgB_2 conductor used for the fabrication of a superconducting joint was monofilament wire with a pure nickel matrix [58, 180]. MgB_2 conductors that were later used for superconducting joint fabrication include mono- and multifilament conductors with Fe, Fe/Cu, and Ni/Fe/Cu, respectively, for the sheath [164, 165]; multifilament wire with Nb barrier, Cu stabilizer, and Monel

as a sheath [113]; and C-doped and undoped mono- and multifilament wires, with Nb barrier, Cu stabilizer, and Monel sheath [26].

Apart from the filamentary nature of the conductor, heat-treatment also plays a vital role that means an unreacted or a reacted conductor. In fact, in some cases, multiple heat-treatments on the conductor have also applied. In the case of MgB_2, however, it was confirmed that only pressing like NbTi, does not work at all because the MgB_2 core of the conductor is fragile and harder than the sheath material, and hence, heat-treatment is mandatory [181]. Different heat-treatment conditions have been used by different groups. According to Li *et al*, the melting point of MgB_2 is high, but at high-temperature, the MgB_2 compound tends to decompose into the non-superconducting material, so recrystallization by heating of already formed MgB_2 is not very effective [164]. Therefore, in most of the cases, for joint formation between two MgB_2 conductors, a mixture of Mg and B is used between the two conductors followed by heat-treatment between 650 °C and 1090 °C [158]. As mentioned earlier, to the best of my knowledge, prior to starting this thesis work, only six groups (including industrial ones) reported a joining process or results. Recently, Siemens Corporate Technology reported their joining process and results [169].

The first superconducting joint between MgB_2 and NbTi was realized by Takahashi *et al* of Hitachi Ltd. and tested at 4.2 K [162]. The closed-loop, including the joint, achieved I_c of 170 A, whereas the estimated joint resistance was below, 10^{-13} Ω in self-field. Nevertheless, the first superconducting joint between MgB_2 conductors was reported by ASG, Italy, by Braccini *et al* [58]. The conductor used for this joint was a monofilament with a pure nickel sheath. The performance of this joint at various temperatures and magnetic fields is shown in figure 2-35.

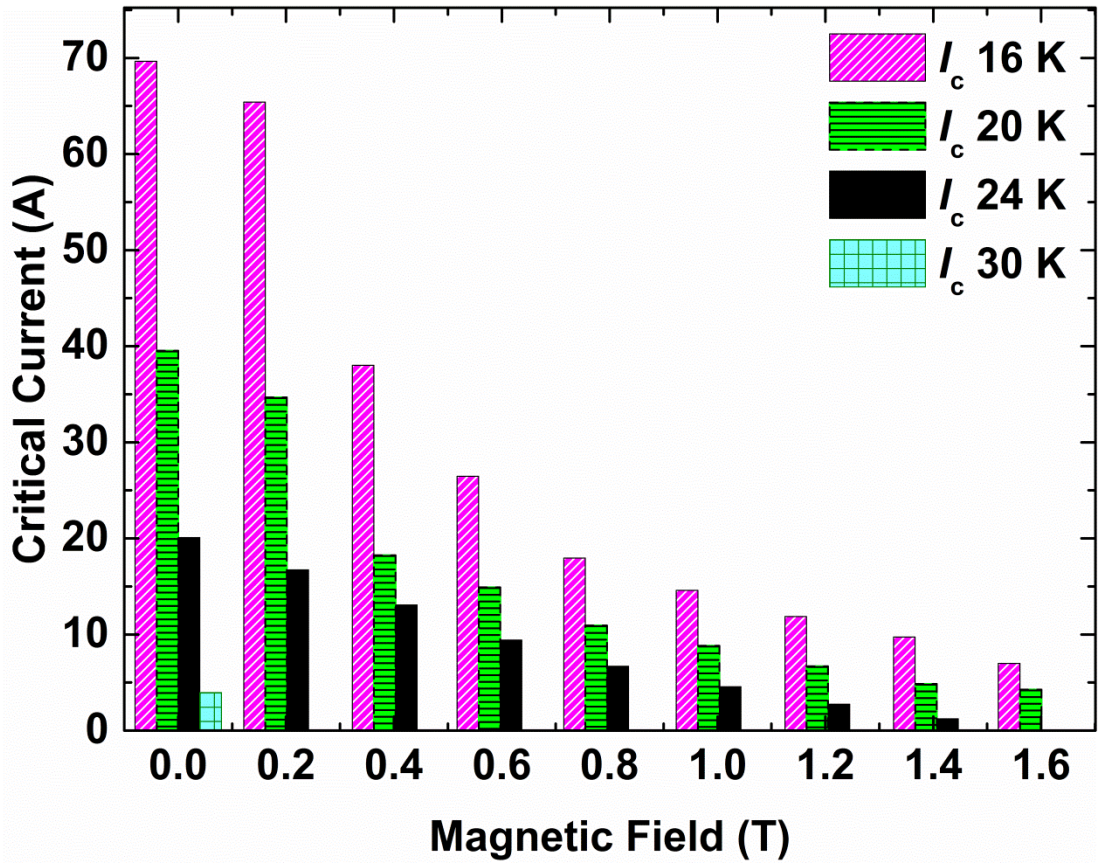

Figure 2-35. Performance of a joint fabricated by Braccini *et al* at various *T* and *B* [58].

As shown in figure 2-35, joint performance was evaluated from 16 K to 30 K, whereas magnetic field ranged from self-field to above 1.5 T. The joint performance at around 15 K and 0.5 T can be utilised as a useful criterion for a good joint, if the MRI system is made to accommodate 1.5 to 2 T central fields, because, in this type of magnet system, it may be possible to place the joint in a location where magnetic field may not be more than 0.5 T using some active or passive shielding. Hence, this joint showed its I_c at 16 K and 0.5 T to be around ~32 A, whereas the roughly calculated joint resistance was found to be less than 10^{-14} Ω, as reported by Penco *et al* [180] of the ASG group, which is acceptable as per the criteria for a persistent joint in a commercial MRI magnet system. Improvement of critical current under these conditions may be desirable for future development.

Later, from the same group, Penco *et al* reported the roughly calculated joint resistance of their joints, which was less than 10^{-14} Ω [180]. This group very recently reported joint I_c > 300 A at 20 K and joint resistance <10^{-14} Ω using fully reacted multifilamentary *ex situ* MgB_2 tape [182].

Table 2-4. The performance of joint fabricated by Li *et al* at 4.2 K, 1 T and 3 T [164].

Sample	Heat-treatment/sheath	Core size (mm^2)	No. of filament(s)	4.2 K, 1 T		4.2 K, 3 T	
				~I_c (A)	R (Ω)	~I_c (A)	R (Ω)
A	Heated once (Fe)	~0.56	1	254	3.65×10^{-10}	54	5.12×10^{-10}
B	Heated twice (Fe)	~0.56	1	244	3.46×10^{-9}	29	1.26×10^{-7}
C	Heated once SiC doped (Fe)	~0.56	1	389	7.44×10^{-12}	-	-
D	Heated twice (Ni/Fe/Cu) (*Ex situ*)	~0.21	14	351	3.76×10^{-9}	-	-

High critical current joints between MgB_2 conductors were fabricated by Li *et al* of the Chinese Academy of Sciences [164]. Different types of sheath materials were used for the conductors (mono- and multifilament) to fabricate joints. The performance of the joints was evaluated at 4.2 K, 1 T/3 T, and the results are shown in table 2-4. In the table, the I_c of the joint is calculated using J_c of the joint divided by the core cross-sectional area [164]. Sample C achieved a joint resistance of 7.44×10^{-12} Ω with I_c of 389 A at 1 T and 4.2 K. The minimum joint resistance of the twice heated joints was found to be in the range of 10^{-9} Ω with I_c of more than 240 A at 1 T and 4.2 K.

Apart from transport measurements of the joints, the Chinese Academy of Science group also conducted a mechanical characterisation of certain joint (sample D in table 2-4). In order to compare mechanical performance, the tensile stress test was carried out on bare tape, and on joints wrapped in Cu foil and without Cu foil. The results are shown in figure 2-36. As shown in the figure, the joint without Cu foil reinforcement withstood very little stress. Whereas irreversible deformation started at 20 N in the Cu foil reinforced joint, but it was still higher than for the bare joint.

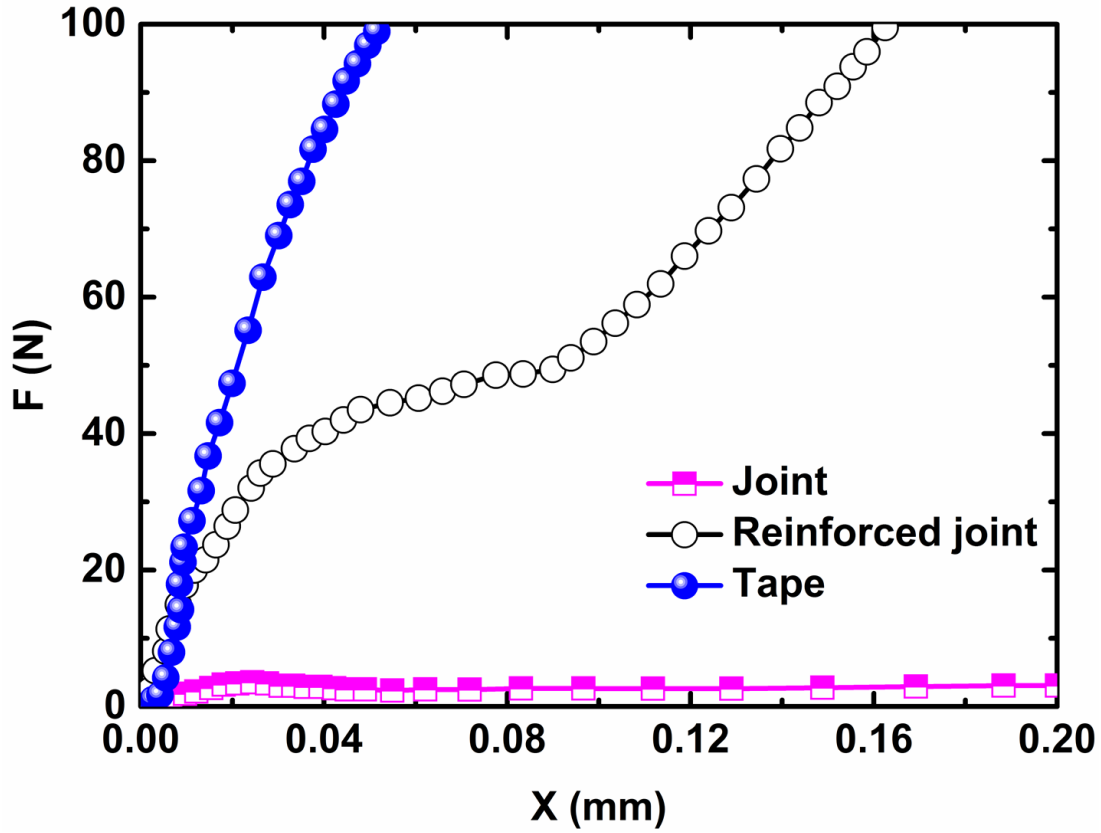

Figure 2-36. Tensile stress results for joints fabricated by Li *et al* using sample D as a conductor [164].

Table 2-5. The performance of joints fabricated by Li *et al* at 4.2 K and 19 K [165].

Coil	Sample	Sheath material(s)	Core type	Filaments	4.2 K	19 K	B_o (mT)
					R (Ω)	R (Ω)	
1	A	Fe	reacted	1	4.13×10^{-11}	7.82×10^{-11}	0.40
2	B	Fe	raw	1	3.03×10^{-13}	8.23×10^{-12}	0.096
3	C	Ni/Fe/Cu	reacted	14	6.24×10^{-11}	-	4.8
4	D	Fe/Cu	raw	1	-	-	235
5	D + E	Fe/Cu	raw	1	3.86×10^{-11}		65.8

Subsequently, the closed-circuit test results for MgB_2 coils with a superconducting joint were reported by Li *et al* [165]. The results are outlined in table 2-5. The detailed specifications of each coil can be found in [165]. The best reported joint using unreacted monofilament conductor achieved a resistance of 3.03×10^{-13} Ω at 0.096 mT and 4.2 K, and the same joint achieved a resistance of 8.23×10^{-12} Ω at 19 K.

Table 2-6. The performance of joints of Yao *et al* with different heat-treatment conditions [113].

No.	Temp./Time	I_c at 4.2 K	I_c at 4.2 K and 0.45 T	I_c at 10 K
		Reacted wire		
1	900 °C/15 min	0	0	0
2	700 °C/15 min	0	0	0
3	675 °C/30 min	~150 A	0	0
4	640 °C/30 min	~150 A	0	0
5	630 °C/1200 min	~0 A	0	0
6	570 °C/2400 min	0 A	0	0
		Non-reacted wire		
7	630 °C/1200 min	~25 A	~25 A	<2 A
8	570 °C/2400 min	~ 50 A	-	~200 A

Table 2-7. Performance of joints fabricated by Park *et al* [26].

Heat treated at 570 °C fir 2400 min in vacuum				Heat treated at 700 °C fir 90 min in Ar atmosphere		
Wire (filaments)	**Powder**	**I_c (A) at 4.2 K**	**I_c (A) at 10 K**	**Wire (filament)**	**Powder**	**I_c (A)**
Undoped (18)	Undoped	123 - 390	6.5 - 103	#2221 (1)	Undoped	> 230 A @10 K, 120 A-160 A @ 20 K (> 270 A @10 K*, 120 A-160 A @ 20 K*)
Undoped (18)	C-doped	0	0	C-doped (1)	Undoped	100 A @10 K, 42 A @ 20 K
#2314 (18)	C-doped	0	0	C-doped (1)	C-doped	110 A @4.2 K, 16 A @ 10 K; 11 @ 16 K

Yao *et al* of the Massachusetts Institute of Technology (MIT) fabricated various joints using 18 + 1 multifilament round wire with Nb as the barrier, Cu as a stabilizer, and Monel as the matrix and employed different heat-treatment conditions [113]. The performance of their joints is shown in table 2-6. As can be seen in the table, the heat-treatment sequence plays an important role in the joint performance. This means that, if heat-treatment is done twice on the wire, then joint does not show superconductivity, even at 4.2 K and 0.45 T. Reacted wire with heat-treatment above 675 °C and below 630 °C does not show superconductivity, whereas with unreacted wire, superconductivity vanishes at 0.45 T or 10 K. The best joint performance in this work was ~200 A current carrying capacity at 10 K in self-field. The absence of superconductivity in Samples 1 and 2 (see table 2-6) is attributed to evaporation of volatile Mg during heat-treatment above 650 °C due to possible poor sealing. Hence, proper sealing is required for the improvement of this joint fabrication process.

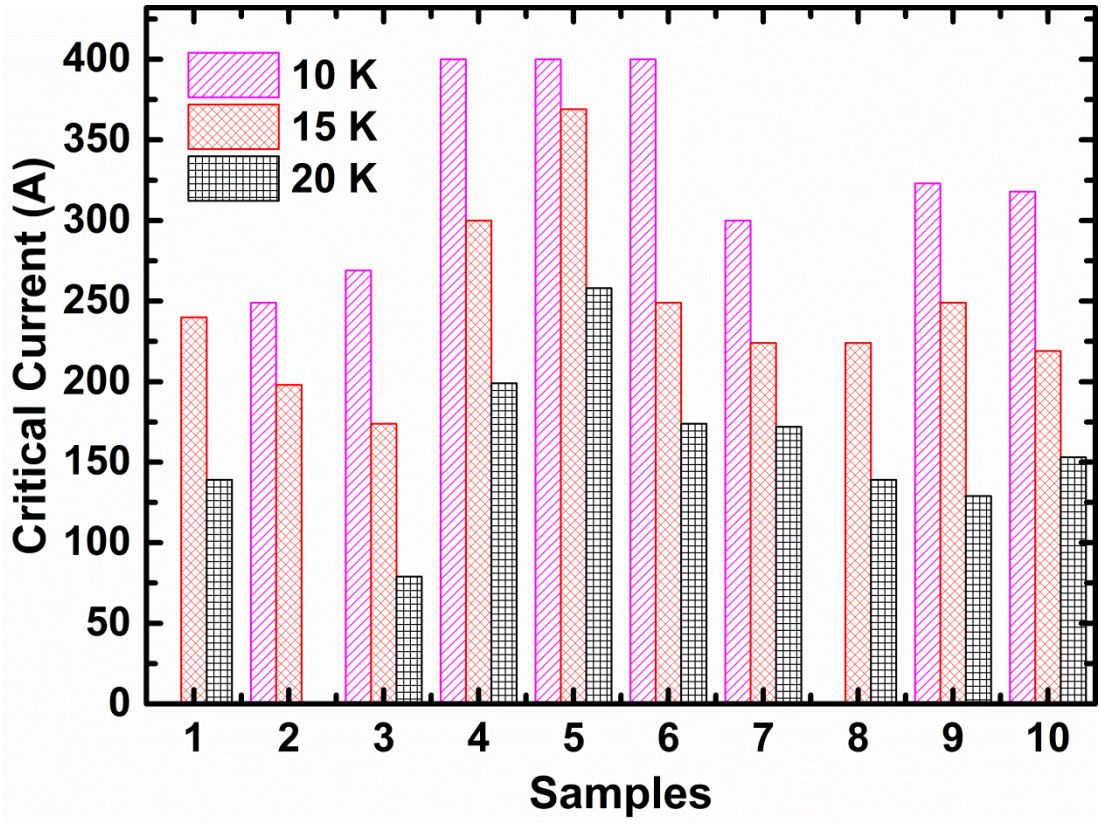

Figure 2-37. Performance of joint fabricated by Ling *et al* [21].

Until then, based on the superconducting joint result reported using different types of MgB_2 wires/tapes, it was confirmed that the most favourable results could be achieved by using unreacted wire for joint fabrication. Hence, Park *et al* of MIT reported joint test results using their improved joining process [26]. They used HTR made unreacted MgB_2 wires (C-doped multifilament (#2314) and undoped monofilament (#2221)) and optimised heat-treatment at 700 °C for 90 min for all their joints. For comparison, however, some joints were also heat treated at 570 °C for 2400 min. The microscopic picture showed broken filaments in the joint. This might have happened during filling with MgB_2 powder and pressing the powder against the filaments. Therefore, they further improved their joint fabrication method, which was reported by Ling *et al* [25]. As can be seen in table 2-7, the C-doped or undoped multifilament wires with C-doped MgB_2 powder do not show superconductivity, even at 4.2 K. The undoped multifilament wire with undoped powder shows I_c of 123 to 390 A at 4.2 K in self-field. On the other hand, at 10 K, the I_c(s) of the joints ranged from 6.5 - 103 A, showing large deviation in the results for joints in self-field.

Similarly, the monofilament undoped (#2221) and C-doped wires were also used with undoped and C-doped powder. Undoped monofilament (#2221) wire using undoped powder achieved the best performance of 270 A@10 K and 120 - 160 A@ 20 K in self-field. According to the authors, the significant deviation in the results between C-doped and undoped wire with C-doped or undoped powder might be due to the large difference in the C-doped and undoped powder density, 0.3 g cm^{-3} and 0.7 g cm^{-3}, respectively. It seems likely, however, that there was some mistake in the measurement or calculation of the powder density (since the typically measured MgB_2 powder density of one of the HTR monofilament wires (#3356, 2wt% C) is 1.145 g cm^{-3} [31]). Eventually, the consistency in the five successive joints with I_c of 140 A at 20 K with undoped monofilament wire (#2221) and undoped Mg + 2B powder encouraged MIT group to use it as the conductor in their 0.5 T MRI magnet system project.

Subsequently, after obtaining encouraging results using monofilament (#2221) MgB_2 wire, Ling *et al* of MIT further improved their original joint fabrication process and developed a new joint fabrication method using monofilament MgB_2 wire [25]. The performance of these joints at various temperatures is shown in figure 2-37. As shown in the figure, on average, all the joints showed critical current above 100 A except for one, indicating better consistency in the joint fabrication process. For evaluating joint resistance, they made a small closed-loop coil, and joint resistance was measured using a field-decay measurement at 15 K, from which, the resistance was found to be less than 1.3×10^{-10} Ω (*B*: ~0.35 T). Still, the resistance value was higher than the required superconducting joint resistance value for MRI application.

Following the above MIT report, this thesis project had reached the point where MgB_2 superconducting joint fabrication was necessary. I had tried almost all the joining processes reported before that, although I could not get satisfactory results to start with. Thus, I developed a new superconducting joint fabrication method (the detailed method is explained in Chapter 3) for unreacted monofilament MgB_2 wires. Joints were fabricated, and the results were encouraging. Similar to previously reported joining processes, my joining process also has the option of using a sealing material to avoid evaporation of volatile Mg during the heat-

treatment process. Several joints were fabricated using the new joining process. All joints were heat-treated at 650°C for 1 hour in Ar inert atmosphere. Figure 2-38 shows the performance of our first joint, in which a sealing material was not used. All the fabricated joints achieved I_c of more than 200 A (maximum limit of the power supply) in self-field at 4.2 K. As can be seen in the figure, I_c was 63.9 A at 10 K in self-field, whereas I_c was 55.5 A at 10 K in 0.5 T.

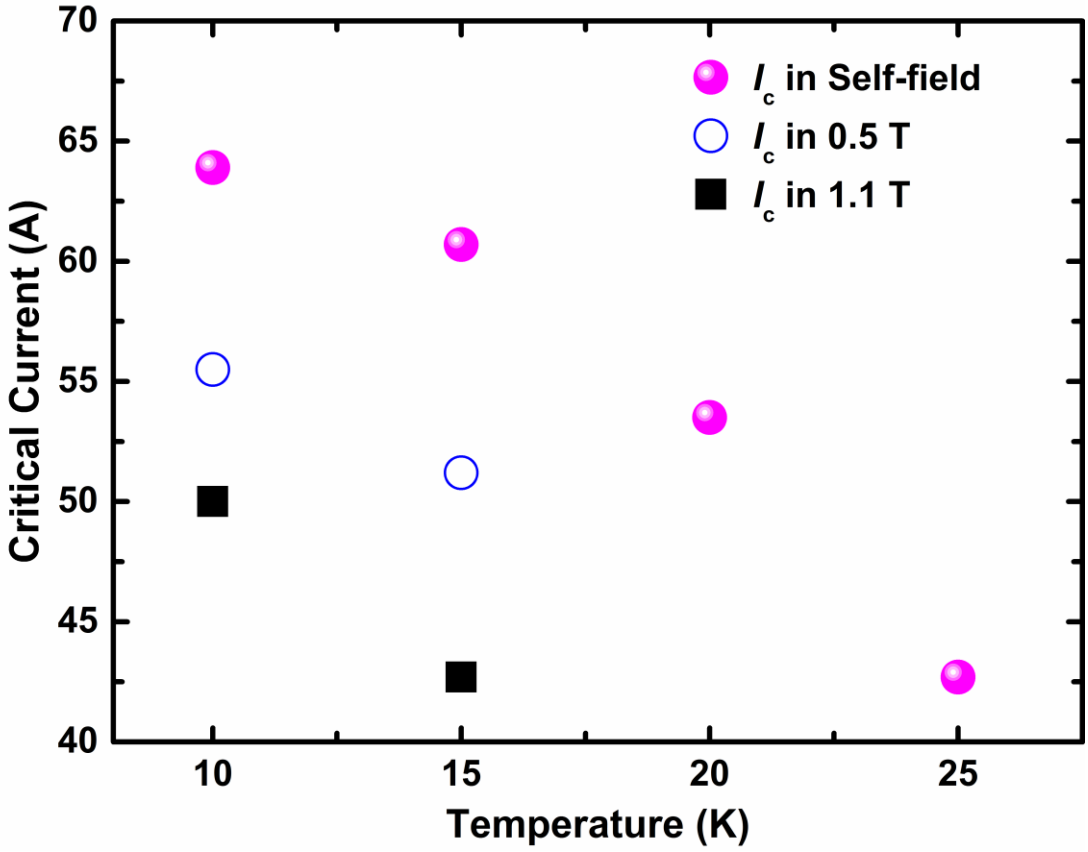

Figure 2-38. Performance of joint 1 without sealing.

Subsequently, two joints were fabricated using the same method, but the sealing material was used to avoid evaporation of Mg. The relative packing density of powder in the joint region was greater in joint 3 compare to joint 2. The performances in self-field of joint 2 and joint 3 are shown in figure 2-39. As can be seen in the figure, in self-field, I_c of joint 2 was 96 A at 9.5 K whereas the joint 3 I_c was 104.47 A at 10.5 K. This shows significant enhancement in the I_c under conditions of high packing density of the powder in the joint region and using the sealing material to avoid evaporation of Mg.

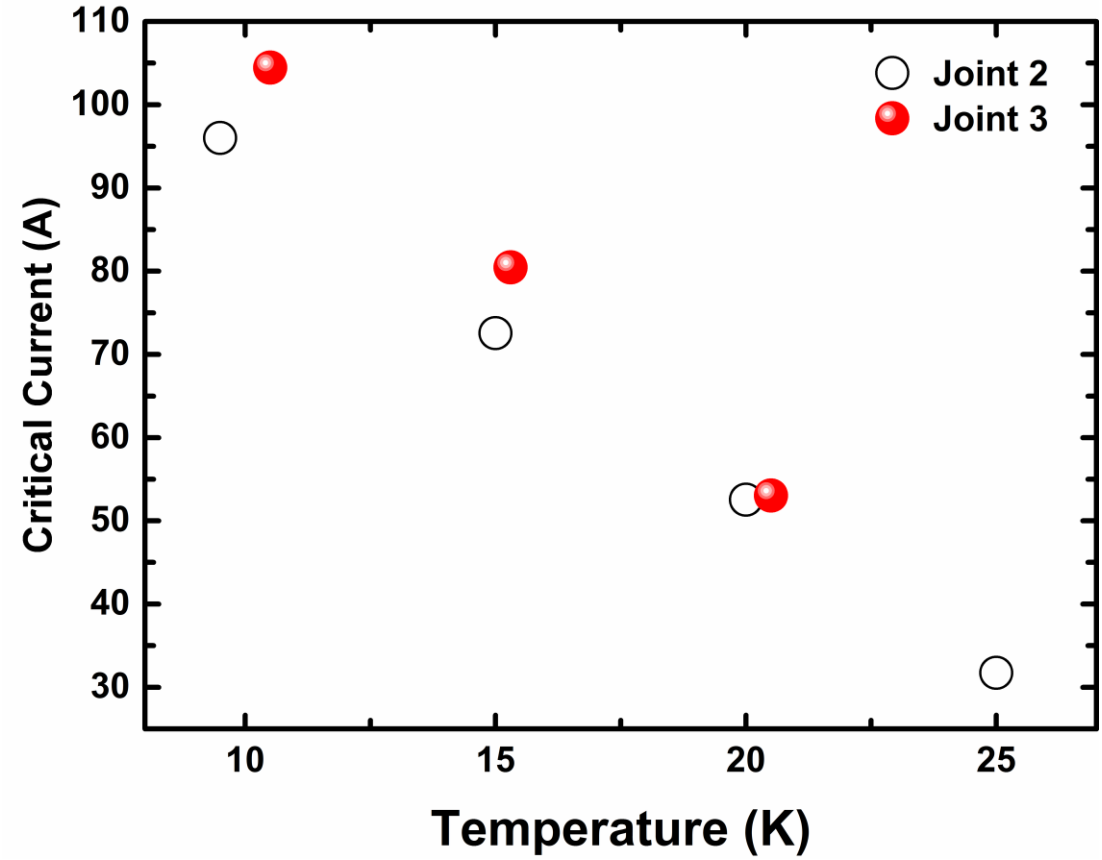

Figure 2-39. Performances of joint 2 and joint 3 in self-field with sealing.

Furthermore, one more joint was fabricated by using different boron purity in the strand and powder for joining two wires to check boron compatibility. The strand was fabricated by using 98.8% pure amorphous boron whereas the MgB_2 powder was prepared using 86% pure crystalline boron. The joint fabrication conditions were kept identical to those for joint 3, but at the temperature of 13 K and self-field, I_c was only 3.23 A. This indicates that, for getting better performance, the precursors of MgB_2 in the strand and powder should be the same.

Recently, Oomen *et al* of Siemens Corporate Technology presented their work at the ASC 2014 on the fully reacted multifilament *ex situ* conductor joining using the hot-press method [169]. In one of their joint, they obtained I_c of about 190 A at 4.2 K in self-field. I_c was only 50 A at 15 K in self-field, however. The typical measured joint resistance using the four-probe method was less than 10^{-9} Ω.

At ASC 2014, Ling *et al* also reported test results on a persistent-mode MgB_2 magnet for MRI application using a helium environment [28]. They operated their 3 coil assembly at 100 A current and 10 - 15 K in persistent-mode.

2.4.5. Summary

This section presented a comprehensive Literature Review on MgB_2 superconducting joints for MRI magnet application including some of my preliminary results of the joints. Based on the review, it is clear that the different joining methods showed different performance at different temperatures and magnetic fields. Nevertheless, all the joining methods utilized a similar joint fabrication process, in which Mg + 2B powder is used as a 'flux' to make the superconducting connection between two unreacted or reacted MgB_2 conductors.

The joints using monofilament unreacted conductor showed very good performance. Joints using *in situ* multifilament conductor showed inconsistent results, however. The joints using *ex situ* multifilament fully reacted conductor showed very promising performance. Nevertheless, it is well known that the in-field performance of *in situ* conductor is much better than that of *ex situ* conductor. Thus, in thesis work, *in situ* conductor was chosen for use in the entire project. The new joining technique developed in this thesis work has been improved significantly over the last 3 years, and some of the best results have been reported. The details will be provided in the respective sections.

2.5. References

[1] https://en.wikipedia.org/wiki/Magnetic_resonance_imaging#History
[2] www.smithsonianmag.com/science-nature/the-indomitable-mri-29126670/?c=y&page=2
[3] Damadian R 1971 Tumor detection by nuclear magnetic resonance *Science* **171** 1151-3
[4] Brenner D J and Hall E J 2007 Computed tomography — An increasing source of radiation exposure *N. Engl. J. Med.* **357** 2277-84
[5] http://hyperphysics.phy-astr.gsu.edu/hbase/nuclear/larmor.html
[6] http://mriquestions.com/why-precession.html
[7] Jin J 1997 *Electromagnetic analysis and design in magnetic resonance imaging* (CRC Press)
[8] Lauterbur P C 1973 Image formation by induced local interactions: Examples employing nuclear magnetic resonance *Nature* **242** 190-1
[9] http://mriquestions.com/callaghan-videos-on-nmr.html
[10] http://mriquestions.com/what-is-k-space.html
[11] www.youtube.com/user/magritek
[12] www.nmrmri.com
[13] www.magnet.fsu.edu/education/tutorials/java/mri/index.html
[14] www.howtolearn.com
[15] http://mriquestions.com/disadvantages.html
[16] http://mriquestions.com/brands-of-scanners.html
[17] www.paramed.it
[18] Lvovsky Y, Stautner E W and Zhang T 2013 Novel technologies and configurations of superconducting magnets for MRI *Supercond. Sci. Technol.* **26** 093001
[19] Wang Z, Van Oort J M and Zou M X 2012 Development of superconducting magnet for high-field MR systems in China *Physica C* **482** 80-6
[20] Kara D C 2013 Production of a viable product in magnetic resonance imaging using MgB_2. (Master's Thesis, Case Western Reserve University)
[21] Jiayin L 2012 Monofilament MgB_2 wire for MRI magnets. (Master's thesis, Massachusetts Institute of Technology)
[22] Li X, Zhang D, Zhang J, Gao Z, Dai S, Zhang Z, Xia D, Zhang G, Wang D, Ma Y, Lin L and Xiao L 2011 A small 1.5 T persistent current operating test magnet using MgB_2 wire with high j_c joints *IEEE Trans. Appl. Supercond.* **21** 1616-9
[23] Modica M, Angius S, Bertora L, Damiani D, Marabotto M, Nardelli D, Perrella M, Razeti M and Tassisto M 2007 Design, construction and tests of MgB_2 coils for the development of a cryogen free magnet *IEEE Trans. Appl. Supercond.* **17** 2196-9
[24] Razeti M, Angius S, Bertora L, Damiani D, Marabotto R, Modica M, Nardelli D, Perrella M and Tassisto M 2008 Construction and operation of cryogen free MgB_2 magnets for open MRI systems *IEEE Trans. Appl. Supercond.* **18** 882-6
[25] Ling J, Voccio J, Kim Y, Hahn S, Bascuñán J, Park D K and Iwasa Y 2013 Monofilament MgB_2 wire for a whole-body MRI magnet: Superconducting joints and test coils *IEEE Trans. Appl. Supercond.* **23** 6200304

[26] Park D K, Ling J, Rindfleisch M, Voccio J, Hahn S, Bascuñán J, Tomsic M and Iwasa Y 2012 MgB_2 for MRI magnets: Test coils and superconducting joints results *IEEE Trans. Appl. Supercond.* **22** 4400305
[27] Yao W, Bascuñán J, Kim W S, Hahn S, Lee H and Iwasa Y 2008 A solid nitrogen cooled MgB_2 "demonstration" coil for MRI applications *IEEE Trans. Appl. Supercond.* **18** 912-5
[28] Jiayin L, Voccio J P, Seungyong H, Youngjae K, Jungbin S, Juan B and Iwasa Y 2015 Construction and persistent-mode operation of MgB_2 coils in the range 10-15 K for a 0.5-T/240-mm cold bore MRI magnet *IEEE Trans. Appl. Supercond.* **25** 1-5
[29] Mine S, Song H, Xu M, Marte J, Buresh S, Stautner W, Immer C, Laskaris E T and Amm K 2012 Test coil for the development of a compact 3 T MgB_2 magnet *IEE Trans. Appl. Supercond.* **22** 4
[30] Kim H S, Kovacs C, Rindfleisch M, Yue J, Doll D, Tomsic M, Sumption M D and Collings E W 2016 Demonstration of a conduction cooled react and wind MgB_2 coil segment for MRI applications *IEEE Trans. Appl. Supercond.* **26** 1-5
[31] Patel D, Md Shahriar Al H, Khay Wai S, Qiu W, Kobayashi H, Zongqing M, Seong Jun K, Hong J, Jin Yong P, Choi S, Maeda M, Shahabuddin M, Rindfleisch M, Tomsic M, Dou S X and Kim J H 2016 Evaluation of persistent-mode operation in a superconducting MgB_2 coil in solid nitrogen *Supercond. Sci. Technol.* **29** 4LT02-9
[32] Patel D, Hossain M S A, See K W, Xu X, Barua S, Ma Z, Choi S, Tomsic M and Kim J H 2015 MgB_2 superconducting joints for persistent current operation *Supercond. Sci. Technol.* **28** 065017
[33] Hori C, Nakagawa R, Imamura Y and Tanaka H 2016 Development of a test conduction-cooled MgB_2 coil *IEEE Trans. Appl. Supercond.* **26** 4
[34] Nagamatsu J, Nakagawa N, Muranaka T, Zenitani Y and Akimitsu J 2001 Superconductivity at 39 K in magnesium diboride *Nature* **410** 63-4
[35] Buzea C and Yamashita T 2001 Review of the superconducting properties of MgB_2 *Supercond. Sci. Technol.* **14** 115-46
[36] Cosmus T C and Parizh M 2011 Advances in whole-body MRI magnets *IEEE Trans. Appl. Supercond.* **21** 2104-9
[37] Vinod K, Kumar R G A and Syamaprasad U 2007 Prospects for MgB_2 superconductors for magnet application *Supercond. Sci. Technol.* **20** R1
[38] Ravindran P, Vajeeston P, Vidya R, Kjekshus A and Fjellvåg H 2001 Detailed electronic structure studies on superconducting MgB_2 and related compounds *Phys. Rev. B* **64** 224509
[39] Jin S, Mavoori H, Bower C and van Dover R B 2001 High critical currents in iron-clad superconducting MgB_2 wires *Nature* **411** 563-5
[40] Martinez-Samper P, Rodrigo J G, Rubio-Bollinger G, Suderow H, Vieira S, Lee S and Tajima S 2003 Scanning tunneling spectroscopy in MgB_2 *Physica C* **385** 233-43
[41] Bud'ko S L, Lapertot G, Petrovic C, Cunningham C E, Anderson N and Canfield P C 2001 Boron isotope effect in superconducting MgB_2 *Phy. Rev. Lett.* **86** 1877-80
[42] Larbalestier D C, Cooley L D, Rikel M O, Polyanskii A A, Jiang J, Patnaik S, Cai X Y, Feldmann D M, Gurevich A, Squitieri A A, Naus M T, Eom C B, Hellstrom E E, Cava R J, Regan K A, Rogado N, Hayward M A, He T, Slusky

J S, Khalifah P, Inumaru K and Haas M 2001 Strongly linked current flow in polycrystalline forms of the superconductor MgB_2 *Nature* **410** 186-9
[43] Hata S, Yoshidome T, Sosiati H, Tomokiyo Y, Kuwano N, Matsumoto A, Kitaguchi H and Kumakura H 2006 Microstructures of MgB_2/Fe tapes fabricated by an in situ powder-in-tube method using MgH_2 as a precursor powder *Supercond. Sci. Technol.* **19** 161
[44] Finnemore D K, Ostenson J E, Bud'ko S L, Lapertot G and Canfield P C 2001 Thermodynamic and Transport Properties of Superconducting $Mg^{10}B_2$ *Phys. Rev. Lett.* **86** 2420-2
[45] Choi H J, Roundy D, Sun H, Cohen M L and Louie S G 2002 The origin of the anomalous superconducting properties of MgB_2 *Nature* **418** 758-60
[46] www.qm.phy.cam.ac.uk
[47] Canfield P C, Finnemore D K, Bud'ko S L, Ostenson J E, Lapertot G, Cunningham C E and Petrovic C 2001 Superconductivity in dense MgB_2 wires *Phys. Rev. Lett.* **86** 2423-6
[48] Kunchur M N, Lee S-I and Kang W N 2003 Pair-breaking critical current density of magnesium diboride *Phys. Rev. B* **68** 064516
[49] Goldacker W, Schlachter S I, Obst B, Liu B, Reiner J and Zimmer S 2004 Development and performance of thin steel reinforced MgB_2 wires and low-temperature in situ processing for further improvements *Supercond. Sci. Technol.* **17** S363
[50] Bud'ko S L, Petrovic C, Lapertot G, Cunningham C E, Canfield P C, Jung M H and Lacerda A H 2001 Magnetoresistivity and H_{c2} (T) in MgB_2 *Phys. Rev. B* **63** 220503
[51] Sumption M D, Bhatia M, Rindfleisch M, Tomsic M, Soltanian S, Dou S X and Collings E W 2005 Large upper critical field and irreversibility field in MgB_2 wires with SiC additions *Appl. Phys. Lett.* **86** 092507
[52] Iwasa Y 2009 *Case studies in superconducting magnets, design and operation issues* (New York: Springer)
[53] Tomsic M, Rindfleisch M, Yue J, McFadden K, Phillips J, Sumption M D, Bhatia M, Bohnenstiehl S and Collings E W 2007 Overview of MgB_2 superconductor applications *Int. J. Appl. Ceram. Technol.* **4** 250-9
[54] Ciszek M, Rogacki K and Karpinski J 2011 Effect of carbon substitution on low magnetic field AC losses in MgB_2 single crystals *Physica C* **471** 794-7
[55] Hossain M S A, Kim J H, Xu X, Wang X L, Rindfleisch M, Tomic M, Sumption M D, Collings E W and Dou S X 2007 Significant enhancement of H_{c2} and H_{irr} in MgB_2+$C_4H_6O_5$ bulks at a low sintering temperature of 600 °C *Supercond. Sci. Technol.* **20** L51
[56] Xi X X 2009 MgB_2 thin films *Supercond. Sci. Technol.* **22** 043001
[57] Kumakura H, Matsumoto A, Nakane T and Kitaguchi H 2007 Fabrication and properties of powder-in-tube-processed MgB_2 tape conductors *Physica C* **456** 196-202
[58] Braccini V, Nardelli D, Penco R and Grasso G 2007 Development of *ex situ* processed MgB_2 wires and their applications to magnets *Physica C* **456** 209-17
[59] Tomsic M, Rindfleisch M, Yue J J, McFadden K, Doll D, Phillips J, Sumption M D, Bhatia M, Bohnenstiehl S and Collings E W 2007 Development of magnesium diboride (MgB_2) wires and magnets using *in situ* strand fabrication method *Physica C* **456** 203-8

[60] Li G 2015 Connectivity, doping, and anisotropy in highly dense magnesium diboride (MgB_2). (Ph.D. thesis, The Ohio State University)
[61] Ionescu A M, Aldica G, Popa S, Enculescu M, Sandu V, Pasuk I, Kuncser A, Miu L and Badica P 2016 Spark plasma sintered MgB_2 co-added with c-BN and C-60 *Mater. Chem. Phys.* **170** 201-9
[62] Wang S, Wang X Y, Zhou Z Y, Yang F S, Yang J and Fu X H 2016 Preparation, microstructure of B film and its applications in MgB_2 superconducting Josephson junction *Acta Phys. Sinica* **65**
[63] Koparan E T, Savaskan B, Guner S B and Celik S 2016 Effects of Bi-2212 addition on the levitation force properties of bulk MgB_2 superconductors *Appl. Phys. Mat. Sci. Proc.* **122** 46
[64] Eisterer M 2007 Magnetic properties and critical currents of MgB_2 *Supercond. Sci. Technol.* **20** R47-R73
[65] Collings E W, Sumption M D, Bhatia M, Susner M A and Bohnenstiehl S D 2008 Prospects for improving the intrinsic and extrinsic properties of magnesium diboride superconducting strands *Supercond. Sci. Technol.* **21** 103001
[66] Oh S, Kim J H, Cho K, Lee C, Kim C J, Dou S X, Rindfleisch M, Tomsic M and Ahn J H 2009 A comparative study on field, temperature, and strain dependences of the critical current for doped and undoped MgB_2 wires based on the percolation model *J. Appl. Phys.* **106** 063912
[67] Hossain M S A, Senatore C, Flükiger R, Rindfleisch M A, Tomsic M J, Kim J H and Dou S X 2009 The enhanced J_c and B_{irr} of in situ MgB_2 wires and tapes alloyed with $C_4H_6O_5$ (malic acid) after cold high pressure densification *Supercond. Sci. Technol.* **22** 095004
[68] Hossain M S A, Senatore C, Rindfleisch M and Flükiger R 2011 Improvement of J_c by cold high pressure densification of binary, 18-filament *in situ* MgB_2 wires *Supercond. Sci. Technol.* **24** 075013
[69] Susner M A, Sumption M D, Bhatia M, Peng X, Tomsic M J, Rindfleisch M A and Collings E W 2007 Influence of Mg/B ratio and SiC doping on microstructure and high field transport J_c in MgB_2 strands *Physica C* **456** 180-7
[70] Tomsic M 2004 Method for manufecturing MgB_2 intermetallic superconductor wires *US Patent Specification 6687975*
[71] Patel D, Hossain M S A, Motaman A, Barua S, Shahabuddin M and Kim J H 2014 Rational design of MgB_2 conductors toward practical applications *Cryogenics* **63** 160-5
[72] Fujii H, Ozawa K and Kitaguchi H 2012 Improved critical current density in *ex situ* processed carbon-substituted MgB_2 tapes by Mg addition *Supercond. Sci. and Technol.* **25** 6200405
[73] Kumar R G A, Vinod K, Varghese N and Syamaprasad U 2007 Reactivity of sheath materials with Mg/B in MgB_2 conductor fabrication *Supercond. Sci. Technol.* **20** 222-7
[74] www.diboride.biz
[75] Yamamoto A, Tanaka H, Shimoyama J, Ogino H, Kishio K and Matsushita T 2012 Towards the realization of higher connectivity in MgB_2 conductors: *in-situ* or sintered e*x-situ*? *J. J. Appl. Phys.* **51** 010105

[76] Pachla W, Kovác P, Diduszko R, Mazur A, Hušek I, Morawski A and Presz A 2003 Effects of the high-pressure treatment of *ex situ* MgB_2 superconductors *Supercond. Sci. Technol.* **16** 7
[77] Mizutani S, Yamamoto A, Shimoyama J, Ogino H and Kishio K 2014 Understanding routes for high connectivity in *ex situ* MgB_2 by self-sintering *Supercond. Sci. Technol.* **27** 044012
[78] Kulich M, Flukiger R L, Senatore C, Tropeano M and Piccardo R 2013 Effect of cold high pressure deformation on the properties of *ex situ* MgB_2 wires *Supercond. Sci. Technol.* **26** 105019
[79] Grasso G, Malagoli A, Ferdeghini C, Roncallo S, Braccini V, Siri A S and Cimberle M R 2001 Large transport critical currents in unsintered MgB_2 superconducting tapes *Appl. Phys. Lett.* **79** 230-2
[80] Flükiger R, Suo H L, Musolino N, Beneduce C, Toulemonde P and Lezza P 2003 Superconducting properties of MgB_2 tapes and wires *Physica C* **385** 286-305
[81] Dhallé M, Toulemonde P, Beneduce C, Musolino N, Decroux M and Flükiger R 2001 Transport and inductive critical current densities in superconducting MgB_2 *Physica C* **363** 155-65
[82] Siri A S, Bellingeri E, Ferdeghini C, Roncallo S, Braccini V, Modica M, Tumino A, Grasso G and Malagoli A 2003 Fabrication and characterization of Ni-sheathed MgB_2 superconducting tapes *Int. J. Mod. Phys. B* **17** 461-7
[83] Kováč P, Melišek T, Kopera L, Hušek I, Polak M and Kulich M 2009 Progress in electrical and mechanical properties of rectangular MgB_2 wires *Supercond. Sci. Technol.* **22** 075026
[84] Kario A, Grinenko V, Kauffmann A, Hassler W, Rodig C, Kovac P, Melisek T and Holzapfel B 2012 Isotropic behavior of critical current for MgB_2 *ex situ* tapes with 5 wt.% carbon addition *Physica C* **483** 222-4
[85] Tomsic M *Private communication*
[86] Mine S, Xu M F, Buresh S, Stautner W, Immer C, Laskaris E T, Amm K and Grasso G 2013 Second test coil for the development of a compact 3T MgB_2 magnet *IEEE Trans. Appl. Supercond.* **23** 4601404
[87] Li G Z, Sumption M D, Susner M A, Yang Y, Reddy K M, Rindfleisch M A, Tomsic M J, Thong C J and Collings E W 2012 The critical current density of advanced internal-Mg-diffusion-processed MgB_2 wires *Supercond. Sci. Technol.* **25** 115023
[88] Ye S, Song M, Matsumoto A, Togano K, Takeguchi M, Ohmura T and Kumakura H 2013 High-performance MgB_2 superconducting wires for use under liquid-helium-free conditions fabricated using an internal Mg diffusion process *Supercond. Sci. Technol.* **26** 125003
[89] Giunchi G 2003 High density MgB_2 obtained by reactive liquid Mg infiltration *Int. J. Mod. Phys. B* **17** 453-60
[90] Giunchi G, Ceresara S, Ripamonti G, Di Zenobio A, Rossi S, Chiarelli S, Spadoni M, Wesche R and Bruzzone P L 2003 High performance new MgB_2 superconducting hollow wires *Supercond. Sci. Technol.* **16** 285-91
[91] Giunchi G, Ripamonti G, Perini E, Cavallin T and Bassani E 2007 Advancements in the reactive liquid Mg infiltration technique to produce long superconducting MgB_2 tubular wires *IEEE Trans. Appl. Supercond.* **17** 2761-5

[92] Hur J M, Togano K, Matsumoto A, Kumakura H, Wada H and Kimura K 2008 Fabrication of high-performance MgB2 wires by an internal Mg diffusion process *Supercond. Sci. Technol.* **21**) 032001
[93] Wang D, Xu D, Zhang X, Yao C, Yuan P, Yanwei, Oguro H, Awaji S and Watanabe K 2016 Uniform transport performance of a 100 m-class multifilament MgB_2 wire fabricated by an internal Mg diffusion process *Supercond. Sci. Technol.* **29** 65003-11
[94] Li G Z, Yang Y, Susner M A, Sumption M D and Collings E W 2012 Critical current densities and n-values of MgB_2 strands over a wide range of temperatures and fields *Supercond. Sci. Technol.* **25** 025001
[95] Kumakura H, Hur J, Togano K, Matsumoto A, Wada H and Kimura K 2011 Superconducting properties of diffusion-processed multifilamentary MgB_2 wires *IEEE Trans. Appl. Supercond.* **21** 2643-8
[96] Ye S J, Matsumoto A, Togano K and Kumakura H 2011 Enhancement of the critical current density of internal Mg diffusion processed MgB_2 wires by the addition of both SiC and liquid aromatic hydrocarbon *Physica C* **471** 1133-6
[97] Susner M A, Yang Y, Sumption M D, Collings E W, Rindfleisch M A, Tomsic M J and Marzik J V 2011 Enhanced critical fields and superconducting properties of pre-doped B powder-type MgB_2 strands *Supercond. Sci. Technol.* **24** 012001
[98] Marzik J V, Suplinskas R J, Wilke R H T, Canfield P C, Finnemore D K, Rindfleisch M, Margolies J and Hannahs S T 2005 Plasma synthesized doped B powders for MgB_2 superconductors *Physica C* **423** 83-8
[99] Marzik J V, Lewis R C, Nickles M R, Finnemore D K, Yue J, Tomsic M, Rindfleisch M and Sumption M D 2010 *Adv. Cryo. Eng,* **1219** 295-301
[100] Ye S J, Matsumoto A, Togano K, Ohmura T and Kumakura H 2013 The critical current properties of 37-filament internal Mg diffusion-processed MgB_2 wires *Supercond. Sci. Technol.* **26** 105027
[101] Kim J H, Oh S, Kumakura H, Matsumoto A, Heo Y-U, Song K-S, Kang Y-M, Maeda M, Rindfleisch M, Tomsic M, Choi S and Dou S X 2011 Tailored materials for high-performance MgB_2 wire *Adv. Mater.* **23** 4942-6
[102] Maeda M, Al Hossain M S, Motaman A, Kim J H, Kario A, Rindfleisch M, Tomsic M and Dou S X 2013 Synergetic combination of LIMD with CHPD for the production of economical and high performance MgB_2 wires *IEEE Trans. Appl. Supercond*. **23** 6200704
[103] Kim J H, Heo Y-U, Matsumoto A, Kumakura H, Rindfleisch M, Tomsic M and Dou S X 2010 Comparative study of mono- and multi-filament MgB_2 wires with different boron powders and malic acid addition *Supercond. Sci. Technol.* **23** 075014
[104] Patel D, Maeda M, Choi S, Kim S J, Shahabuddin M, Parakandy J M, Hossain M S A and Kim J H 2014 Multiwalled carbon nanotube-derived superior electrical, mechanical and thermal properties in MgB_2 wires *Scr. Mater.* **88** 13-6
[105] Kováč P, Kopera L, Melišek T and Hušek I 2014 Electro-mechanical behaviour of in situ W added MgB_2 wire *Cryogenics* **60** 5-8
[106] Kitaguchi H and Kumakura H 2005 Superconducting and mechanical performance and the strain effects of a multifilamentary MgB_2/Ni tape *Supercond. Sci. Technol.* **18** S284

[107] Lvovsky Y 2009 Index loss effect in n-value measurements of commercial superconductors *IEEE Trans. Appl. Supercond.* **19** 2313-6
[108] Kim J H, Dou S X, Matsumoto A, Choi S, Kiyoshi T and Kumakura H 2010 Correlation between critical current density and n-value in MgB_2/Nb/Monel superconductor wires *Physica C* **470** 1207-10
[109] Yukikazu Iwasa, David C. Larbalestier, Michiya Okada, Roberto Penco, Michael D. Sumption and Xiaoxing Xi 2006 A round table discussion on MgB_2 toward a wide market or a niche production?—A summary *IEEE Trans. Appl. Supercond.* **16** 1457-64
[110] Iwasa Y 2006 HTS and NMR/MRI magnets: Unique features, opportunities, and challenges *Physica C* **445-448** 1088-94
[111] Iwasa Y, Bascuñán J, Hahn S and Park D K 2012 Solid-cryogen cooling technique for superconducting magnets of NMR and MRI *Phys. Proc.* **36** 1348-53
[112] Yao W, Bascuñán J, Hahn S and Iwasa Y 2010 MgB_2 coils for MRI applications *IEEE Trans. Appl. Supercond.* **20** 756-9
[113] Yao W, Bascuñán J, Hahn S and Iwasa Y 2009 A superconducting joint technique for MgB_2 round wires *IEEE Trans. Appl. Supercond.* **19** 2261-4
[114] Dalessandro R B, Bocchi M, Rossi V and Martini L E 2007 Test results on 500 kVA-class MgB_2-based fault current limiter prototypes *IEEE Trans. Appl. Supercond.* **17** 1776-9
[115] Singh N K, Tumilty R M, Burt G M, Bright C G, Brozio C C, Roberts D A, Smith A C and Husband M 2010 System-level studies of a MgB_2 superconducting fault-current limiter in an active distribution network *IEEE Trans. Appl. Supercond.* **20** 54-60
[116] Ye L, Majoros M, Campbell A M, Coombs T, Harrison S, Sargent P, Haslett M and Husband M 2007 MgB_2 sample tests for possible applications of superconducting fault current limiters *IEEE Trans. Appl. Supercond.* **17** 2826-9
[117] Pei X Z, Smith A C, Husband M and Rindfleisch M 2012 Experimental tests on a superconducting fault current limiter using three-strand MgB_2 wire *IEEE Trans. Appl. Supercond.* **22** 5600405
[118] Ye L, Majoros M, Campbell A M, Coombs T, Astill D, Harrison S, Husband M, Rindfleisch M and Tomisc M 2007 Experimental studies of the quench behaviour of MgB_2 superconducting wires for fault current limiter applications *Supercond. Sci. Technol.* **20** 621-8
[119] Tomsic M, Rindfleisch M, Yue J, McFadden K, Phillips J, Sumption M D, Bhatia M, Bohnenstiehl S and Collings E W 2007 Overview of MgB_2 superconductor applications *Int. J. Appl. Ceram. Technol.* **4** 250-9
[120] Hascicek Y S, Akin Y, Baldwin T W, Rindfleisch M M, Yue J, Sumption M D and Tomsic M 2009 A MgB_2 12.5 kVA superconductor transformer *Supercond. Sci. Technol.* **22** 065002
[121] Arnold G and Wolf J 2005 Liquid hydrogen for automotive application next generation fuel for FC and ICE vehicles *Teion Kogaku (J. Cryo. Soc. Jpn.)* **40** 221-30
[122] Kajikawa K and Nakamura T 2009 Proposal of a fully superconducting motor for liquid hydrogen pump with MgB_2 wire *IEEE Trans. Appl. Supercond.* **19** 1669-73

[123] Nakamura T, Yamada Y, Nishio H, Kajikawa K, Sugano M, Amemiya N, Wakuda T, Takahashi M and Okada M 2012 Development and fundamental study on a superconducting induction/synchronous motor incorporated with MgB_2 cage windings *Supercond. Sci. Technol.* **25** 014004

[124] Nakamura T, Nishio H, Amemiya N, Kajikawa K and Wakuda T 2012 Performance of induction/synchronous motor having MgB_2 cage windings for liquid hydrogen circulation pump *IEEE Trans. Appl. Supercond.* **22** 5200404

[125] Kajikawa K, Kuga H, Inoue T, Watanabe K, Uchida Y, Nakamura T, Kobayashi H, Hongo M, Kojima T, Taguchi H, Naruo Y, Wakuda T and Tanaka K 2012 Development of a liquid hydrogen transfer pump system with MgB_2 wires *Cryogenics* **52** 615-9

[126] Kajikawa K, Uchida Y, Nakamura T, Kobayashi H, Wakuda T and Tanaka K 2013 Development of stator windings for fully superconducting motor with MgB_2 wires *IEEE Trans. Appl. Supercond.* **23** 5201604

[127] Bellomo G, Musenich R, Sorbi M and Volpini G 2006 MgB_2 coils for particle accelerators *IEEE Trans. Appl. Supercond.* **16** 1439-41

[128] Collings E W, Kawabata S, Bhatia M, Tomsic M and Sumption M D 2006 Magnesium diboride superconducting strand for accelerator and light source applications *IEEE Trans. Appl. Supercond.* **16** 1445-8

[129] Tajima T, Haberkorn N F, Civale L, Schulze R K, Inoue H, Guo J, Dolgashev V A, Martin D W, Tantawi S G, Yoneda C G, Moeckly B H, Yung C, Proslier T, Pellin M, Matsumoto A and Watanabe E 2012 *Adv. Cryogenic Eng.*, (Melville: A. Inst. Phys.) pp 297-304

[130] Tuttle J, Pourrahimi S, Canavan E, DiPirro M and Shirron P 2006 A lightweight low-current 10 K magnet for space-flight ADRs *Cryogenics* **46** 196-200

[131] Ohara T, Kumakura H and Wada H 2001 Magnetic separation using superconducting magnets *Physica C* **357** 1272-80

[132] Zhu Z, Wang M, Ning F, Yang H, Wang K, Zhao L, Zhang G, Hou Z, Yao W and Liu Z 2013 The Development of 5.5 T high gradient superconducting magnetic separator *J. Supercond. Nov. Magnet.* **26** 3187-91

[133] Atomura N, Takahashi T, Amata H, Iwasaki T, Son K, Miyagi D, Tsuda M, Hamajima T, Shintomi T, Makida Y, Takao T, Munakata K and Kajiwara M 2012 Conceptual design of MgB_2 coil for the 100 MJ SMES of advanced superconducting power conditioning system (ASPCS) *Adv. Supercond.*,**27** pp 400-3

[134] Oga Y, Noguchi S and Tsuda M 2013 Comparison of optimal configuration of SMES magnet wound with MgB_2 and YBCO conductors *IEEE Trans. Appl. Supercond*. **23** 5700204

[135] Sander M, Gehring R and Neumann H 2013 LIQHYSMES-A 48 GJ toroidal MgB_2-SMES for buffering minute and second fluctuations *IEEE Trans. Appl. Supercond.* **23** 5700505

[136] Shintomi T, Asami T, Suzuki G, Ota N, Takao T, Makida Y, Hamajima T, Tsuda M, Miyagi D, Kajiwara M and Hirose J 2013 Design study of MgB_2 SMES coil for effective use of renewable energy *IEEE Trans. Appl. Supercond.* **23** 5700304

[137] Nomura S, Akita S, Shimada R and Shintomi T 2006 Design considerations for SMES systems using MgB_2 and/or high-temperature superconductors *IEEE Trans. Appl. Supercond.* **16** 590-3
[138] Kuriyama T, Urata M, Yazawa T, Yamamoto K, Ohtani Y, Koyanagi K, Masegi T, Yamada Y, Nomura S, Maeda H, Nakagome H and Horigami O 1994 Cryocooler directly cooled 6 T NbTi superconducting magnet system with 180-mm room-temperature bore *Cryogenics* **34** 643-6
[139] Nemoto K, Terai M, Igarashi M, Okutomi T, Hirano S, Kuwano K, Kusada S, Yamashita T, Yanase Y, Kuriyama T, Tosaka T, Tasaki K, Marukawa K, Hanai S, Yamaji M and Nakao H 2006 HTS magnet for maglev applications (2) - Magnet structure and performance *IEEE Trans. Appl. Supercond.* **16** 1104-7
[140] Bascuñán J, Lee H, Bobrov E S, Hahn S, Iwasa Y, Tomsic M and Rindfleisch M 2006 A 0.6 T/650 mm RT bore solid nitrogen cooled MgB_2 demonstration coil for MRI - A status report *IEEE Trans. Appl. Supercond.* **16** 1427-30
[141] Hales P, Jones H, Milward S and Harrison S 2005 Investigation into the use of solid nitrogen to create a "Thermal Battery" for cooling a portable high-temperature superconducting magnet *Cryogenics* **45** 109-15
[142] Haid B J, Lee H, Iwasa Y, Oh S S, Kwon Y K and Ryu K S 2002 Design analysis of a solid nitrogen cooled "permanent" high-temperature superconducting magnet system *Cryogenics* **42** 617-34
[143] Nakamura T, Muta I, Okude K, Fujio A and Hoshino T 2002 Solidification of nitrogen refrigerant and its effect on thermal stability of HTSC tape *Physica C* **372-376** 1434-7
[144] Haid B, Lee H, Iwasa Y, Oh S S, Ha H S, Kwon Y K and Ryu K S 2001 Stand-alone solid nitrogen cooled "permanent" high-temperature superconducting magnet system *IEEE Trans. Appl. Supercond.* **11** 2244-7
[145] Isogami H, Haid B J and Iwasa Y 2001 Thermal behavior of a solid nitrogen impregnated high-temperature superconducting pancake test coil under transient heating *IEEE Trans. Appl. Supercond.* **11** 1852-5
[146] Haid B J, Lee H, Iwasa Y, Oh S S, Kwon Y K and Ryu K S 2002 A "permanent" high-temperature superconducting magnet operated in thermal communication with a mass of solid nitrogen *Cryogenics* **42** 229-44
[147] Juan Bascuñán, Haigun Lee, Yukikazu Iwasa, Michael Tomsic and Michael Sumption 2004 MgB_2 model coils - preliminary test results *Paper 5LH05 ASC*
[148] Song J B, Kim K L, Kim K J, Lee J H, Kim H M, Kim W S, Yim S W, Kim H R, Hyun O B and Lee H G 2008 The design, fabrication and testing of a cooling system using solid nitrogen for a resistive high-Tc superconducting fault current limiter *Supercond. Sci. Technol.* **21** 115023
[149] Bascuñán J, Hahn S, Ahn M and Iwasa Y 2010 Construction and test of a 500 MHz/200 mm RT bore solid cryogen cooled Nb_3Sn MRI magnet *AIP Confer. Proc.* **1218** 523-30
[150] Kim K L, Song J B, Choi J H, Kim S H, Koh D Y, Seong K C, Chang H M and Lee H G 2010 The design and testing of a cooling system using mixed solid cryogen for a portable superconducting magnetic energy storage system *Supercond. Sci. Technol.* **23** 125006
[151] Pradhan S, Sharma A N, Tanna V L, Zkhan Z, Prasad U, Doshi K, Raval D C, Khan F, Gupta N C, Tank J, Gupta M K, Santra P, Biswas P, Parekh T,

Masand H, Sharma D, Srivastava A and Patel H 2012 SST-1 status and plans *IEEE Trans. Plasm. Sci.* **40** 614-21
[152] Koloskova L A, Krupskii I N, Manzhelii V G and Gorodilov B Y 1973 Thermal conductivity of solid nitrogen and carbon monoxide *Sov. Phys. Solid State* **15** 1278
[153] Scott T A 1976 Solid and liquid nitrogen *Phys. Rep., Sec. C Phys. Lett.* **27** 89
[154] V.A. Rabinovich, A.A. Vasserman, V.I. Nedostup and L.S. Veksler 1988 *Thermophysical properties of neon, argon, krypton, and xenon* (New York: Hemisphere Publishing Corp.)
[155] Nakamura T, Higashikawa K, Muta I, Fujio A, Okude K and Hoshino T 2003 Improvement of dissipative property in HTS coil impregnated with solid nitrogen *Physica C* **386** 415-8
[156] Nakamura T, Higashikawa K, Muta I and Hoshino T 2004 Performance of conduction-cooled HTS tape with the aid of solid nitrogen–liquid neon mixture *Physica C* **412–414, Part 2** 1221-4
[157] Song J-B and Lee H 2012 Mixed cryogen cooling systems for HTS power applications: A status report of progress in Korea University *Cryogenics* **52** 648-55
[158] Brittles G D, Mousavi T, Grovenor C R M, Aksoy C and Speller S C 2015 Persistent current joints between technological superconductors *Supercond. Sci. Technol.* **28** 093001
[159] Liu J, Cheng J and Wang Q 2013 Evaluation of NbTi superconducting joints for 400 MHz NMR magnet *IEEE Trans. Appl. Supercond.* **23** 34-9
[160] Seeber B 1998 *Handbook of Applied Superconductivity* (Bristol : Inst. Phys. Pub.)
[161] Ichiki Y, Wakuda T and Tanaka K 2012 Joint of superconducting wires and method for joining superconducting wires. (US20120108435 A1)
[162] Takahashi M, Tanaka K, Okada M, Kitaguchi H and Kumakura H 2006 Relaxation of trapped high magnetic field in 100 m-long class MgB_2 solenoid coil in persistent current mode operation *IEEE Trans. Appl. Supercond.* **16** 1431-4
[163] Nardelli D, Marabotto R and Laurenti A 2009 Superconducting coil having a granular superconducting junction. (US20090264295 A1)
[164] Li X H, Ye L Y, Jin M J, Du X J, Gao Z S, Zhang Z C, Kong L Q, Yang X L, Xiao L Y and Ma Y W 2008 High critical current joint of MgB_2 tapes using Mg and B powder mixture as flux *Supercond. Sci. Technol.* **21** 025017
[165] Li X H, Ye L Y, Gao Z S, Wang D L, Lin L Z, Zhang G M, Dai S T, Ma Y W and Xiao L Y 2010 Close circuit test of MgB_2 coil with superconducting joints and a persistent current switch *J. Phys. Conf.* **234** 022020
[166] Hahn S, Iwasa Y, Bascuñán J, Voccio J P, Ling J, Song J and Kim Y 2015 Persistent-mode MRI magnet fabricated from reacted, monofilamentary MgB_2 wires and joints (PCT/US2014/046526).
[167] Tenbrink F, Aubele A, Gluecklich V, Sailer B and Schlenga K 2010 Superconducting connection between MgB_2 superconducting wires via a compressed element made from HTS powder. (US: Google Patents)
[168] Doll D W and Tomsic M J 2014 Low loss joint for superconducting wire. (US8812069 B2)

[169] Oomen M P 2014 Superconducting joints between MgB_2 wires for MRI magnets (ASC, Charlotte 2014)
[170] Lakrimi M 2013 Methods for forming joints between magnesium diboride conductors. (Google Patents)
[171] Wilson M N 1983 *Superconducting magnets* (Oxford University Press)
[172] Patel D, Md Shahriar Al H, Shahabuddin M, Yanmaz E, Pradhan S, Tomsic M, Choi S and Jung Ho K 2016 A new approach to a superconducting joining process for carbon-doped MgB_2 conductor *Supercond. Sci. Technol.* **29**, 095001
[173] Anderson P W and Kim Y B 1964 Hard superconductivity: theory of the motion of abrikosov flux lines *Rev. Mod. Phys.* **36** 39-43
[174] Kim Y B, Hempstead C F and Strnad A R 1965 Flux-flow resistance in type-II superconductors *Phys. Rev.* **139** A1163-A72
[175] Warnes W H 1988 A model for the resistive critical current transition in composite superconductors *J. Appl. Phys.* **63** 1651-62
[176] Ryan D T 1997 Critical currents of commercial superconductors in the picovolt per metre regime. (DPhil Thesis, University of Oxford)
[177] David M J T and Damian P H 2005 Relationship between the n -value and critical current in Nb_3Sn superconducting wires exhibiting intrinsic and extrinsic behaviour *Supercond. Sci. Technol.* **18** S297
[178] Keys S A 2003 *Handbook of superconducting materials: characterization of conductors* (Bristol: Inst. Phys. Pub.)
[179] Iwasa Y 1976 Superconducting joint between multifilamentary wires 2. Joint evaluation technique *Cryogenics* **16** 217-9
[180] Penco R and Grasso G 2007 Recent development of MgB_2-based large scale applications *IEEE Trans. Appl. Supercond.* **17** 2291-4
[181] Takayasu M 1999 Electric characteristics of contact junctions between NbTi multifilamentary wires *IEEE Trans. Appl. Supercond.* **9** 4628-32
[182] Nardelli D, Angius S, Capelluto A, Damiani D, Marabotto R, Modica M, Perrella M and Tassisto M 2010 Persistent mode MgB_2 short windings *IEEE Trans. Appl. Supercond.* **20** 1998-2001

2.6. Note: Chapter Publication and Text Usage Detail

Some portion of this Literature Review has been published as a review paper in the *Cryogenics* (see below ref. 1). Some of the written text in this Literature Review has been taken from my published papers, as shown below.

[1] **Patel D**, Hossain M S A, Motaman A, Barua S, Shahabuddin M and Kim J H 2014 Rational design of MgB_2 conductors toward practical applications *Cryogenics* **63** 160-5

[2] **Patel D**, Hossain M S A, See K W, Xu X, Barua S, Ma Z, Choi S, Tomsic M and Kim J H 2015 MgB_2 superconducting joints for persistent current operation *Supercond. Sci. Technol.* **28** 065017

[3] **Patel D**, Md Shahriar Al H, Khay Wai S, Qiu W, Kobayashi H, Zongqing M, Seong Jun K, Hong J, Jin Yong P, Choi S, Maeda M, Shahabuddin M, Rindfleisch M, Tomsic M, Dou S X and Kim J H 2016 Evaluation of persistent-mode operation in a superconducting MgB_2 coil in solid nitrogen *Supercond. Sci. Technol.* **29** 4LT02-9

[4] **Patel D**, Md Shahriar Al H, Maeda M, Shahabuddin M, Yanmaz E, Pradhan S, Tomsic M, Choi S and Jung Ho K 2016 A new approach to a superconducting joining process for carbon-doped MgB_2 conductor *Supercond. Sci. Technol*. **29** 095001

The Scope of the Thesis

Based on the Literature Review, the thesis project 'Design and fabrication of solid nitrogen (SN_2) cooled magnesium diboride (MgB_2) based persistent magnet for magnetic resonance imaging (MRI) application' was planned to be pursued in three steps. They are outlined one by one below. Each step was considered as a milestone toward completion of the project on time.

Step 1: Design and fabrication of the SN_2 cooling system

The ultimate aim of the project was to demonstrate an MgB_2 based persistent magnet in SN_2, which meets the technical requirements to be applicable in MRI. As a suitable SN_2 cooling system was not available at the University of Wollongong, it was a prime requirement to design and fabricate the SN_2 cooling system to test the MgB_2 based persistent magnet. Therefore, in the first step, the SN_2 cooling system was designed, and an order was placed for commercial fabrication. Based on the prospective size of the magnet to be fabricated, the overall size of the SN_2 cooling system was finalized.

As mentioned in section 2.3.4.1 of the Literature Review, the thermal contact between the magnet and the cryogen would be poor if the liquid nitrogen (LN_2) was frozen by vacuum pumping. Hence, reducing the temperature was better done by conduction cooling using a cryocooler. Thus, in the SN_2 cooling system, a two-stage Gifford-McMahon cryocooler was planned to be used for freezing LN_2 by conduction cooling. Furthermore, as mentioned in section 2.3.4.2 of the Literature Review, various reported SN_2 cooling systems faced different types of problems, such as poor contact between the cryocooler and the SN_2 chamber, possibly leaks between two dissimilar materials joined at low-temperature or limitations in achieving a low enough temperature due to unexpected heat loads. To avoid all these problems, the SN_2 cooling system was designed using stainless steel, except for the radiation shield (as no leak tight joint was required for the radiation shield), and the contact between the cryocooler and the SN_2 chamber was designed such that the poor contact problem could be avoided. To predict all types of heat loads, detailed finite element (FE) analysis was carried out for simulating the temperature gradient across

the entire cooling system, which has not been done before for any SN_2 cooling system design.

In addition, as mentioned in section 2.3.4.3 of the Literature Review, a cooling system using only SN_2 has a potential thermal contact problem from repeated thermal disturbances, such as local heating or an over-current, leading to a problem called the thermal dry-out phenomenon. It was proposed that a small amount of the liquid cryogen can solve the problem of dry-out, through what is called mixed-cooling operation. Hence, the SN_2 cooling system was designed such that, if required, the mixed-cooling operation could be performed. The detailed design, fabrication, installation, and testing of the SN_2 cooling system is presented in Chapter 4.

Step 2: Superconducting joint fabrication for MgB_2 conductors

Following the design and placement of the order for the commercial fabrication of the SN_2 cooling system, the next step was to fabricate the superconducting joints for the MgB_2 conductors. As mentioned in section 2.4 of the Literature Review, the fabrication of high-performance superconducting joints for MgB_2 conductors was very challenging. Thus, only a few groups (university and industrial groups) have reported high performance using MgB_2 conductors. In particular, reports of superconducting joints using *in-situ* MgB_2 conductors were very limited, and the fabrication of the joints involved several areas of practical know-how rather than reported information in the literature. Of course, superconducting joints using reacted multifilament MgB_2 conductor were highly desirable, but as mentioned in section 2.4.4 of the Literature Review, there was no such reacted MgB_2 conductor joint which showed superconductivity above 10 K (the expected operation temperature of the MgB_2 based MRI magnet). Initially, I also tried to fabricate superconducting joints using reacted MgB_2 conductor, but I was unable to achieve any success. Hence, it was decided to try joining using unreacted multifilament conductors. Nevertheless, as mentioned in section 2.4.4 of the Literature Review, joint performance using unreacted multifilament MgB_2 conductor has been rather inconsistent, and I also found a similar problem after several trials. In the meantime, it was reported (section 2.4.2 of the Literature Review) that monofilament MgB_2

conductor can be used in magnet windings above 10 K without the flux jumping which triggers quench. Therefore, I tried joining using unreacted monofilament. I was able to achieve very good performance which could be suitable for MRI application. The superconducting joining process for MgB_2 conductors is presented in Chapter 5 as an MgB_2 superconducting joints for persistent current operation.

Furthermore, as mentioned in the section 2.4.4 of the Literature Review, the joining process for MgB_2 conductor does not lead to a very good performance in the case where the conductor used for joining is a carbon (C)-doped conductor. (As mentioned in the section 2.2.4 of the Literature Review, the high field performance of MgB_2 conductor can be significantly enhanced by doping with C.) A similar effect was also observed in the case of my joining process; hence, I further modified the joining process and developed a new approach to fabricating superconducting joints using C-doped MgB_2 conductors. The superconducting joining process for C-doped MgB_2 conductors is presented in Chapter 6 as a new approach to a superconducting joining process for C-doped MgB_2 conductors.

Step 3: Demonstration of the MgB_2 based persistent magnet in SN_2

To successfully complete the thesis project, the final and third step was to demonstrate an MgB_2 based persistent magnet operating in SN_2. As can be seen in section 2.4.4 in the Literature Review, there have been no reports on the demonstration of an MgB_2 based persistent magnet in SN_2, so this thesis work has been the first to demonstrate an MgB_2 based persistent magnet in SN_2. The demonstration of the MgB_2 based persistent magnet in SN_2 is presented in Chapter 7 as an evaluation of persistent-mode operation of superconducting MgB_2 coil in SN_2.

Apart from above-mentioned work, a conventional solenoid coil using multifilament MgB_2 conductor was also designed, fabricated, and tested in the SN_2. The coil was able to carry 200 A current at 28 K in SN_2. The test results on the solenoid coil are presented in Chapter 8, which covers the design, fabrication, and transport measurements of the MgB_2 solenoid coil in Sn_2. Chapter 9, presents the thesis conclusions and future prospects.

Chapter 3

3. Experimental Procedures

3.1. Sample Preparation

In this thesis work, three types of samples were prepared, magnesium diboride (MgB_2) wires, MgB_2 superconducting joints, and MgB_2 solenoid coils. Some of the wires for the joints and coil winding were purchased from a commercial vendor.

3.1.1. MgB_2 Wires

Two types of monofilament MgB_2 wires were prepared in this thesis work, one with an iron (Fe) sheath and the other with a niobium (Nb) barrier and Monel sheath.

3.1.1.1. Monofilament MgB_2 Wire with Fe Sheath

Monofilament MgB_2 wire was fabricated by the powder-in-tube (PIT) technique, using an *in situ* process [1]. The details of the PIT technique and *in situ* process have already described in section 2.2.3.1 of the Literature Review in Chapter 2. To fabricate wire, magnesium (99%, 325 mesh) from Sigma-Aldrich and amorphous boron (98.8 %, ~400 nm) powder from Pavezyum were used as the starting materials with the stoichiometric composition of Mg : B = 1 : 2 [2, 3]. The mixed power was packed into Fe tube with an outer diameter (O.D.) of 6.30 mm and an inner diameter (I.D.) of 4.11 mm. The two ends of the tube were sealed using aluminum (Al) foil. The composite wire was swaged and subsequently drawn to an O.D. of 1.00 mm. The big swaging machine, as shown in figure 3-1 with dies, was used to reduce the diameter of the wire to 3 mm. Then, the drawing process was used to reach the final size of the wire. The small swaging machine shown in figure 3-2 was used to prepare the tip of the wire to insert it in the die of the drawing machine, as shown in figure 3-3. The average reduction in the cross-sectional area of the wire during swaging and the drawing process was ~5%. The short samples cut from the fabricated long wires (see figure 3-4) were then wrapped in zirconia foil and heat treated at 650 – 700 °C for 30 - 90 min under high-purity argon (99.9%) atmosphere.

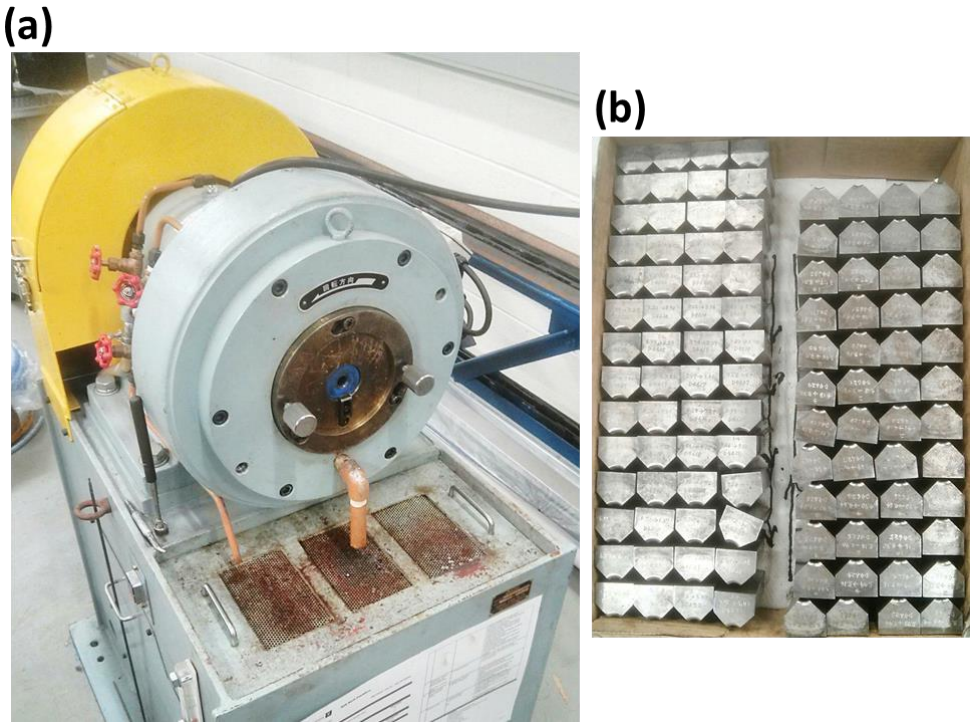

Figure 3-1.(a) Big swaging machine to swage wire to 3 mm, (b) big swaging machine dies.

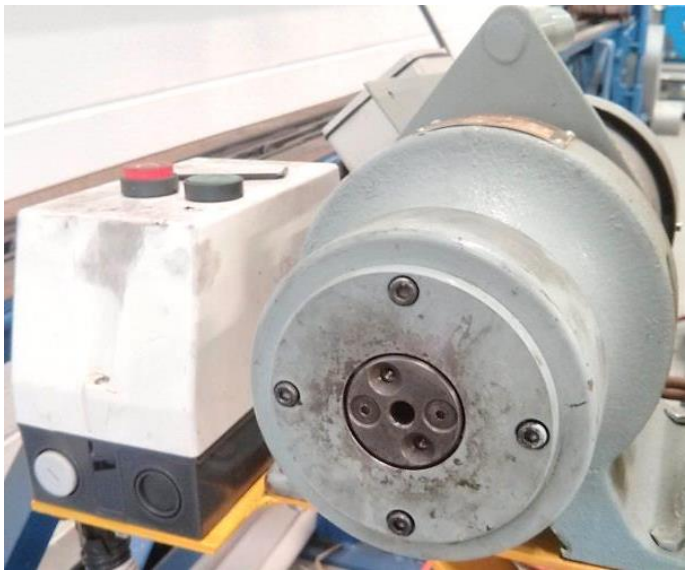

Figure 3-2. The small swaging machine to prepare the tip of the wire for drawing below 3 mm.

Figure 3-3. The drawing machine with dies.

3.1.1.2. Monofilament MgB_2 Wire with Nb Barrier and Monel Sheath

To fabricate the monofilament MgB_2 wire with Nb barrier and Monel sheath, an appropriate tube (concentric Nb tube inside and Monel tube outside) was prepared. One end of the tube was blocked using Al foil and it was filled with magnesium (99%, 325 mesh) from Sigma-Aldrich and amorphous boron (98.8 %, ~400 nm) powder from Pavezyum as the starting materials with the stoichiometric composition of Mg : B = 1 : 2 [2, 3]. Following the filling with powder, the open end of the tube was closed using Al foil. Subsequently, wire 0.84 mm in diameter was prepared using the same method outlined in the previous section.

Figure 3-4. Monofilament MgB_2 wire. Visually, both wires (Fe-sheathed and Monel sheathed with Nb barrier) look similar.

3.1.2. Superconducting Joints

In this thesis work, two types of superconducting joints using unreacted monofilament wires were prepared, one with Fe-sheathed monofilament wire and the other with Nb barrier and Monel sheathed wire.

3.1.2.1. Superconducting Joints using Monofilament MgB_2 Wire with Fe Sheath

To fabricate superconducting joints using monofilament Fe-sheathed wire, the metallic sheath material of the two wires was partially peeled off using mechanical polishing until the MgB_2 core was exposed. After removing the metallic sheath, the exposed cores of the wires were aligned and made to face each other using commercially available super glue. The two aligned wires were then fixed in a

suitable SS316 enclosure with an inner bore diameter of 6 mm, using a high-temperature sealing material from Copaltite [4]. The curing of the sealing material was carried out at 150 °C for 15 min in a drying oven. For the next step, mixed powder from the same batch (Mg + 2B) that was used for wire fabrication was then packed into the enclosure bore. The packed powder density was estimated to be 1.96 g cm^{-3} ± 4%. Again, the sealing material was applied on the top edge of the enclosure to hermetically seal the enclosure to avoid Mg evaporation during the heat-treatment process. For compacting the Mg + 2B powder to make close contact with the wire core, ~0.93 GPa of pressure was applied, using a suitable SS316 plug. Again, the curing of the sealing material was carried out at 150 °C for 15 min in the drying oven. One of the joints fabricated using above method is shown in figure 3-5 before heat-treatment process. Finally, the joints were heat-treated in high purity Ar inert atmosphere at 700 °C for 90 min. The joints were allowed to cool down naturally to room temperature (RT) before removing them from the furnace. A detailed pictorial representation of the joining process is presented in Chapter 5 [1].

Figure 3-5. Joint fabricated using Fe-sheathed wire prior to heat-treatment.

3.1.2.2. Superconducting Joints using Monofilament MgB_2 Wire with Nb Barrier and Monel Sheath

To fabricate superconducting joints using monofilament MgB_2 wire with the Nb barrier and Monel sheath, firstly, a predefined length (~7 mm) of the Monel sheath was chemically etched away with nitric acid from the joining area of the wires. Then, the Nb barrier of the wire (~4mm in length) was partially peeled off until the MgB_2 core was exposed using mechanical polishing. After peeling off the Nb barrier, the exposed MgB_2 cores of the two wires were aligned and made to face each other using super glue. The two aligned wires were fixed in an SS enclosure (I.D. of 6 mm) using a high-temperature sealing material (Resbond 907GF) [5]. The sealing material was allowed to cure for 24 h at RT in air. The filling of the joint with Mg (99%, 325 mesh, Sigma-Aldrich) + C-encapsulated B (98.8%, ~400 nm, C-doping 2 wt%, amorphous, Pavezyum) powder was performed in Ar protective atmosphere (in an Ar glove box) to minimize trapping of oxygen while filling the joint with powder [2, 3]. An SS plug was used to compact the powder inside the enclosure. The gauge pressure for pressing the plug was <0.35 GPa. In the next step after pressing the powder, the sealing material was applied to the remaining gaps on the SS enclosure, and the joint was then taken out of the Ar glove box. Again, the sealing material was allowed to cure for 24 h at RT (in air) prior to heat-treatment. Finally, the joint was heat-treated in Ar atmosphere at 690 °C for 30 min. One of the joint fabricated using the above-mentioned method is shown in figure 3-6. A pictorial representation of the joining process is presented in Chapter 6.

3.1.3. Solenoid Coil Fabrication

In this thesis work, three types of coils were fabricated: closed-loop coils with one superconducting joint, a closed-loop coil with a persistent-current-switch (PCS), and conventional solenoid coils, as shown in figure 3-7. All coils were fabricated using the wind and react fabrication process. The details of the coils are presented in Chapters 5, 7, and 8, respectively.

Figure 3-6. As prepared joint using Nb barrier and Monel sheathed wire.

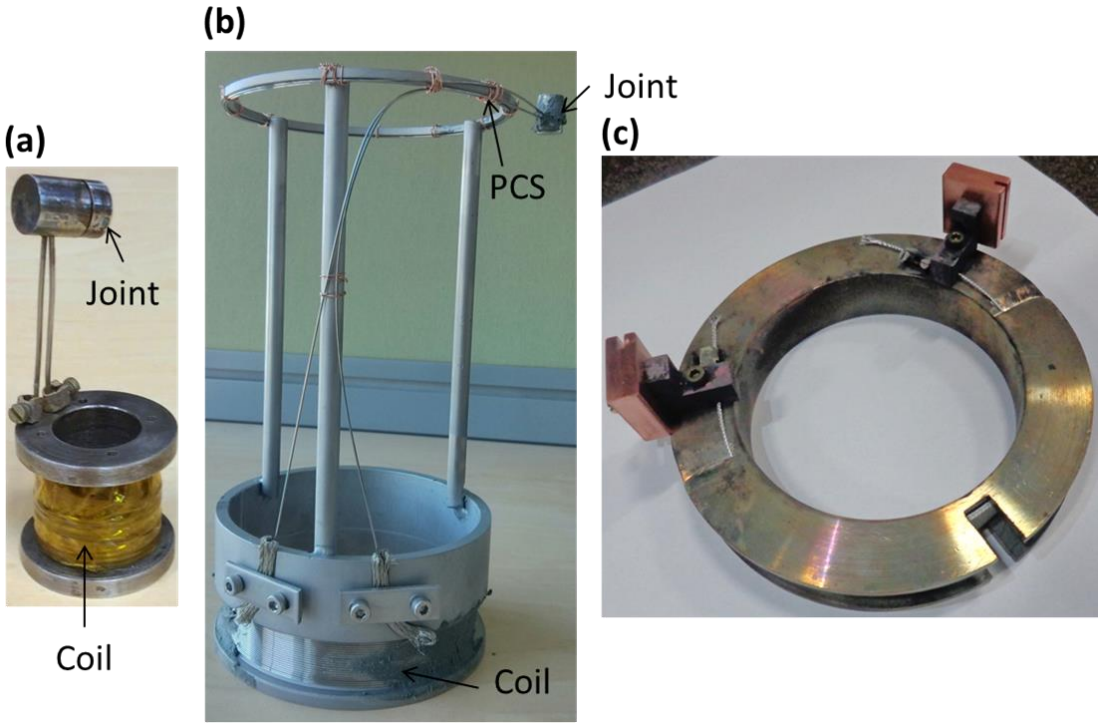

Figure 3-7. (a) Closed-loop coil with one joint, (b) closed-loop coil with PCS, and (c) solenoid coil.

3.1.4. Sample Preparation for Joint Fabrication and Characterization

3.1.4.1. Cross-sectioning of Wires and Joints

To make superconducting joints or to visualize cross-sections (longitudinal and transverse) of the wires and joints using a scanning electron microscope (SEM), it was necessary to cross-section wires and joints. For cross-sectioning wires for joint fabrication, a Leica EM TXP was used, as shown in the figure 3-8. This TXP uses a diamond cutter to cut the wire, which is installed using wax on the mounting holder. In addition, it allows the user to use different protective fluids while cutting the sample. To cut joints, a Struers Accutom – 50 device, as shown in figure 3-9, was used.

Figure 3-8. Leica EM TXP [6].

3.1.4.2. Mounting and Polishing of Wires and Joints

Following the cross-sectioning of the wires and joints to observe the cross-sections using a microscope, it was necessary to mount the samples on a suitable holder for polishing.

To mount samples, a Struers CitoPress – 20 device, as shown in figure 3-10, was used with PolyFast (conductive, bakelite resin with carbon filler) thermosetting material [7].

To polish the samples, a Struers Tegramin – 25 device (using water), as shown in figure 3-11, was used. The 250 mm diameter polishing discs allowed coarse initial polishing (800 grits) to final fine polishing down to 1 μm diamond size.

Figure 3-9. Struers Accutom – 50, joint after cross-sectioning (inset) [7].

Figure 3-10. Struers CitoPress – 20 [7].

Figure 3-11. Struers Tegramin – 25 [7].

3.2. Characterization Techniques

In this thesis work, two types of samples characterization techniques were used, (i) phase and structural, and (ii) electromagnetic. The tools used for these characterizations are presented in following subsections.

3.2.1. Phase and Structural Characterization

The MgB_2 material was prepared by the solid-state reaction process using Mg and B powders. It is well known that the performance of the MgB_2 material greatly depends on its phase and structure [1, 8-13]. Thus, to examine the phase of the MgB_2 material, X-ray diffraction (XRD) was used, whereas, for observation of the structure, a scanning electron microscopy was used.

3.2.1.1. X-ray Diffraction

X-ray powder diffraction is the analytical method used for identifying phase in the crystalline material, and it can also give information on the unit cell dimensions, grain size, etc. of the material. X-rays are waves of electromagnetic

radiation with wavelengths of 0.01 to 10 nm. Crystals are composed of regular arrays of atoms, and the wavelength of the X-rays is within the interatomic distance between two atoms in the crystalline material. When X-rays are incident on the crystal, atoms within the crystal scatter the X-rays, mainly through the atomic electrons. The scattering results in secondary spherical X-ray waves. This type of scattering called **elastic scattering**. The ordered atoms produce ordered spherical waves. Most of the spherical waves cancel each other out due to destructive interference; nevertheless, in some directions, they produce constructive interference as per Bragg's law:

$$2d_{hkl} \sin\theta = n\lambda \tag{3.1}$$

where d_{hkl} is the distance between two planes with Miller index (*hkl*), θ is the incident angle, *n* is any integer, and λ is the wavelength of the X-ray beam.

Bragg's law is satisfied (means diffraction XRD patterns are produced) when the combination of the distance between planes and the incident X-ray angle is such that $2d \sin\theta$ is equal to the integer multiple of the wavelength of the incident X-rays (see figure 3-12).

The MgB_2 phase formation into wires and joints was investigated using XRD. To perform XRD analysis, the powder was taken from the wires by peeling off the sheath materials; on the other hand, the joints were longitudinally cut to take out the MgB_2 powder ingot. The ingot was ground into a fine powder. The XRD device (Mini-materials Analyser, GBC Scientific Equipment, USA) was used with Cu Kα (λ = 1.54056 Å) radiation for the XRD analysis [14]. The XRD data of the samples were collected from angles of 20° to 80°, using a 1° per min scan rate and 0.02° step size. One of the XRD patterns collected in this work is presented in figure 3-13.

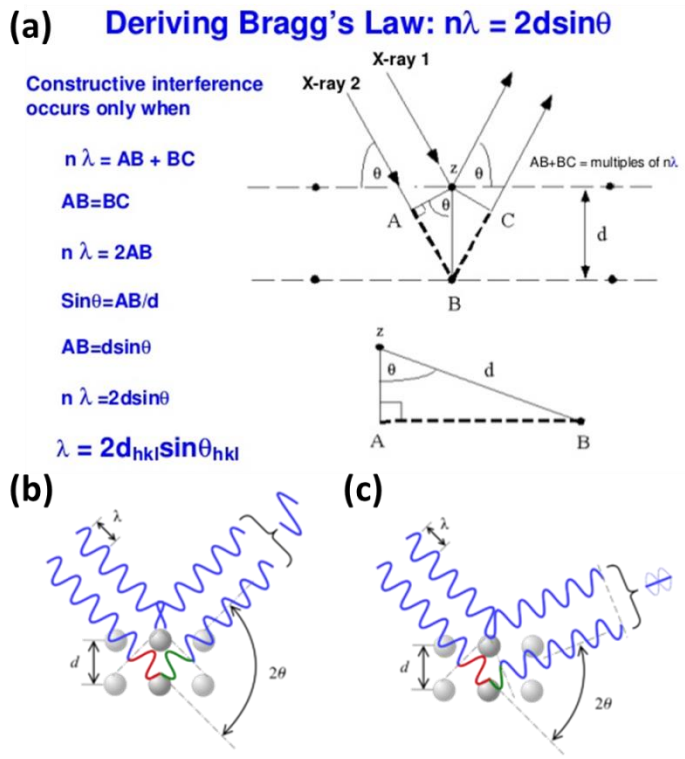

Figure 3-12. (a) Derivation of Bragg's law, and the specific angles where (b) constructive and (c) destructive interference takes place [15, 16].

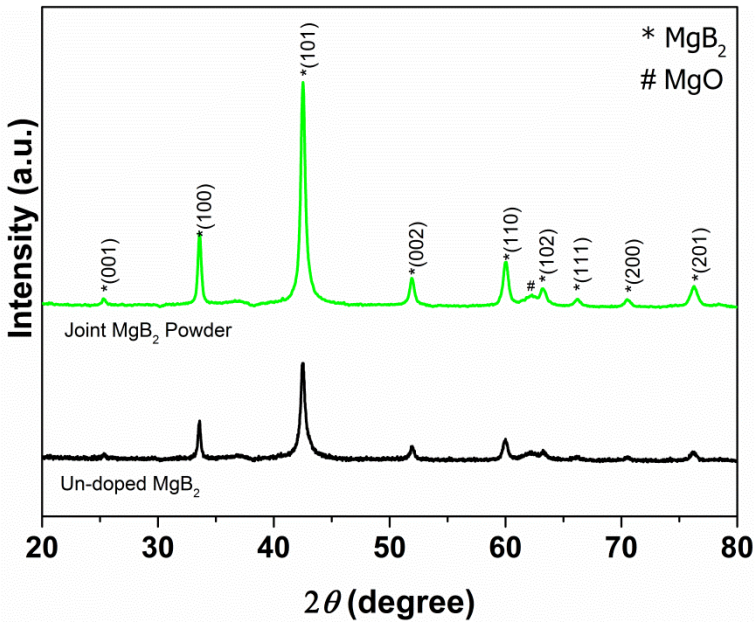

Figure 3-13. XRD patterns of MgB_2 powder from a joint and reference undoped MgB_2 power with indexed planes.

3.2.1.2. Scanning Electron Microscopy

Scanning electron microscopy was conducted using a scanning electron microscope (SEM) [17]. An SEM uses a focused beam of an electron to produce an image of the sample. The focused beam of electrons interacts with the atoms of the sample and produces different types of signals. These signals contain information regarding the surface topography and composition of the sample. A typical SEM can attain resolutions down to 1 nm. In SEM, the sample can be observed in a low vacuum, high vacuum, and, in fact, in a cryogenic environment, too. Most SEM uses secondary electrons (emitted from very close to the sample surface) emitted as a result of interaction between the incident electron beam and the atoms in the sample to observe surface topography. In this thesis, a JEOL JSM-6490LA, low vacuum SEM was used [18]. For surface topography, a secondary electron detector was used, whereas for energy-dispersive X-ray spectroscopy (EDS), a backscattered electron (BSE) detector was used. The SEM image and the corresponding EDS maps of one of the joint cross-sections are shown in figure 3-14.

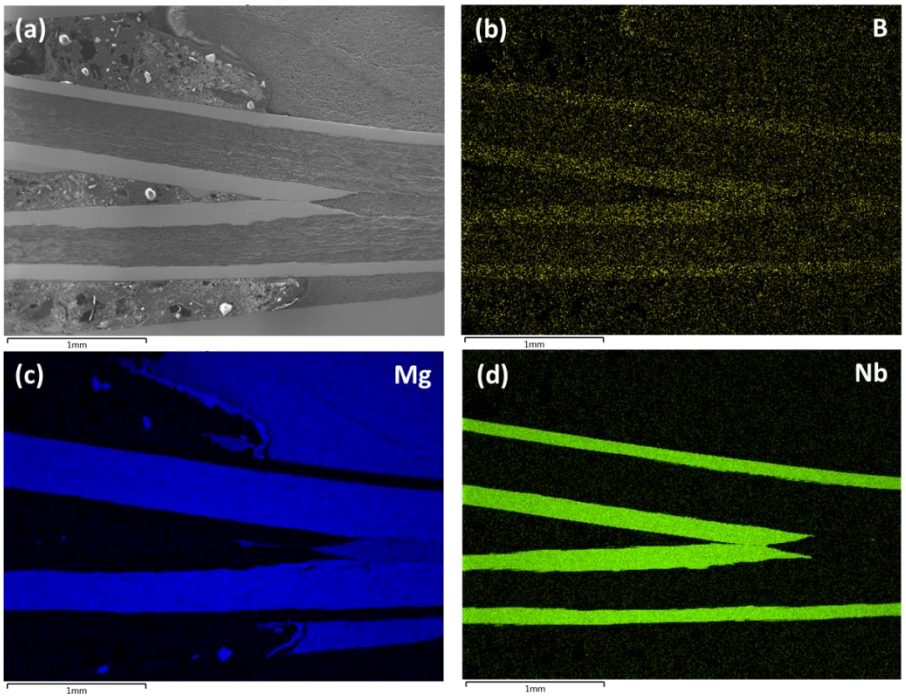

Figure 3-14. SEM image of the cross-section of a joint, and EDS maps of (b) B, (c) Mg, and (c) Nb.

3.2.2. Electromagnetic Characterization

The electromagnetic properties of the wires and joints such as critical temperature (T_c) and transport current (I_c) were measured using an American Magnetics re-condensing 15 T Superconducting (AMS) magnet, as shown in figure 3-15 [19].

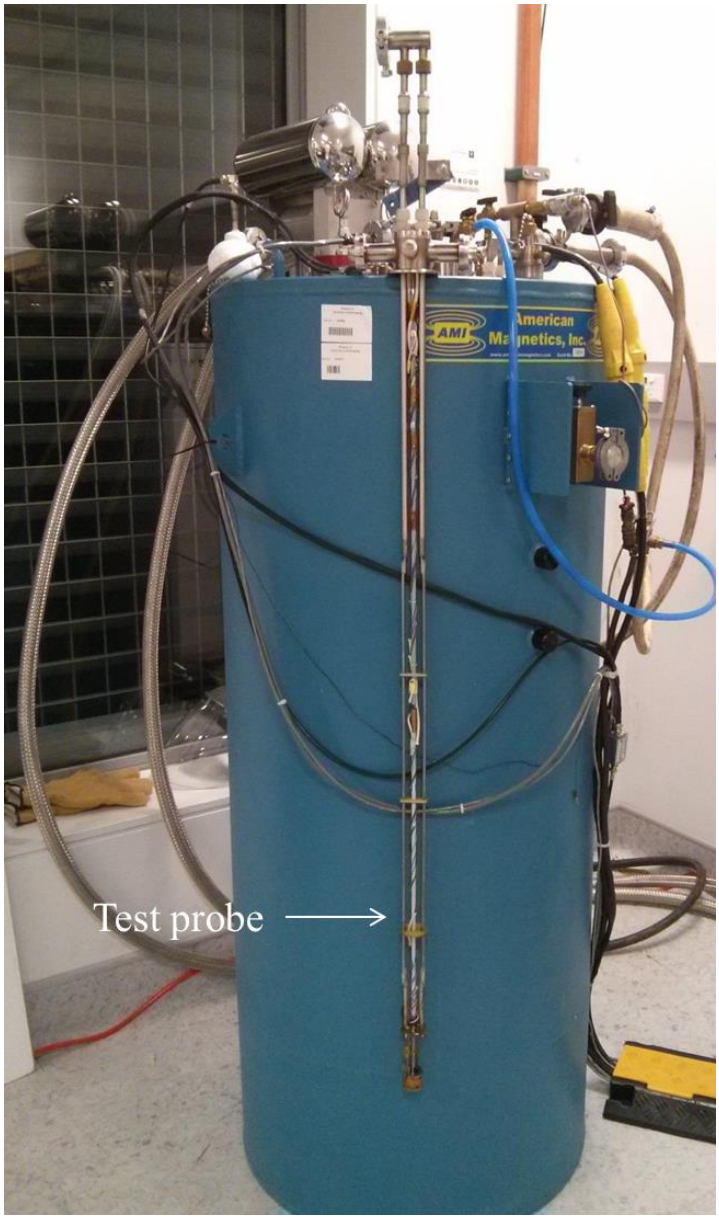

Figure 3-15. American Magnetics Superconducting (AMS) magnet with a test probe. The bottom section of the test probe is replaceable with current leads to perform transport measurements of the wires or joints.

3.2.2.1. Critical Temperature Measurement (T_c)

To measure T_c of the wires and the joints, the variable temperature insert (VTI) of the AMS magnet was used [19]. The typical set-up of the test probe for T_c measurements on joints and wires is shown in figure 3-16. To measure T_c, firstly, current up to 1 A was passed through the specimen at around 50 K temperature, and the voltages across the specimen were acquired using a Keithley Nanovoltmeter model 2182A via the LabVIEW interface until the superconducting transition occurred [20]. The measured voltages were converted into resistance using Ohm's law. The resistance vs. temperature plot of one of the joints to determine the T_c is shown in figure 3-17.

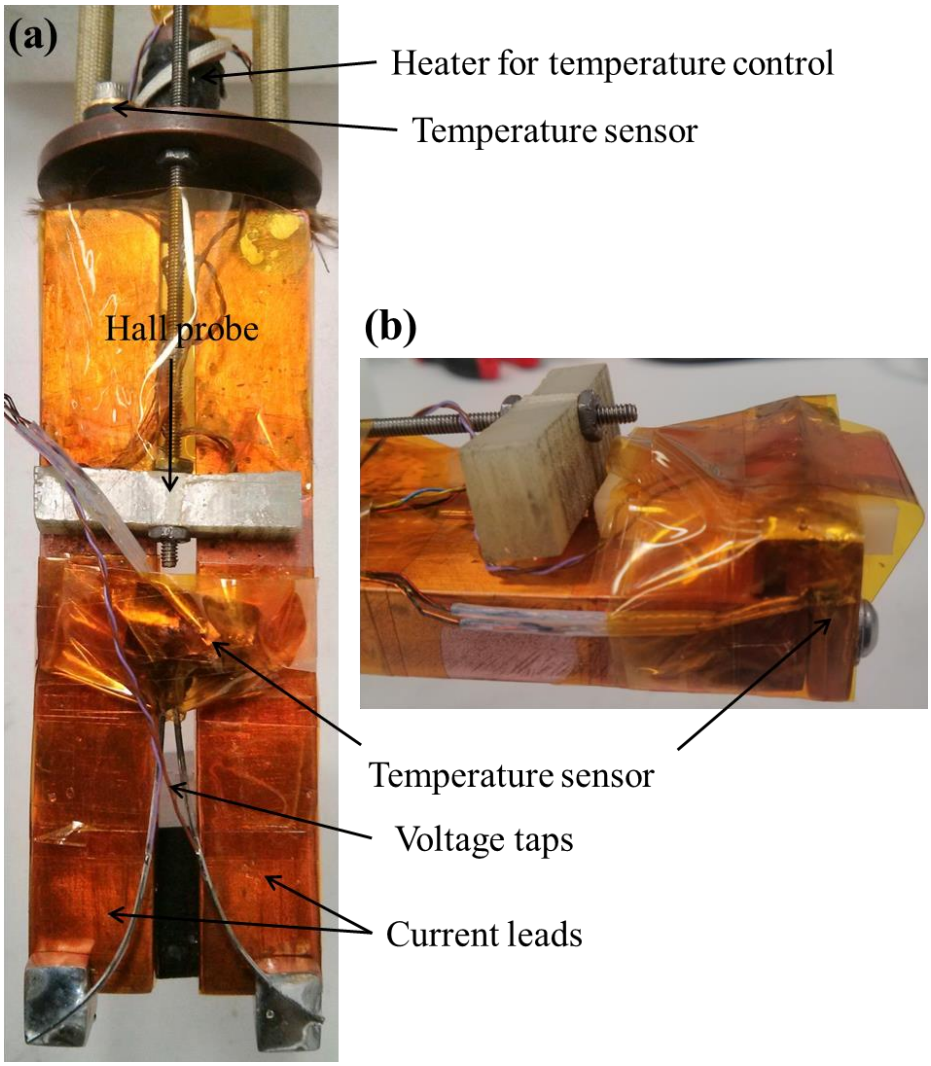

Figure 3-16. Test probe set-up for T_c measurements of (a) joint and (b) wire.

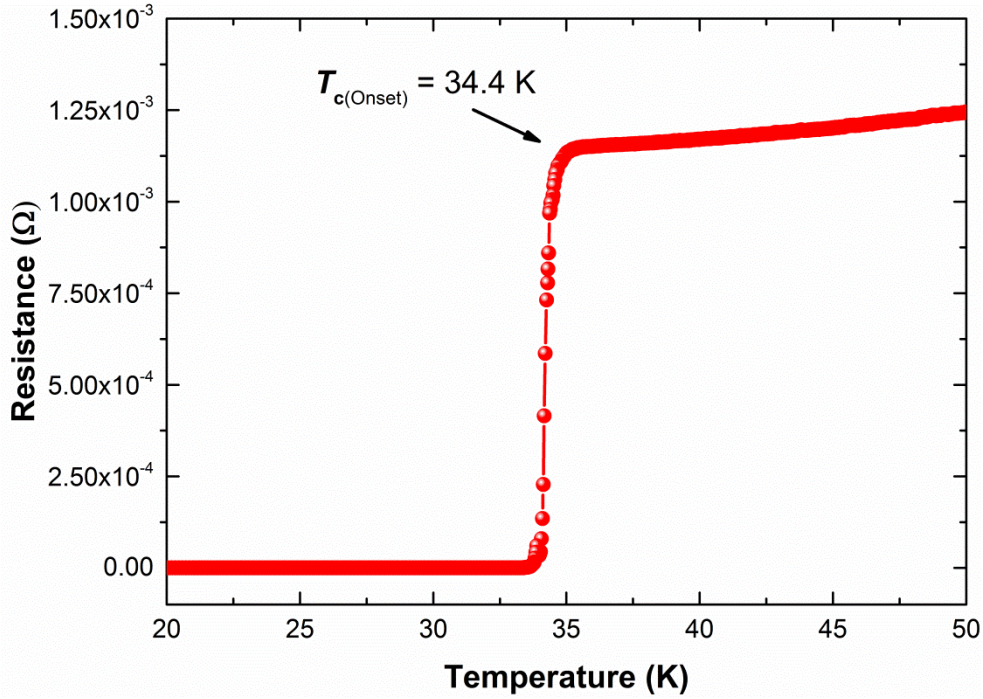

Figure 3-17. Resistance vs. temperature plot of one of the joints to determine T_c.

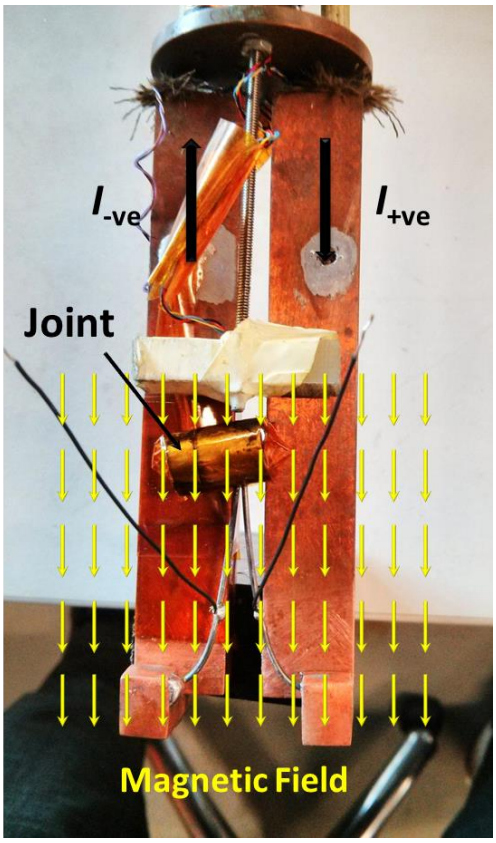

Figure 3-18. The bottom of the test probe for I_c measurements.

3.2.2.2. Critical Current Measurement (I_c)

To measure I_c of the wires and joints at different temperatures and in different magnetic fields, a similar set-up to that used for T_c measurements was used. For I_c measurements, however, current up to 200 A (the maximum limit of the power supply) was passed through the sample, and voltages were measured across the finite length. From the voltage vs. current plot, I_c was determined, using the 1 μV cm^{-1} criterion.

For applying an external magnetic field to the sample, the VTI is housed in the superconducting solenoid magnet with PCS. Thus, for I_c measurements in different external magnetic fields, the test probe shown in figure 3-15 (with the bottom part replaced with current leads, as shown in figure 3-16) was inserted in the VTI of the AMS magnet. To measure the magnetic field in the vicinity of the test sample, a uniaxial Hall probe was used, as shown in figure 3-16(a). The temperature control was accomplished by controlling a small needle valve through which liquid helium (LHe) enters into the VTI, and by controlling the power of two heaters (one at the bottom of the VTI and one at the top of the current leads, as shown in figure 3-16). One voltage taps were used to measured voltage during transport measurements (see figure 3-16). The bottom of the test probe for I_c measurements is shown in figure 3-18. The typical voltage vs. current curve of one of the joints is shown in figure 3-19.

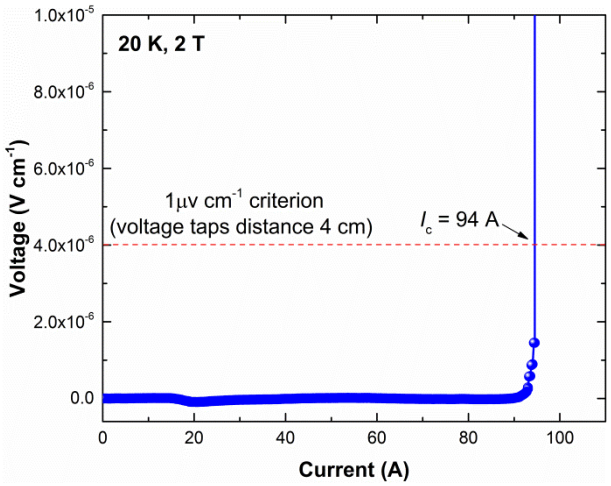

Figure 3-19. Voltage vs. current curve of one of the joint at 20 K, 2 T [1].

3.3. References

[1] Patel D, Hossain M S A, See K W, Xu X, Barua S, Ma Z, Choi S, Tomsic M and Kim J H 2015 MgB_2 superconducting joints for persistent current operation *Supercond. Sci. Technol.* **28** 065017
[2] www.sigmaaldrich.com
[3] www.pavezyum.com.tr
[4] www.copaltite.com
[5] www.cotronics.com
[6] www.leica-microsystems.com
[7] www.struers.com
[8] Vinod K, Kumar R G A and Syamaprasad U 2007 Prospects for MgB_2 superconductors for magnet application *Supercond. Sci. Technol.* **20** R1
[9] Collings E W, Sumption M D, Bhatia M, Susner M A and Bohnenstiehl S D 2008 Prospects for improving the intrinsic and extrinsic properties of magnesium diboride superconducting strands *Supercond. Sci. Technol.* **21** 103001
[10] Serquis A, Civale L, Hammon D L, Liao X Z, Coulter J Y, Zhu Y T, Jaime M, Peterson D E, Mueller F M, Nesterenko V F and Gu Y 2003 Hot isostatic pressing of powder in tube MgB_2 wires *Appl. Phys. Lett.* **82** 2847-9
[11] Kim J H, Oh S, Heo Y U, Hata S, Kumakura H, Matsumoto A, Mitsuhara M, Choi S, Shimada Y, Maeda M, MacManus-Driscoll J L and Dou S X 2012 Microscopic role of carbon on MgB_2 wire for critical current density comparable to NbTi *NPG Asia Mater.* **4** e3
[12] Susner M A, Sumption M D, Bhatia M, Peng X, Tomsic M J, Rindfleisch M A and Collings E W 2007 Influence of Mg/B ratio and SiC doping on microstructure and high field transport J_c in MgB_2 strands *Physica C* **456** 180-7
[13] Maeda M 2011 Densification and connectivity in polycrystalline MgB_2 materials for improvement of critical current density. (Ph.D. Thesis, University of Wollongong)
[14] www.gbcsci.com
[15] www.slideshare.net/chem_engine/x-ray-diffraction-39221132
[16] http://en.openei.org/wiki/X-Ray_Diffraction_(XRD
[17] https://en.wikipedia.org/wiki/Scanning_electron_microscope
[18] www.jeol.co.jp
[19] www.americanmagnetics.com
[20] www.tek.co

3.4. Note: Text Usage Detail

Some of the written text in this Chapter has been taken from my published papers, as shown below.

[1] **Patel D**, Hossain M S A, Motaman A, Barua S, Shahabuddin M and Kim J H 2014 Rational design of MgB_2 conductors toward practical applications *Cryogenics* **63** 160-5

[2] **Patel D**, Hossain M S A, See K W, Xu X, Barua S, Ma Z, Choi S, Tomsic M and Kim J H 2015 MgB_2 superconducting joints for persistent current operation *Supercond. Sci. Technol.* **28** 065017

[3] **Patel D**, Md Shahriar Al H, Khay Wai S, Qiu W, Kobayashi H, Zongqing M, Seong Jun K, Hong J, Jin Yong P, Choi S, Maeda M, Shahabuddin M, Rindfleisch M, Tomsic M, Dou S X and Kim J H 2016 Evaluation of persistent-mode operation in a superconducting MgB_2 coil in solid nitrogen *Supercond. Sci. Technol.* **29** 4LT02-9

Chapter 4

4. Design, Fabrication, Installation, and Testing of Solid Nitrogen Cooling System

4.1. Introduction

The continuously soaring price of liquid helium (LHe) has increased the demands for the use of alternative cryogens more than ever for various applications of superconductors. As mentioned in the Literature Review, specifically for magnesium diboride (MgB_2) superconductor based magnetic resonance imaging (MRI) magnets to operate around 20 K, inexpensive and lightweight SN_2 is the most promising choice because SN_2 has a high heat capacity compared to other solid cryogens (see Chapter 2). Solid neon (LNe) is ruled out of the choice because it is about 200 times more expensive than SN_2 on a volume basis [1, 2].

As already mentioned in the Literature Review, there are three major benefits to using SN_2 as a cryogen: (i) enhanced thermal stability against premature quenches due to the higher heat capacity, (ii) simpler system dynamics, and (iii) the possibility of operation of the magnet in the absence of the cooling source, i.e., cryocooler [3]. Nevertheless, a cooling system using only SN_2 has a potential thermal contact problem from repeated thermal disturbances, such as a local heating or an over-current, called the thermal dry-out phenomenon [4]. The Kyoto group proposed that a small amount of the liquid cryogen in SN_2 can solve the problem of dry-out [2, 5-7]. In fact, recently, Song *et al* proposed the use of mixed cryogens such as SN_2-liquid nitrogen (LN_2), SN_2- LNe, and solid argon (Ar) – LN_2 to avoid the dry-out problem [8]. The operation of a mixed cryogen cooling is performed once SN_2 is formed in the SN_2 chamber. A suitable gas is slowly injected into the system, and the gas changes its phase and is transformed to a liquid so that the solid and liquid cryogens remain in the cooling chamber in mixed form. For demonstrating a laboratory-scale MgB_2 based persistent magnet in SN_2, the design, fabrication, and installation of an SN_2 cooling system was carried out. The cooling system was designed to have the option of operating in mixed cooling mode.

Furthermore, Nakamura *et al* reported that the thermal contact between the magnet and the cryogen would be poor if the formation of SN_2 was done by vacuum pumping [5]. Therefore, the reduction in temperature in the cooling system was designed to be carried out by conduction cooling using the cryocooler.

The SN_2 cooling systems designed prior to this thesis work have already been presented in section 2.3.4.2 of the Literature Review. The previously reported SN_2 cooling systems experienced the following issues: (i) probable leaks in dissimilar material joints, (ii) poor thermal contact between the cryocooler and the SN_2 chamber, and (iii) high known or unknown heat loads, which prevented the system from reaching a sufficiently low-temperature. Therefore, the cooling system for this thesis project was designed in such a way that all these problems could be eliminated.

In particular, to avoid dissimilar material joints, the entire cooling system was designed using stainless steel (SS), except for the radiation shield, to avoid any low-temperature leaks. In addition, the connection between the cryocooler and the SN_2 chamber was designed such that no poor thermal contact problem arises. Finally, detailed analytical and finite element (FE) analysis (thermal and structural) was carried out to simulate the system response, which had not been done before.

In this thesis Chapter, therefore, details of the design, fabrication, installation, and testing of the SN_2 cooling system are presented.

4.2. Cooling System Description

A three-dimensional (3D) model of the designed cooling system is shown in figure 4-1. The cooling system consists of the cryostat, radiation shield, SN_2 chamber, connecting tubes, and cryocooler. Except for the radiation shield, all parts, i.e., the cryostat, SN_2 chamber, and all connecting tubes were made from SS304L, whereas the radiation shield was constructed from oxygen-free, high-conductive (OFHC) copper (Cu). The cooling system was conduction cooled with a Sumitomo model RDK-408E2 Gifford-McMahon two-stage cryocooler having a cooling capacity of 40 W at 43 K at the 1^{st} stage, and 1 W at 4.2 K at the 2^{nd} stage. The 1^{st} stage and the 2^{nd} stage were thermally connected with the radiation shield, and the SN_2 chamber through an OFHC Cu bar, respectively. For charging the magnet,

hybrid current leads using brass and a high-temperature superconductor (HTS) were designed. The transition part (brass to HTS) was designed to be thermally connected with the first stage of the cryocooler through the radiation shield.

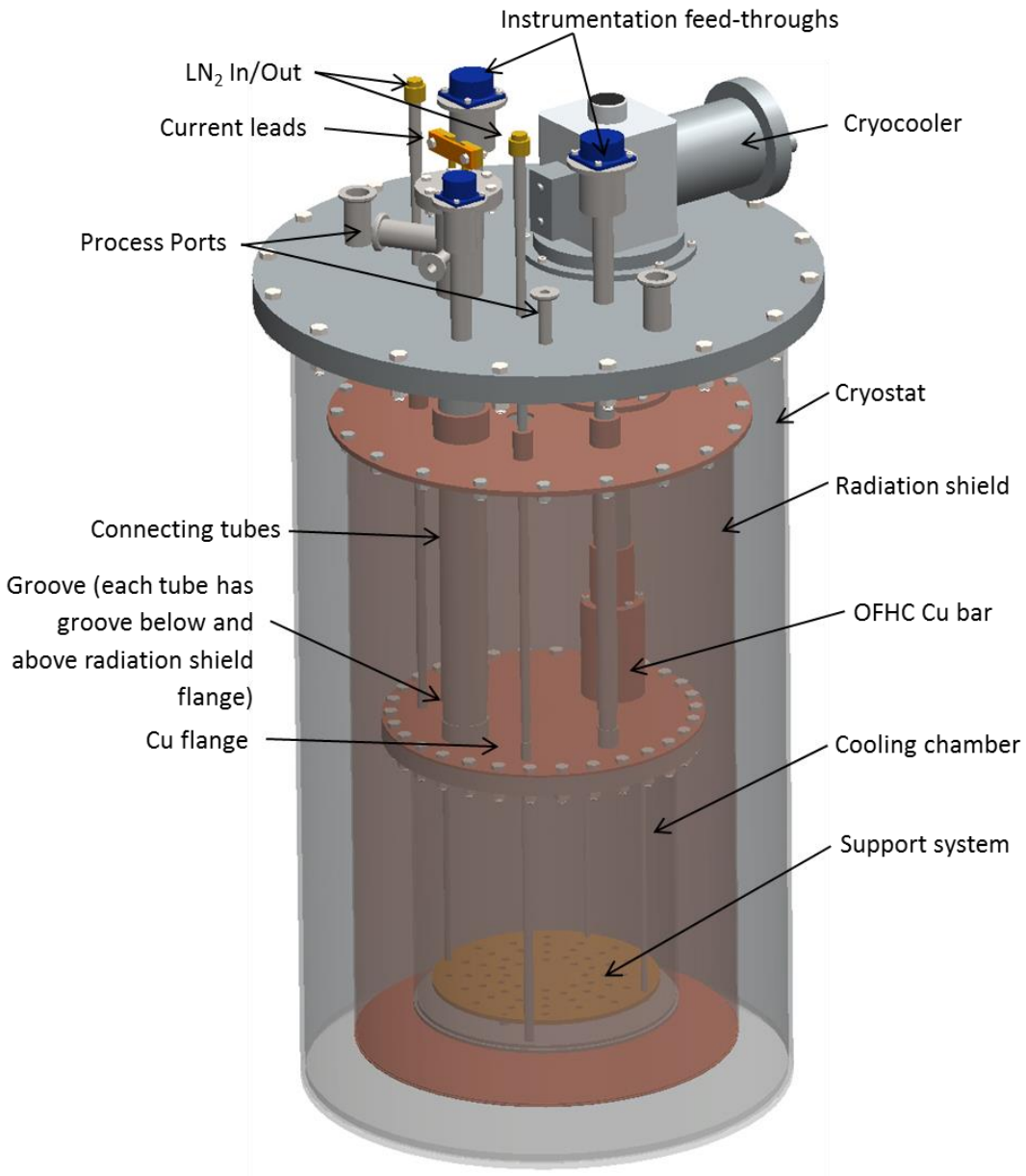

Figure 4-1. 3D model of the designed cooling system [9].

The tubes coming from room temperature (RT) to the SN_2 chamber were required to be brazed at the radiation shield to give support to the radiation shield. Hence, it was not feasible to use thin wall tubes due to possible deformation while brazing with the radiation shield. Nevertheless, the conduction heat load from RT to the radiation shield, and the radiation shield to the SN_2 chamber through the

connecting tubes was minimized by designing the 20 mm short groove so that only a 0.5 mm thickness of the tube remained at the optimised location. In fact, a longer groove would be better, but, as per the requirement of this system, the 20 mm groove length was kept. The optimization of the groove location was mandatory because the groove should be at the location where the thermal conductivity and temperature gradient are minimal with low cross-section area. Hence, even though more power is available for the conduction, due to the groove's lower capability of driving conduction, the overall stationary conduction heat load can be reduced.

Previously, Patel *et al* suggested that thermal anchoring of the instrumentation wires is mandatory to measure the temperature with higher accuracy and intercept the heat flow that is reaching critical parts of the system [10]. Hence, in order to decrease the conduction heat load from RT through the instrumentation wires to the SN_2 chamber, all the wires were designed to be thermally anchored at the radiation shield. Finally, suitable paths were kept for performing the mixed cooling operation.

Figure 4-2 presents a two-dimensional (2D) cross-sectional front view of the cooling system with key dimensions. The overall height of the cooling system, radiation shield, and SN_2 chamber was 1065 mm, 688 mm, and 322 mm, respectively. The outer diameter (O.D.) of the cryostat, radiation shield, and the SN_2 chamber was 508 mm, 396 mm, and 273.10 mm, respectively. The connecting Cu bar from the 2^{nd} stage of the cryocooler to the SN_2 chamber was 99.5 mm long, and the distance between the radiation shield and the SN_2 chamber was 333 mm. The gap in-between the SN_2 chamber, radiation shield, and the cryostat was 30 mm.

4.3. Thermal Design

The optimal design of the cooling system greatly depends on the precise estimation of various heat loads. For estimating the total thermal heat load on the SN_2 chamber and the radiation shield, the conduction, radiation, and the residual gas conduction heat loads were taken into account, whereas the radiation transmission and the gaseous conduction through the connecting tubes were neglected, because, in this type of the system, they are approximately 20 and 10 times lower than the conduction heat load of the connecting tubes, respectively [3]. The conduction heat load (Q) was estimated using equation (4.1).

$$Q = \frac{A}{L}\int_{T_L}^{T_H} K\, dT \tag{4.1}$$

The radiation heat load (Q_{rad}) is estimated by Stephen-Boltzmann law using Equation (4.2) :

$$Q_{rad} = \varepsilon \cdot \sigma \cdot \left({T_H}^4 - {T_L}^4\right) \cdot A \tag{4.2}$$

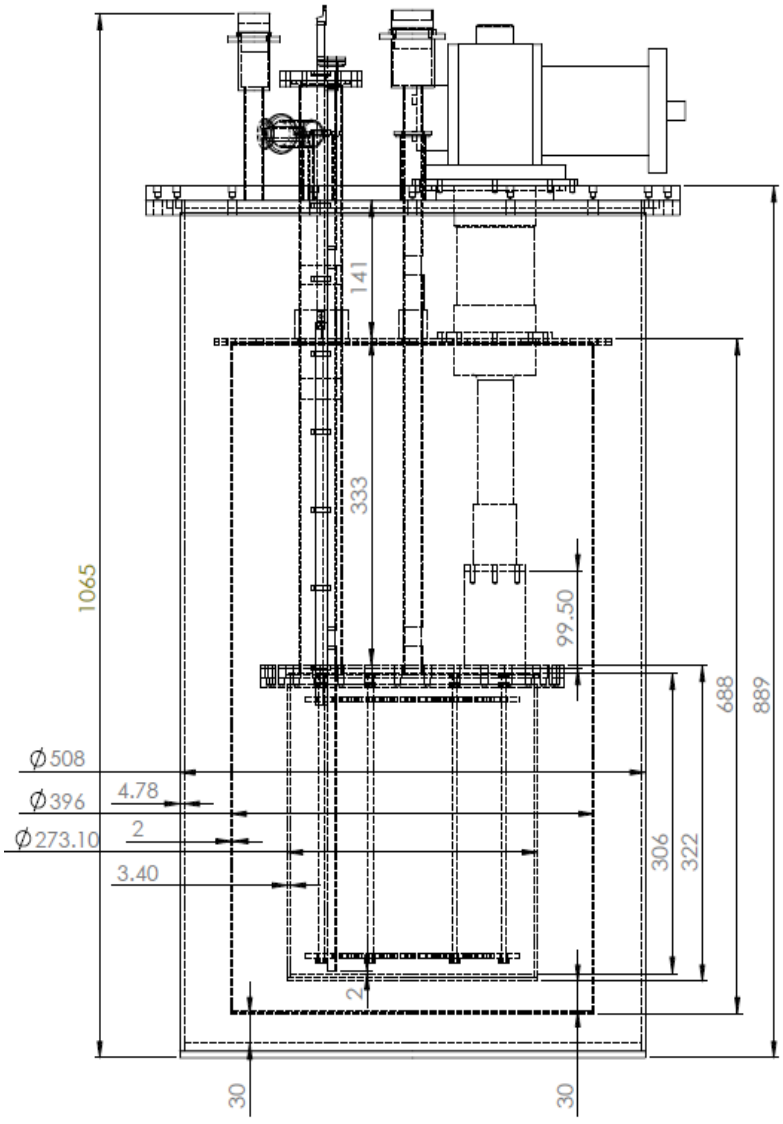

Figure 4-2. 2D cross-sectional front view of the designed cooling system.

The radiation configuration of this system resembles parallel flanges, so the effective total emissivity was calculated using equation (4.3) [2].

$$\varepsilon = \frac{(\varepsilon_L) \cdot (\varepsilon_H)}{\varepsilon_L + \varepsilon_H - \varepsilon_L \varepsilon_H} \tag{4.3}$$

In most cryogenic experiments or apparatus, the radiation heat load is minimised by wrapping multiple layers of multilayer insulation (MLI) around a cold body; in our case, it was 10, and hence, in the presence of the MLI layers, equation (4.2) can be modified to equation (4.4). This equation is only valid when a hot body is not touching the MLI, because if a hot body is touching the MLI, then the conduction heat load through the MLI needs to be taken into account.

$$Q_{rad} = \frac{\varepsilon}{N+1} \cdot \sigma \cdot \left({T_H}^4 - {T_L}^4\right) \cdot A \tag{4.4}$$

For estimating the residual gas conduction(Q_{rgc}), equation (4.5) was used, [2, 11], although the empirical values in watts per meter squared (W m^{-2}) of the cold body area, as given in [2, 11], were used for the residual gas conduction calculations for the radiation shield and the SN_2 chamber.

$$Q_{rgc} = \eta_{rgc} \cdot P_{rgc} \cdot (T_H - T_L) \tag{4.5}$$

where η_{rgc} is dependent on the high and the low-temperature, but also depends on the accommodation coefficient [2].

The conduction, radiation, and the residual gas conduction heat loads were calculated for the radiation shield and the SN_2 chamber, using some of the critical estimated temperature inputs from the FE analysis to increase the practicality of the estimations.

The conduction heat load on the radiation shield comes from the connecting tubes, anchored instrumentation wires, and anchored current leads, and the joule heating due to current in the brass section of the current leads. Using FE analysis, the temperature of all the tubes below the radiation shield was estimated to be less than 48.5 K. Prior to calculating the radiation heat load on the radiation shield, the overall temperature of the radiation shield was estimated by FE analysis, as shown in figure 4-3. The maximum temperature point on the radiation shield was considered to be the temperature of the radiation shield for subsequent radiation heat load calculations. The Cu was regarded as OFHC Cu with residual resistivity ratio (RRR)

of 50. The maximum temperature on the radiation shield was estimated to be 54.305 K, as shown in figure 4-3.

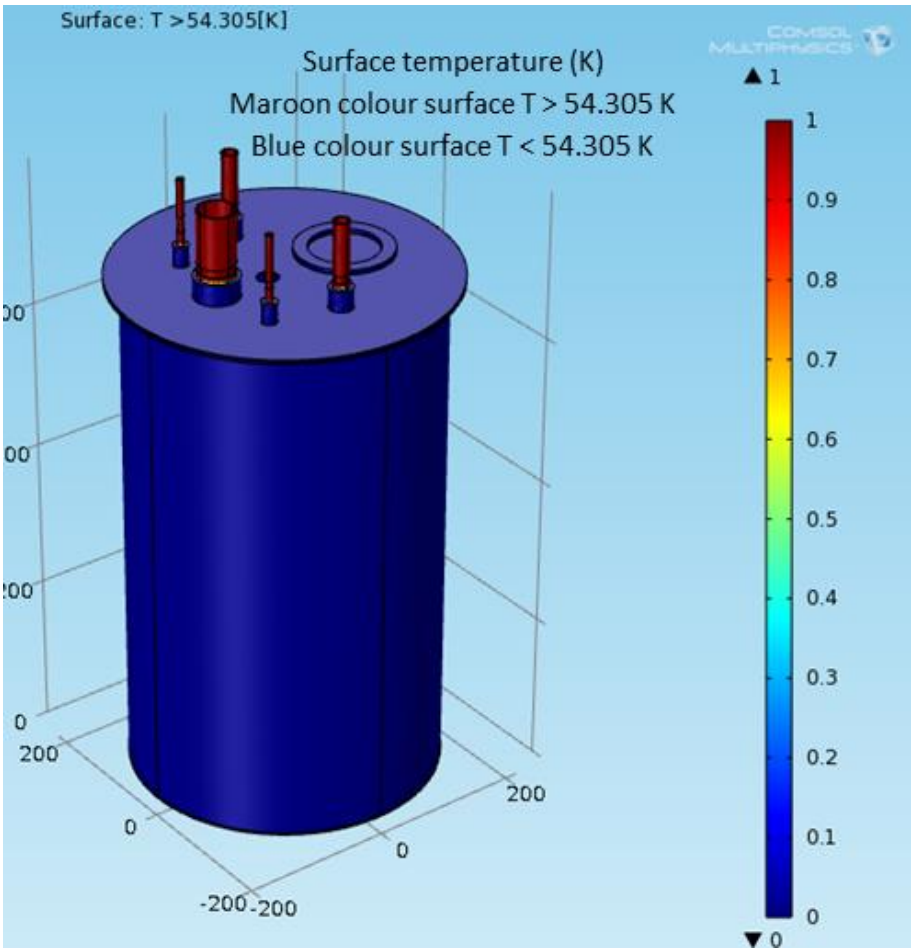

Figure 4-3. Temperature distribution in the radiation shield.

The residual gas conduction takes place due to un-evacuated gases remaining in the system. In order to keep the residual gas conduction as low as possible, the vacuum in-between the cryostat, radiation shield, and the SN_2 chamber was designed to be kept at $\leq 1.33 \times 10^{-5}$ mbar.

Table 4-1. Summary of the various thermal heat loads in the designed cooling system. The design of the hybrid current leads is presented in section 4.5.

Thermal heat loads	**Radiation shield (W)**	**SN_2 chamber (W)**
Conduction through tubes	6.971	0.015
Conduction through instrumentation wires	1.219	0.124
Conduction through current leads	7.450	0.232
Joule heating through current leads	14.897	0.026
Radiation	2.627	0.006
Residual gas conduction (while operation above 20.28 K)	0.341	0.079
Total (W)	33.505	0.482

Like the radiation shield, the conduction heat load on the SN_2 chamber comes from the connecting tubes, instrumentation wires, HTS part of the current leads, and the joule heating due to the inherent resistance of the HTS tape. The linear distance between the Cu radiation shield and the SN_2 chamber could be set to a maximum of 333 mm to minimize the conduction heat load.

All calculated heat loads on the radiation shield and the SN_2 chamber are listed in table 4-1 (see section 4.5 for current leads design). The total estimated heat load on the radiation shield and SN_2 chamber were 33.505 W and 0.482 W, respectively. These values were well below the available cooling power of 40 W at 43 K at the 1st stage and 1 W at 4.2 K at the 2nd stage of the cryocooler. As can be seen in table 4-1, an additional ~16% (~6.5 W), and ~52% (~0.52 W) of the cooling power remained at the 1st and 2nd stage of the cryocooler, respectively.

4.4. Structural Design

The 2007 ASME Boiler and Pressure Vessel Code VIII, Division 2 [12], and the 2007 ASME Boiler and Pressure Vessel Code II, Part D Properties of Materials [13] were utilized for estimating all wall thicknesses, all cylinders, and the head flanges, apart from the radiation shield.

As mentioned above, the SN_2 chamber and the cryostat were designed to be fabricated using SS304L (henceforth called SS), whereas the radiation shield was constructed from OFHC Cu. Cu with higher thermal conductivity was impractical for fabricating the SN_2 chamber to avoid any joining of dissimilar materials. Therefore, it was mandatory to use the SS, even though there was the drawback of its lower thermal conductivity. Moreover, there could be a temperature gradient in the system if the system was not designed rationally. Hence, the system was designed such that

the required uniformity of temperature was maintained, and this was confirmed by the FE analysis. The SN_2 chamber and the cryostat were designed for an internal 0.3 MPa pressure (gauge) because under the operation conditions, the pressure inside the SN_2 chamber was envisaged to run up to a maximum of 0.15 MPa during LN_2 transfer and gas boil off, and there would vacuum inside the cryostat. The cryostat was designed with the internal pressure of 0.3 MPa by envisaging the results of any accidental leak in the system.

4.4.1. Solid Nitrogen Chamber

As per the ASTM A312M, and the ASME B36.19M-2004 codes, a pipe with an inner diameter (I.D.) of 266.3 mm was found to match the dimension requirement, and the thickness was estimated by the ASME codes. According to ASME 2007 Section VIII, Division 2, the minimum required thickness t of a cylindrical cylinder subject to an internal pressure was estimated by equation (4.6).

$$t = \frac{D}{2} \cdot \left(exp\left[\frac{P}{SE}\right] - 1 \right) \tag{4.6}$$

The required cylinder thickness with a safety factor 5 was calculated to be 1.7 mm, but for obtaining the required temperature uniformity across the SN_2 chamber, the nearest available standard wall thickness pipe with schedule 10S was chosen, which had a wall thickness of 3.4 mm.

The thicknesses of all the flanges were also determined by the ASME 2007 Section VIII, Division II code, section 4.6.2.2 [12], as per the welded blank flange criteria. The top flange of the SN_2 chamber was designed to be bolted on the collar of the SN_2 chamber. In order to use the welded blank flange criteria, about thirty structural bolts of M8 were designed to be used to avoid any displacement. Equation (4.7) was used for estimating the required thickness t of the bottom and the top flanges of the SN_2 chamber.

$$t = d \cdot \left(\sqrt{\frac{CP}{S_{ho}E}} \right) \tag{4.7}$$

The calculated flange thickness was 7.84 mm, so the flange thickness of 8 mm was chosen. Similarly, the upper flanges and the collar thickness were kept

≥7.84 mm, although for making the indium seal mechanism for sealing the SN_2 chamber, the top collar, and the top flange were designed to be 10 mm thick. The effective thickness of the top flange was kept at 8 mm, however, including the 3 mm thick Cu flange on the top of the top flange, which was designed to be bolted on the top flange (see figure 4-1). Apiezon N® grease was used to improve the thermal contact between the Cu and the SS flanges [14]. The Cu flange has the unique purpose of maintaining the temperature uniformity in the entire SN_2 chamber (details presented later in section 4.6).

4.4.2. Radiation Shield

The dimensions of the radiation shield were based on the dimensions of the SN_2 chamber, the Cu bar between the 2^{nd} stage of the cryocooler and the SN_2 chamber, and the 30 mm gap in-between SN_2 chamber, radiation shield, and the cryostat, respectively. The wall thickness was not designed as per the ASME codes, however, because the entire radiation shield would remain in the vacuum during operation. Nevertheless, for the thermal and the structural integrity, a 2 mm thickness was estimated to be optimal from the FE analysis (details presented in section 4.6). On the other hand, 3 mm thick flanges were designed to be used for the bottom and the top flanges of the radiation shield.

4.4.3. Cryostat

The cryostat was the outermost chamber where the SN_2 chamber and the radiation shield were designed to be housed and supported using the connecting tubes from the top flange of the cryostat (see figure 4-1). All the structural loads of the system were ultimately transferred to the top flange of the cryostat, which distributes the load over the entire structure of the cryostat; hence, the structural integrity of the cryostat was the apex requirement. Under the normal operation conditions, the cryostat was designed to be in a vacuum; hence, for estimating the wall thickness of the cryostat components, the pressure vessel under an external pressure section of the ASME codes, with a design by rule requirement, was used [12, 13].

The available standard I.D. as per ASTM A312M and ASME B36.19M-2004 was chosen to be near the required I.D. of 498.44 mm for estimating the wall

thickness of the cylinder. As per this section, for checking the allowable external pressure, an arbitrary wall thickness of a cylinder needed to be assumed first. The standard thickness of 4.78 mm was chosen, and the remaining calculations were done to check its suitability for the external pressure requirement. The O.D. of the cylinder was thus 508 mm, whereas the required height was 854 mm.

As per the ASME code, if $\frac{D_o}{t} \leq 2000$ (in our case, 106.27), the 2007 ASME VIII, Division 2, section 4.4 code was the one to be used for the estimation. Equations (4.8) to (4.14) were to be used for determining the allowable external pressure. Only those equations are shown that are applicable to this design [12].

$$F_{he} = \frac{1.6 \cdot C_h \cdot E_y \cdot t}{D_0} \tag{4.8}$$

$$C_h = 1.12 \cdot {M_x}^{-1.058} \; for \; 13 < M_x < 2\left(\frac{D_o}{t}\right)^{0.94} \tag{4.9}$$

$$M_x = \left(\frac{L}{\sqrt{R_0 \, t}}\right) \tag{4.10}$$

$$F_{ic} = F_{he} \; for \; \frac{F_{he}}{S_y} \leq 0.552 \tag{4.11}$$

$$FS = 2.0 \; for \; F_{ic} \leq 0.55 S_y \tag{4.12}$$

$$\boldsymbol{P_a = 2F_{ha}\left(\frac{t}{D_o}\right)} \tag{4.13}$$

$$F_{ha} = \left(\frac{F_{ic}}{FS}\right) \tag{4.14}$$

The calculated values of M_x, $2\left(\frac{D_o}{t}\right)^{0.94}$, C_h, F_{he}, $\frac{F_{he}}{S_y}$, F_{ic}, and FS were 24.50, 160.65, 0.0379, 0.546, 113.7, and 2, respectively. Thus, the allowable external pressure P_a calculated from equation (4.13) was 1.07 MPa. Based on this thickness, 0.449 MPa of internal pressure was calculated to be safe, with a safety factor of 5 (using equation (4.6)). The required thickness of the end flanges of the cryostat was estimated to be 14.62 mm (similar to the end thickness calculation of the SN_2 chamber); however, 15 mm thick flanges were chosen.

The wall thicknesses of all the process tubes were estimated from equation (4.6) using welding factor 1. Therefore, for 0.3 MPa (gauge) maximum internal

pressures with a safety factor of 5, the required wall thicknesses of the tubes were 0.042 mm, 0.245 mm, and 0.098 mm, respectively for the LN_2 supply/return, current leads, and the instrumentation feed-through tube. The effective tubes thickness was designed to be 0.5 mm, however.

4.5. Thermoelectric Design and Analysis of Hybrid Current Leads

To limit the conduction heat load to a minimum via the current leads, conventional Cu current leads were not desirable. Therefore, to keep the conductive heat load and joule heating to the SN_2 chamber at a minimum, DI-BSCCO (Sumitomo) and brass based hybrid current leads with a current capacity of 150 A were designed [15]. Due to their low thermal conductivity compare to Cu, the normal section of the hybrid current leads was designed using brass [2]. As per [2, 16], to minimise conductive heat load along with joule heating due to current, the ratio l/A of the conductor was chosen such that equation (4.15) was satisfied, so that both heat loads would be at a minimum.

$$\left(\frac{I \cdot l}{A}\right) = \sqrt{\frac{2 \cdot \widetilde{K} \cdot (T_H - T_L)}{\tilde{\rho}}} \tag{4.15}$$

To absorb conductive and joule heat, the joint locations between the HTS and the normal parts of the current leads were designed to be thermally connected with the 1st stage of the cryocooler using copper braid with suitable insulation. Using equation (4.15), for l of 305 mm and I of 150 A, the optimal diameter of the brass current lead was 8.163 mm. This diameter of the brass section led to 7.450 W and 14.897 W conductive and joule heat load, respectively, on the radiation shield.

The HTS part of the individual hybrid current lead was designed using a high-temperature (HT) type of DI-BSCCO tape (in each current lead) manufactured by Sumitomo and a G-10 housing [15]. The typical HT type of DI-BSCCO tape had critical current, I_c, from 170 A - 200 A in self-field at 77 K. Hence, it was accepted that it would comfortably take a 150 A current when was to be operated below 48.85 K. The 3D model of the hybrid current lead is shown in figure 4-4. The conductive and joule heat load to the SN_2 chamber from the pair of current leads was estimated

to be 0.259 W and 0.026 W, respectively, for l of 395 mm from 48.85 K to 4.5 K at the SN_2 chamber.

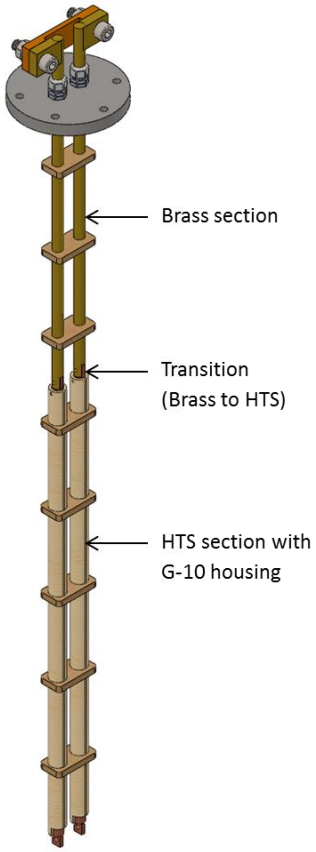

Figure 4-4. 3D Model of hybrid current leads.

An FE analysis of the simplified model of the designed hybrid current leads was also carried out, in which, out of the two leads, one lead was modelled. Temperatures of 293.15 K, 48.85 K, and 4.5 K were set at the top, transition region, and bottom of the current lead, respectively. In addition, a 150 A current was set in the current lead. Under experimental conditions, the temperature at the anchoring area could be somewhat different due to conduction and joule heating. Figure 4-5(a) shows the temperature distribution in the current lead, whereas figure 4-5 (b) shows the temperature distribution above and below 48.85 K.

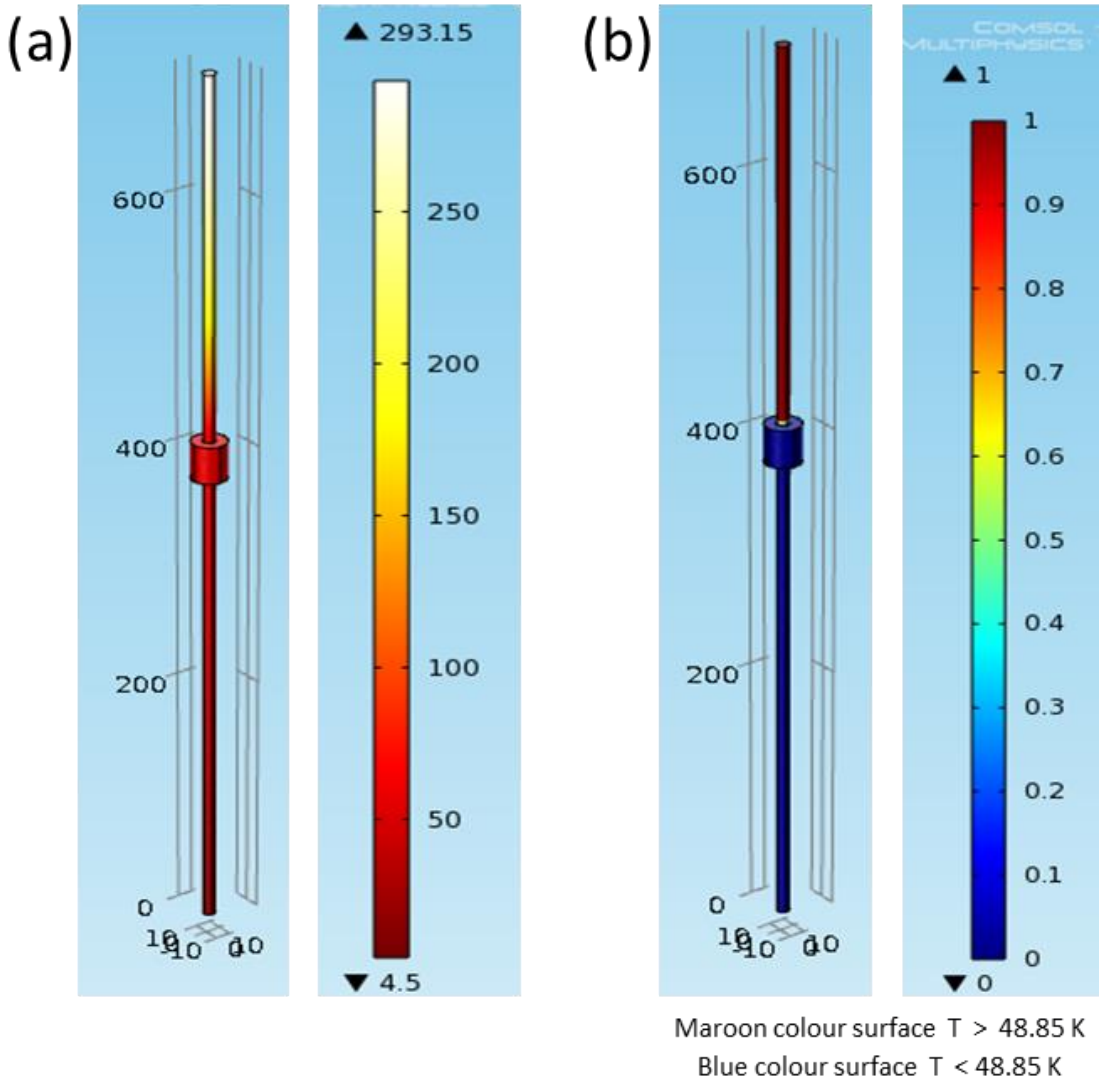

Figure 4-5. (a) Temperature distribution in the current lead, and (b) temperature distribution in the current lead above and below 48.85 K.

4.6. Finite Element (FE) Analysis

The stationary FE analysis of the entire cooling system was conducted to confirm the thermal and structural integrity in three parts (due to limitations in the computation power): (i) the SN_2 chamber with connecting tubes up to the radiation shield and Cu bar, (ii) the radiation shield with tubes up to the top flange of the cryostat, and (iii) the cryostat with connecting tubes up to the SN_2 chamber. In each analysis, the temperature distribution, von Mises stress, and total displacement due to the loading conditions were determined, except for the temperature distribution in the cryostat, because it was designed to remain in RT.

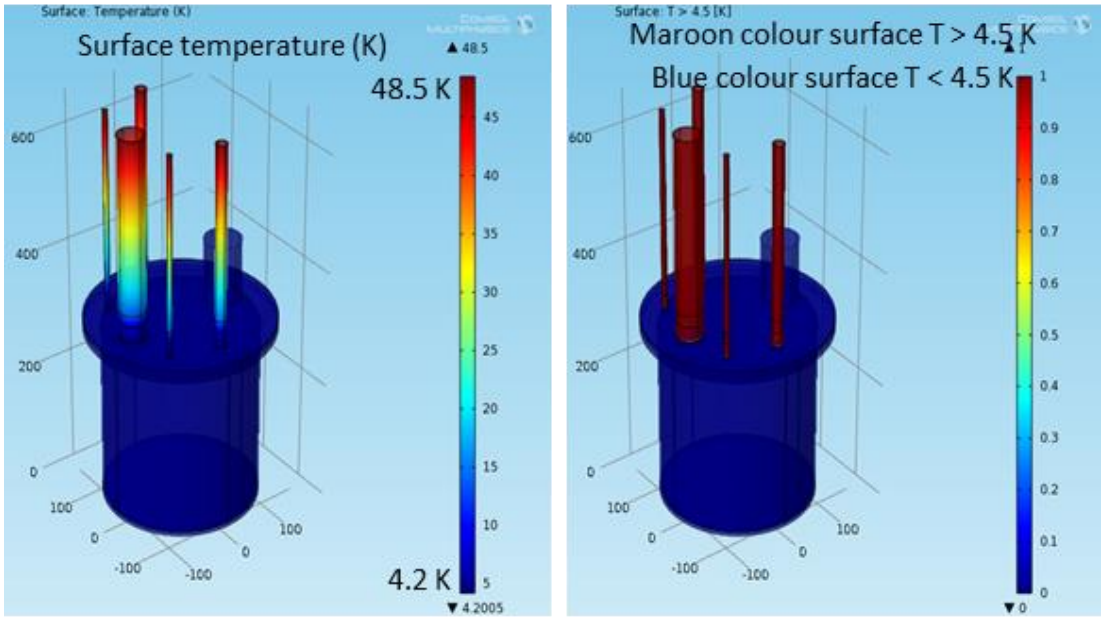

Figure 4-6. Temperature distribution in the SN_2 chamber.

The FE model shown in figure 4-6 was used for the analysis of the SN_2 chamber. Note that the 3 mm thick Cu flange was placed on the top of the SN_2 chamber together with SN_2 in the SN_2 chamber. The left side image in figure 4-6 shows the temperature distribution on the SN_2 chamber, while the right side image shows the temperature below and above 4.5 K. It can be clearly seen that a 4.5 K uniform temperature was achieved in the SN_2 chamber.

The von Mises stress and the exaggerated total displacement of the SN_2 chamber are shown in figure 4-7 (a), and (b), respectively. The maximum von Mises stress and total displacement under appropriate loading conditions were estimated to be 9.1681 MPa and 0.0037 mm, respectively. The allowable stress in SS304 is 138 MPa, so 9.1681 MPa was acceptable, and 0.00374 mm displacement was also acceptable displacement [12, 13]. Based on this simulation, it was anticipated that flexibility in the connecting Cu bar was not required.

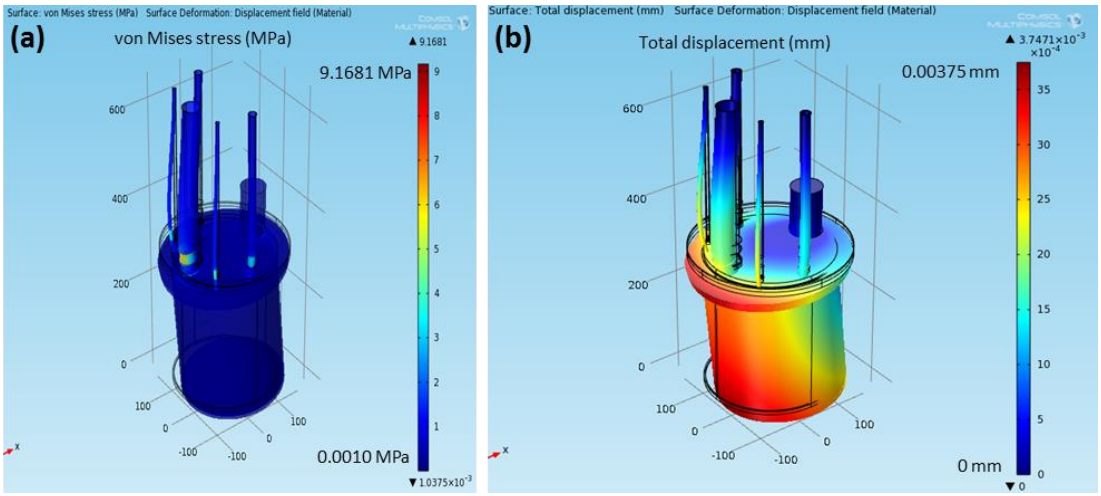

Figure 4-7. (a) von Mises stress, and (b) displacement in the SN_2 chamber.

Furthermore, the effect of SN_2 on the temperature distribution of the SN_2 chamber was also simulated. If the SN_2 chamber was not filled with SN_2, the hot spot was remained at the bottom, as shown in figure 4-8(a).

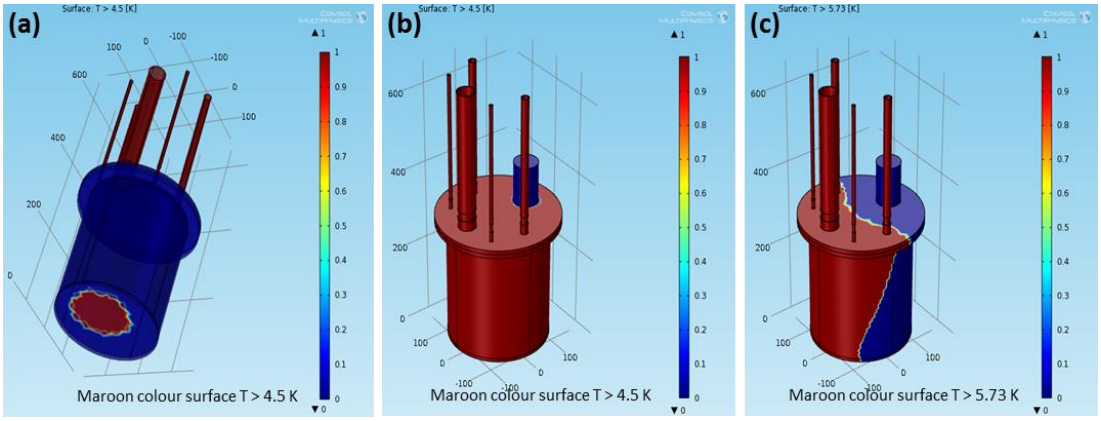

Figure 4-8. (a) Temperature distribution without SN_2, (b) temperature distribution without Cu flange and with SN_2 >4.5 K, and (c) temperature distribution without Cu flange and with SN_2 >5.73 K in the SN_2 chamber.

In particular, as specifically mentioned previously, the Cu flange on the top of the SN_2 chamber was mandatory for achieving a uniform 4.5 K temperature of the SN_2 chamber, which was confirmed by the FE simulation. As can be seen in figure 4-8(b), when the Cu flange was not placed on the top of the SN_2 chamber (even though SN_2 was present in the SN_2 chamber), a uniform 4.5 K temperature of the SN_2 chamber could not be achieved. Interestingly, as can be seen in figure 4-8(c), there

was a direct temperature gradient on the SN_2 chamber. As can be seen in the figure 4-8(c), the cooling power of the cryocooler was not able to absorb the conduction heat load from the far end side of the SN_2 chamber due to the lower thermal conductivity of the SS. Therefore, the 3 mm Cu flange on the top of the top flange of the SN_2 chamber was found to be very effective for eliminating such a temperature gradient across the SN_2 chamber (see figure 4-6). Therefore, following the placement of the Cu flange, as can be seen in figure 4-6, a uniform 4.5 K temperature could be achieved. These simulation results suggested that, especially if the SN_2 chamber was to be made of SS and cooled by conduction cooling, FE analysis had better be done to find the temperature distribution, even though the overall heat load on the SN_2 chamber was less than available cooling power.

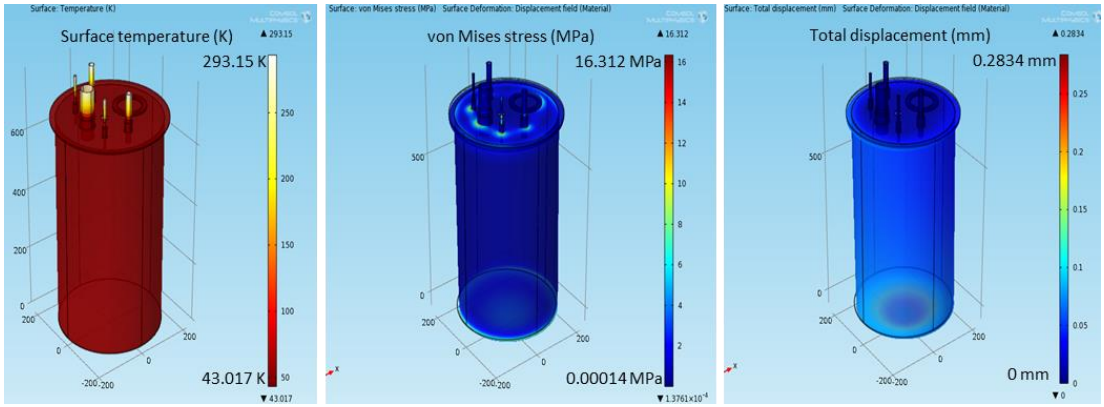

Figure 4-9. (a) Temperature distribution, (b) von Mises stress and (c) total displacement in the radiation shield.

For FE analysis of the radiation shield with the process tubes up to the top flange of the cryostat, the FE model shown in the figure 4-9 was used. Figure 4-9(a), (b), and (c) show the temperature distribution, von Mises stress, and total displacement in the radiation shield, respectively, under loading conditions. The maximum von Mises stress and total displacement were 16.312 MP and 0.2834 mm, respectively. The yield strength of Cu (1/4 hard) at 77 K is 275 MPa [2], and hence, 16.312 MPa was well below the yield strength of Cu; similarly, 0.2834 mm displacement was also acceptable as per operation requirements.

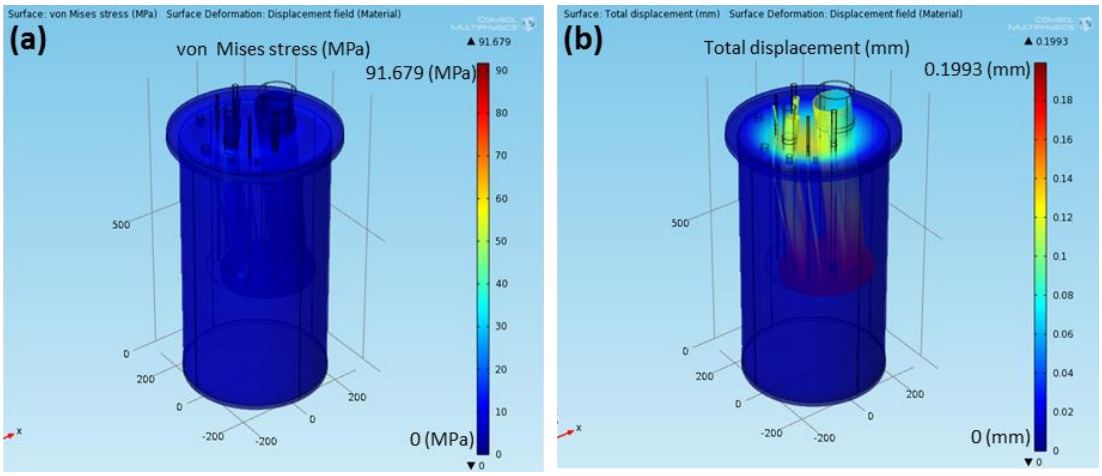

Figure 4-10. (a) von Mises Stress and (b) total displacement in the cryostat.

The cryostat was designed to be connected to the SN_2 chamber and radiation shield through connecting tubes from the top flange. Hence, integrity evaluation of the cryostat along with the connecting tubes was mandatory. The best possible model close to the operation conditions was developed. The cryostat was modelled with the connecting tubes and the top flange of the SN_2 chamber. To avoid a large model size of the cryocooler, SS pipe 4 mm in thickness and the exact O.D. of the cryocooler was modelled. The 4 mm thick pipe was assumed to be reasonable because the total weight of the cryocooler was about 35 kg, and it was rigid enough to give support to the respective components with which it was designed to be tightened, irrespective of its allowable stress from the optimum performance point of view.

The possibility of failure of the grooves (see figure 4-1 and section 4.2) in each connecting tube was evaluated in this analysis. The pressure of 0.1 MPa (gauge) was set on the entire outer surface of the cryostat, whereas the actual loading conditions were also applied on the remaining structures. Figure 4-10(a) and (b) shows the von Mises stress and total displacement in the cryostat, respectively. The maximum von Mises stress was 91.679 MPa, which was below the allowable stress value of 138 MPa for SS, and similarly, 0.199 mm displacement was also acceptable [12, 13]. A summary of the structural design parameters and FE analysis results is presented in table 4-2.

Table 4-2. Summary of structural design parameters and FE analysis. All the pressure values are in gauge.

Structural design parameters	**SN_2 chamber**	**Radiation shield**	**Cryostat**
Design Pressure (MPa)	0.3 (internal)	-	0.3 (internal)
Allowable Pressure (MPa)	0.3 (internal)	-	0.449 (internal), 1.07 (external)
Calculated cylinder thickness (mm)	1.7	-	-
Cylinder thickness (mm)	3.4	2	4.78
Calculated end flange thickness (mm)	7.84	-	14.62
End flange thickness (mm)	8	3	15
FE analysed von Misses stress (MPa)	9.1681	16.312	91.679
FE analysed total displacement (mm)	0.00374	0.2834	0.1993

Based on the design and analysis of the SN_2 cooling system, an order was placed for its commercial fabrication. Based on the bidding process, the fabrication order was placed with Aditya High Vacuum Pty. Ltd., Ahmedabad, Gujarat, India [17]. The following section of this chapter presents the fabrication details of the cooling system.

Figure 4-11. As received cooling system from the manufacturer.

4.7. Installation of the Cooling System

Figure 4-11 shows the cooling system as received from the manufacturer. The manufacturer was able to meet all the technical requirements given to them when placing the order.

Figure 4-12 shows the cooling system without the cryostat, radiation shield, or cryocooler. Soon after receiving the cooling system, the first step of the installation was to install the cryocooler.

Figure 4-12. Cooling system without the cryostat, radiation shield, or cryocooler.

Figure 4-13 shows the cooling system after installation of the cryocooler. To improve the thermal contact between the connecting parts to both stages of the cryocooler, Apiezon N® grease was used in the interfaces [14].

Figure 4-13. Cooling system after installation of the cryocooler.

Figure 4-14 shows an open cooling system with the radiation shield around the SN_2 chamber.

Figure 4-14. The open cooling system with the radiation shield around the SN_2 chamber.

4.7.1. Fabrication and Testing of the Hybrid Current Leads

Following the installation of the cryocooler, the next step of the installation process was to fabricate and test the hybrid current leads. Figure 4-15 shows the fabricated hybrid current leads. Instead of one HT type of DI-BISCCO tape, two samarium bismuth copper oxide (SmBCO) tapes were used for the fabrication of the HTS section. Instead of designed DI-BISCCO, SmBCO was chosen due to its availability and high performance. In addition, instead of designed one HTS tape, two SmBCO tapes were used to operate current leads up to 200 A current instead of designed 150 A. As a result of these changes, the estimated thermal heat load on the radiation shield and SN_2 chamber was changed somewhat, however, within the available cooling power.

A single SmBCO tape was able to carry 200 A current at 77 K. Thus, the current leads were tested in an LN_2 bath with 200 A safely. The testing sequence for the fabrication of the current leads with 200 A current was as follows: testing of (i) a short sample of SmBCO tape, (ii) an individual HTS module with G-10 support, (iii) an individual current lead with a brass section, and (iv) two current leads together with an HTS link. Following successful testing of the current leads, the transition regions (brass to HTS) were wrapped using Cu wires, as shown in figure 4-16 and were soldered to make good electrical contact.

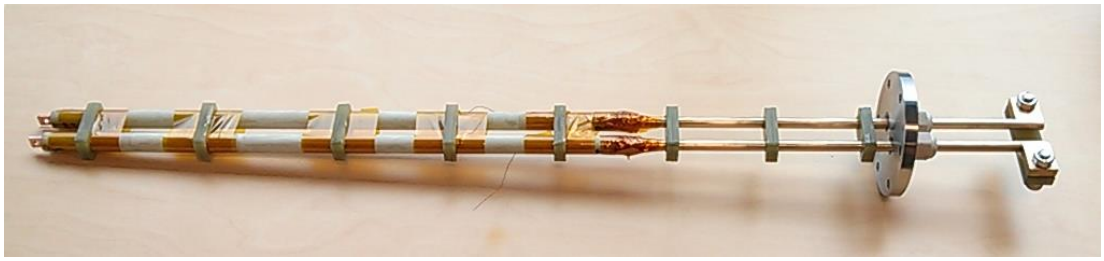

Figure 4-15. Fabricated hybrid current leads.

Figure 4-16. Current leads with transition parts wrapped with Cu wires.

To make good thermal contact with the transition region of the current leads to the 1st stage of the cryocooler via the current lead insertion tube (see figure 4-1), Kapton tape was first wrapped on the individual transition region of the current lead. A Cu tube was installed between two insulated current leads (to allow gas to be passed during LN_2 transfer), and a Cu braid was wrapped around both current leads in a circular shape. Cu foil was wrapped around the Cu braid (Apiezon N® grease was used to improve thermal contact with the current lead tube during installation, see figure 4-17). The current leads were fitted with two pairs of voltage taps (one pair for each current lead) to monitor the voltage drop while charging. The currents leads were tested with 200 A current before final installation, again. The fabricated and tested current leads are shown in figure 4-17. In addition, the resistance (insulation) between the two currents leads, as well as the current leads to the SS flange (can be seen in the figure 4-17, with the negative terminal of the Megger connected to it) was found to be >1 GΩ at 1 kV.

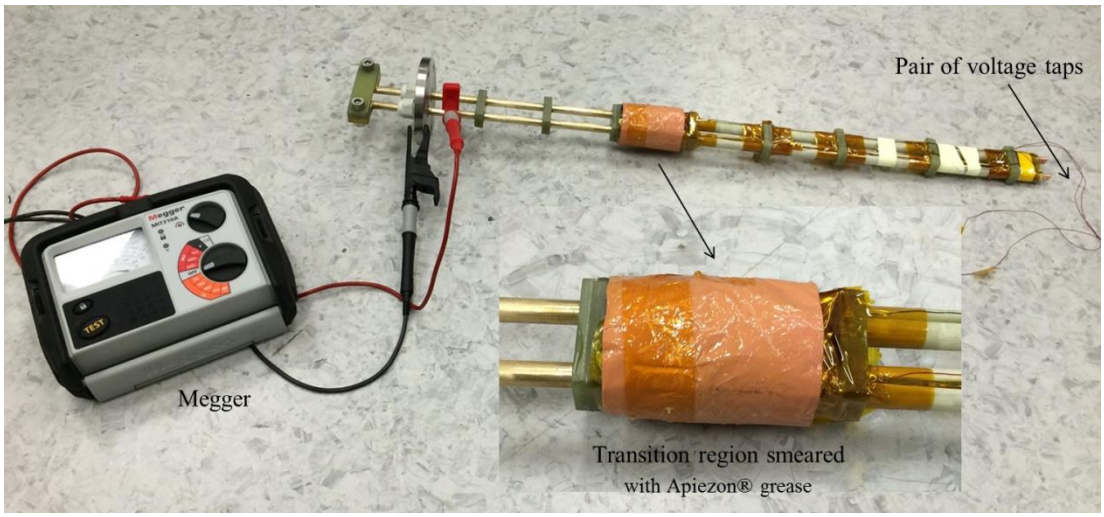

Figure 4-17. Fabricated and tested hybrid current leads (ready for the installation).

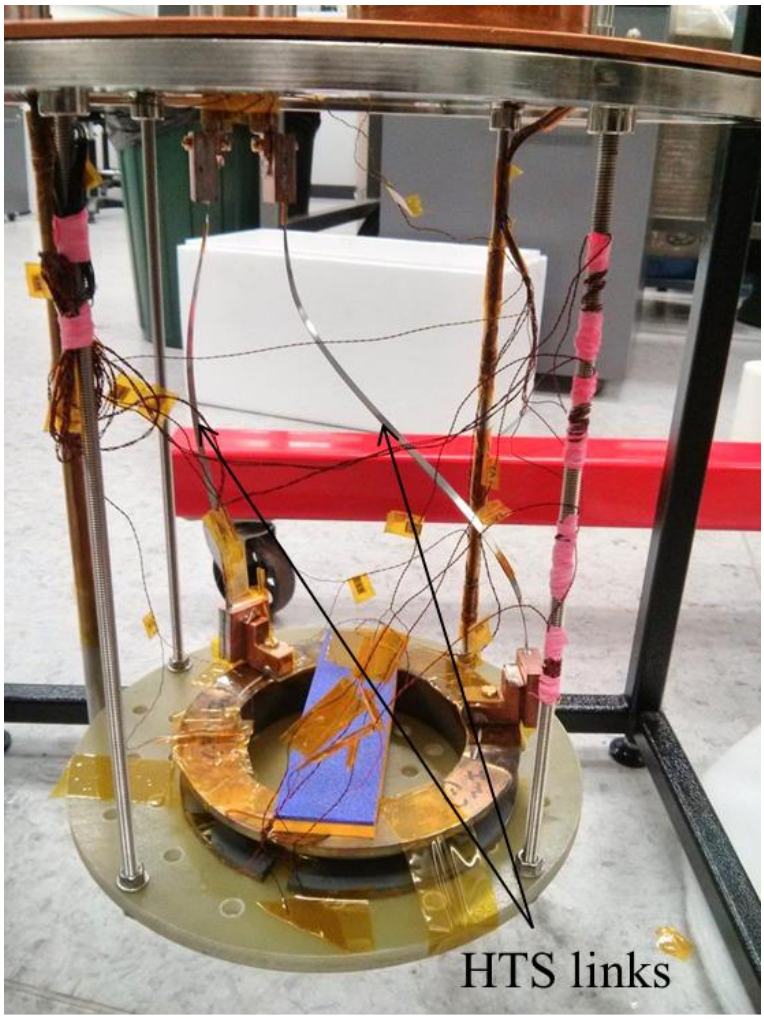

Figure 4-18. HTS links installed in the SN_2 chamber.

4.7.1.1. HTS Links from Current Leads to Coil Terminals

The HTS links were fabricated to connect the current leads to the coil terminals for current charging. The sole purpose of these links was to reduce joule heating while current charging. Figure 4-18 shows the HTS links installed in the SN_2 chamber between the current leads to the coil terminations. Two SmBCO tapes were used to fabricate the links with copper blocks at the ends for the connection. These links were also tested at 200 A in an LN_2 bath at 77 K prior to installation.

4.7.2. Copper Flange Installation

Following the installation of the current leads, the next step in the installation process was to install the Cu flange on the SN_2 chamber (see figure 4-1). As already discussed in section 4.6, the Cu flange was going to play very important role in providing temperature uniformity across the SN_2 chamber, and therefore, the thermal contact between the top flange of the SN_2 chamber and the Cu flange was vital. To improve thermal contact, as shown in figure 4-19, Apiezon N® grease was smeared in a sufficient amount, and then the Cu flange was finally placed on the SN_2 chamber.

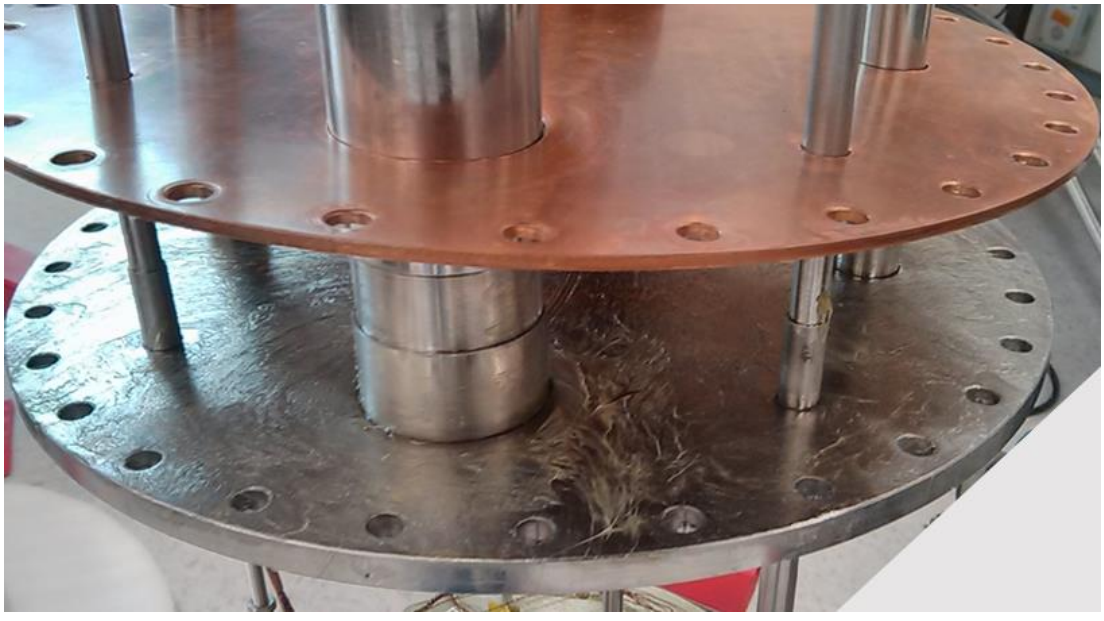

Figure 4-19. Cu flange prior to final installation on the top of the SN_2 chamber.

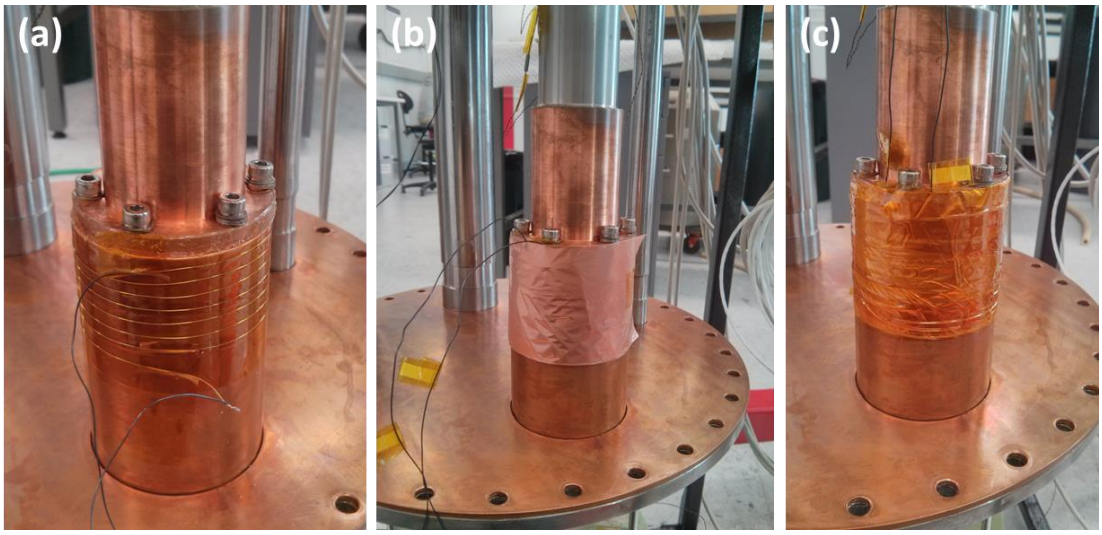

Figure 4-20. (a) Heater installed on the Cu connector (with Kapton tape used for the insulation), (b) Cu foil wrapped around the heater, and (c) Kapton tape wrapped around the Cu foil.

4.7.3. Heater for Temperature Control

The temperature in the SN_2 chamber was designed to be controlled using a heater on the 2nd stage of the cryocooler. For this purpose, the heater was installed on the Cu bar (installation steps are shown in figure 4-20). Lakeshore 32 American Wire Gauge (AWG) Nichrome wire with 50 Ω resistances was used for the heater. The heater power was controlled using a Cryocon 32B [18].

4.7.4. Voltage Measurement

The SN_2 chamber was equipped with four pairs of voltage taps to measure the voltage drop in the coil to be tested. The voltages were measured using Keithley Nanovoltmeter model 2182A [19]. The voltage taps coming from RT to the SN_2 were thermally anchored at the 1st stage of the cryocooler through process tubes (see figure 4-1). For thermal anchoring, the wires were non-inductively anchored on the Cu tube, and then Cu foil was wrapped around the wire in a circular shape. Prior to final installation, Apiezon N® grease was smeared around the Cu foil to improve thermal contact with the process tube, as shown in figure 4-21.

Figure 4-21. Thermal anchoring of the instrumentation wires.

4.7.5. Temperature Sensors

For temperature measurement, a total of seven carbon ceramic sensors (CCS, Temati, UK) were used [20]. Of the seven sensors, four sensors were installed inside SN_2 chamber, whereas three sensors were installed outside the SN_2 chamber. Similar to the voltage tap wires, the temperature sensor wires were also thermally anchored on to the 1st stage of the cryocooler via process tubes or directly on the radiation shield.

Inside the SN_2 chamber, one sensor was installed on the top flange to monitor the LN_2 level, whereas other sensors could be freely installed as per requirements. On the outside of the SN_2 chamber, one sensor was installed on the Cu bar to measure the temperature of the cryocooler 2nd stage (see figure 4-22), and one sensor was installed on the bottom of the radiation shield (diagonal to the cryocooler location) to measure the temperature of the radiation shield. The temperatures were

monitored using a Lakeshore 218 temperature monitor, a Lakeshore 325 temperature controller, and a Cryocon 32 B [18, 21].

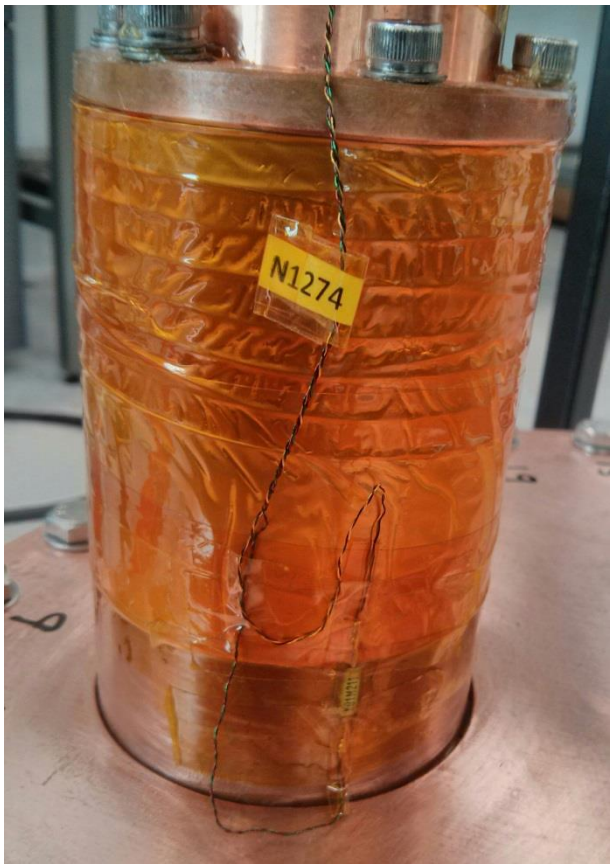

Figure 4-22. Temperature sensor on the Cu bar.

4.7.6. Hall Sensors

The SN_2 chamber was equipped with the three Hall sensor wire pairs. During experiments, however, only one uniaxial Hall sensor was used to measure the central field of the coil. Figure 4-23 shows the Hall sensor installed in the centre of the solenoid during the first experiment. A Lakeshore Gaussmeter model 425 was used to acquire the magnetic field [21].

Figure 4-23. Hall sensor installed in the centre of the solenoid.

4.7.7. Indium Sealing

To seal the LN_2 chamber for leak tightness at low-temperature, indium wire 2 mm in diameter was used. Figure 4-24 shows the indium wire on the SN_2 chamber top flange. Later, this sealing was successfully tested for leak tightness.

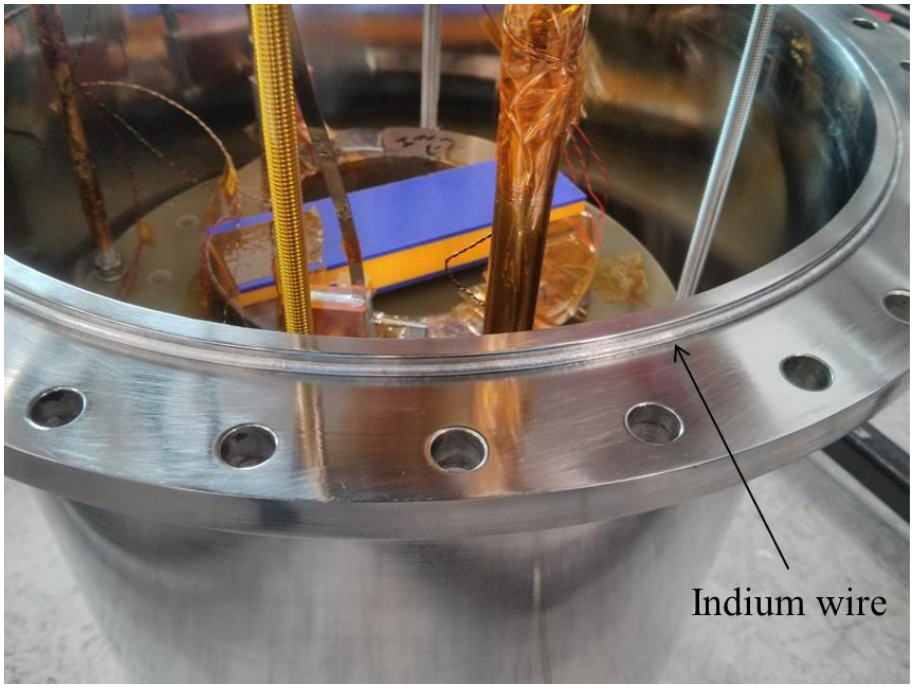

Figure 4-24. Indium wire (2 mm diameter) for sealing.

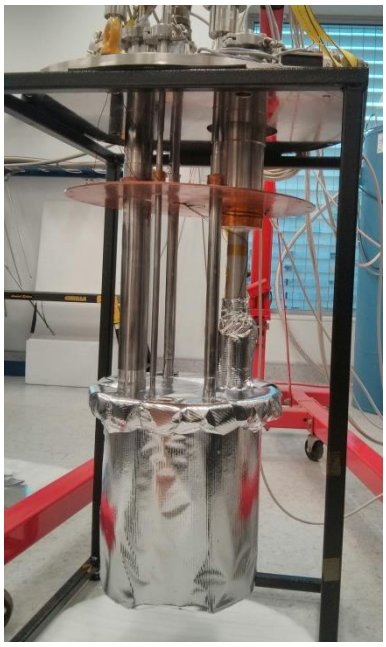

Figure 4-25. SN_2 chamber wrapped with MLI.

4.7.8. Multilayer Insulation

As mentioned in sections 4.2 and 4.3, MLI with 10 layers was used for reducing the radiation heat load on the radiation shield as well as the SN_2 chamber. The MLI was prepared in such a way that it could be reused. Figure 4-25 shows the SN_2 chamber wrapped with MLI. MLI was not wrapped on the process tubes or cryocooler other than on the Cu bar, as shown in the figure. Figure 4-26 shows the radiation shield wrapped with MLI. Again, MLI was not wrapped on the process tubes.

4.7.9. Power Supply

For charging the coils in the SN_2 chamber, a Cryomagnetics – 4G (200 A) power supply was used [22]. The power supply was remotely controlled using the LabVIEW program.

Figure 4-26. Radiation shield wrapped with MLI.

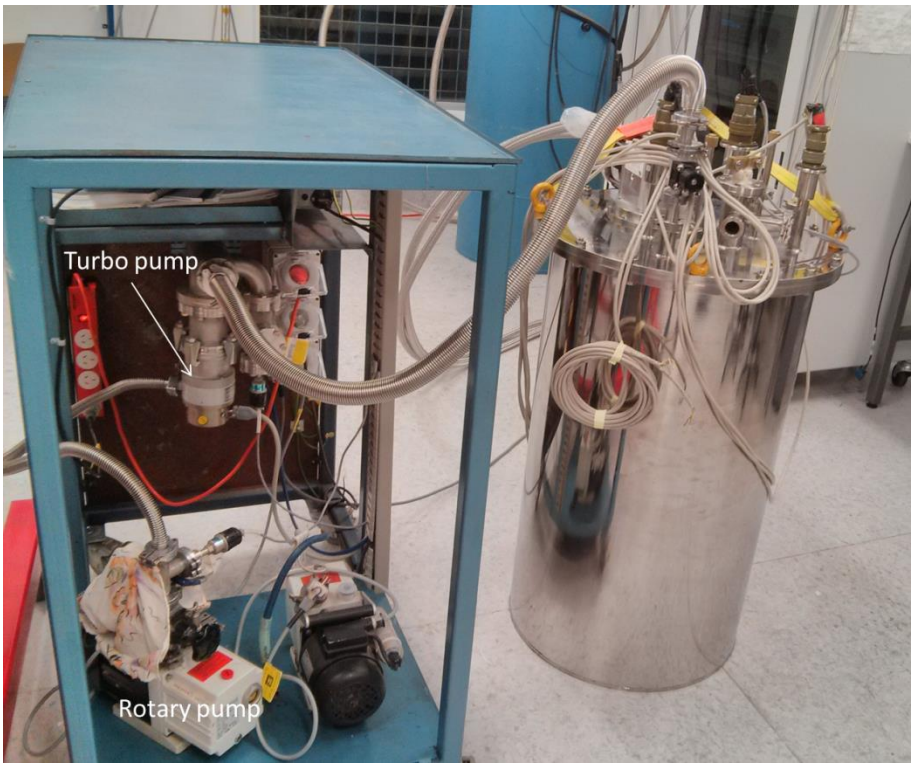

Figure 4-27. Cooling system with a turbomolecular pump station.

4.7.10. Vacuum System

The vacuum in the cooling system was created using a small turbomolecular pumping station, as shown in figure 4-27. The pumping capacity of the turbopump was 55 litre s^{-1}.A Penning gauge and a Pirani gauge were installed on the pumping port of the turbo and rotary pump, respectively. Vacuum < 2 x 10^{-6} torr was achieved after overnight pumping.

4.7.11. Data Acquisition and Control

For data acquisition, an NI PXI – 1045 (see figure 4-28) was used with the LabVIEW data acquisition platform. This PXI has a CPU NI PXI-8110 inbuilt. All the instruments were connected to the PXI with either GPIB or RS-232 interfaces. The graphical user interface (GUI) of the LabVIEW data acquisition program is shown in figure 4-29.

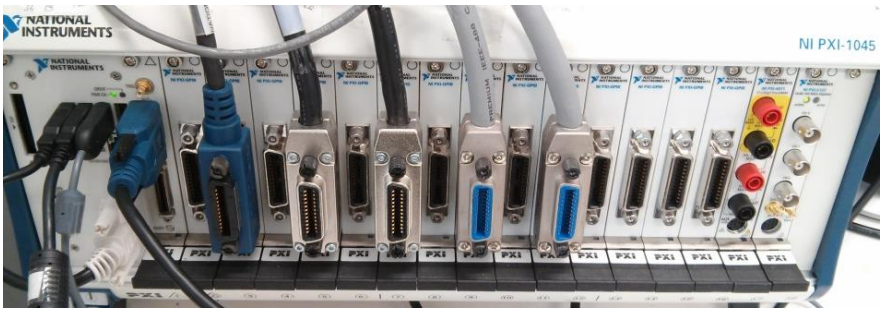

Figure 4-28. NI PXI-1045 with inbuilt CPU NI PXI 8110.

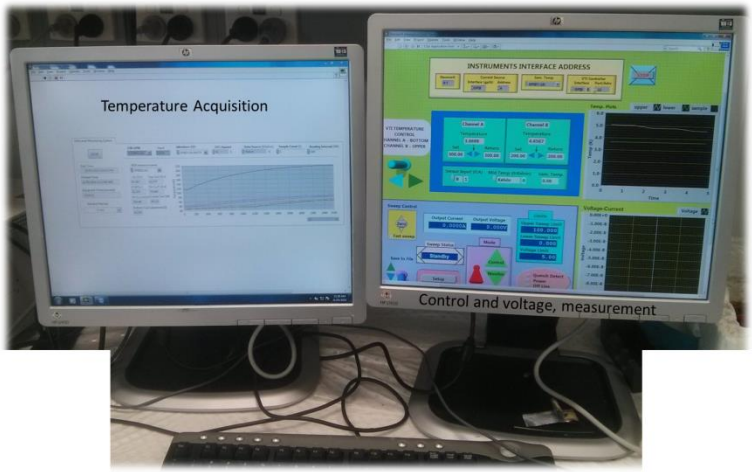

Figure 4-29. GUI of the LabVIEW program for data acquisition.

4.8. Cooling System Testing

4.8.1. MgB_2 Solenoid Coil

To test the SN_2 cooling system, an MgB_2 solenoid coil was fabricated using the 'wind and react' method. A photograph of the fabricated solenoid coil is shown in figure 4-30(a). This coil was installed in the SN_2 chamber, as shown in figure 4-30(b). The specifications of the solenoid coil are listed in table 4-3. The coil was heat-treated in high purity Ar inert atmosphere at 675 °C for 60 min. Inductance was measured using an LCR meter at 1 kHz frequency, as well as was calculated from the induced inductive voltage while charging the coil. The field constant of the solenoid was calculated using the standard solenoid magnetic field formula [23]. The critical current of the coil was measured using the 1 μV cm^{-1} criterion. The distance between voltage taps was 11 m.

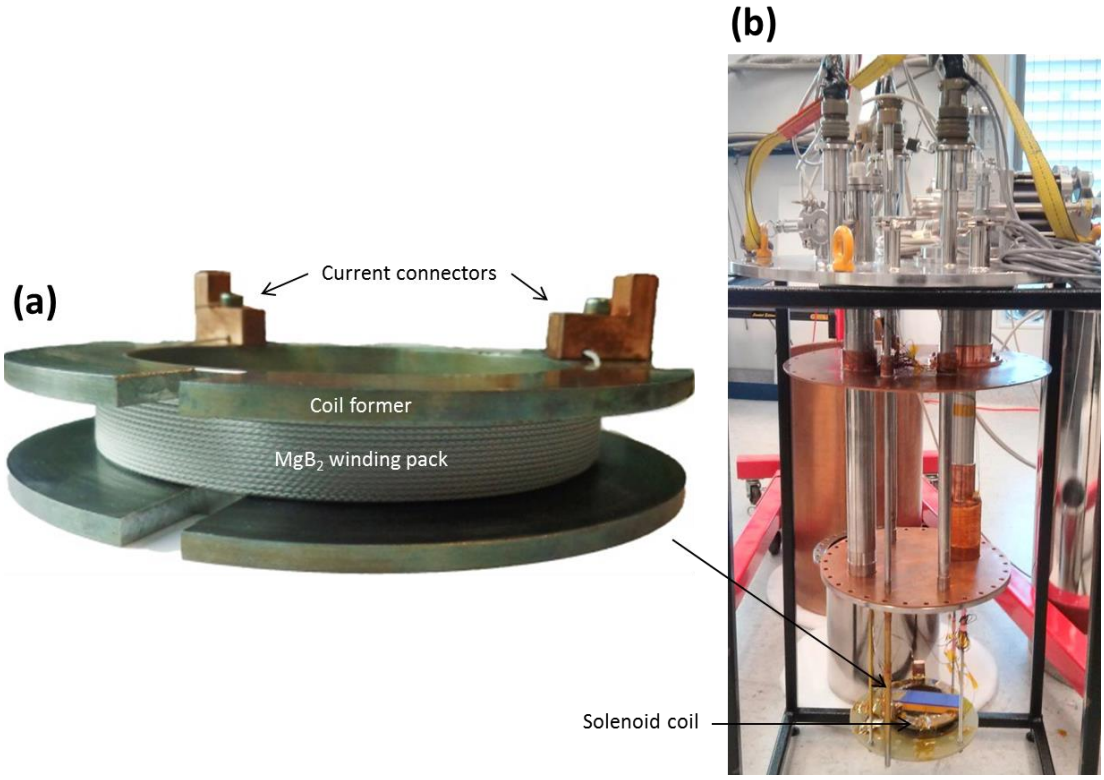

Figure 4-30. (a) Photograph of the MgB_2 solenoid coil, (b) SN_2 cooling system (SN_2 chamber, radiation shield, and cryostat removed).

Table 4-3. The specifications of the MgB_2 solenoid coil.

Parameters	**Specifications**
Coil type	Solenoid
Winding method	Wind and react
Strand (HTR 1535-46)	MgB_2/Nb/Monel
Filament count	30
Insulation	S-glass
Wire diameter with insulation (mm)	1
Wire diameter without insulation (mm)	0.84
SC fill factor of the wire (%)	17.6
Coil I.D. (mm)	115.28
Coil O.D. (mm)	119.28
Coil height (mm)	15.7
Turns per layer	15
Total layers	2
Coil filling factor (%)	75
Impregnation	No
L (μH)	135 (measured at 1 kHz) 200 (observed in inductive voltages)
Field constant at z = 0 (G A^{-1})	3.18 (Calculated) 3.20 (Measured) + 0.6 % (field error)

4.8.2. Temperature Measurements

As shown in figure 4-31, six cryogenic CCS temperature sensors (out of seven, one was malfunctioning) were installed using Apiezon® N grease and Kapton® tape to make them thermally well-coupled with the measurement location to monitor the temperature [14, 20, 24, 25]. A 50 Ω Nichrome (100 AWG) heater was installed on the Cu bar near the 2nd stage of the cryocooler to control the temperature [21]. The heater was controlled using a Cryocon 32B [18]. A Hall sensor with 0.1 G sensitivity was installed at the centre of the coil to measure the magnetic field generated by the coil. The HTS links were used to connect the coil with the current leads.

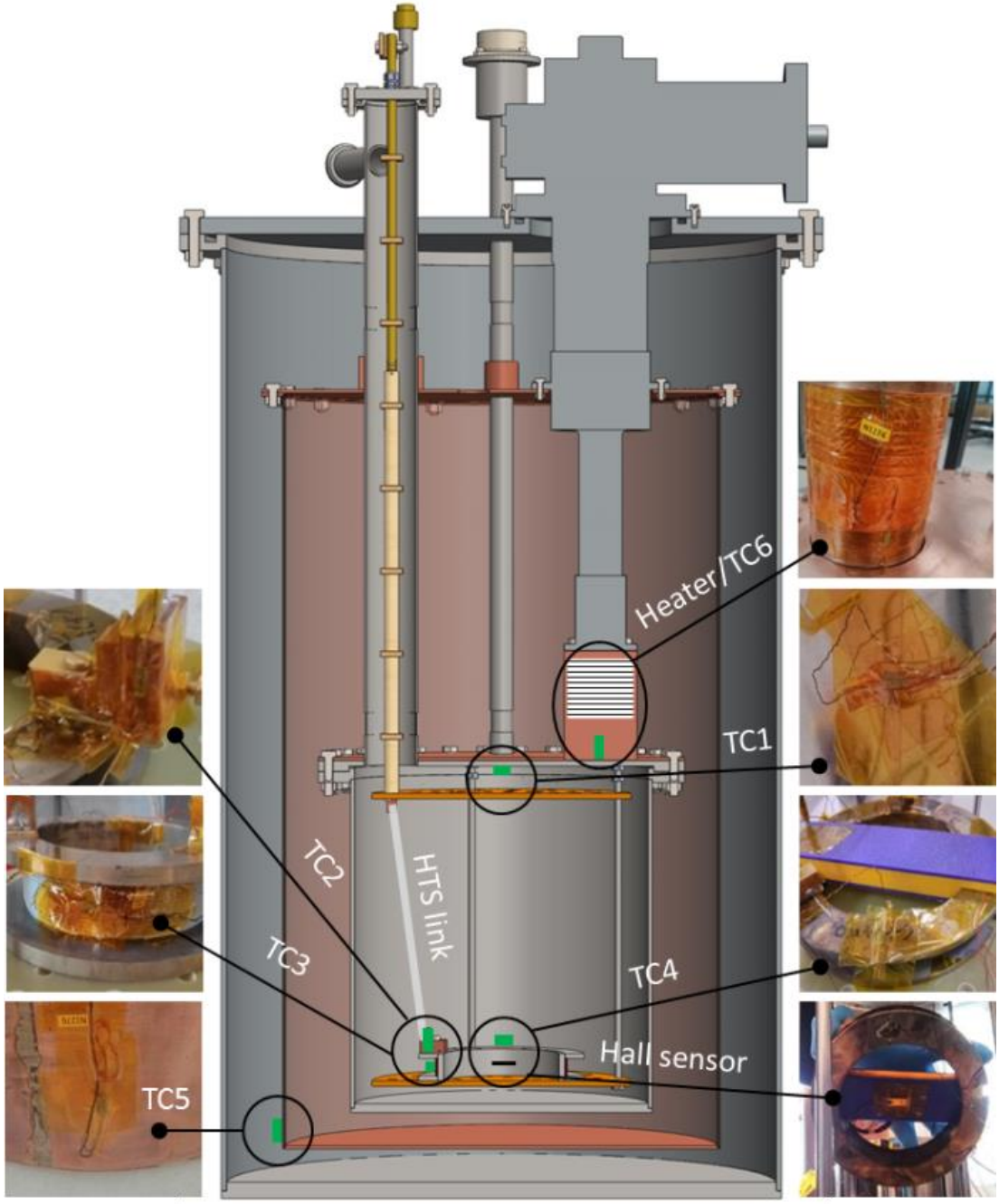

Figure 4-31. A cross-sectional view of the SN_2 cooling system, including a schematic representation of the temperature sensors/heater/Hall sensor with the corresponding photographs.

In order to cool down the SN_2 chamber, the required vacuum was created surrounding the SN_2 chamber and radiation shield. LN_2 was transferred into the SN_2 chamber until a uniform temperature of 77 K was reached in the SN_2 chamber, and then the cryocooler was switched ON. LN_2 was poured into the SN_2 chamber several

times until it was completely filled with LN_2. Vacuum pumping was not used for forming SN_2 [5].

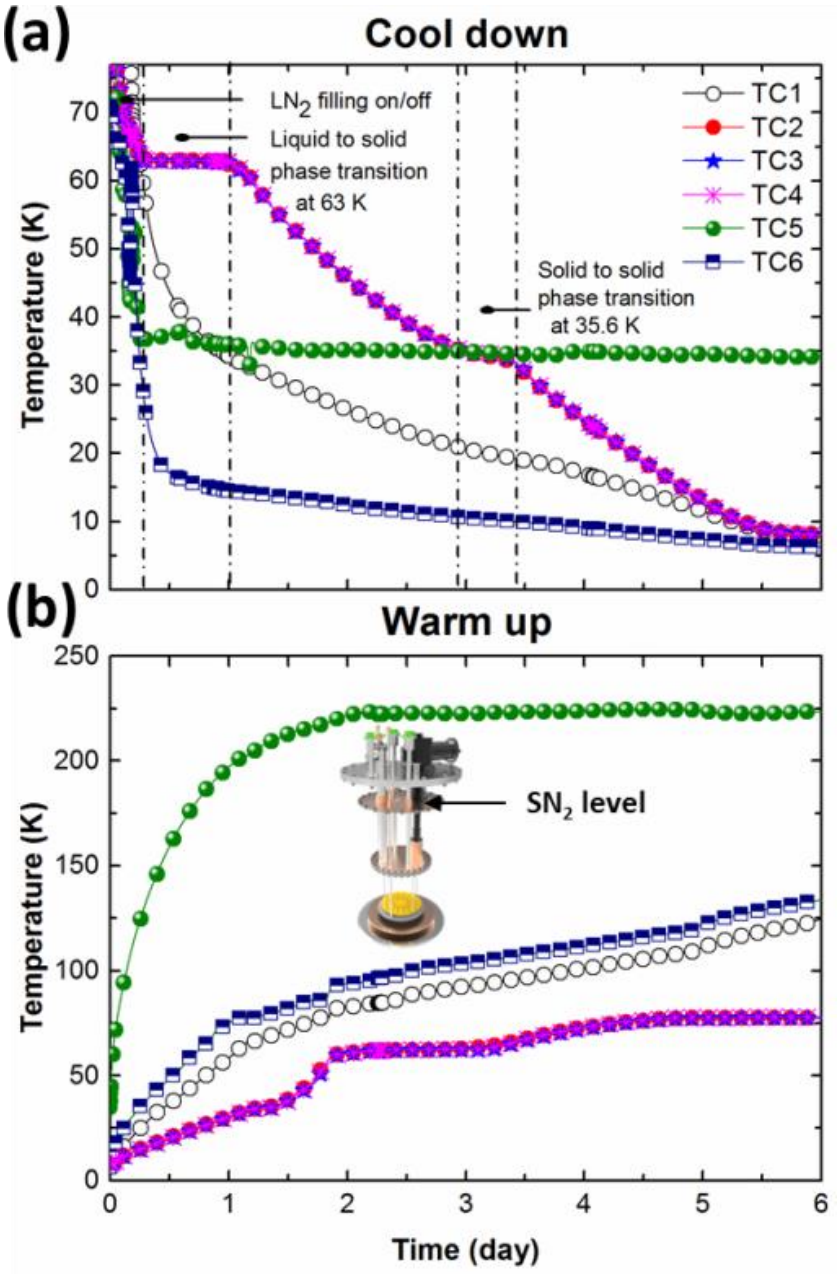

Figure 4-32. (a) Cool down and (b) warm up curves of the SN_2 cooling system. Temperature sensor locations: TC1 (at the top of the SN_2 chamber (inside)), TC2 (on the positive current lead current connector), TC3 (centre of the coil winding pack), TC4 (top of the coil former near the positive current lead), TC5 (bottom of the radiation shield), and TC6 (bottom of the Cu bar attached to the 2nd stage of the cryocooler). The inset in (b) shows the level of the SN_2.

4.8.3. Cool Down and Warm Up

Figure 4-32 shows the cool down and warm up curves of the SN_2 cooling system. As can be seen in figure 4-32(a), in about 6 days, 17 L of SN_2 was cooled down to 8 K. It was observed that the SN_2 level was as high as the top flange of the radiation shield inside the SN_2 chamber (inset of figure 4-32(b)). Thus, the SN_2 itself was delivering an additional conductive heat load from the radiation shield to the SN_2 chamber. This prevented the SN_2 chamber from reaching an even lower temperature. As can be seen in figure 4-32(a), liquid to solid and solid to solid phase transitions was observed at 63 K (~0.7 day) and 35.6 K (~0.5 day), respectively [26]. The overall cool down was smooth. The temperature of the radiation shield was constant around 36 K. The decreasing trend in the temperatures inside the SN_2 chamber around the coil (TC2, TC3, TC4) was uniform. There was no noticeable temperature gradient across the coil. Eventually, at the end of the 6 days, the temperature in the entire SN_2 chamber was ~8 K. These results show that the Cu plate on the top of the SN_2 chamber worked quite well, and it improved the temperature uniformity of the entire SN_2 chamber significantly.

Figure 4-32(b) shows the warm up trend of the SN_2 cooling system. As can be seen in the figure, as soon as the cryocooler was switched off, the temperature of the radiation shield started to increase rapidly. In contrast, the temperature of the SN_2 chamber was increasing very slowly, even though cryocooler was connected to the SN_2 chamber in the off condition. Like the cool down trend, the warm up trend of the SN_2 around the coil was quite uniform, without any noticeable temperature gradient. This indicates that even when the cooling source was off, the temperature of the coil increased very slowly. With 17 L of SN_2, it took almost 1 day to increase the temperature from 8 K to 25 K, even though the cryocooler was delivering a significant conduction heat load. The warming time could be greatly improved with thermal disconnection of the cryocooler from the SN_2 chamber. Therefore, longer maintenance time or less re-cooling time will be possible in the event of a problem or power failure in the commercial MRI systems.

Figure 4-33. LN_2 cooling of the current leads.

4.8.4. Current Charging

To measure the field constant of the MgB_2 solenoid coil, firstly, the coil was energized up to 40 A current at 20.5 K. It was observed, however, that the HTS sections of the current leads were developing a voltage drop when the current was increased to more than 10 A. The voltage drop was indicating that the thermal contact of the transition region with the 1st stage of the cryocooler (at that time, the 1st stage was ~36 K) via the connecting tube was not good enough for the high conductive heat load via the brass section, even though SN_2 level was up to the transition region (see inset of figure 4-32(b)). Thus, it was decided to slowly introduce LN_2 from one of the ports on the current lead tube, as shown in figure 4-33. Following the cooling of the current lead top sections using LN_2, no voltage drop was observed while current charging across the HTS section.

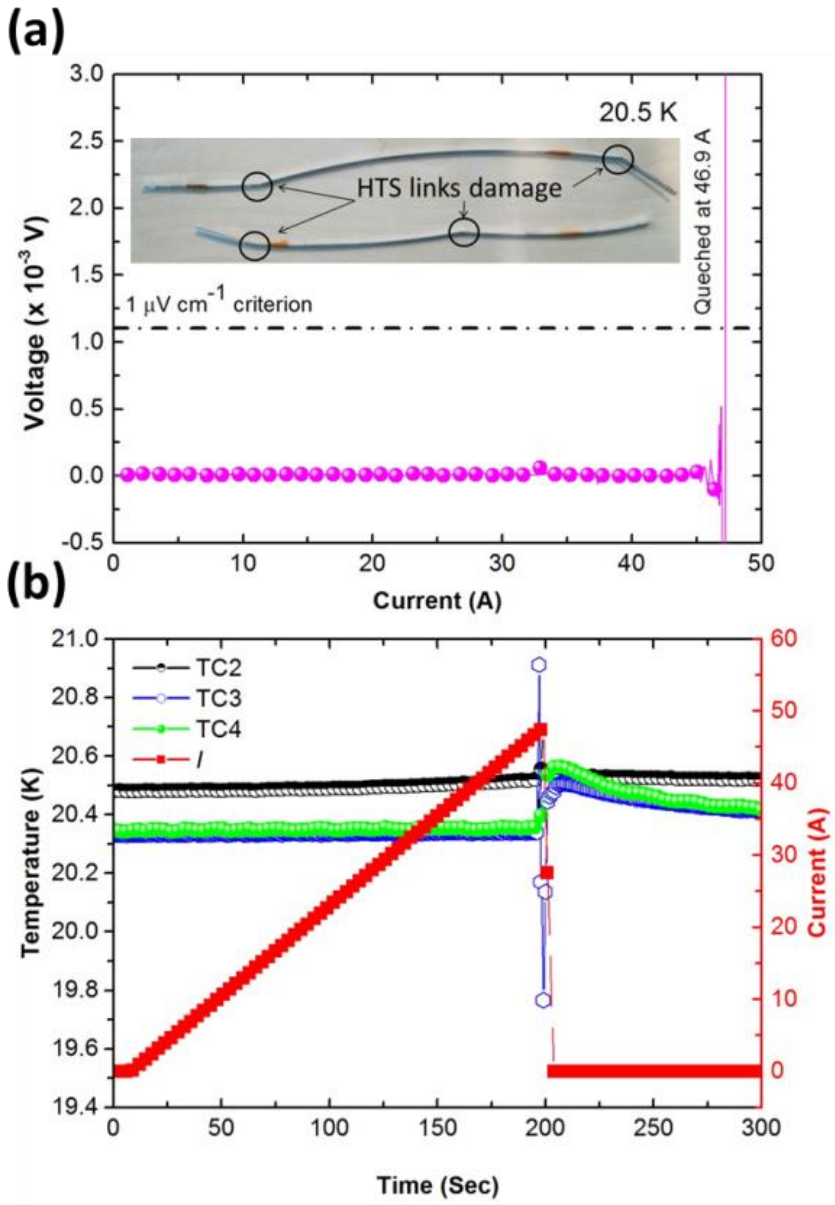

Figure 4-34. (a) Voltage vs. current at 20.5 K (inset: photograph of damage to HTS links), and (b) temperature, current and time characteristics of the MgB_2 solenoid coil.

Again, to measure the field constant of the MgB_2 solenoid coil, the coil was energized up to 40 A current at 20.5 K. The measured field constant of the solenoid coil was 3.20 G A^{-1} compare to the calculated field constant of 3.18 G A^{-1} [23]. This result shows only +0.6 % field error and indicates that the fabricated coil was wound in a fairly uniform way. Figure 4-34(a) shows the current vs. voltage characteristics of the coil at 20.5 K. As can be seen in the figure, the coil was prematurely quenched at 46.9 A. As soon as coil was quenched, temperature spikes were observed (figure

4-34(b)). Nevertheless, the maximum temperature increase on the coil winding pack was limited to only 0.6 K. This indicates that the coil under SN_2 was thermally stable. To examine the reason for the premature quench of the coil, the SN_2 chamber was warmed to RT. It was observed that both HTS links were severely damaged at two locations in each current lead as shown in the inset of figure 4-34(a). These current leads could have played a role in the premature quenching of the coil. In later experiments, the HTS links were replaced by flexible Cu leads.

The performance of hybrid current leads was later evaluated in subsequent experiments. The hybrid current leads were capable of carrying 200 A current, although LN_2 cooling was required for the brass section.

4.9. Summary

The conduction cooled SN_2 cooling system with the option of operation in mixed cooling mode was designed, fabricated, installed, and tested. The design of the cooling system was conducted using the optimal combination of analytical, empirical, and FE analysis. The unique approach for achieving a uniform temperature in the low thermal conductivity SS chamber using a Cu flange was proposed, simulated, and experimentally verified. The cooling system was designed such that the total estimated thermal heat load on the radiation shield and SN_2 chamber was about 33.505 W and 0.482 W, respectively. These heat loads were ~16% and ~52% less than the available cooling power at the 1^{st} and 2^{nd} stages of the cryocooler, respectively. During the actual cool down, however, it was observed that SN_2 level was as high as the radiation shield top flange. Thus, the SN_2 was delivering an additional conductive heat load onto the SN_2 chamber, which prevented the SN_2 chamber from reaching the temperature of the 2^{nd} stage of the cryocooler, so that it remained at 8 K.

In addition, the detailed installation procedure of the cooling system was presented. The HTS modules of the current leads were fabricated using two SmBCO tapes instead of the designed single DI-BISCCO tape. Furthermore, the current leads were tested and used at 200 A current despite being designed for 150 A current. No leaks in the system were observed, which means that the indium seal mechanism worked very well. The system cool down was smooth. The thermal contact between

the 1st stage and the 2nd stage with the radiation shield and LN_2 chamber, respectively, appeared to be excellent. Poor thermal contact between the transition region of the current leads and the 1st stage of the cryocooler was observed, however. Thus, LN_2 cooling was necessary for the brass section of the current lead. A premature quench in the MgB_2 solenoid coil was observed. After the system warms up, it was observed that the HTS links had been damaged during cool down. This might have played a role in the premature quench. Thus, in subsequent experiments, Cu links were used instead of HTS. In all, the system operation was well within the operation requirements for subsequent experiments.

4.10. References

[1] Hales P, Jones H, Milward S and Harrison S 2005 Investigation into the use of solid nitrogen to create a "Thermal Battery" for cooling a portable high-temperature superconducting magnet *Cryogenics* **45** 109-15

[2] Iwasa Y 2009 *Case studies in superconducting magnets, design and operation issues* (New York: Springer)

[3] Haid B J, Lee H, Iwasa Y, Oh S S, Kwon Y K and Ryu K S 2002 Design analysis of a solid nitrogen cooled "permanent" high-temperature superconducting magnet system *Cryogenics* **42** 617-34

[4] Kim K L, Song J B, Choi J H, Kim S H, Koh D Y, Seong K C, Chang H M and Lee H G 2010 The design and testing of a cooling system using mixed solid cryogen for a portable superconducting magnetic energy storage system *Supercond. Sci. Technol.* **23** 125006

[5] Nakamura T, Muta I, Okude K, Fujio A and Hoshino T 2002 Solidification of nitrogen refrigerant and its effect on thermal stability of HTSC tape *Physica C* **372-376** 1434-7

[6] Nakamura T, Higashikawa K, Muta I, Fujio A, Okude K and Hoshino T 2003 Improvement of dissipative property in HTS coil impregnated with solid nitrogen *Physica C* **386** 415-8

[7] Nakamura T, Higashikawa K, Muta I and Hoshino T 2004 Performance of conduction-cooled HTS tape with the aid of solid nitrogen–liquid neon mixture *Physica C* **412–414, Part 2** 1221-4

[8] Song J-B and Lee H 2012 Mixed cryogen cooling systems for HTS power applications: A status report of progress in Korea University *Cryogenics* **52** 648-55

[9] Patel D, Md Shahriar Al H, Khay Wai S, Qiu W, Kobayashi H, Zongqing M, Seong Jun K, Hong J, Jin Yong P, Choi S, Maeda M, Shahabuddin M, Rindfleisch M, Tomsic M, Dou S X and Kim J H 2016 Evaluation of persistent-mode operation in a superconducting MgB_2 coil in solid nitrogen *Supercond. Sci. Technol.* **29** 4LT02-9

[10] Patel D, Sharma A N, Prasad U, Khristi Y, Varmora P, Doshi K and Pradhan S 2013 Thermal anchoring of wires in large scale superconducting coil test experiment *Fus. Eng. Des.* **88** 374-9

[11] Takashi Noguchi 1993 Vacuum insulation for a cryostat *Cryogenic Engineering (in Japanese)* **28,** 355

[12] ASME 2007 *2007 ASME boilers and pressure vessel code, VIII, Division 2, alternative rules for constructing of pressure vessel* (New York: ASME)

[13] ASME 2007 *2007 ASME boiler & pressure vessel code, II, part D, properties (matrix) materials* (New York: ASME)

[14] www.apiezon.com

[15] http://global-sei.com/super/hts_e/

[16] Richard McFee 1959 Optimum input leads for cryogenic apparatus *Rev. Sci. Instr.* **30**

[17] www.adityahighvacuum.com

[18] www.cryocon.com

[19] www.tek.com

[20] www.temati-uk.com

[21] www.lakeshore.com
[22] www.cryomagnetics.com
[23] Wilson M N 1983 *Superconducting magnets* (Oxford University Press)
[24] www.kaptontape.com
[25] Patel D, Hossain M S A, See K W, Xu X, Barua S, Ma Z, Choi S, Tomsic M and Kim J H 2015 MgB_2 superconducting joints for persistent current operation *Supercond. Sci. Technol.* **28** 065017
[26] Song J B, Kim K L, Kim K J, Lee J H, Kim H M, Kim W S, Yim S W, Kim H R, Hyun O B and Lee H G 2008 The design, fabrication and testing of a cooling system using solid nitrogen for a resistive high-T_c superconducting fault current limiter *Supercond. Sci. Technol.* **21** 115023

4.11. Note: Chapter Publication and Text Usage Detail

The design portion of this Chapter with the coil testing portion of Chapter 8 is under preparation for the submission to the Scientific Reports as below paper. Some of the written text in this Chapter has been taken from my paper (under preparation), as shown below.

[1] **Patel D**, Md Shahriar Al H, Khay Wai S, Qiu W, Jie H, Seong Jun K, Choi S, Maeda M, Shahabuddin M, Tomsic M and Kim J H 2016 Solid cryogen for MgB_2 superconducting MRI magnet (Under Preparation)

Chapter 5

5. MgB_2 Superconducting Joints for Persistent Current Operation

5.1. Introduction

Magnetic resonance imaging (MRI) is the key technology for diagnosing critical injuries and diseases. In commercially available MRI systems, superconducting magnets based on niobium titanium (NbTi), are used for producing the high and precise magnetic fields required under persistent-mode for better image quality. It is well known that superconducting MRI magnets are currently operated in expensive liquid helium (LHe) bath at 4.2 K. The soaring LHe prices and possible shortages have increased the demand for LHe-free MRI magnets more than ever [1]. Magnesium diboride (MgB_2), which was found to be superconducting in 2001 [2], is considered as a promising candidate for LHe-free operation in MRI due to its relatively low material and fabrication costs compared to high-temperature superconductors. In addition, its transition temperature of 39 K allows it to operate at higher temperatures up to 25 K [3-6]. Owing to these benefits [7, 8], there have been many recent reports on MgB_2-conductor-based MRI magnets [9-14]. In fact, *PARAmed* has already commercialized LHe-free MRI systems, called as "open sky MRI". These MRIs are not operated in persistent-mode, however. Therefore, a precise power supply is needed, which leads to high-cost operation. In general, MRI magnets are operated in the persistent-mode to retain magnetic field stability throughout the spherical imaging volume, to keep the long-term drift rate of the magnetic field under 0.1 ppm h^{-1}, and to maintain overall stable operation [15]. The development of a highly reliable and consistent superconducting joint technique for MgB_2 conductors is considered to be the most critical challenge for its wide application in the MRI market.

Several superconducting joint techniques between MgB_2 conductors have been reported [13, 16-23]. The first joint between MgB_2 and NbTi for an MgB_2 coil operated at 4.2 K under persistent-mode was reported by Hitachi in 2005 [16].

However, a first successful MgB_2-MgB_2 joint was reported in 2006 by ASG Superconductors, which was confirmed by field-decay measurement of an MgB_2 closed-loop coil [17, 18]. Later, Nardelli and co-workers further developed and reported the lowest joint resistance as low as 10^{-14} Ω at 20 K for an *ex situ* multifilament MgB_2 tape [24]. Most recently in 2013, Ling *et al* reported their concept for joining unreacted monofilament MgB_2 wires, resulting in consistent critical current capacities [12], although their closed-loop coil fabricated via the "wind and react" method achieved joint resistance of only 1.3 x 10^{-10} Ω at 15 K in self-field, which needs to improve by at least an order of magnitude for practical MRI application. It is thus necessary to further improve the state-of-the-art superconducting joint, to give it low joint resistance in the order of 10^{-12} Ω for persistent-mode MgB_2 magnet operation.

In this study, therefore, of a joint technique for unreacted monofilament MgB_2 conductor, test results at different temperatures and magnetic fields that include a comparison of the critical current (I_c) of the joint with the wire, the closed-loop coil, and the microstructural analysis of the joints are presented in detail.

5.2. Experimental Details

Monofilament MgB_2 wire was fabricated by a powder-in-tube (PIT) technique, using an *in situ* process. The detailed method for fabricating wires was reported elsewhere [8]. Magnesium (99 %, 325 mesh) from Sigma-Aldrich and amorphous boron (98.8 %, ~400 nm) powder from Pavezyum were used as the starting materials with the stoichiometric composition of Mg : B = 1 : 2. The mixed power was packed into an iron (Fe) tube with an outer diameter (O.D.) of 6.30 mm and an inner diameter (I.D.) of 4.11 mm. The composite wire was swaged and subsequently drawn to an O.D. of 1.00 mm.

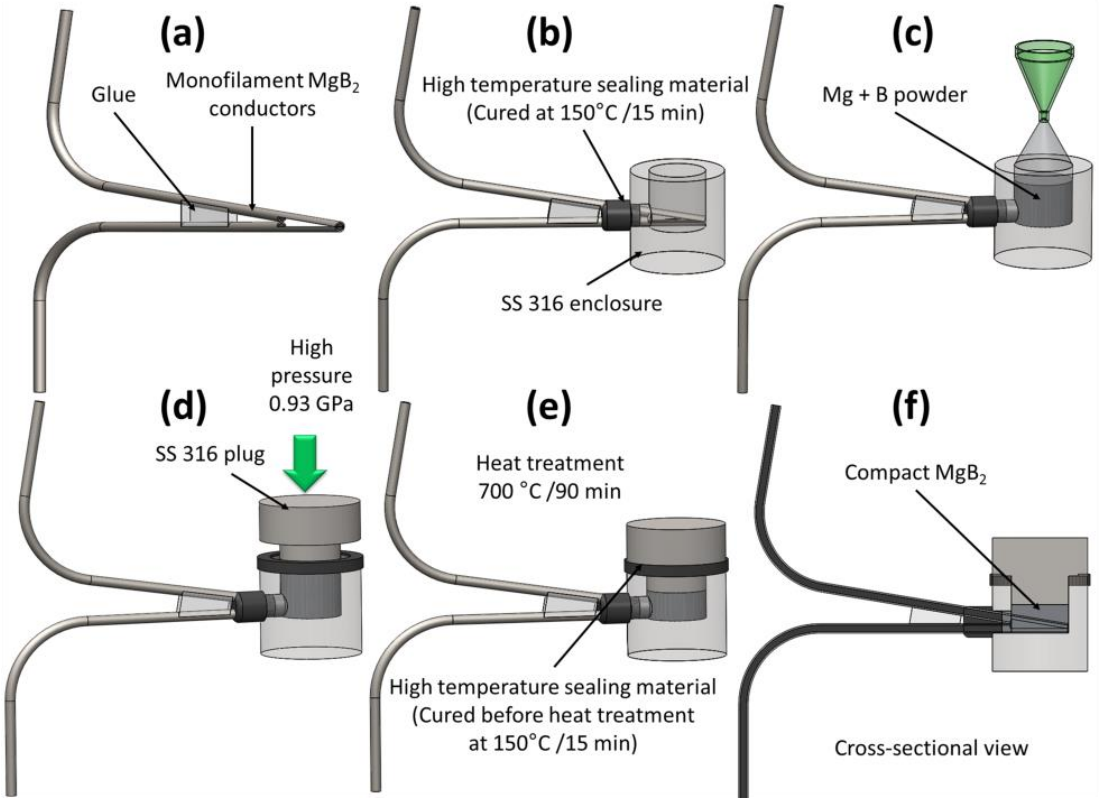

Figure 5-1. Joint configuration and fabrication steps for unreacted monofilament MgB_2 wires.

Figure 5-1 shows the joint configuration and fabrication steps for unreacted monofilament MgB_2 wires. As shown in figure 5-1(a), the metallic sheath material of the two wires was partially peeled off using mechanical polishing until the MgB_2 core was exposed. After removing the metallic sheath, exposed cores of the wires were aligned and made to face each other using conventionally available super glue. The two aligned wires were then fixed in a suitable SS316 enclosure having an inner bore diameter of 6 mm, using a high-temperature sealing material from Copaltite, as shown in figure 5-1(b) [25]. The curing of the sealing material was carried out at 150 °C for 15 min in a drying oven. For the next step, mixed powder from the same batch (Mg + 2B) used for wire fabrication was then packed into the enclosure bore, as shown in figure 5-1(c). The packed powder density was estimated to be 1.96 g cm^{-3} ± 4 %. As shown in figure 5-1(d), the sealing material was applied on the top edge of the enclosure to hermetically seal the enclosure to avoid Mg evaporation during the heat-treatment process. For compacting Mg + 2B powder to make close contact with the wire core, ~0.93 GPa of pressure was applied, using a suitable SS316 plug.

Again, the curing of the sealing material was carried out at 150 °C for 15 min in the drying oven. Finally, the joints were heat treated in high purity argon (Ar) inert atmosphere at 700 °C for 90 min as shown in figure 5-1(e). The joints were allowed to cool down naturally to room temperature (RT) before removing from the furnace. Figure 5-1(f) shows a longitudinal cross-sectional view of the as-prepared joint specimen after a final heat-treatment.

The I_cs of the joints were measured using an American Magnetics Superconducting (AMS) magnet with DC currents up to 200 A (since 200 A was the limit of the power supply), different temperatures up to 25 K, and magnetic fields in the range of 0 – 2 T, using the standard four-probe method with the criterion of 1 μV cm^{-1}.

To observe the longitudinal cross-section, the joints were cut from the appropriate location in the centre of the enclosure. Scanning electron microscopy of all the joints was conducted using a JEOL low-vacuum scanning electron microscope (SEM).

To measure the joint resistance, a small closed-loop coil was fabricated using the same conductor through the "wind and react" method and evaluated using the field-decay method. The selected specifications of the closed-loop coil are listed in table 5-1. Inductance was calculated using equation (5.1) because the insulation was not used in the closed-loop coil [26]. Later, the two ends of the wire were connected using the same joining technique mentioned earlier. The entire coil assembly was heat-treated in high purity Ar inert atmosphere at 700 °C for 90 min.

Table 5-1. Selected specifications of the closed-loop coil.

I.D. (mm)	**O.D. (mm)**	**Height (mm)**	**Turns**	**Inductance (L, μH)**
20	24	15	28	14 ± 7 %

$$L \cong \mu_0 a_1 N^2 \left(\frac{\alpha+1}{2}\right)\left\{\ln\left[\frac{2(\alpha+1)}{\beta}\right]-0.5\right\} \tag{5.1}$$

where L is the inductance of the coil, μ_0 is the permeability of free space ($\mu_0 = 1.26$ x 10^{-6} H m^{-1}), a_1 is the inner radius of the coil, N is the number of turns, α is the

ratio of outer radius to the inner radius of the coil, β is the ratio of half of the length of the coil to the inner radius.

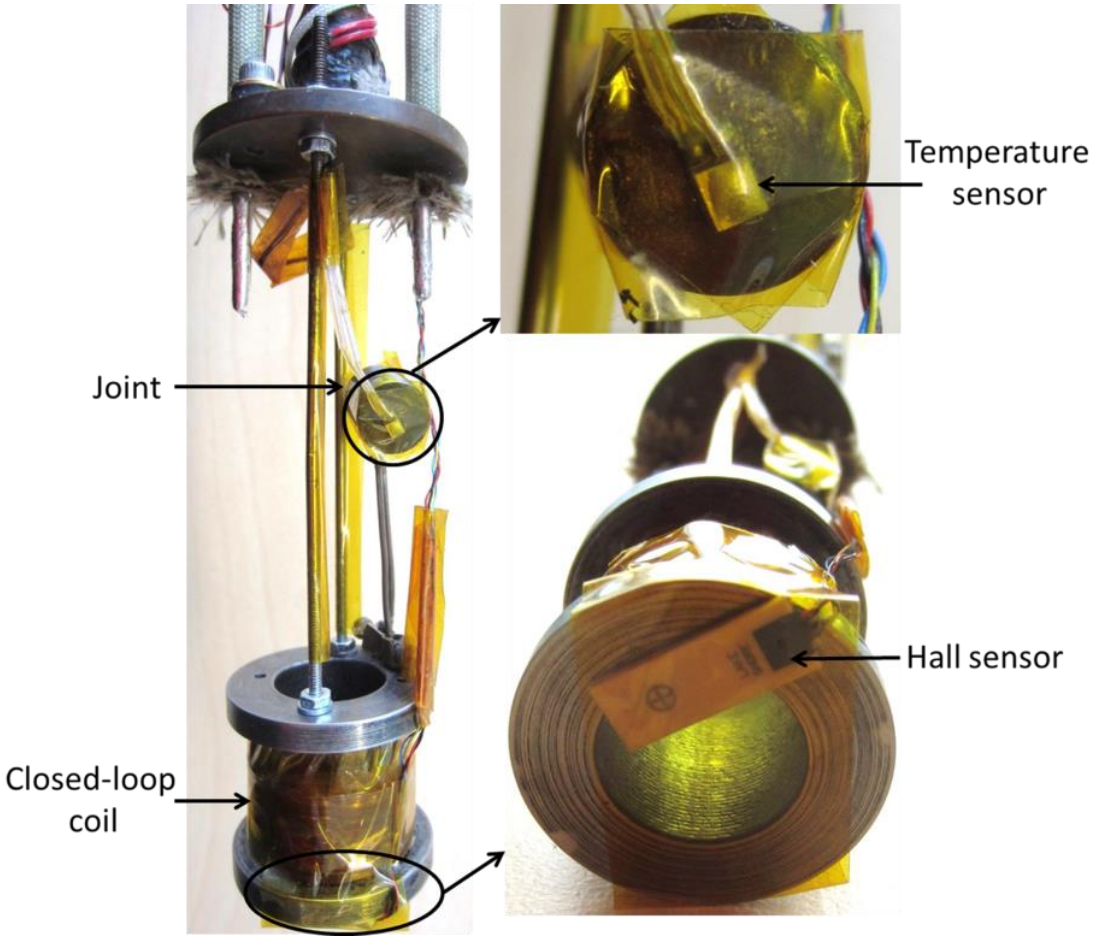

Figure 5-2. Field-decay measurement set-up.

To determine joint resistance, a field-decay measurement was carried out. The field-decay measurement set-up is shown in figure 5-2. A Hall sensor with 0.1 G sensitivity was installed at the bottom of the closed-loop coil to measure the magnetic field generated by the coil. The cryogenic Cernox™ SD package temperature sensor was also installed using Apiezon® N grease and Kapton® tape for thermally well-coupled with the joint to monitor the temperature [27], during the closed-loop coil measurement as well as short joint measurement (not shown here). The test probe was then inserted into the bore of the variable temperature insert (VTI) of the AMS magnet (see Chapter 3). First, a magnetization test of the closed-loop coil was carried out to check for any magnetization effect on the coil at RT because Fe was present in the coil as a wire sheath. But, we did not observe any

noticeable magnetization effect. External magnet field was applied up to 1.42 T and then decreased to zero with a ramp-down rate of ~0.17 T s^{-1}. A similar magnetic field and ramp-down rate applied during the actual field-decay measurement to induce current in the closed-loop. Owing to the limitations of our equipment, the field-decay measurement was carried at 4.2 K.

5.3. Results and Discussion

To evaluate the current-carrying capacity of the jointed MgB_2 conductor, firstly, we carried out I_c measurements, as shown in figure 5-3. Unjoined and jointed wires (inset of figure 5-3) were heat-treated under the same conditions for comparative study. As can be seen in the figure, the I_c values of the unjoined wire under 2 T were measured to be 64 A and 155 A, respectively, at 25 K and 20 K. After mechanical pressing and heat-treatment, the joined wires showed electrical performance fading, leading to ~35% I_c degradation. The *n*-values, however, which are extracted from the power law of voltage vs. current characteristic, did not show any noticeable difference between the jointed and unjoined wire. Regardless of the presence or absence of the joint, a very sharp transition appeared near the criterion of 1 μV cm^{-1}. Compared to low-temperature superconductors such as NbTi and niobium tin (Nb_3Sn), however, the *n*-value of the MgB_2 conductor still shows a relatively smooth transition from the superconducting state to the resistive one. In particular, it is well-known that both the I_c and the *n*-value are close to the microstructures.

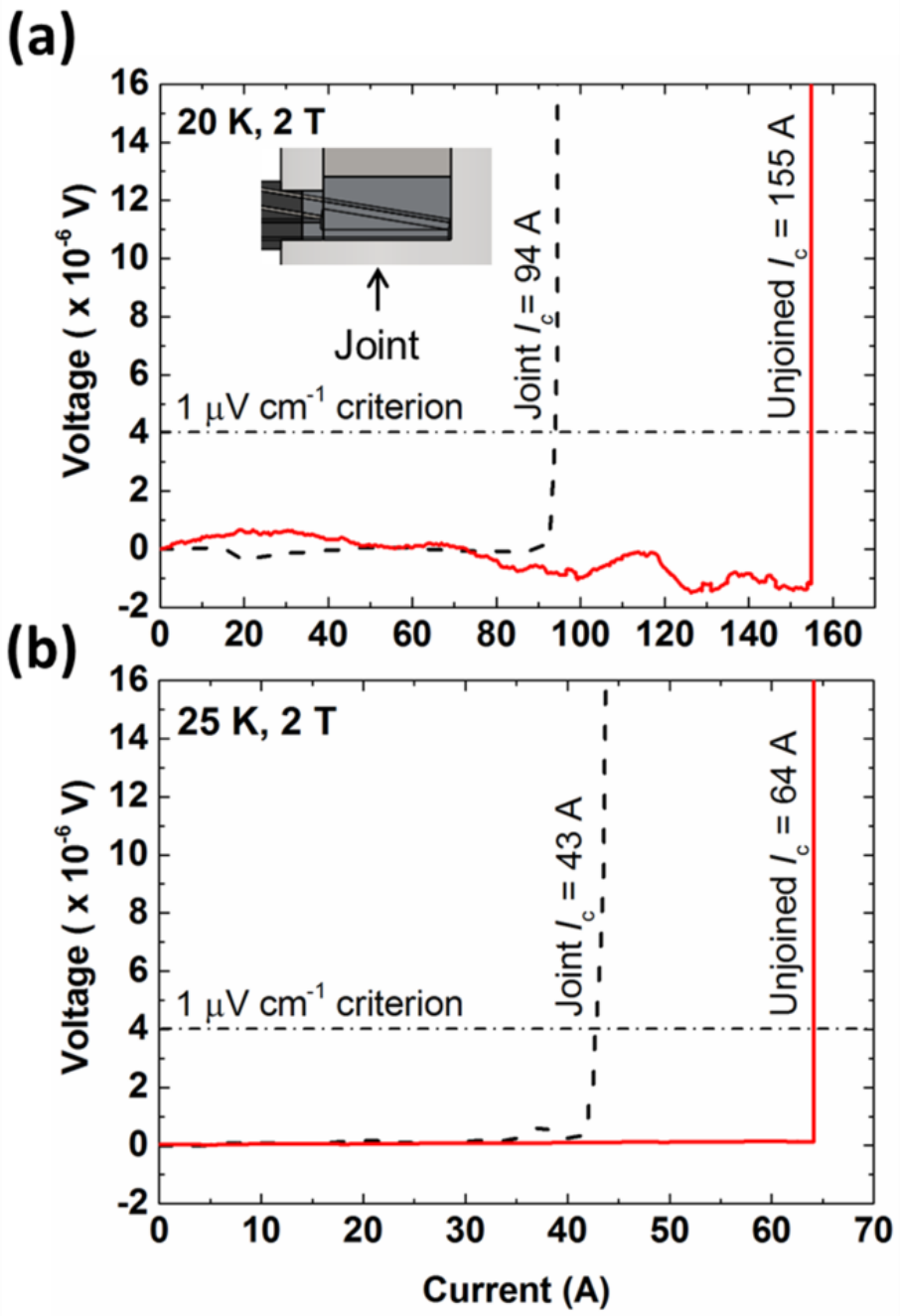

Figure 5-3. Current and voltage characteristics of the jointed (inset figure) and unjoined wires at (a) 20 K, 2 T, and (b) 25 K, 2 T. The distance between voltage taps was 4 cm.

To determine the reason for the current fading, a detailed microstructure analysis was conducted using SEM. Figure 5-4 shows a schematic representation of a longitudinal cross-section of a joint and SEM images of the specified areas in a schematic. As has been described, core-exposed MgB_2 wires were put into Mg + 2B powders contained in an SS316 enclosure. Thus, we expect that some porous regions

might still exist, even after pressing and heat-treatment processes. The total length of the wire inside joint was ~5.63 mm and direct MgB_2 core to core contact length was ~2.38 mm. The remaining length was connected through porous bulk MgB_2 between two cores. Figure 5-4(a) shows a schematic representation of a longitudinal cross-section of a joint (not scaled). Figure 5-4(b) depicts a bulk region formed by the Mg + 2B powders between wire cores. We observed that porous microstructure exists. On the other hand, the interface between wire cores has a denser structure with less porosity, as can be seen in figure 5-4(c). Most importantly, as can be seen in figure 5-4(d), the interface between the bulk and the wire core shows different microstructure. This might result in microstructural defects, such as micro-/macro-cracks.

To examine this point, we carried out further microstructure analysis. It is worth noting that pressure was vertically applied to the MgB_2 wires. As expected from this, micro-/macro-cracks were observed, as can be seen in figure 5-4(e). External pressure helps MgB_2 formation in the Mg + 2B bulk area, but this can induce microstructural defects, resulting in degradation of current-carrying capacity. In fact, by avoiding the cracks, the performance of the joints can be further improved. During MgB_2 formation, micro-/macro-cracks were not healed during the heat-treatment process. As a result, we need to determine the optimized pressure conditions.

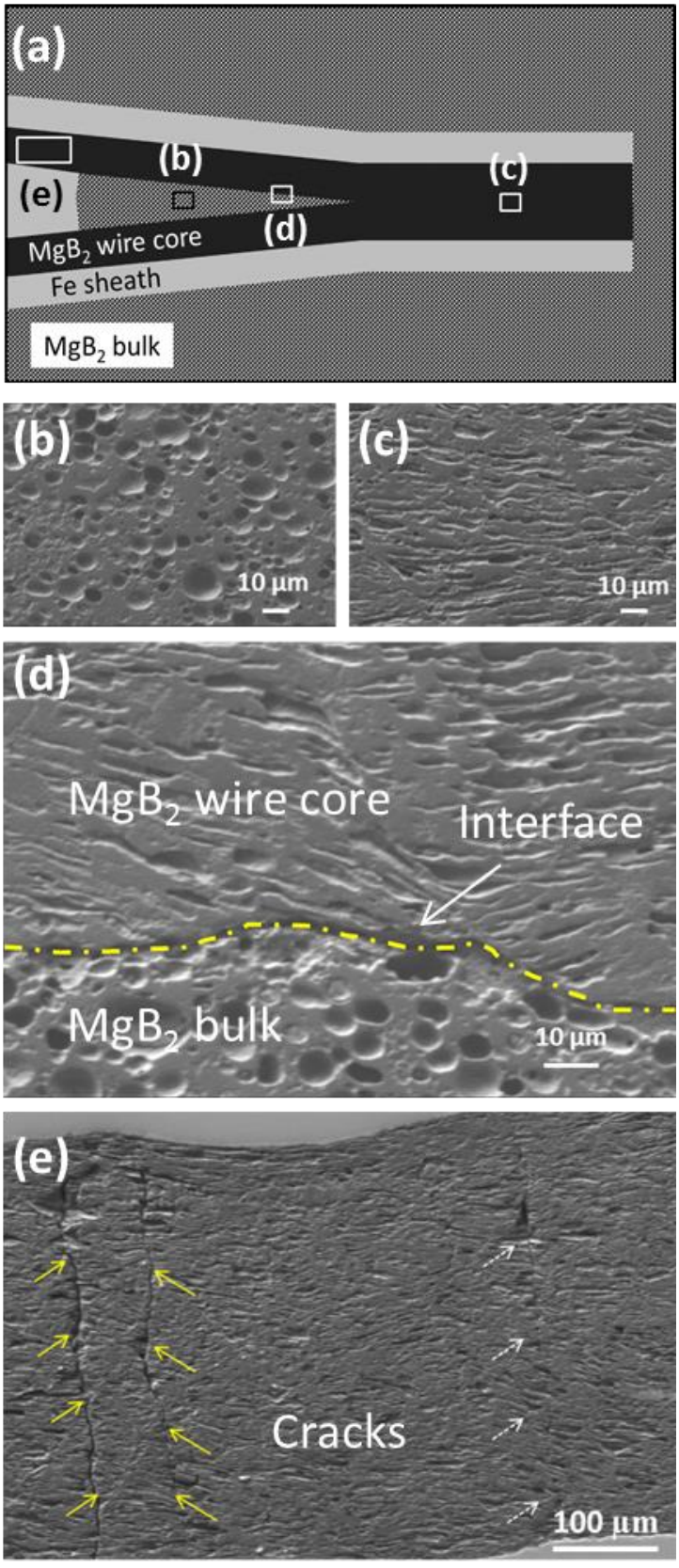

Figure 5-4. (a) Schematic representation of a longitudinal cross-section of a joint (not scaled), SEM images of the jointed wires area represented in a schematic: (b) bulk MgB_2

region, interfaces between (c) MgB_2 wire cores, and (d) MgB_2 bulk and wire core, and (e) cracks in the joint (yellow (solid) and white (dashed) arrows are showing macro and micro cracks, respectively).

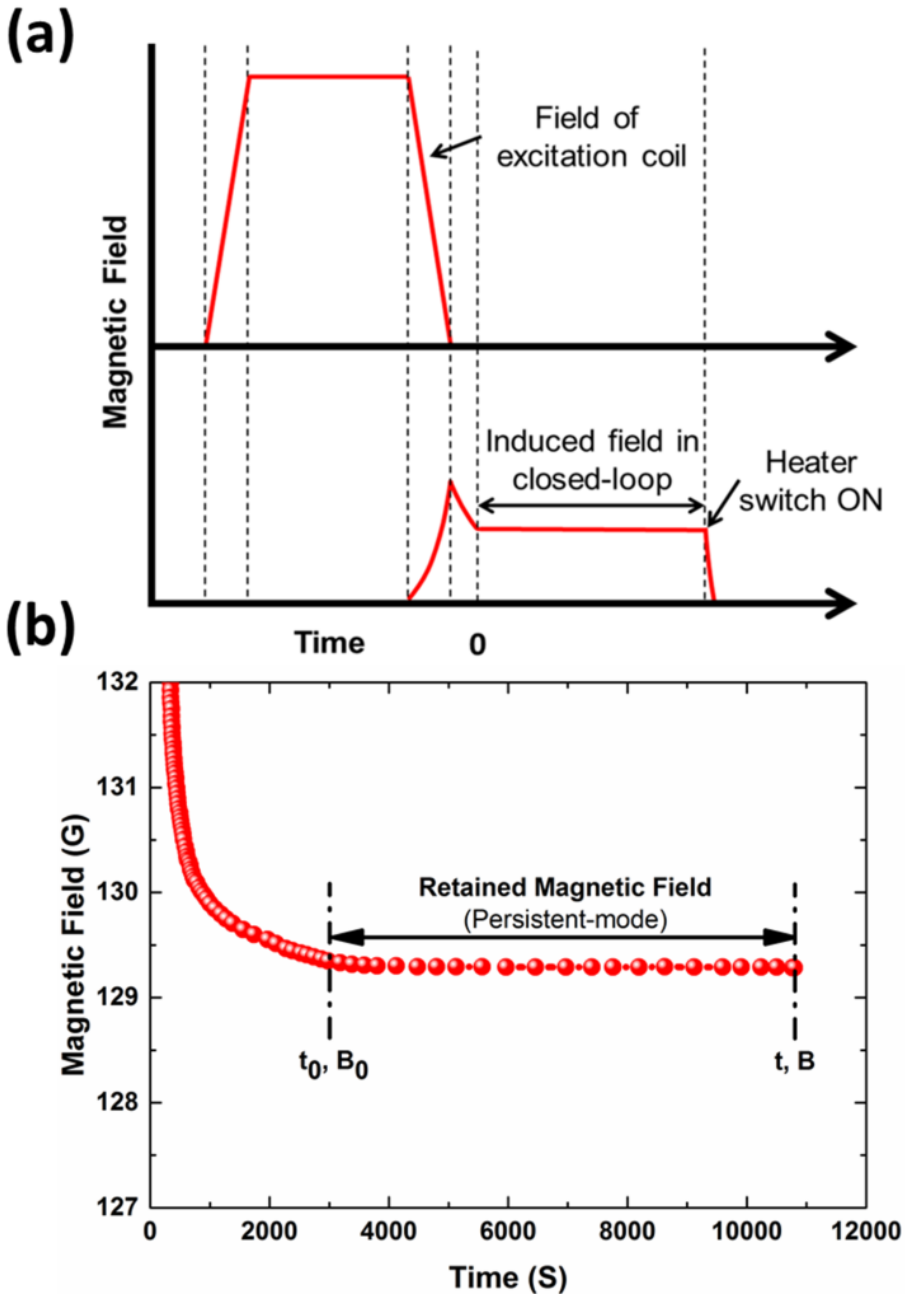

Figure 5-5. (a) The schematic of the operating procedure of the field-decay measurement method. (b) Time decay curve of the captured magnetic field (y-axis field is the induced field in the closed-loop coil).

As was described above, superconducting joint resistance between MgB_2 wires can be evaluated by field-decay measurements, i.e., the decay of the induced current

in the superconducting closed circuit. The decay behaviour normally has two stages as shown in the schematic of the operating procedure of the field-decay measurement method in figure 5-5(a). The first stage shows exponentially decreasing current with a high decay rate, due to the lower *n*-value and the small difference between the induced current and I_c of the closed-loop coil [26, 28]. In the second stage, the decay is very slow and depends on the joint resistance. The field-decay measurement results obtained from our system are shown in figure 5-5(b). During the entire field-decay measurement period, the joint was exposed to only self-field at 4.2 K. The magnetic field was allowed to stabilize for about 3000 s, and at this point, was considered to be the initial magnetic field B_0 at time t_0 for the resistance estimation. About 0.1 gauss decay in retained magnetic field was observed in 7764 s. The retained magnetic field after 0.1 gauss decay was 129.3 G which corresponds to 30.8 A current based on finite element analysis.

The joint resistance was estimated from temporal decay of magnetic field in the time constant of *L* - *R* circuit:

$$B = B_0 \, e^{-\left(\frac{R}{L}\right) t} \tag{5.2}$$

where *B* is the magnetic field at time *t*, B_0 is the magnetic field at a time t_o, *L* is the inductance of the closed-loop coil, *R* is the joint resistance, and *t* is the decay time in seconds. The joint resistance was estimated to be 1.4×10^{-12} Ω at 4.2 K. The same joint technique will be applied to make an MgB_2 based persistent current switch (PCS). For practical MRI application, however, the joint technique without any electromagnetic performance fading will be a major challenge for long-term operation.

5.4. Conclusions

We fabricated and evaluated superconducting joints and determined their joint resistance with unreacted MgB_2 wire. The I_c results for the jointed wires demonstrated consistent performance, which is promising from the viewpoint of "wind and react" magnets. Despite the performance consistency in the joint performance, about 60 to 66% of the current was retained after the joint was installed. A field-decay measurement of the closed-loop coil was also conducted to

estimate the joint resistance, which was about 1.4×10^{-12} Ω. Optimisation of the wire cutting, heat-treatment conditions, and powder density in the joint is required, however, for further performance enhancement. The SEM observations showed very good MgB_2 core to core contact in the joint, but some cracks were also induced in this region. These should be avoided for reliable joint processing.

5.5. References

[1] Wang Z, Van Oort J M and Zou M X 2012 Development of superconducting magnet for high-field MR systems in China *Physica C* **482** 80-6

[2] Nagamatsu J, Nakagawa N, Muranaka T, Zenitani Y and Akimitsu J 2001 Superconductivity at 39 K in magnesium diboride *Nature* **410** 63-4

[3] Canfield P C, Finnemore D K, Bud'ko S L, Ostenson J E, Lapertot G, Cunningham C E and Petrovic C 2001 Superconductivity in dense MgB_2 wires *Phys. Rev. Lett.* **86** 2423-6

[4] Glowacki B A, Majoros M, Vickers M, Evetts J E, Shi Y and McDougall I 2001 Superconductivity of powder-in-tube MgB_2 wires *Supercond. Sci. Technol.* **14** 193-9

[5] Larbalestier D, Gurevich A, Feldmann D M and Polyanski A 2001 High-T_c superconducting materials for electric power applications *Nature* **414** 368-77

[6] Tomsic M, Rindfleisch M, Yue J, McFadden K, Phillips J, Sumption M D, Bhatia M, Bohnenstiehl S and Collings E W 2007 Overview of MgB_2 superconductor applications *Int. J. Appl. Ceram. Technol.* **4** 250-9

[7] Patel D, Hossain M S A, Motaman A, Barua S, Shahabuddin M and Kim J H 2014 Rational design of MgB_2 conductors toward practical applications *Cryogenics* **63** 160-5

[8] Patel D, Maeda M, Choi S, Kim S J, Shahabuddin M, Parakandy J M, Hossain M S A and Kim J H 2014 Multiwalled carbon nanotube-derived superior electrical, mechanical and thermal properties in MgB_2 wires *Scr. Mater.* **88** 13-6

[9] Li X, Zhang D, Zhang J, Gao Z, Dai S, Zhang Z, Xia D, Zhang G, Wang D, Ma Y, Lin L and Xiao L 2011 A small 1.5 T persistent current operating test magnet using MgB_2 wire with high j_c joints *IEEE Trans. Appl. Supercond.* **21** 1616-9

[10] Modica M, Angius S, Bertora L, Damiani D, Marabotto M, Nardelli D, Perrella M, Razeti M and Tassisto M 2007 Design, construction and tests of MgB_2 coils for the development of a cryogen free magnet *IEEE Trans. Appl. Supercond.* **17** 2196-9

[11] Razeti M, Angius S, Bertora L, Damiani D, Marabotto R, Modica M, Nardelli D, Perrella M and Tassisto M 2008 Construction and operation of cryogen free MgB_2 magnets for open MRI systems *IEEE Trans. Appl. Supercond.* **18** 882-6

[12] Ling J, Voccio J, Kim Y, Hahn S, Bascuñán J, Park D K and Iwasa Y 2013 Monofilament MgB_2 wire for a whole-body MRI magnet: Superconducting joints and test coils *IEEE Trans. Appl. Supercond.* **23** 6200304

[13] Park D K, Ling J, Rindfleisch M, Voccio J, Hahn S, Bascuñán J, Tomsic M and Iwasa Y 2012 MgB_2 for MRI magnets: Test coils and superconducting joints results *IEEE Trans. Appl. Supercond.* **22** 4400305

[14] Yao W, Bascuñán J, Kim W S, Hahn S, Lee H and Iwasa Y 2008 A solid nitrogen cooled MgB_2 "demonstration" coil for MRI applications *IEEE Trans. Appl. Supercond.* **18** 912-5

[15] Lvovsky Y, Stautner E W and Zhang T 2013 Novel technologies and configurations of superconducting magnets for MRI *Supercond. Sci. Technol.* **26** 093001

[16] Takahashi M, Tanaka K, Okada M, Kitaguchi H and Kumakura H 2006 Relaxation of trapped high magnetic field in 100 m-long class MgB_2 solenoid coil in persistent current mode operation *IEEE Trans. Appl. Supercond.* **16** 1431-4
[17] Penco R and Grasso G 2007 Recent development of MgB_2-based large scale applications *IEEE Trans. Appl. Supercond.* **17** 2291-4
[18] Braccini V, Nardelli D, Penco R and Grasso G 2007 Development of *ex situ* processed MgB_2 wires and their applications to magnets *Physica C* **456** 209-17
[19] Li X H, Ye L Y, Jin M J, Du X J, Gao Z S, Zhang Z C, Kong L Q, Yang X L, Xiao L Y and Ma Y W 2008 High critical current joint of MgB_2 tapes using Mg and B powder mixture as flux *Supercond. Sci. Technol.* **21** 025017
[20] Yao W, Bascuñán J, Hahn S and Iwasa Y 2009 A superconducting joint technique for MgB_2 round wires *IEEE Trans. Appl. Supercond.* **19** 2261-4
[21] Li X, Ye L, Zhang D, Wang D and Ma Y 2010 Joints in MgB_2 tapes and wires for persistent current operating magnet *IEEE Trans. Appl. Supercond.* **20** 1528-31
[22] Giunchi G, Saglietti L, Ripamonti G, Albisetti A F, Bassani E and Perini E 2010 Superconducting joints between MgB_2 wires and bulks *IEEE Trans. Appl. Supercond.* **20** 1524-7
[23] Wozniak M, Glowacki B A, Setiadinata S B and Thomas A M 2013 Pulsed magnetic field assisted technique for joining MgB_2 conductors for persistent mode MRI magnets *IEEE Trans. Appl. Supercond.* **23** 6200104
[24] Nardelli D, Angius S, Capelluto A, Damiani D, Marabotto R, Modica M, Perrella M and Tassisto M 2010 Persistent mode MgB_2 short windings *IEEE Trans. Appl. Supercond.* **20** 1998-2001
[25] www.copaltite.com
[26] Iwasa Y 2009 *Case studies in superconducting magnets, design and operation issues* (New York: Springer)
[27] www.lakeshore.com
[28] Kim J H, Dou S X, Matsumoto A, Choi S, Kiyoshi T and Kumakura H 2010 Correlation between critical current density and n-value in MgB_2/Nb/Monel superconductor wires *Physica C* **470** 1207-10

5.6. Note: Chapter Publication and Text Usage Detail

This Chapter has been published in Superconductor Science and Technology as a paper (see below reference). The written text in this Chapter has been taken from my published paper, as shown below.

[1] **Patel D**, Hossain M S A, See K W, Xu X, Barua S, Ma Z, Choi S, Tomsic M and Kim J H 2015 MgB_2 superconducting joints for persistent current operation *Supercond. Sci. Technol.* **28** 065017

Chapter 6

6. A New Approach to a Superconducting Joining Process for Carbon-Doped MgB2 Conductor

6.1. Introduction

Magnesium diboride (MgB_2), which has a critical temperature (T_c) of 39 K, was found to be superconducting in 2001 [1]. Since then, the performance of MgB_2 material and the manufacturing technology for long-length conductors have been improved significantly [2-7]. Recently, magnet-grade MgB_2 conductors have been commercially available in long-length pieces for employment in various practical applications [5, 6, 8-10]. In particular, the high-T_c of MgB_2 can enable liquid helium (LHe)-free operation up to 25 K. Therefore, there is strong interest worldwide in employing MgB_2 for magnetic resonance imaging (MRI) based on an LHe-free MRI magnet system [11-16]. A special LHe-free MRI system can offer lower principal and maintenance costs, which may make MRI affordable for developing and underdeveloped countries [17].

The 'open sky MRI' has already been commercialized using MgB_2 conductor [18]. These MRIs, however, are operated in a driven-mode due to the difficulties in making reliable superconducting joints between MgB_2 conductors. Usually, MRI magnets require a persistent-mode operation to obtain high-quality images [11, 19]. Therefore, for wide applicability of MgB_2 in MRI, still more work needs to be done on the joining process. So far, there have been several reports on joining both *in situ* and *ex situ* MgB_2 conductors [6, 16, 20-27]. Comparison of our joint performance values with various literature is summarized in table 6-1.

In the case of *in situ* MgB_2 conductor joints, it has been reported that unreacted monofilament conductor joints can certainly give reliable performance [13, 16, 21-23]. Several coils with a persistent-current switch or joint(s) have been fabricated using an *in situ* monofilament MgB_2 conductor via the wind and react method [13,

16, 21-23, 28]. These coils showed stable persistent-mode operation. It is well known that the high-field performance of *in situ* MgB_2 can be significantly improved by carbon (C)-doping [2, 3, 7, 29-32]. Thus, it is desirable to use C-doped MgB_2 conductor where high in-field performance is required. However, most of the high-performance joint results have been reported for *in situ* MgB_2 conductors without C-dopant for low-field operation (see table 6-1) [13, 16, 21-23]. Park *et al* reported that the critical current (I_c) of an unreacted *in situ* undoped monofilament wire joint was >230 A at 10 K [22]. On the other hand, when they used an unreacted *in situ* C-doped monofilament wire under the same experimental conditions, the I_c of the joint was only 16 A at 10 K. To the best of our knowledge, there has been no report on high-performance joints using an unreacted *in situ* C-doped monofilament MgB_2 conductor at 20 K. There is thus a need for a superior joining approach for *in situ* C-doped conductors.

Table 6-1. Comparison of our joint performance values with various literature.

Joint details	**I_c or current carrying capacity**	**Joint resistance**
Multifilament		
Ex situ tape [26]	>300 A at 20 K, self-field	$<10^{-14}$ Ω at 20 K
Ex situ tape (fully reacted) [33]	50 A at 15 K, self-field	$<10^{-9}$ Ω at 15 K, self-field, four-probe
In situ wire (undoped) [22]	103 A at 10 K, self-field	-
Monofilament		
In situ wire (undoped) [22]	160 A at 20 K, self-field	$<10^{-12}$ Ω at 10.5 K
In situ wire (undoped) [16]	94 A at 20 K, 2 T	1.4×10^{-12} Ω at 4.2 K
In situ wire (undoped) [23]	270 A at 20 K, self-field	$<1.3 \times 10^{-10}$ Ω at 15 K
In situ wire (C-doped) [22]	11 A at 16 K, self-field	-
In situ wire (C-doped) (this study)	>200 A, 20 K, self-field	$<1.8 \times 10^{-13}$ Ω at 16.7 ± 4.7 K

In this study, therefore, a superconducting joining process for an unreacted *in situ* C-doped monofilament MgB_2 wires has been investigated in detail, and the persistent-mode performance of the solenoid closed-loop coil was systematically evaluated.

6.2. Experimental Details

A C-doped monofilament MgB_2 wire was fabricated via an *in situ* process by Hyper Tech Research Inc. [8]. The diameter of the wire was 0.84 mm with a niobium (Nb) barrier and a Monel outer sheath. The superconducting fill factor and the amount of C-dopant in the wire were 21% and 2 wt%, respectively. Figure 6-1 presents a cross-sectional image of the MgB_2 wire used in this work.

We already reported the joining concept for unreacted *in situ* undoped monofilament MgB_2 wires [16]. More reliable joining using an unreacted *in situ* C-doped MgB_2 conductor is still required, however [22]. In the literature so far, there have been no reports showing superior current carrying capacity (i.e., current carrying retention >60%) with C-doped wire at 20 K. Therefore, it is necessary to study a new approach to the superconducting joining process for C-doped MgB_2 conductors.

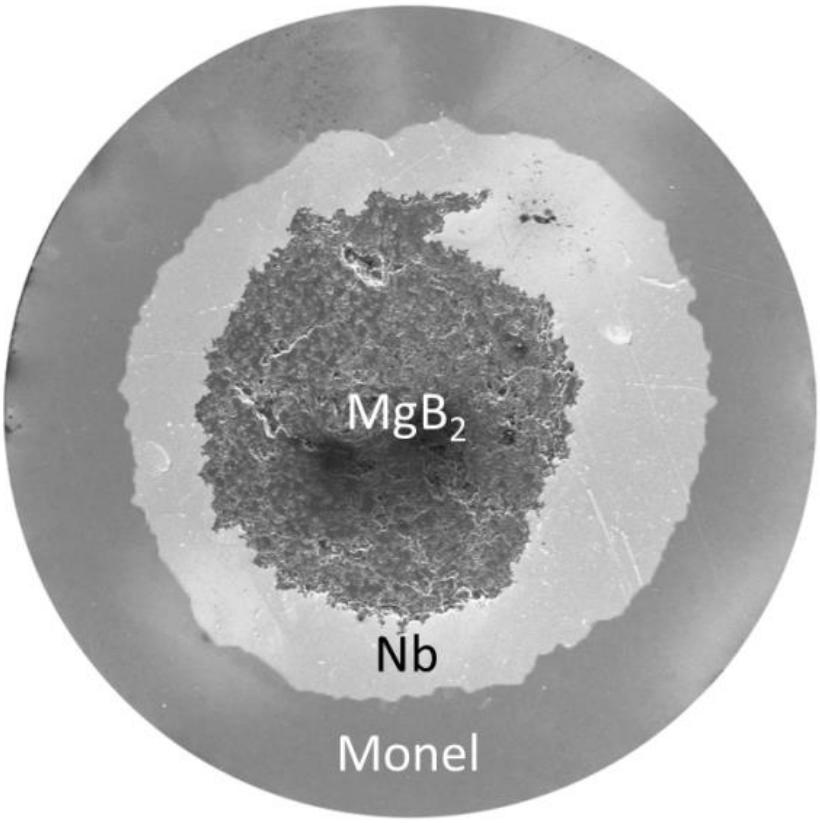

Figure 6-1. Cross-sectional image of the monofilament MgB_2 wire (Monel sheath, Nb barrier).

Figure 6-2 shows the key steps in our modified superconducting joint fabrication process for an unreacted *in situ* C-doped monofilament MgB_2 wire. Firstly, a predefined length (~7 mm) of the Monel sheath was chemically etched away using nitric acid from the joining area of the wires. Then, the Nb barrier of the wire (~4 mm in length) was partially peeled off until the MgB_2 core was exposed using mechanical polishing. After peeling off the Nb barrier, the exposed MgB_2 cores of two wires were aligned and made to face each other using super glue. As shown in figure 6-2, the two aligned wires were fixed in a stainless steel (SS) enclosure (inner diameter of 6 mm) using a high-temperature sealing material (Resbond 907GF) [34]. The sealing material was allowed to cure for 24 h at room temperature (RT) in air. In our original joining process, the sealing material needed to be cured at 150 °C for 15 min in an oven [16]. For the modified joining process, RT curing of the sealing material can offer better flexibility in handling the joints. After curing the sealing material, previously, packing Mg + 2B powder into the joint was performed in air. In the modified joining process, however, filling in the joint with Mg (99%, 325 mesh, Sigma-Aldrich) + C-encapsulated B (98.8%, ~400 nm, C-doping 2 wt%, amorphous, Pavezyum) powder was performed in an argon (Ar) protective atmosphere (in an Ar glove box) to minimize trapping of oxygen while filling the joint with powder [35, 36]. An SS plug was used to compact the powder inside the enclosure (figure 6-2). The uniaxial pressure for pressing the plug was <0.35 GPa, which was much lower than 0.95 GPa reported in our previous work (i.e., *in situ* undoped monofilament MgB_2 wires) [16]. It should be noted that the applied pressure for the power compaction is more sensitive for C-doped MgB_2 wire joining. In the next step after pressing the powder, the sealing material was applied to the remaining gaps on the SS enclosure, and the joint was then taken out of the Ar glove box. Again, the sealing material was allowed to cure for 24 h at RT (in air) prior to heat-treatment. Finally, the joint was heat-treated in Ar atmosphere at 690 °C for 30 min, which are the best conditions for our MgB_2 wire.

The field dependence (up to 2 T) of the I_c of the joint and wire without a joint was investigated using the variable temperature insert (VTI) of an American Magnetics Superconducting (AMS) magnet with direct-current up to 200 A (the maximum power supply capacity) and 20 K operating temperature, using the

standard four-probe method with the criterion of 0.1 μV cm^{-1} (the criterion of 1 μV cm^{-1} is the one that has been most commonly used for MgB_2 conductors).

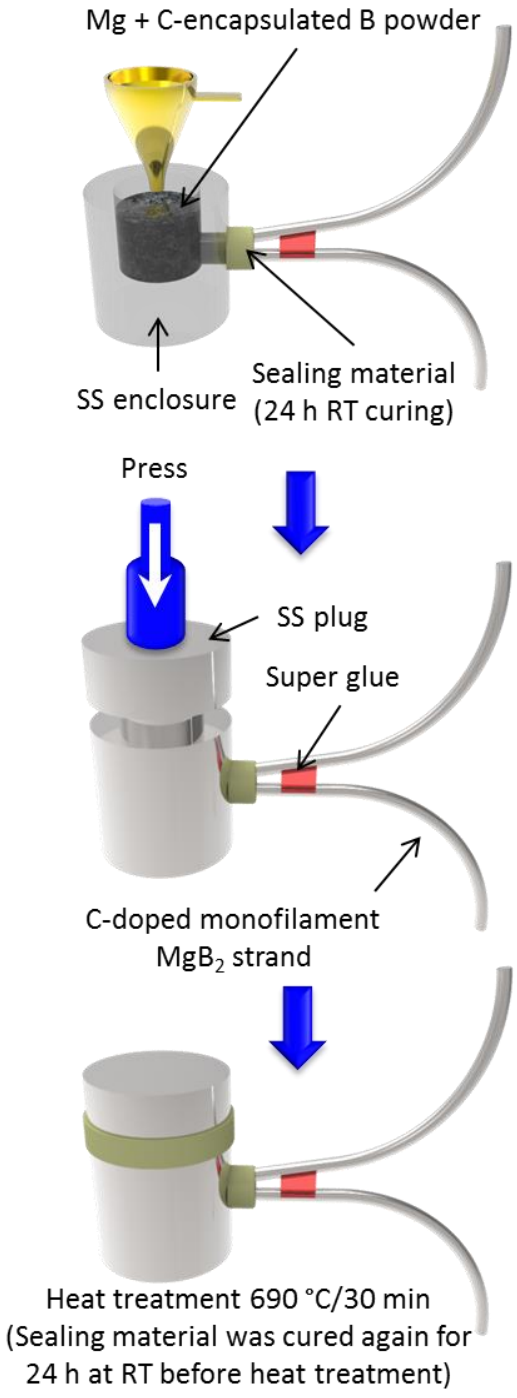

Figure 6-2. Superconducting joint fabrication process for an unreacted *in situ* C-doped monofilament MgB_2 wire.

The joint was then longitudinally cut to take out the MgB_2 powder ingot to perform X-ray diffraction (XRD) analysis. The ingot was ground into a fine powder. The XRD device (Mini-materials Analyser, GBC Scientific Equipment, USA) was used with Cu Kα (λ = 1.54056 Å) radiation for the XRD analysis [37]. Finally, a solenoid closed-loop coil was fabricated via the wind and react method using the same wire and joining process discussed earlier to evaluate the joint resistance using a field-decay method [16]. The coil with the joint was heat-treated in Ar atmosphere at 690 °C for 30 min. The inductance of the fabricated coil was calculated using the finite element (FE) method implemented with COMSOL Multiphysics software [38]. The specifications of the solenoid closed-loop coil are listed in table 6-2. After heat-treatment of the coil, the coil was mounted on the test probe. The detailed field-decay measurement set-up is described in our previous paper [16].

Table 6-2. Specifications of the solenoid closed-loop coil.

Parameters	**Specifications**
Coil Type	Solenoid (closed-loop)
Wire type	C-doped (*in situ* mono)
Winding method	Wind and react
No. of joints	1
Inner diameter (mm)	20
Outer diameter (mm)	26.72
Height (mm)	9.24
Turns	42
Computed parameters from FE analysis	
Inductance (μH)	29
Trapped current (A)	104.7
Field at the coil centre (T)	0.22
Pick field on the conductor (T)	0.35
Field on the joint (T)	3.8×10^{-4} + self-field

The closed-loop coil was inserted into the VTI of the AMS magnet to perform a field-decay measurement. The background magnetic field was increased to 0.24 T with a ramping rate of 10 mT s^{-1}. The closed-loop coil was then cooled down to ~12

K. To induce a current in the closed-loop coil, the background magnetic field was linearly decreased to zero at the ramp-down rate of 0.19 mT s^{-1}. The field-decay in the solenoid closed-loop coil was observed over 48 h.

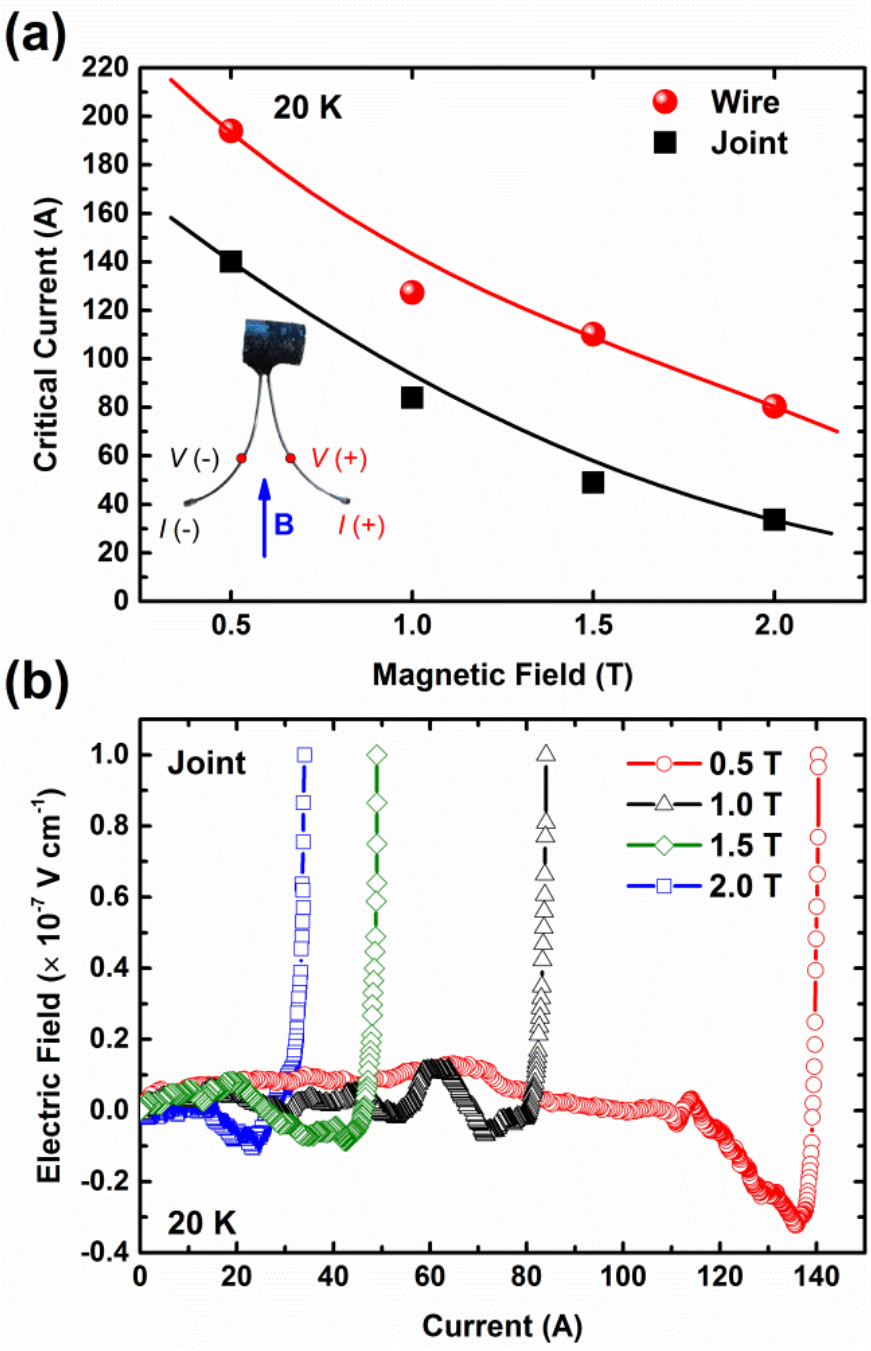

Figure 6-3. (a) Critical current vs. magnetic field characteristics of the wire (i.e., without a joint) and the joint, (b) electric field vs. current characteristics of the joint in different magnetic fields at 20 K. The direction of applied magnetic field for I_c measurement is shown

in the inset of figure 6-3(a). The distance between voltage taps on the joint sample was 4 cm (criterion: 0.1 μV cm^{-1}).

6.3. Results and Discussion

Figure 6-3(a) shows the magnetic field dependence of I_c at 20 K for the wire without a joint and joint. In self-field at 20 K, the I_c of the joint was >200 A, so the I_c results are shown from 0.5 T. The self-field performance of the joint at 20 K for the *in situ* C-doped monofilament MgB_2 wire is comparable to the performance of the joint for the *in situ* undoped monofilament MgB_2 wire [22, 23]. The I_c values of the wire without a joint and joint in 0.5 T at 20 K were measured to be 194 A and 140 A, respectively. This result means that the performance of the joint was approximately 72% of the performance of our wire without a joint. To the best of our knowledge, such significantly enhanced joint performance at 20 K with *in situ* C-doped MgB_2 monofilament wire is reported in this work for the first time [22]. Nevertheless, the joined wire also showed strong field dependent I_c in the field up to 2 T, and performance fading was also observed. These are preliminary results, so there is still room to further improve the joint performance.

The electric field vs. current characteristics of the joint at 20 K is shown in figure 6-3(b) as a function of external magnetic field. As can be seen in the figure, the superconducting to normal transition region appears very sharp in the range of 0.01 to 0.1 μV cm^{-1} criterion. This indicates that our joint technique was successful [39]. Furthermore, the joint performance is expected to be strongly dependent on the grain connectivity between the two MgB_2 wires and the phase formation of MgB_2 bulk inside the joint [16]. During the heat-treatment process, the sealing material always remains in close contact with the MgB_2 powder (figure 6-2) in the joint. Therefore, there was room for the sealing material to diffuse or react with the MgB_2 powder inside the joint during the heat-treatment process. Hence, XRD analysis was carefully carried out to look for impurity phases inside the joined part. Figure 6-4 shows XRD patterns of powder samples taken out of the wire and the joint. From our results, well developed MgB_2 phase was observed with only a small fraction of MgO. In the XRD pattern of the wire sample, Nb phase was also observed. This Nb might have come from the Nb barrier while taking the powder out from the wire. On the other hand, in the joint powder sample, MgB_2 was a major phase, and no foreign

phases existed, except for MgO as a minor phase. The calculated values of MgO fraction in the wire and the joint were 7.7 wt% and 13.3 wt%, respectively. These results confirm that the sealing material did not diffuse into or react with the MgB_2 during the heat-treatment process inside the joint.

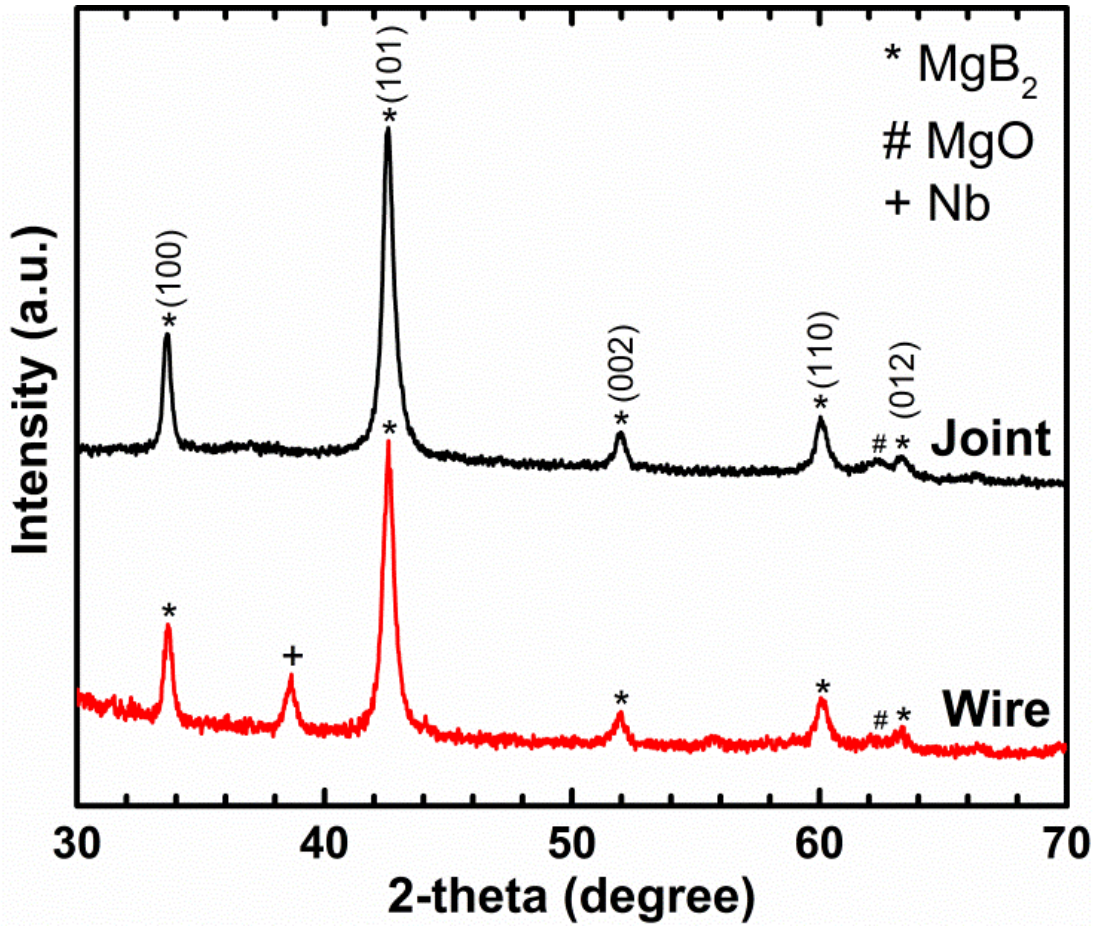

Figure 6-4. XRD patterns of the MgB_2 powder samples from the wire (i.e., without a joint) and the joint.

Under the same experimental conditions, a solenoid closed-loop coil was fabricated to evaluate the precise joint resistance using a field-decay measurement. Figure 6-5(a) shows a digital image of the solenoid closed-loop coil fabricated in this experiment. Figure 6-5(b) shows the magnetic field and temperature vs. time characteristics of the solenoid closed-loop coil during the initial induction of the current. Before starting the field-decay measurement, the coil temperature was adjusted to ~12 K. As can be seen in figure 6-5(b), when the background field started to decrease, the field began to be induced in the solenoid closed-loop coil. When the

background field was decreased to zero, the induced field in the closed-loop coil was 0.09074 T at the Hall sensor location (bottom of the coil near the coil winding) [16]. This magnetic field was equivalent to 104.7 A in the closed-loop coil based on FE analysis. Then, the coil was left in the persistent-mode for 48 h (figure 6-5(c)).

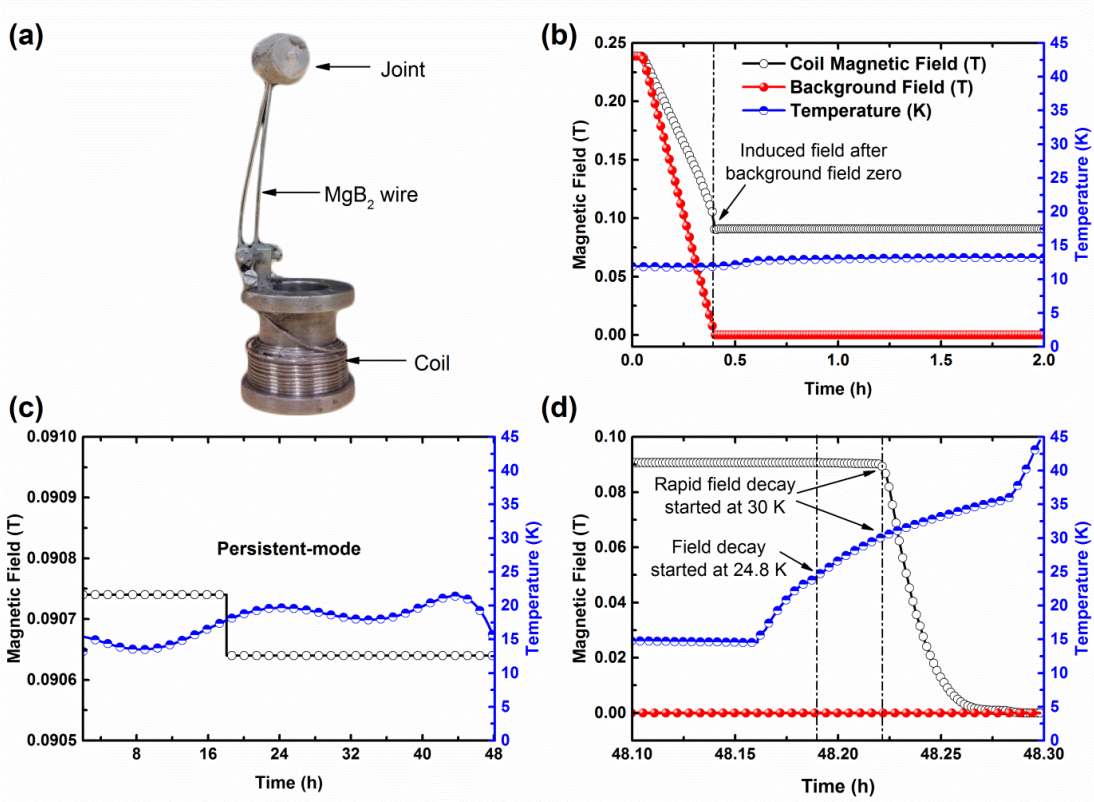

Figure 6-5. (a) A digital image of the solenoid closed-loop coil, (b) magnetic field (*B*) and temperature (*T*) vs. time (*t*) characteristics of the solenoid closed-loop coil during initial induction of the current, (c) *B*, *T* vs. *t* characteristics while the coil was in the persistent-mode, and (d) *B*, *T* vs. *t* characteristics as the temperature of the coil increased after 48 h of persistent-mode operation. The legends in figure 6-5(b), 6-5(c) and 6-5(d) are the same.

Our VTI system has a manual temperature control, so precise temperature control for a very long time period was very difficult to achieve. Hence, during persistent-mode, the temperature deviation in the VTI was from 12 K to 21.4 K. Close to 48 h, the temperature of the coil was controlled to ~15 K. In the 48 h of persistent-mode operation of the closed-loop coil, 0.1 mT decay in the magnetic field was observed (figure 6-5(c)). Eventually, at the end of 48 h, as shown in figure 6-5(d), the temperature of the VTI was increased. The decay of the magnetic field

started at 24.8 K, and rapid decay of the magnetic field was observed at 30 K. Some of the computed parameters of the solenoid closed-loop coil during the field-decay measurement are shown in table 6-2. Therefore, based on 29 μH inductance and 0.1 mT decay in 48 h, the calculated total circuit resistance of the solenoid closed-loop coil was $<1.8 \times 10^{-13}$ Ω [16]. This circuit resistance is acceptable for MRI application. These findings show the promising potential of the *in situ* C-doped monofilament MgB_2 wire. Moreover, this technique will pave the way for developing the joint of *in situ* and *ex situ* multifilamentary MgB_2 wire/tape conductors.

6.4. Conclusions

This study presented a new approach to a superconducting joining process for an unreacted *in situ* C-doped monofilament MgB_2 wire and evaluation of the joint resistance through a field-decay measurement. The new joining approach for C-doped MgB_2 conductor showed significantly enhanced performance compared to reported results to date. According to the literature, joint fabricated in this study using the unreacted *in situ* C-doped MgB_2 monofilament wire was the first to achieve an I_c value >200 A in self-field at 20 K. The joint demonstrated current retention of up to 72% in different magnetic fields at 20 K. The results presented here are preliminary results, so still there is room to further improve the joint performance. The XRD analysis showed no diffusion or reaction of the sealing material with the MgB_2 powder inside the joint. The solenoid closed-loop coil showed very reliable persistent-mode operation for a period of 48 h at temperatures up to 21.4 K in self-field. The estimated total circuit resistance was $<1.8 \times 10^{-13}$ Ω at 16.7 ± 4.7 K temperature. These superconducting joint performance results demonstrate the potential of MgB_2 conductors for MRI application based on an LHe-free system.

6.5. References

[1] Nagamatsu J, Nakagawa N, Muranaka T, Zenitani Y and Akimitsu J 2001 Superconductivity at 39 K in magnesium diboride *Nature* **410** 63-4

[2] Kim J H, Oh S, Heo Y U, Hata S, Kumakura H, Matsumoto A, Mitsuhara M, Choi S, Shimada Y, Maeda M, MacManus-Driscoll J L and Dou S X 2012 Microscopic role of carbon on MgB_2 wire for critical current density comparable to NbTi *NPG Asia Mater.* **4** e3

[3] Hossain M S A, Kim J H, Xu X, Wang X L, Rindfleisch M, Tomic M, Sumption M D, Collings E W and Dou S X 2007 Significant enhancement of H_{c2} and H_{irr} in MgB_2+$C_4H_6O_5$ bulks at a low sintering temperature of 600 °C *Supercond. Sci. Technol.* **20** L51

[4] Dou S X, Braccini V, Soltanian S, Klie R, Zhu Y, Li S, Wang X L and Larbalestier D 2004 Nanoscale-SiC doping for enhancing J_c and H_{c2} in superconducting MgB_2 *J. Appl. Phys.* **96** 7549-55

[5] Tomsic M, Rindfleisch M, Yue J, McFadden K, Phillips J, Sumption M D, Bhatia M, Bohnenstiehl S and Collings E W 2007 Overview of MgB_2 superconductor applications *Int. J. Appl. Ceram. Technol.* **4** 250-9

[6] Braccini V, Nardelli D, Penco R and Grasso G 2007 Development of *ex situ* processed MgB_2 wires and their applications to magnets *Physica C* **456** 209-17

[7] Patel D, Hossain M S A, Motaman A, Barua S, Shahabuddin M and Kim J H 2014 Rational design of MgB_2 conductors toward practical applications *Cryogenics* **63** 160-5

[8] www.hypertechresearch.com

[9] www.columbussuperconductors.com

[10] www.epochwires.com

[11] Lvovsky Y, Stautner E W and Zhang T 2013 Novel technologies and configurations of superconducting magnets for MRI *Supercond. Sci. Technol.* **26** 093001

[12] Bascuñán J, Lee H, Bobrov E S, Hahn S, Iwasa Y, Tomsic M and Rindfleisch M 2006 A 0.6 T/650 mm RT bore solid nitrogen cooled MgB_2 demonstration coil for MRI - A status report *IEEE Trans. Appl. Supercond.* **16** 1427-30

[13] Jiayin L, Voccio J P, Seungyong H, Youngjae K, Jungbin S, Juan B and Iwasa Y 2015 Construction and persistent-mode operation of MgB_2 coils in the range 10-15 K for a 0.5-T/240-mm cold bore MRI magnet *IEEE Trans. Appl. Supercond.* **25** 1-5

[14] Li X H, Du X J, Bao Q, Kong L Q, Ye L Y and Xiao L Y 2009 Design, development and experiment of a 1.5T MgB_2 superconducting test magnet *Cryogenics* **49** 286-90

[15] Modica M, Angius S, Bertora L, Damiani D, Marabotto M, Nardelli D, Perrella M, Razeti M and Tassisto M 2007 Design, construction and tests of MgB_2 coils for the development of a cryogen free magnet *IEEE Trans. Appl. Supercond.* **17** 2196-9

[16] Patel D, Hossain M S A, See K W, Xu X, Barua S, Ma Z, Choi S, Tomsic M and Kim J H 2015 MgB_2 superconducting joints for persistent current operation *Supercond. Sci. Technol.* **28** 065017

[17] Kara D C 2013 Production of a viable product in magnetic resonance imaging using MgB_2. (Master's Thesis, Case Western Reserve University)

[18] www.paramed.it
[19] Cosmus T C and Parizh M 2011 Advances in whole-body MRI magnets *IEEE Trans. Appl. Supercond.* **21** 2104-9
[20] Takahashi M, Tanaka K, Okada M, Kitaguchi H and Kumakura H 2006 Relaxation of trapped high magnetic field in 100 m-long class MgB_2 solenoid coil in persistent current mode operation *IEEE Trans. Appl. Supercond.* **16** 1431-4
[21] Yao W, Bascuñán J, Hahn S and Iwasa Y 2009 A superconducting joint technique for MgB_2 round wires *IEEE Trans. Appl. Supercond.* **19** 2261-4
[22] Park D K, Ling J, Rindfleisch M, Voccio J, Hahn S, Bascuñán J, Tomsic M and Iwasa Y 2012 MgB_2 for MRI magnets: Test coils and superconducting joints results *IEEE Trans. Appl. Supercond.* **22** 4400305
[23] Ling J, Voccio J, Kim Y, Hahn S, Bascuñán J, Park D K and Iwasa Y 2013 Monofilament MgB_2 wire for a whole-body MRI magnet: Superconducting joints and test coils *IEEE Trans. Appl. Supercond.* **23** 6200304
[24] Penco R and Grasso G 2007 Recent development of MgB_2-based large scale applications *IEEE Trans. Appl. Supercond.* **17** 2291-4
[25] Li X H, Ye L Y, Jin M J, Du X J, Gao Z S, Zhang Z C, Kong L Q, Yang X L, Xiao L Y and Ma Y W 2008 High critical current joint of MgB_2 tapes using Mg and B powder mixture as flux *Supercond. Sci. Technol.* **21** 025017
[26] Nardelli D, Angius S, Capelluto A, Damiani D, Marabotto R, Modica M, Perrella M and Tassisto M 2010 Persistent mode MgB_2 short windings *IEEE Trans. Appl. Supercond.* **20** 1998-2001
[27] Wozniak M, Glowacki B A, Setiadinata S B and Thomas A M 2013 Pulsed magnetic field assisted technique for joining MgB_2 conductors for persistent mode MRI magnets *IEEE Trans. Appl. Supercond.* **23** 6200104
[28] Patel D, Md Shahriar Al H, Khay Wai S, Qiu W, Kobayashi H, Zongqing M, Seong Jun K, Hong J, Jin Yong P, Choi S, Maeda M, Shahabuddin M, Rindfleisch M, Tomsic M, Dou S X and Kim J H 2016 Evaluation of persistent-mode operation in a superconducting MgB_2 coil in solid nitrogen *Supercond. Sci. Technol.* **29** 4LT02-9
[29] Patel D, Maeda M, Choi S, Kim S J, Shahabuddin M, Parakandy J M, Hossain M S A and Kim J H 2014 Multiwalled carbon nanotube-derived superior electrical, mechanical and thermal properties in MgB_2 wires *Scr. Mater.* **88** 13-6
[30] Kim J H, Heo Y-U, Matsumoto A, Kumakura H, Rindfleisch M, Tomsic M and Dou S X 2010 Comparative study of mono- and multi-filament MgB_2 wires with different boron powders and malic acid addition *Supercond. Sci. Technol.* **23** 075014
[31] Collings E W, Sumption M D, Bhatia M, Susner M A and Bohnenstiehl S D 2008 Prospects for improving the intrinsic and extrinsic properties of magnesium diboride superconducting strands *Supercond. Sci. Technol.* **21** 103001
[32] Kim J H, Oh S, Kumakura H, Matsumoto A, Heo Y-U, Song K-S, Kang Y-M, Maeda M, Rindfleisch M, Tomsic M, Choi S and Dou S X 2011 Tailored materials for high-performance MgB_2 wire *Adv. Mater.* **23** 4942-6
[33] Oomen M P 2014 Superconducting joints between MgB_2 wires for MRI magnets (ASC, Charlotte 2014)

[34] www.cotronics.com
[35] www.pavezyum.com.tr
[36] www.sigmaaldrich.com
[37] www.gbcsci.com
[38] www.comsol.com
[39] Iwasa Y 2009 *Case studies in superconducting magnets, design and operation issues* (New York: Springer)

6.6. Note: Chapter Publication and Text Usage Detail

This Chapter has been published in Superconductor Science and Technology as a paper (see below reference). The written text in this Chapter has been taken from my below paper.

[1] **Patel D**, Md Shahriar Al H, Maeda M, Shahabuddin M, Yanmaz E, Pradhan S, Tomsic M, Choi S and Jung Ho K 2016 A new approach to a superconducting joining process for carbon-doped MgB_2 conductor *Supercond. Sci. Technol.* **29** 095001

Chapter 7

7. Evaluation of Persistent-mode Operation in Superconducting MgB_2 Coil in Solid Nitrogen

7.1. Introduction

Physicians and surgeons rely critically on magnetic resonance imaging (MRI) scans to diagnose and treat critical injuries and medical conditions. In an MRI system, high, stable (<0.1 ppm h^{-1}), and uniform (≤10 ppm in 50 cm diameter of spherical volume (DSV)) magnetic fields are required for obtaining high-resolution images of the human body. The unique possibilities for the operation of superconducting magnets (i.e., persistent-mode) make them ideal for MRI with a central field strength >0.35 T [1]. Thus, in the majority of commercially available MRI systems, superconducting persistent magnets based on niobium titanium (NbTi) have been used [2]. These magnets, which are cooled in an expensive liquid helium (LHe) bath at 4.2 K, cannot currently be avoided. Thus, the high operation costs of MRI systems obstruct their extensive use in developing and underdeveloped countries [3].

To fulfil the above requirements, the magnesium diboride (MgB_2) magnet, which can be operated at around 20 K in an LHe-free manner, is considered as one of the best potential candidates for next-generation MRI application [4, 5]. It has been reported that the heat capacity of MgB_2 magnets can be significantly enhanced by cooling them using solid nitrogen (SN_2) with a cryocooler [6]. The high heat capacity of SN_2 is well known to enable a magnet to operate for a certain time period in the absence of a cooling source (i.e., cryocooler) [7], which is suitable for areas where power failure is common. Takahashi *et al* reported the first successful persistent-mode coil with joints between MgB_2 and NbTi wires [8]. Jiayin *et al* reported the operating results for MgB_2 persistent-mode coils in a helium environment [9]. Nardelli *et al* also reported on persistent-mode operation with a short MgB_2 tape

winding operating with conduction cooling [10]. Until now, however, there have been no reports on persistent-mode operation in an SN_2 cooled system with an MgB_2 coil.

In this study, the fabrication of an MgB_2 coil and its persistent-current switch (PCS), a newly developed SN_2 cooling system, and the operation of the coil in persistent-mode are presented in detail.

7.2. Experimental Details

Hyper Tech Research Inc. supplied monofilamentary carbon-doped MgB_2 wire (strand no. 3356) for the coil. The wire was 0.84 mm in diameter, constructed with an MgB_2 filament (diameter – 0.4 mm), a niobium inner barrier (thickness - 0.10 mm) and a Monel outer sheath (thickness - 0.12 mm). Figure 7-1(a) presents a digital photograph of the coil, which was fabricated via the wind and react method with a heat-treatment at 690 °C for 30 min in argon (Ar) atmosphere. The whole coil was assembled with the main MgB_2 coil at the bottom and the PCS at the top. The PCS was made by extending the two ends of the coil and joining them together. The diameter of the PCS was 113.5 mm with two non-inductively wound turns, and its estimated wire resistance ~7.1 mΩ m^{-1} at 40 K. The inner diameter and the height of the coil were 109 mm and 20 mm, respectively. The coil was wound in a single layer (22 turns) without any insulation. The calculated inductance of the coil was 86.7 ± 0.02 μH using equation (7.1) [11].

$$L \cong \mu_0 a_1 N^2 \left(\frac{\alpha+1}{2}\right)\left(\ln\left\{\left[\frac{2(\alpha+1)}{\beta}\right]\left[1+\frac{\beta^2}{2(1+\alpha^2)}\right]\right\}-\frac{1}{2}\left[1+\frac{\beta^2}{4(1+\alpha^2)}\right]\right) \quad (7.1)$$

where L is the inductance of the coil, μ_0 is the permeability of free space ($\mu_0 = 1.26$ x 10^{-6} H m^{-1}), a_1 is the inner radius of the coil, N is the number of turns, α is the ratio of outer radius to the inner radius of the coil, β is the ratio of half of the length of the coil to the inner radius.

The joining process developed at the University of Wollongong include [12]: (i) etching the Monel from the area of the wires to be joined, (ii) polishing the ends of the two wires until the MgB_2 core was exposed, (iii) aligning the two wires together using glue, (iv) mounting the two wires in a stainless steel (SS) enclosure using a high-temperature sealing material, (v) packing the Mg + 2B composite powder in the

SS enclosure in Ar atmosphere, (vi) pressing the powder using SS plug, and (vii) sealing the remaining gaps using a high-temperature sealing material.

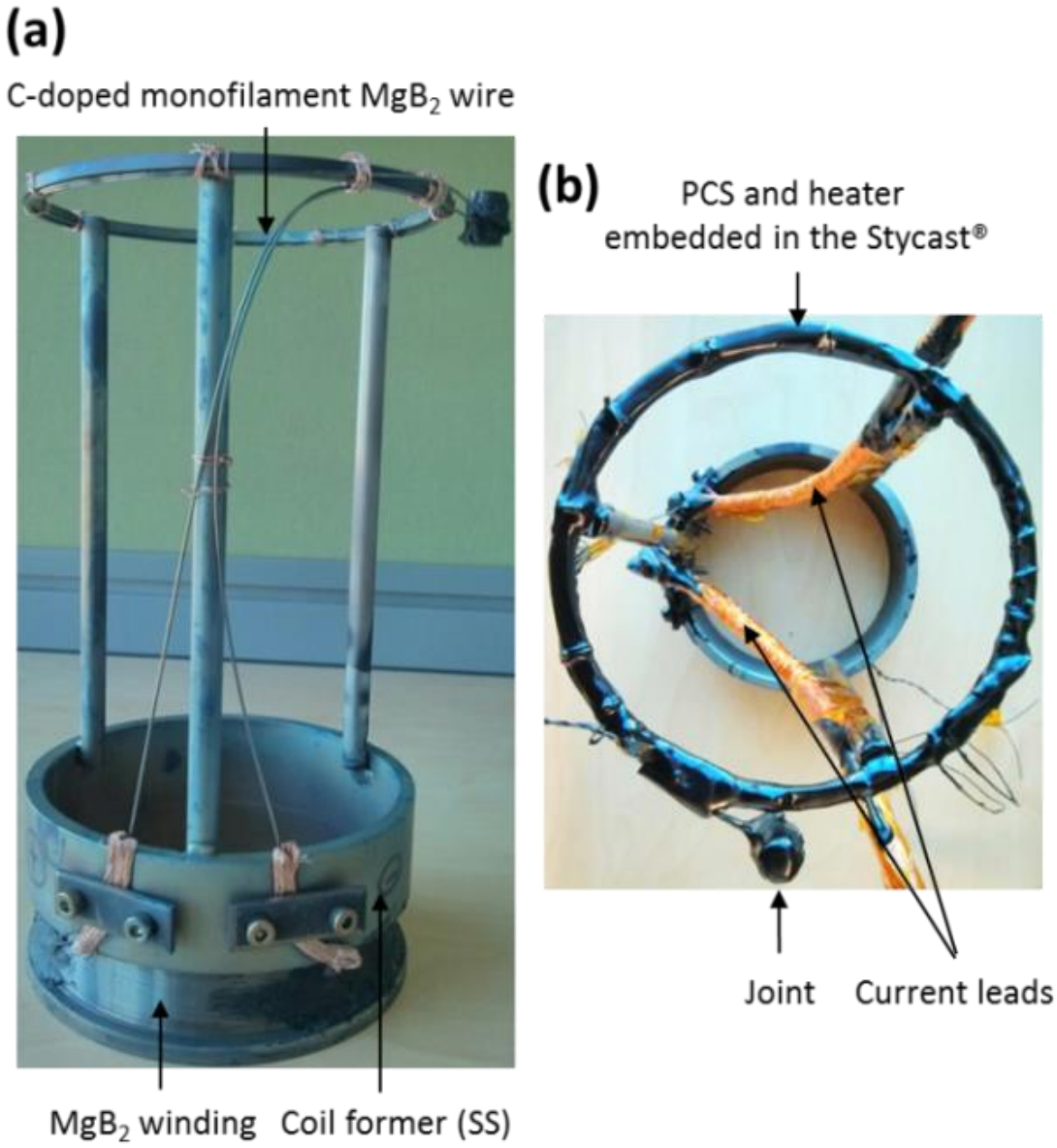

Figure 7-1. (a) Digital photograph of the fabricated coil after heat-treatment, (b) top view of the coil after applying Stycast® 2850 FT (Catalyst 9) epoxy.

To charge the current into the main coil, the PCS was needed to be heated up to a resistive state. This was achieved using a 47 Ω Nichrome heater (Lakeshore, 32 AWG) wound on the PCS. Copper (Cu) current leads were installed between the PCS and the coil. Three pairs of voltage taps were attached, one each from the coil, the PCS, and the joint, to monitor the voltage drops during charging of the coil. A top view of the coil after applying epoxy encapsulant Stycast® is shown in figure 7-1(b).

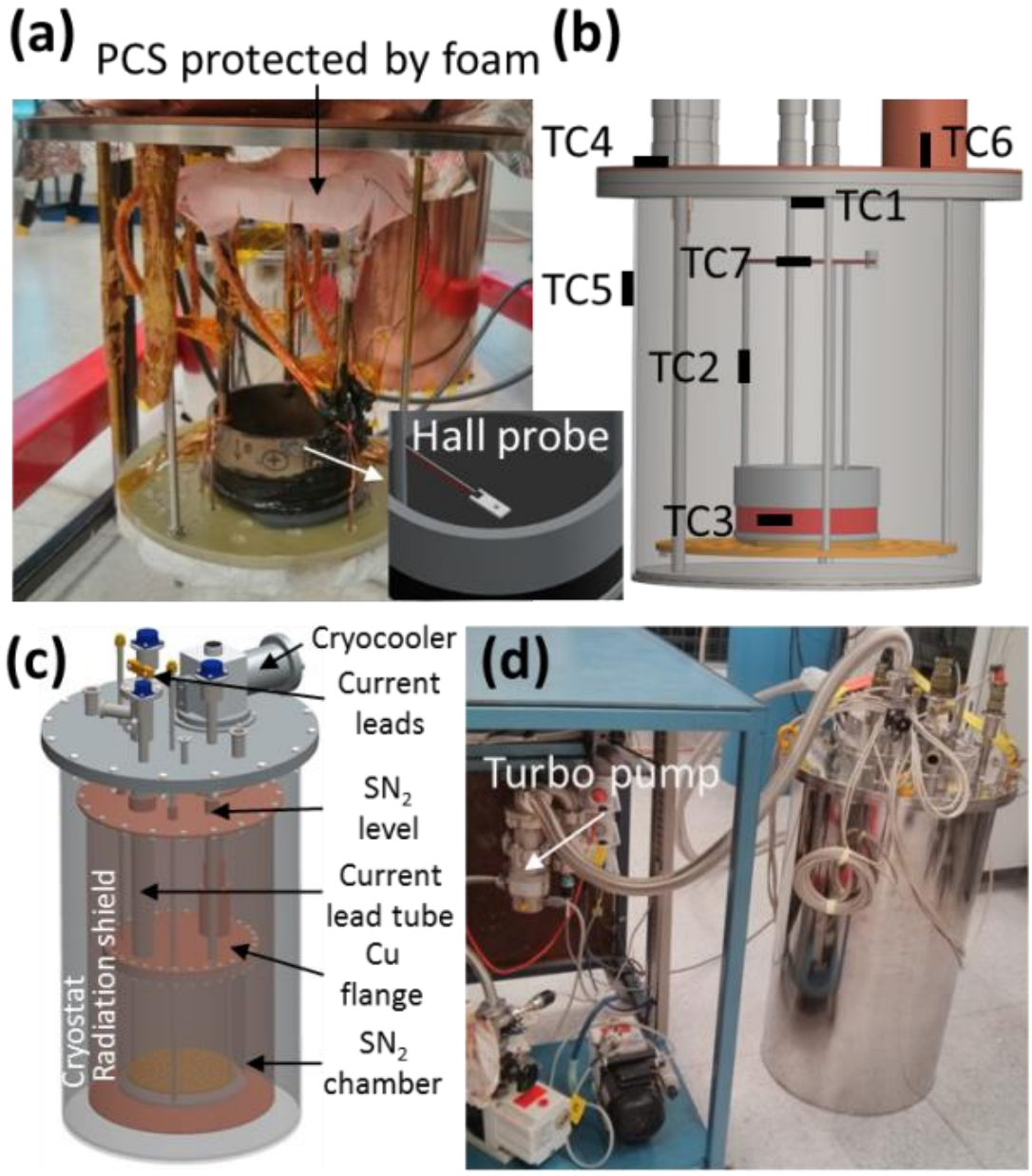

Figure 7-2. (a) Photograph of the installed coil in the SN_2 chamber, with a 3D model of the Hall probe location (the centre of the coil at z = 0) shown in the inset; (b) schematic diagram of the temperature sensor locations (TC1 – at the top of the SN_2 chamber (inside), TC2 – at the centre, between the coil and the PCS, TC3 – at the coil winding, TC4 – on top of the SN_2 chamber near the current lead tube, TC5 –100 mm below the top collar of the SN_2 chamber, TC – 6, at the bottom of the Cu bar below the cryocooler, TC7 – at the PCS); (c) 3D model of the SN_2 cooling system, and (d) photograph of the experimental set-up.

Figure 7-2(a) shows the coil installed in the SN_2 chamber. Prior to installing the whole coil in the SN_2 chamber, the PCS was covered with expanded polyethylene

(EPE) foam to enable easy temperature control under the SN_2 for charging the coil. A Hall probe with 0.1 G sensitivity was installed at the centre of the coil to detect the magnetic field (*B*) generated by the coil (figure 7-2(a) inset). Seven cryogenic temperature sensors were also installed to monitor the temperatures of the SN_2 chamber and the coil, as shown in figure 7-2(b). Figure 7-2(c) shows a three-dimensional (3D) model of the SN_2 cooling system. The Gifford-McMahon two-stage cryocooler (Sumitomo, RDK-408E2) was used in the cooling system featuring a 1^{st} stage cooling capacity of 40 W at 43 K and 2^{nd} stage of 1 W at 4.2 K. Figure 7-2(d) shows the assembled SN_2 cooling system.

7.3. Results and Discussion

To cool down the coil in SN_2, the system was first evacuated using a turbo vacuum pump (figure 7-2(d)). The SN_2 chamber was mechanically sealed using indium wire. A vacuum of $<2 \times 10^{-6}$ torr in the system was achieved, and then liquid nitrogen (LN_2) was introduced into the SN_2 chamber. When the temperature at TC6, as shown in figure 7-2(b), reached 280 K, the cryocooler was switched on. The purpose of the early switching on of the cryocooler was to avoid the rapid evaporation of LN_2. Once the SN_2 chamber was fully filled with LN_2, both the inlet and the outlet were closed, and a non-return valve was installed. The temperature of the radiation shield remained at 36 K throughout the experiment.

Figure 7-3 shows the temperature profiles of the SN_2 chamber during the system cool down. The total volume of SN_2 in the chamber was about 16 L. It took about 4.56 days to reach the minimum temperature of 7.2 K in the SN_2 chamber, whereas the temperature on the 2^{nd} stage of the cryocooler reached 4.85 K. Liquid to solid, and solid to solid phase transitions were observed at ~63 K, and ~35.6 K, respectively. The level of the SN_2 in the chamber reached up to the radiation shield flange (see figure 7-2(c)). Thus, additional heat conduction was taking place from the SN_2 in the current lead and the SN_2 in the tubes running into and out of the chamber. This might have prevented the SN_2 chamber from cooling down to the cryocooler 2^{nd} stage temperature. The temperature inside the SN_2 chamber remained uniform at around 7.4 K ± 0.2 K. However, the temperatures at the TC4 and TC5 locations were around 11.1 K and 10.2 K, respectively. This clearly indicates the high conductive

heat load from the current lead tube (with SN_2) to the SN_2 chamber. In fact, prior to fabricating this system, our finite element method (FEM) simulation predicted similar behaviour even without SN_2 in the current lead tube. The temperature gradient might be due to the lower thermal conductivity of the SS material of the SN_2 chamber. Owing to this, the cryocooler was unable to absorb heat from the far end of the SN_2 chamber. Thus, a 3 mm thick Cu flange was placed on the top of the SN_2 chamber (see figure 7-2(c)). As a result, the FEM simulation showed a negligible temperature gradient after installing the Cu flange on top of the SN_2 chamber.

However, during actual cool down, due to the high conductive heat load through the SN_2 in the current lead tube, the cryocooler (when at 4.85 K) was unable to absorb heat from the far end of the SN_2 chamber, which left a temperature gradient on top of the SN_2 chamber. On the other hand, when the temperature of the SN_2 chamber was controlled to around 18 K, the temperature gradient in the entire SN_2 chamber was reduced to ~1.75 K (not shown here), which indicates that the Cu flange facilitated better heat conduction to the cryocooler.

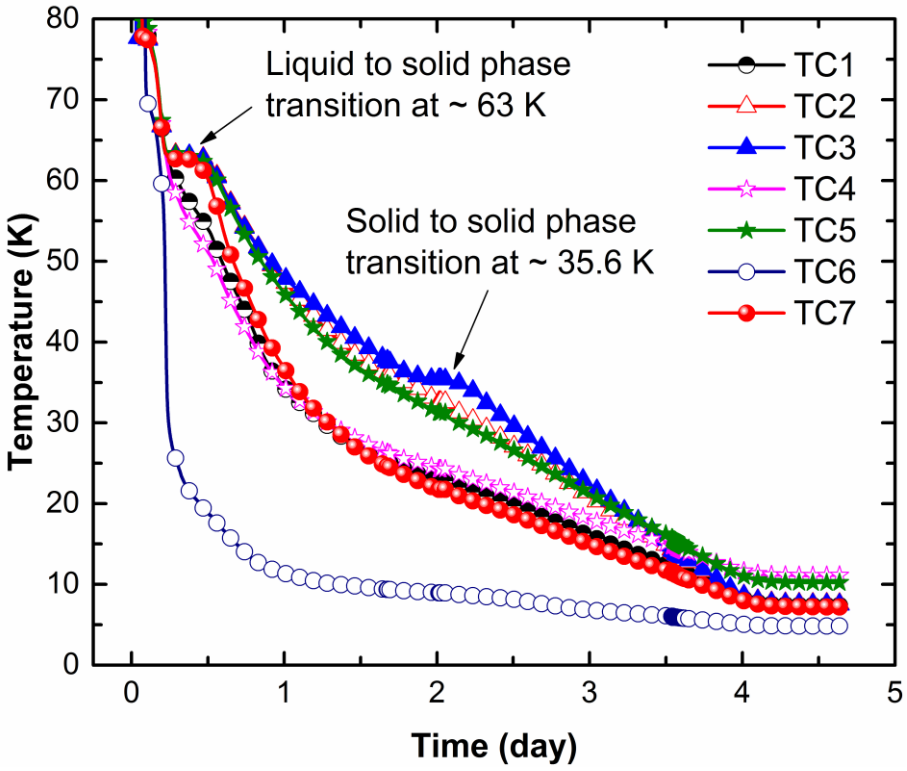

Figure 7-3. Temperature vs. time profiles during cool down of the SN_2 chamber.

7.3.1. PCS Testing

The on/off function of the PCS was evaluated at the PCS temperature of 11.3 K. As can be seen in figure 7-4(a), the PCS reached 45 K in 600 s. The heater power was 3 W. Once the PCS temperature climbed above 45 K, the coil was charged with a ramp rate of 0.1 A s^{-1} up to 10 A. As can be seen in figure 4-4(b), *B* at the centre of the coil was increasing linearly with the current. At 10 A, the *B* at the centre of the coil was 27 gauss (G), which matched the calculated value of 24.8 G. The variation in *B* might be due to misalignment of the Hall probe. During current charging, the inductive voltage was about 8.17 ± 0.12 μV, which is comparable to the 81.7 ± 1.2 μH inductance of the coil. This value is well matched with the calculated inductance of 86.7 ± 0.02 μH. After reaching 10 A, the PCS heater was switched off. It took about 1480 s to cool down the PCS. The reasons for the longer PCS cool down time might be due to over-protection of the PCS, contact between the SN_2 and the PCS (solid phase transition can be seen in figure 7-4(a)), and lower thermal conduction through the SS bars (see figure 7-1) from the surroundings to cool the PCS back down to the initial temperature.

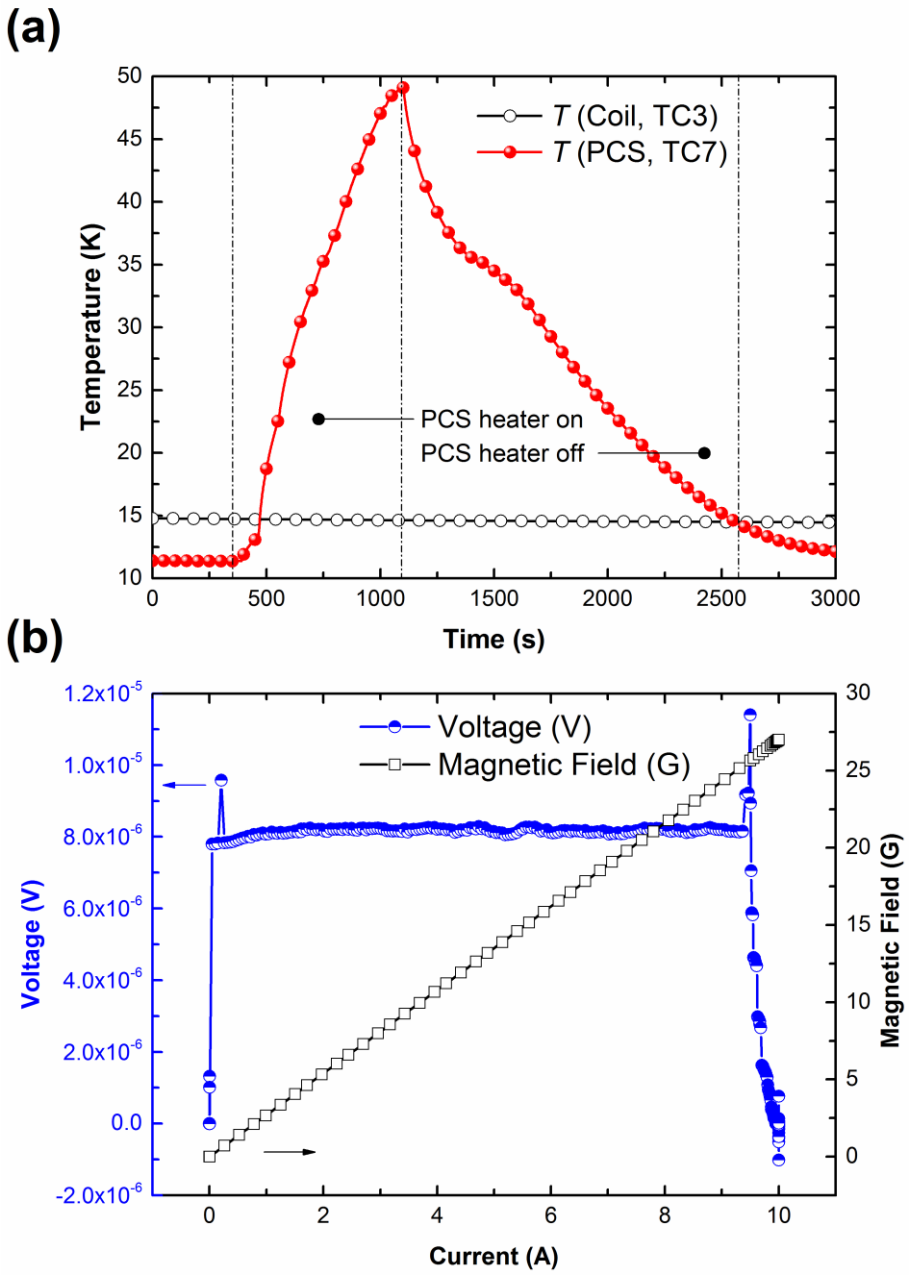

Figure 7-4. (a) Temperature vs. time profile during open/closed operation of PCS, TC3 – at the coil winding, TC7 – at the PCS, and (b) voltage and magnetic field vs. current profiles while charging the coil when the PCS was open.

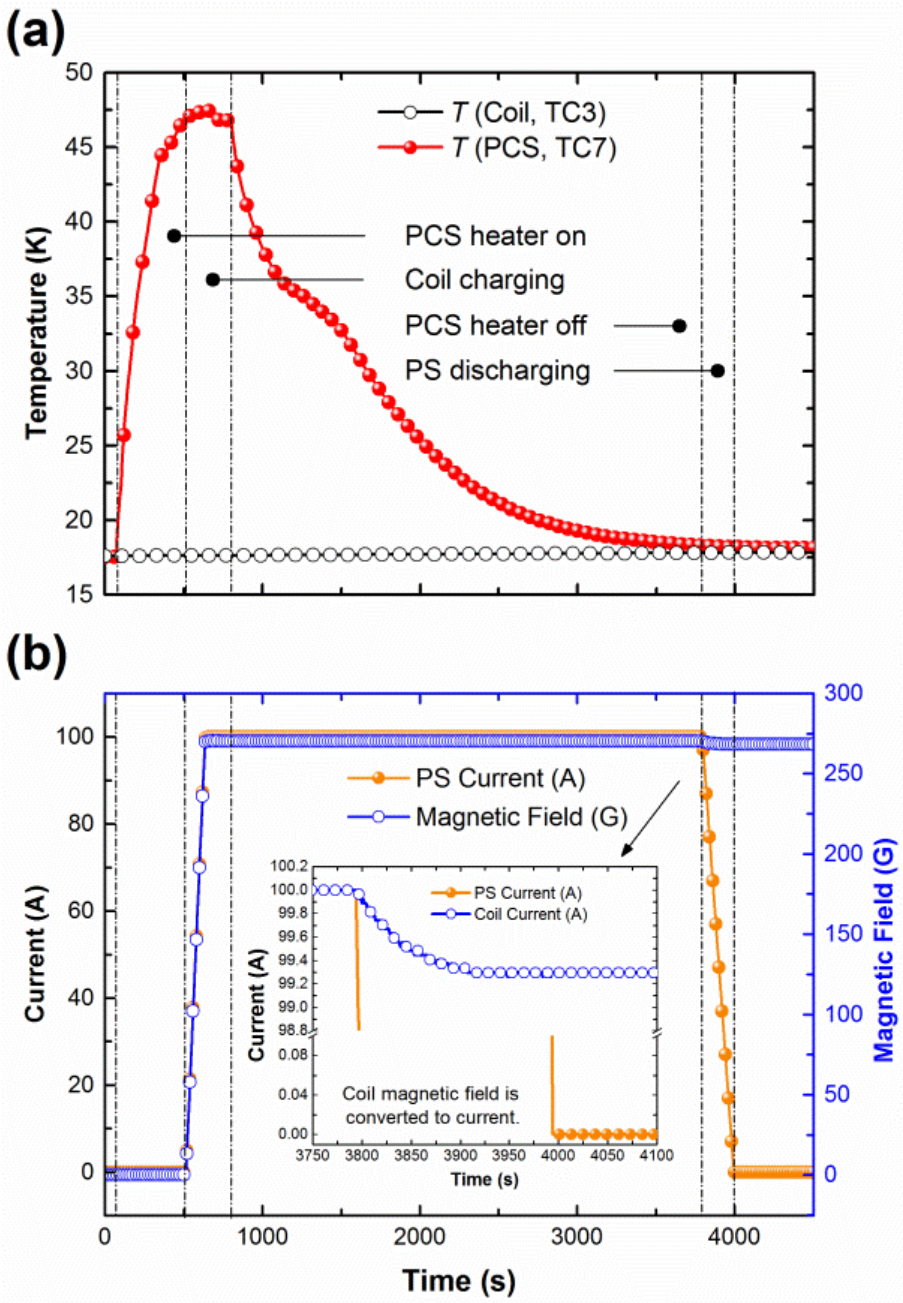

Figure 7-5. Measurements when the coil was put into persistent-mode at 100 A: (a) temperature vs. time (Coil and PCS) profiles, TC3 – at the coil winding, TC7 – at the PCS, (b) current and magnetic field vs. time profiles (inset: magnified plot of the current vs. time plot while discharging the PS (coil magnetic field was converted to current)).

7.3.2. Persistent-Mode Coil Testing at 100 A

The temperature of the coil and the PCS was fixed at around 18 K prior to charging the coil. As can be seen in figure 7-5(a), firstly, the temperature of the PCS was increased above 45 K, and the coil was charged to 100 A with a ramp rate of 0.5

A s^{-1} (figure 7-5(b)). As can be seen in figure 7-5(b), we waited for about 140 s and confirmed the coil constant prior to switching off the PCS heater. It took about 3000 s to cool down the PCS. The enthalpy of the material increases at high-temperature [11], thus the PCS cooling time was longer at 18 K compare to PCS cooling time at 11.3 K during PCS testing at 10 A. Then, the power supply (PS) was discharged with a ramp-down rate of 0.5 A s^{-1}. To check the initial decay generated by the coil while discharging the PS current, the *B* in the coil was converted to current using the coil constant. The inset in figure 7-5(b) shows the magnified profiles of the current vs. time while discharging the PS. Herein, the coil current initially decayed by about 0.7 A, and then remained stable at 99.3 A. Decay in the current showed exponential behaviour. The initial decay might be due to the phenomenon of 'settling' of current in the closed superconducting circuit [13].

As a result, the coil was kept in the persistent-current mode for about 4.75 days. Figure 7-6(a) and (b) shows the *B* and temperature profiles in the coil for the entire persistent-mode duration. In figure 7-6(a), *B* was observed to remain around 268.4 G with ± 0.1 G fluctuation, but without any noticeable decay within the resolution limit of a gauss meter. This fluctuation might be due to the data acquisition instrument. During persistent-mode operation, the joint experienced only self-field with very small influence (2.5 G) from the main coil. The temperature of the coil and the PCS was then increased up to 21 K and 20.6 K, respectively (figure 7-6(b)). If we consider 0.1 G (resolution limit) decay of *B* in the coil in 4.75 days, the calculated total circuit resistance would be $<7.4 \times 10^{-14}$ Ω at 19.5 K ± 1.5 K. The *B* line calculated from the *RL* circuit time constant corresponding to the minimum measurable resistance of 7.4×10^{-14} Ω over the 4.75 days is also included in figure 7-6(a). We further need to consider the effect of *n*-value, indicating a joint quality. It has been reported that the circuit resistance strongly depends on the *n*-value and joint resistance [11]. Especially, low *n*-values make the persistent-mode impossible [14]. Later, the PCS was charged to 200 A without any quench at 20 K. During the attempt to charge the coil to 200 A, a quench occurred when the charging current was 183 A, which damaged the coil. This incident prevented us from carrying out any further experiments. Moreover, in a future test, we will implement quench protection

system in the experiment to avoid damage to the coil while charging at the higher current.

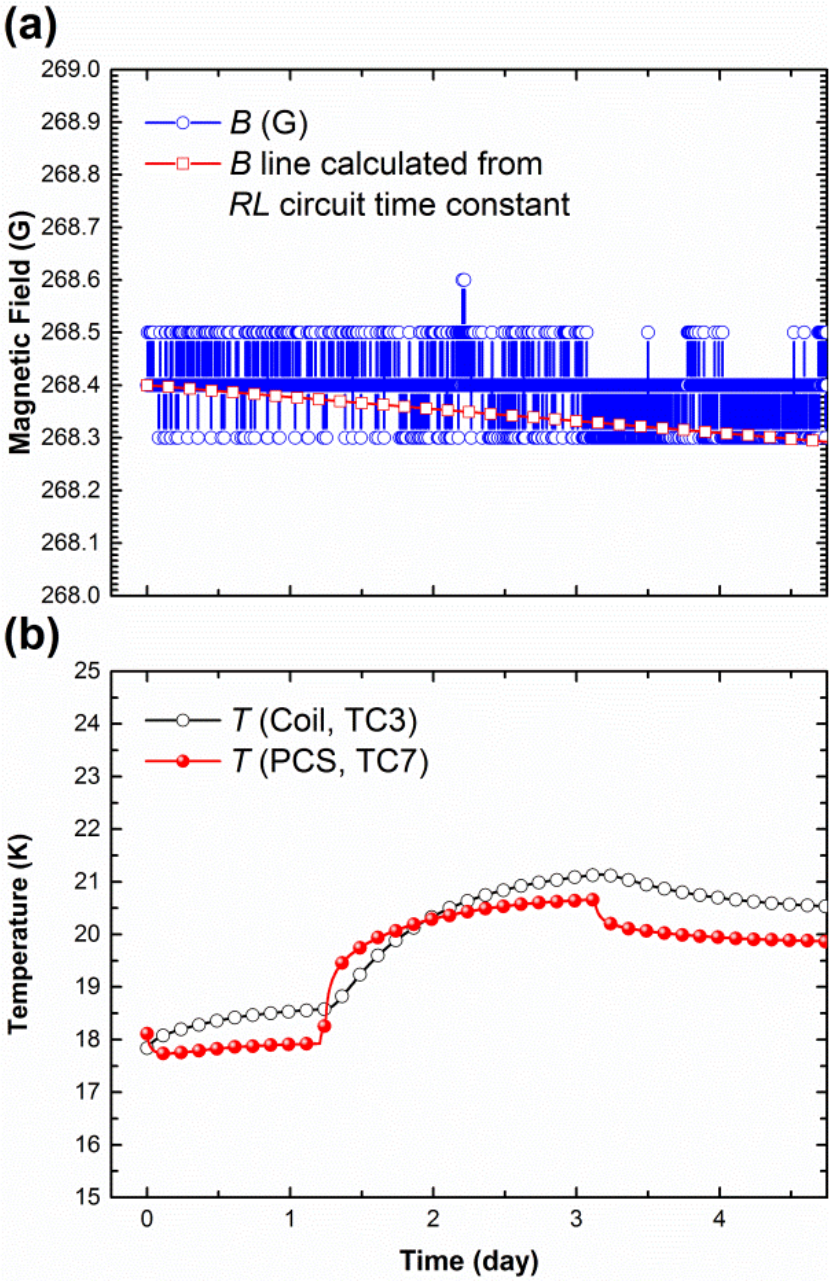

Figure 7-6. Measurements after putting the coil into persistent-mode: (a) magnetic field vs. time profile of the coil including *B* line calculated from *RL* circuit time constant, and (b) temperature vs. time (Coil and PCS, TC3 – at the coil winding, TC7 – at the PCS).

7.4. Conclusions

The MgB_2 coil and the PCS were successfully fabricated through a superconducting-joint technique, and the persistent-current mode of the system was

evaluated with SN_2 cooling and a 100 A operating current. The total circuit resistance was estimated to be $<7.4 \times 10^{-14}$ Ω at 19.5 K ± 1.5 K, in the coil during reasonably long-term persistent-mode operation for 4.75 days. This performance is comparable to the technical requirement for practical MRI application. This joining technique will be further optimized for multifilament MgB_2 conductors in the near future.

7.5. References

[1] Cosmus T C and Parizh M 2011 Advances in whole-body MRI magnets *IEEE Trans. Appl. Supercond.* **21** 2104-9

[2] Lvovsky Y, Stautner E W and Zhang T 2013 Novel technologies and configurations of superconducting magnets for MRI *Supercond. Sci. Technol.* **26** 093001

[3] Kara D C 2013 Production of a viable product in magnetic resonance imaging using MgB_2. (Master's Thesis, Case Western Reserve University)

[4] Modica M, Angius S, Bertora L, Damiani D, Marabotto M, Nardelli D, Perrella M, Razeti M and Tassisto M 2007 Design, construction and tests of MgB_2 coils for the development of a cryogen free magnet *IEEE Trans. Appl. Supercond.* **17** 2196-9

[5] Mine S, Song H, Xu M, Marte J, Buresh S, Stautner W, Immer C, Laskaris E T and Amm K 2012 Test coil for the development of a compact 3 T MgB_2 magnet *IEE Trans. Appl. Supercond.* **22** 4

[6] Bascuñán J, Lee H, Bobrov E S, Hahn S, Iwasa Y, Tomsic M and Rindfleisch M 2006 A 0.6 T/650 mm RT bore solid nitrogen cooled MgB_2 demonstration coil for MRI - A status report *IEEE Trans. Appl. Supercond.* **16** 1427-30

[7] Yao W, Bascuñán J, Kim W S, Hahn S, Lee H and Iwasa Y 2008 A solid nitrogen cooled MgB_2 "demonstration" coil for MRI applications *IEEE Trans. Appl. Supercond.* **18** 912-5

[8] Takahashi M, Tanaka K, Okada M, Kitaguchi H and Kumakura H 2005 Relaxation of a trapped magnetic field in a 100 m long class MgB2 solenoid coil in persistent current mode operation *Supercond. Sci. Technol.* **18** S373-S5

[9] Jiayin L, Voccio J P, Seungyong H, Youngjae K, Jungbin S, Juan B and Iwasa Y 2015 Construction and persistent-mode operation of MgB_2 coils in the range 10-15 K for a 0.5-T/240-mm cold bore MRI magnet *IEEE Trans. Appl. Supercond.* **25** 1-5

[10] Nardelli D, Angius S, Capelluto A, Damiani D, Marabotto R, Modica M, Perrella M and Tassisto M 2010 Persistent mode MgB_2 short windings *IEEE Trans. Appl. Supercond.* **20** 1998-2001

[11] Iwasa Y 2009 *Case studies in superconducting magnets, design and operation issues* (New York: Springer)

[12] Patel D, Hossain M S A, See K W, Xu X, Barua S, Ma Z, Choi S, Tomsic M and Kim J H 2015 MgB_2 superconducting joints for persistent current operation *Supercond. Sci. Technol.* **28** 065017

[13] Brittles G D, Mousavi T, Grovenor C R M, Aksoy C and Speller S C 2015 Persistent current joints between technological superconductors *Supercond. Sci. Technol.* **28** 093001

[14] Patel D, Hossain M S A, Motaman A, Barua S, Shahabuddin M and Kim J H 2014 Rational design of MgB_2 conductors toward practical applications *Cryogenics* **63** 160-5

7.6. Note: Chapter Publication and Text Usage Detail

This Chapter has been published in Superconductor Science and Technology as a Fast Track Communication, Letter (see below reference). The written text in this Chapter has been taken from my published paper, as shown below.

[1] **Patel D**, Md Shahriar Al H, Khay Wai S, Qiu W, Kobayashi H, Zongqing M, Seong Jun K, Hong J, Jin Yong P, Choi S, Maeda M, Shahabuddin M, Rindfleisch M, Tomsic M, Dou S X and Kim J H 2016 Evaluation of persistent-mode operation in a superconducting MgB_2 coil in solid nitrogen *Supercond. Sci. Technol.* **29** 4LT02-9

Chapter 8

8. MgB_2 Solenoid Coil in Solid Nitrogen

8.1. Introduction

Magnetic resonance imaging (MRI) is a non-invasive diagnostic technique that allows doctors to take lifesaving decisions in several health conditions. To produce an image of a body part in MRI, the combination of a strong magnetic field and radio waves are used. In most of the current MRI systems for producing a strong magnetic field, niobium titanium (NbTi) based superconducting magnets are used [1, 2]. NbTi based magnets, however, are cooled at 4.2 K using expensive liquid helium (LHe) bath [3]. The continuously increasing price of LHe and possible shortages in the future has increased the demand for MRI magnets that are LHe-free [1, 3]. Magnesium diboride (MgB_2) has strong potential among the various available commercial superconductors for application in the LHe-free MRI magnets [4-18]. The transition temperature (T_c) of 39 K for MgB_2 offers high-temperature operation up to 30 K, eliminating the use of LHe [19-21].

In particular, for enabling MgB_2 based MRI magnets to operate in an LHe-free manner, inexpensive and lightweight solid nitrogen (SN_2) is a promising choice due to its higher heat capacity with a cryocooler [18, 22-26]. Yao *et al* reported test results on MgB_2 solenoid coils utilizing SN_2 as a cryogen for the first time [18]. Their assembled magnet was prematurely quenched, however, at currents ranging from 79 A to 88 A, even though an individual coil could carry a 100 A current. Most recently, for the very first time, this thesis work reported the operation of an MgB_2 conductor based persistent magnet in SN_2 that was carrying 100 A supercurrent at ~20 K for 4.75 days [27]. This work was done with the aim of MRI application. So far, however, the demonstration of SN_2-cooled MgB_2-based solenoid coils for MRI application is limited to below 100 A around 20 K [18, 27].

In this study, therefore, the design, fabrication, and testing of an MgB_2 solenoid coil carrying 200 A current at 28 K in an SN_2 environment are presented in detail.

8.2. Experimental Details

Figure 8-1(a), (b), and (c) show a 3D model of the SN_2 cooling system, the SN_2 chamber, and the MgB_2 solenoid coil, respectively. The details of the SN_2 cooling system are presented in Chapter 4.

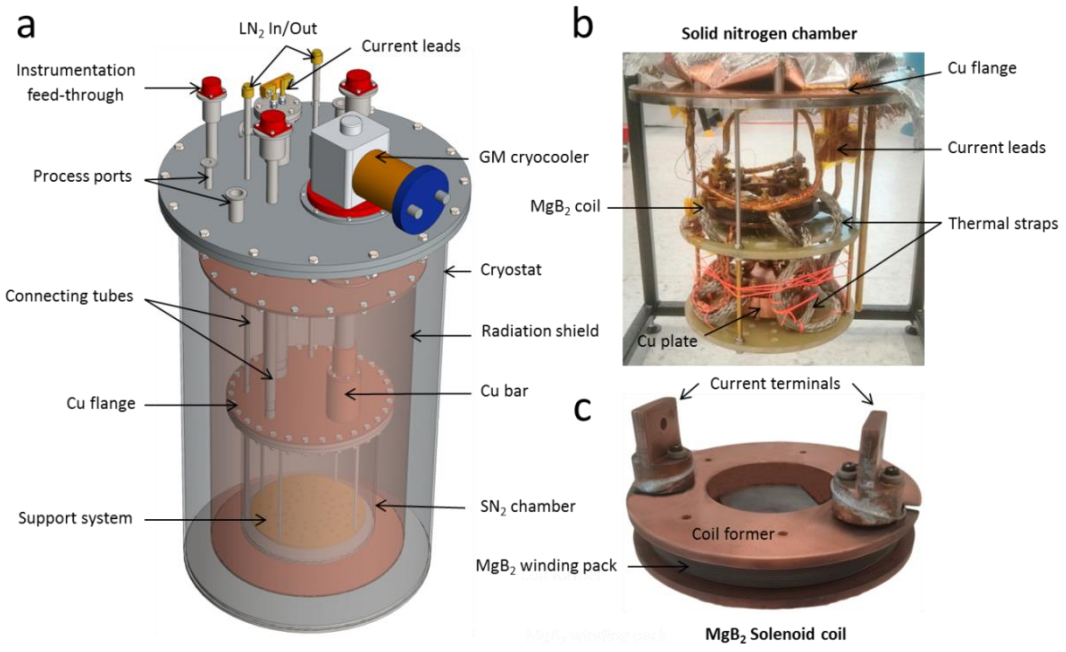

Figure 8-1. (a) 3D model of the SN_2 cooling system, (b) SN_2 chamber, and (c) digital image of the MgB_2 solenoid coil.

$$B_0 = J \cdot a \cdot F(\alpha\beta) \tag{8.1}$$

$$J = \frac{N.I}{(b-a)\cdot l} \tag{8.2}$$

$$F(\alpha\beta) = \mu_0 \cdot \beta \cdot ln\left\{\frac{\alpha + (\alpha^2+\beta^2)^{\frac{1}{2}}}{1+(1+\beta^2)^{\frac{1}{2}}}\right\} \tag{8.3}$$

where B_0 is the magnetic field at the coil centre ($i.e.,\ z = 0$), J is the average overall current density, a is the inner radius of the coil, b is the outer radius of the coil, l is the half length of the coil, N is the total number of turns, I is the current in the coil, μ_0 is the permeability of free space ($\mu_0 = 1.26 \times 10^{-6}$ H m^{-1}), $\alpha = b/a$, $\beta = l/a$.

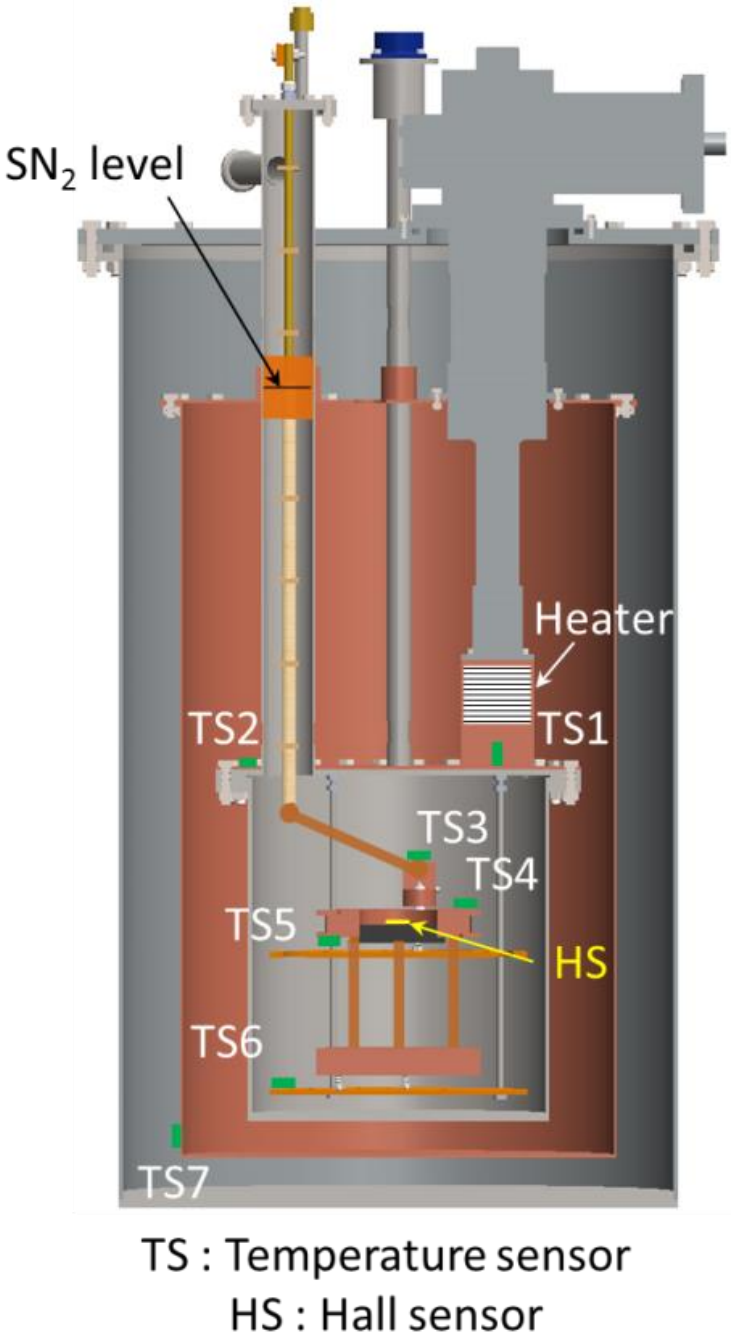

Figure 8-2. Cross-sectional view of the SN_2 cooling system, including a schematic illustration of the temperature sensors, Hall sensor, and heater. The level of SN_2 was as high as the radiation shield flange, as shown in the figure.

The MgB_2 solenoid coil was fabricated using the 'wind and react' method. The coil was installed in the SN_2 chamber, as shown in figure 8-1(b). Copper (Cu) thermal straps were used to minimize the temperature gradient across the coil while it is cooled down from 300 K to 77 K. The specifications of the MgB_2 solenoid coil are

presented in table 8-1. The heat-treatment of the coil was carried out in argon inert atmosphere at 675 °C for 60 min. The inductance of the coil was calculated using finite element (FE) simulation, as well as using induced inductive voltage while charging the coil. The field constant of the solenoid was calculated using FE simulation and verified by the standard solenoid magnetic field formula (using equations (8.1) to (8.3)) [28]. The critical current (I_c) of the coil was evaluated using the 1 μV cm^{-1} criterion. The distance between voltage taps was 9.4 m. The critical temperature (T_c) of the coil was measured by passing 10 mA constant current from 37.6 K until the superconducting transition occurred. The *n*-value of the coil was calculated from the voltage vs. current curve of the coil in the voltage range of 0.1 - 1 $\mu V.cm^{-1}$.

Table 8-1. The specifications of the MgB_2 solenoid coil.

Parameters	**Specifications**
Coil type	Solenoid
Winding method	Wind and react
Strand (HTR S1506)	MgB_2/Nb/Cu/Monel Nb : barrier, Cu : matrix, Monel : sheath
Filament count	36 + 1 (Cu at centre)
Insulation	S-glass
Wire diameter with insulation (mm)	1.3
Wire diameter without insulation (mm)	1.1
SC fill factor of the wire (%)	11.1
Coil I.D./O.D./height (mm)	130/135.2/15
Turns per layer	23 (1^{st} : 11, 2^{nd} : 12)
Total layers	2
Coil filling factor (%)	56
Impregnation	No
Inductance, L (μH)	123 (calculated from FE simulation) 128 (calculated from inductive voltages)
Field constant at z = 0 ($G.A^{-1}$)	2.19 (calculated from FE simulation) 2.22 (measured using Hall sensor)

As shown in figure 8-2, seven cryogenic carbon ceramic (CCS) temperature sensors were used to monitor the temperature of the system together with that of the coil [29-32]. A 50 Ω Nichrome (100 AWG) heater was installed on the Cu bar below the 2^{nd} stage of the cryocooler to control the temperature [33]. The heater was controlled using a Cryocon 32B [34]. At the center of the coil, a Hall sensor (0.1 G sensitivity) was installed to measure the coil magnetic field. Flexible copper leads were used to connect the coil current terminals to the current leads.

8.3. Results and Discussion

For cooling down, the required vacuum was created surrounding the SN_2 chamber and the radiation shield. LN_2 was transferred into the SN_2 chamber until a uniform temperature of 77 K reached in SN_2 chamber, and then, the cryocooler was switched ON. Several times, LN_2 was poured into the SN_2 chamber was completely filled with LN_2. Vacuum pumping was not used for forming SN_2 [35].

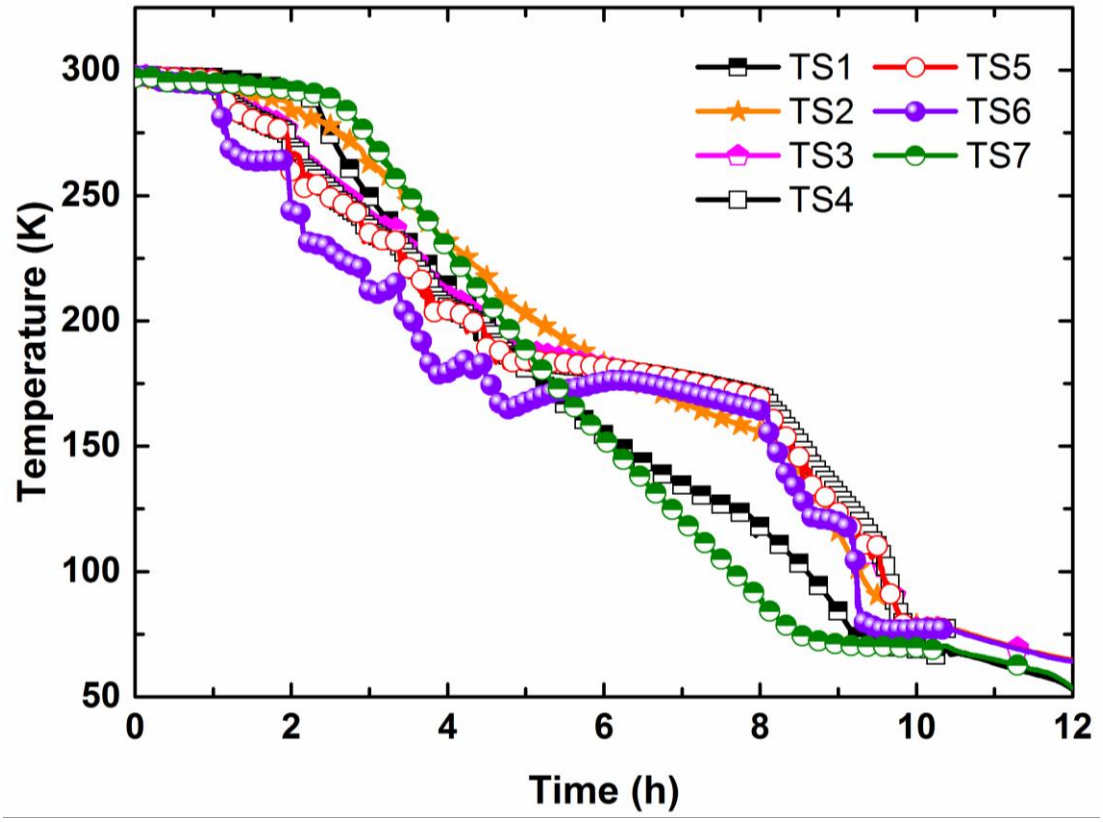

Figure 8-3. Temperature vs. time curves of the cooling system from 300 K to LN_2 temperature. Temperature sensor locations: TS1 (on the Cu bar below the 2nd stage of the cryocooler), TS2 (on the Cu plate of the SN_2 chamber near the current lead tube), TS3 (on the negative current lead termination of the coil), TS4 (on top of the coil), TS5 (on the bottom of the coil), TS6 (on the G10 support plate), TS7 (on the radiation shield bottom, diagonally opposite to the cryocooler 1st stage connection).

Figure 8-3 shows temperature vs. time curves of the cooling system from 300 K to LN_2 temperature. The LN_2 transfer was intentionally interrupted several times to keep temperature gradient at a minimum across the coil. Nevertheless, a temperature gradient of up to 11 K was observed between the coil former and the current

terminals. The temperature gradient was observed because of the air gap between the coil former and the current terminals (see figure 8-1(c)). The air gap was left because it was assumed that the cold gas would cool the coil terminals uniformly with the coil former. If we had used some conductive material such as Cu in-between them, the temperature gradient might be eliminated. Thus, in the future, we will use insulated copper between them to minimize the temperature gradient.

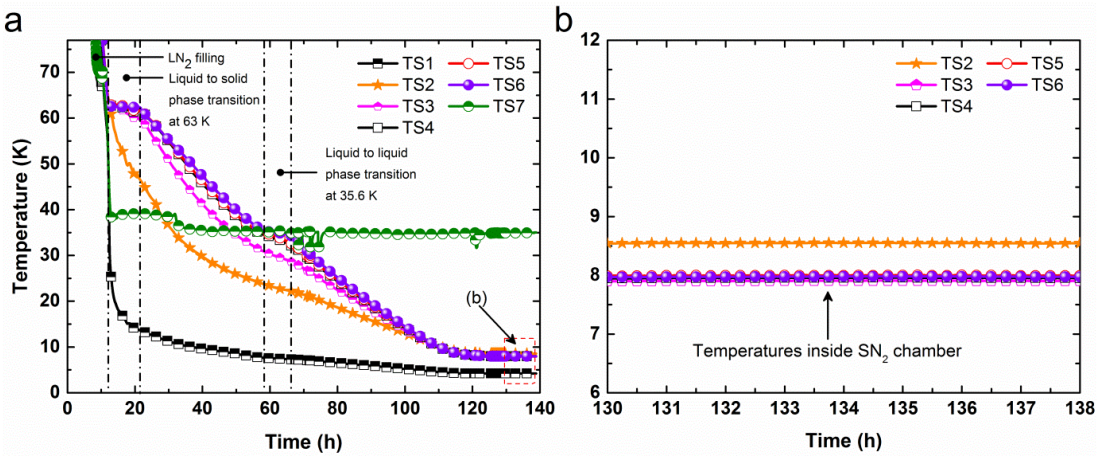

Figure 8-4. Temperature vs. time curves of the cooling system (a) from 77 K, and (b) after 130 h of cool down.

Figure 8-4 shows the cool down curves of the SN_2 cooling system from 77 K. As can be seen in figure 8-4(a), in about 130 h, the SN_2 chamber (16 L SN_2 and 9 kg Cu) was cooled down to a uniform 8 K (see figure 8-4(b)). It was observed that the SN_2 level reached as high as the top flange of the radiation shield inside the SN_2 chamber (see figure 8-2). Thus, the SN_2 itself was delivering additional conductive heat load from the radiation shield to the SN_2 cooling chamber. This prevented the SN_2 chamber from reaching a lower temperature. As can be seen in figure 8-4(a), a two-phase transition was observed at 63 K (liquid to solid for ~9.8 h), and at 35.6 K (solid to solid for ~7.9 h), respectively [36]. Overall, the cool down was smooth. The radiation shield remained at around 36 K throughout the experiment. The decreasing trend in the temperatures of TS4 (coil top) and TS5 (coil bottom) inside the SN_2 chamber was uniform. The small temperature gradient was observed, however, between TS3 (current termination) and TS4 (coil top). As mentioned earlier, this temperature gradient might exist because the cooling between the current

terminations and the coil top was taking place via SN_2 only (see figure 8-1(c)). As mentioned earlier, in the future, we will use insulated copper between them to minimize the temperature gradient. Eventually, at the end of the 130 h, the temperature in the entire SN_2 chamber was ~8 K, as shown in figure 8-4(b). These results show that the Cu plate (for details see Chapter 4) on the SN_2 chamber worked quite well, and it significantly improved the temperature uniformity of the entire SN_2 chamber. Nevertheless, the TS2 (on Cu the flange near current lead tube (see figure 8-2)) temperature was 0.5 K higher than the SN_2 chamber temperature. As mentioned earlier, the SN_2 inside the current lead tube was delivering an additional conductive heat load to the SN_2 chamber, and TS2 was installed right next to the current lead tube, so TS2 was showing a slightly higher temperature.

Figure 8-5(a) shows the resistance vs. temperature curve of the coil at 10 mA constant current. As can be seen in figure 8-5(a), the superconducting transition started at 36.25 K and finished at 35 K. Below 35 K, the coil resistance was below a measurable level. The measured T_c of the coil was 1 K higher than in the previously reported results of the coil, which used a similar type of MgB_2 wire [37]. To measure the field constant of the coil, firstly, the coil was energized up to 10 A current at 31.5 K. The measured and calculated field constant of the solenoid coil was 2.22 G A^{-1}, and 2.19 G A^{-1}, respectively [28]. This indicates that the fabricated coil was wound uniformly. The slight variation in the field constant, however, might be due to the alignment error of the Hall sensor.

Figure 8-6 shows the critical current (I_c) measurement results for the coil at 31.5 K. Figure 8-6(a) shows the voltage vs. current curve of the coil. The I_c of the coil was measured to be 79 A using the 1 μV cm^{-1} criterion. The superconducting to normal transition appeared smooth. The *n*-value, which indicates the quality of a superconducting material, was calculated to be 26 [27, 31, 38]. The n-value is strongly dependent on the microstructural uniformity of a superconductor [38]. The *n*-value of the MgB_2 conductor should be greater than 50 at any given temperature and magnetic field for better suitability of that conductor for persistent-mode magnet application in MRI [26]. Figure 8-6(b) shows the current, temperature vs. time curves of the I_c measurement at 31.5 K. As can be seen in figure 8-6(b), during superconducting to normal transition, the temperature on the coil increased by only

~0.5 K. This indicates that in the SN_2 environment, the thermal stability of the coil was improved.

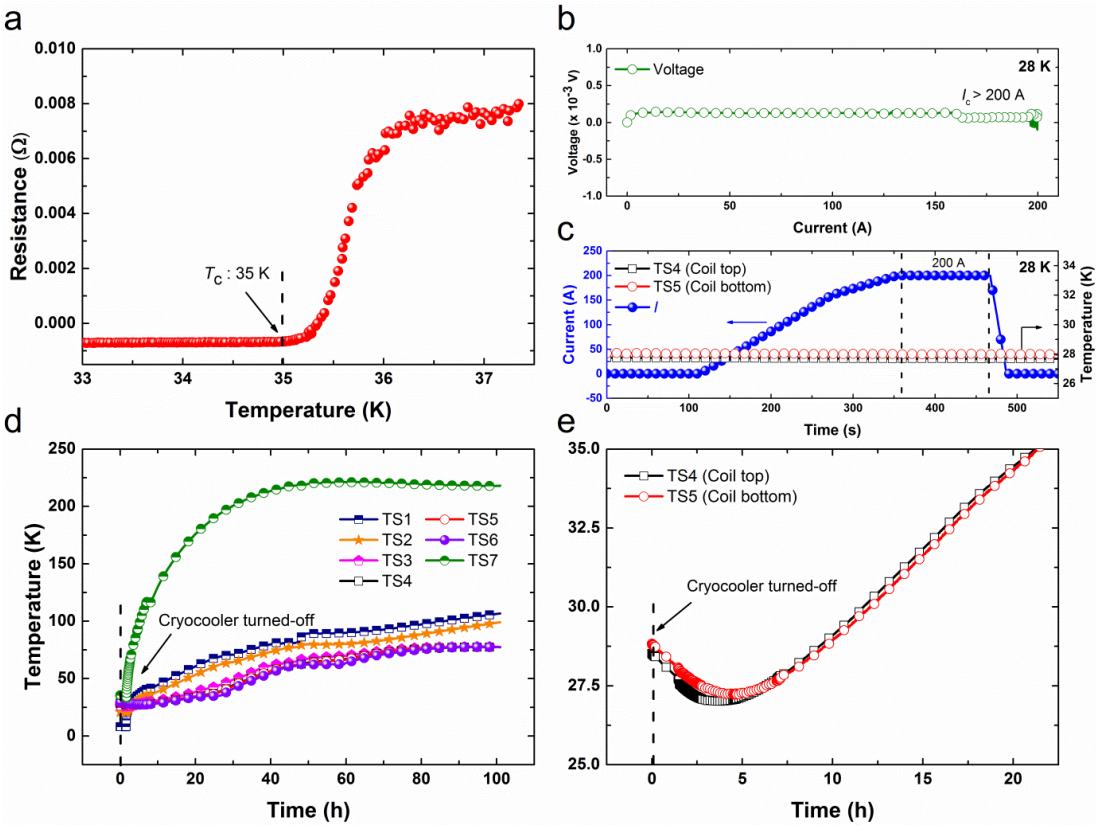

Figure 8-5. (a) Resistance vs. temperature curve, (b) voltage vs. current curve (at 28 K), (c) current, temperature vs. time curves (at 28 K) of the MgB_2 solenoid coil, (d) temperature vs. time curves of the cooling system, and (e) temperature vs. time curves of the temperatures on the coil after turning-off the cryocooler at ~28 K temperature.

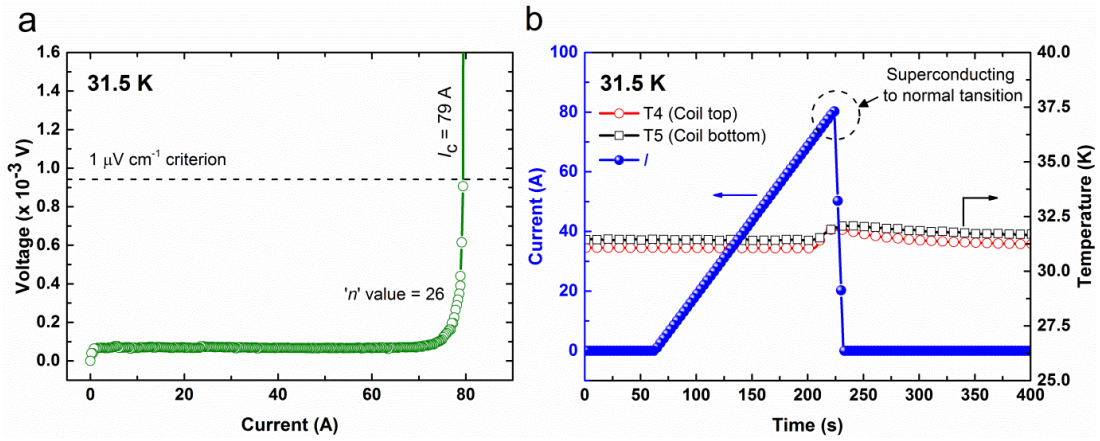

Figure 8-6. (a) Voltage vs. current, (b) current, temperature vs. time curves of the coil at 31.5 K.

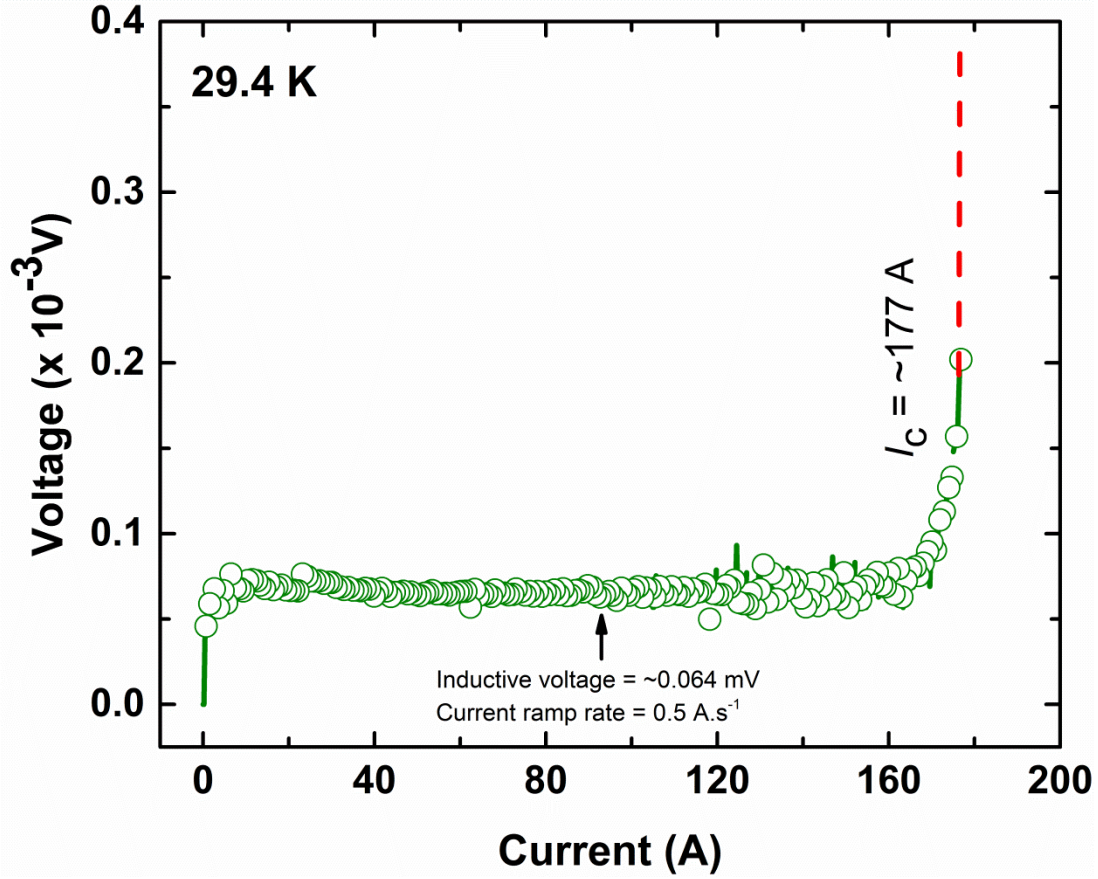

Figure 8-7. Voltage vs. current curve of the coil at 29.4 K.

At 29.4 K, again, the I_c of the coil was measured (see figure 8-7). The current was not passed until a full transition occurred as per the 1 μV cm^{-1} criterions to avoid unforeseen damage to the coil due to the transient resistive heating. As mentioned earlier, SN_2 has high heat capacity to provide thermal stability to the magnet, but on the other hand, it has very poor thermal diffusivity in the event of transient heating above 10 K (see section 2.3.4.3 of Literature Review) [26]. This means that due to the poor diffusivity of SN_2, the hot-spot temperature of the magnet can be rapidly increased [28]. This can lead to magnet damage. Therefore, SN_2 is more suitable in a magnet system where heat dissipation is slow, such a persistent magnet for MRI. As shown in figure 8-7, as soon as the transition was observed, the current was decreased from 177 A. This indicates that the coil had I_c of ~177 A at 29.4 K. Moreover, during coil charging at 0.5 A s^{-1}, ~0.064 mV inductive voltage was observed. This voltage indicates that the coil has an inductance of 128 μH, which matches the FE simulated inductance of the coil as shown in table 8-1.

Figure 8-5(b) and (c) show the I_c measurement results on the coil at 28 K. Up to 160 A, current was ramped at 1 A s^{-1}, and then at 0.5 A s^{-1} to 200 A. Figure 8-5(b) shows the voltage vs. current curve of the coil. As shown in the figure, the coil I_c was greater than 200 A at 28 K. Figure 8-5(c) shows the current, temperature vs. time curves of the coil. As shown in the figure, 200 A constant current was maintained for 113 seconds prior to discharge. During the entire charging and discharging cycle, the coil temperatures remained constant. These results show that the MgB_2 coil stability was greatly enhanced in the SN_2 environment. This work was the first to show such stable high current operation for any MgB_2 coil in an SN_2 environment above 25 K [18, 27], which is very promising for the advanced technology needed to develop low-cost MRI [39].

Following the 28 K measurement, the coil was allowed to cool down to the minimum achievable temperature. During cool down, the coil was charged with the full 200 A current several times to see any effects of SN_2 contraction on the coil performance [26], and no performance variation was observed. It is worth noting that the coil was not impregnated to avoid conductor movement during coil charging. The SN_2 acts quite well in place of epoxy and provides very good mechanical and thermal stability to the coil. After cooling down to 8 K, the coil temperature was maintained at 28 K, and again, the coil was able to carry the 200 A current without any performance degradation during the thermal cycle. In the end, at ~28 K coil temperature, the cryocooler was turned off to see the warm up characteristics of the coil.

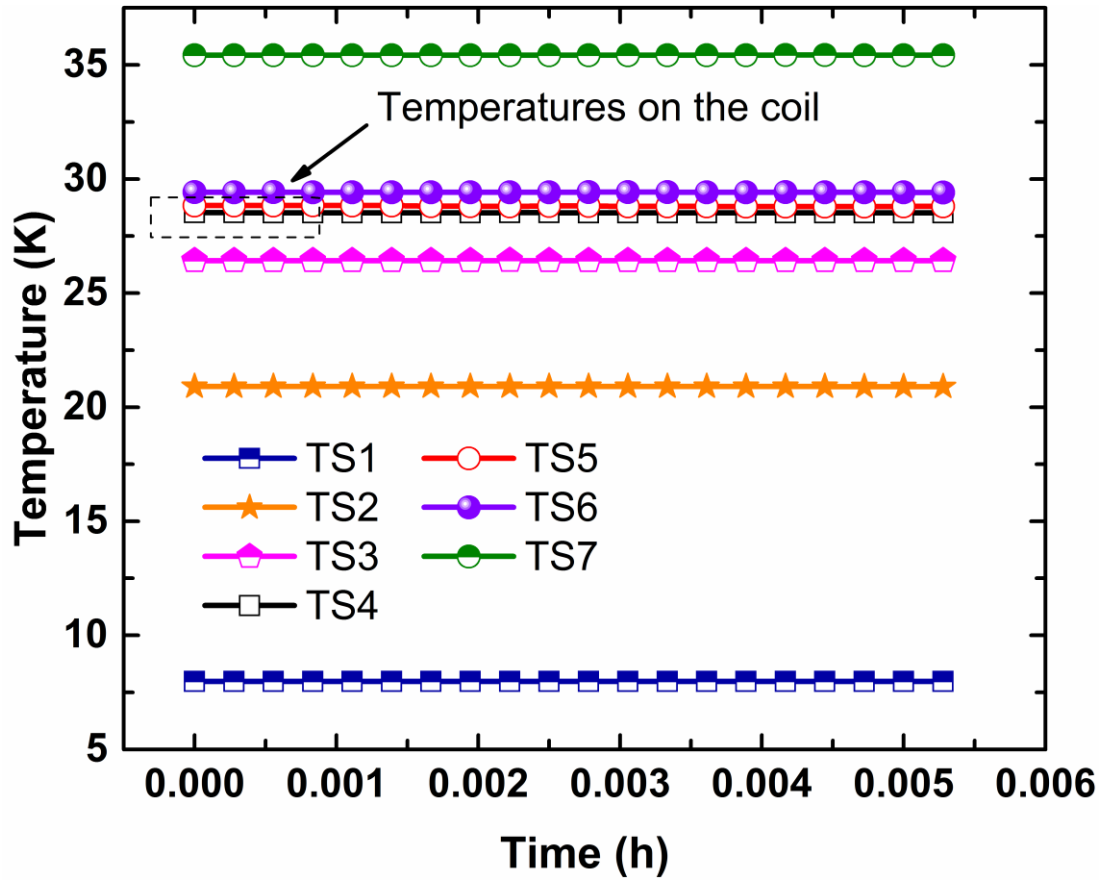

Figure 8-8. Temperatures vs. time curves of the cooling system soon after turning off the cryocooler.

Figure 8-5(d) shows the temperature vs. time curves of the cooling system for 100 h after switching off the cryocooler. As can be seen in the figure, as soon as cryocooler was switched off, the temperature of the radiation shield (only conduction cooling) started to increase rapidly. On the other hand, the temperature of the SN_2 chamber was increasing very slowly, even though the cryocooler was connected to the SN_2 cooling chamber in the off condition. Like cool down, the warm up of the SN_2 around the coil was quite uniform. Figure 8-5(e) shows the temperature vs. time plot of the coil up to 35 K, which is the T_c of the coil. Soon after turning off the cryocooler, the temperatures on the coil were decreased for some time to achieve temperature equilibrium with other temperatures in the SN_2 chamber (see figure 8-8). The temperature variation occurred during the temperature control process. As shown in figure 8-5(e), once the temperature equilibrium was achieved, the temperatures on the coil increased slowly and uniformly compared to a pure

conduction cooling system. It took about 21 h to reach T_c of the coil, whereas it took 14.5 hours to reach 31.5 K, even though cryocooler was delivering a significant conduction heat load to the SN_2 chamber. The warming up time can be greatly improved by thermally disconnecting the cryocooler from the SN_2 chamber. Therefore, it can offer longer maintenance time or less re-cooling time in the event of problems or power failure in the commercial MRI systems.

8.4. Conclusions

The high current operation of an MgB_2 solenoid coil in the SN_2 environment was successfully achieved for the first time. The multifilament MgB_2-conductor-based solenoid coil achieved its highest current carrying capacity of 200 A at 28 K in SN_2 with enhanced thermal stability. Furthermore, upon turning-off the cryocooler at ~28 K, it took about 21 h for the coil to reach 35 K (T_c of the coil) in SN_2. Such a slow warming up of the SN_2 can offer longer maintenance time, less re-cooling time, or even cooling-source free operation of the MRI magnet in the event of power failure.

8.5. References

[1] Lvovsky Y, Stautner E W and Zhang T 2013 Novel technologies and configurations of superconducting magnets for MRI *Supercond. Sci. Technol.* **26** 093001

[2] Cosmus T C and Parizh M 2011 Advances in whole-body MRI magnets *IEEE Trans. Appl. Supercond.* **21** 2104-9

[3] Wang Z, Van Oort J M and Zou M X 2012 Development of superconducting magnet for high-field MR systems in China *Physica C* **482** 80-6

[4] Mine S, Song H, Xu M, Marte J, Buresh S, Stautner W, Immer C, Laskaris E T and Amm K 2012 Test coil for the development of a compact 3T MgB_2 magnet *IEEE Trans. Appl. Supercond.* **22** 4400604

[5] Mine S, Xu M F, Buresh S, Stautner W, Immer C, Laskaris E T, Amm K and Grasso G 2013 Second test coil for the development of a compact 3T MgB_2 magnet *IEEE Trans. Appl. Supercond.* **23** 4601404

[6] Patel D, Hossain M S A, Motaman A, Barua S, Shahabuddin M and Kim J H 2014 Rational design of MgB_2 conductors toward practical applications *Cryogenics* **63** 160-5

[7] Kim J H, Oh S, Heo Y U, Hata S, Kumakura H, Matsumoto A, Mitsuhara M, Choi S, Shimada Y, Maeda M, MacManus-Driscoll J L and Dou S X 2012 Microscopic role of carbon on MgB_2 wire for critical current density comparable to NbTi *NPG Asia Mater.* **4** e3

[8] Kim J H, Oh S, Kumakura H, Matsumoto A, Heo Y-U, Song K-S, Kang Y-M, Maeda M, Rindfleisch M, Tomsic M, Choi S and Dou S X 2011 Tailored materials for high-performance MgB_2 wire *Adv. Mater.* **23** 4942-6

[9] Tomsic M, Rindfleisch M, Yue J, McFadden K, Phillips J, Sumption M D, Bhatia M, Bohnenstiehl S and Collings E W 2007 Overview of MgB_2 superconductor applications *Int. J. Appl. Ceram. Technol.* **4** 250-9

[10] Tomsic M, Rindfleisch M, Yue J J, McFadden K, Doll D, Phillips J, Sumption M D, Bhatia M, Bohnenstiehl S and Collings E W 2007 Development of magnesium diboride (MgB_2) wires and magnets using in situ strand fabrication method *Physica C* **456** 203-8

[11] Braccini V, Nardelli D, Penco R and Grasso G 2007 Development of *ex situ* processed MgB_2 wires and their applications to magnets *Physica C* **456** 209-17

[12] Modica M, Angius S, Bertora L, Damiani D, Marabotto M, Nardelli D, Perrella M, Razeti M and Tassisto M 2007 Design, construction and tests of MgB_2 coils for the development of a cryogen free magnet *IEEE Trans. Appl. Supercond.* **17** 2196-9

[13] Musenich R, Fabbricatore P, Farinon S, Greco M, Modica M, Marabotto R, Penco R, Razeti M and Nardelli D 2006 The behaviour of cryogen-free MgB_2 react and wind coils *Supercond. Sci. Technol.* **19** S126-S31

[14] Nardelli D, Angius S, Capelluto A, Damiani D, Marabotto R, Modica M, Perrella M and Tassisto M 2010 Persistent mode MgB_2 short windings *IEEE Trans. Appl. Supercond.* **20** 1998-2001

[15] Park D K, Ling J, Rindfleisch M, Voccio J, Hahn S, Bascuñán J, Tomsic M and Iwasa Y 2012 MgB_2 for MRI magnets: Test coils and superconducting joints results *IEEE Trans. Appl. Supercond.* **22** 4400305

[16] Razeti M, Angius S, Bertora L, Damiani D, Marabotto R, Modica M, Nardelli D, Perrella M and Tassisto M 2008 Construction and operation of cryogen free MgB_2 magnets for open MRI systems *IEEE Trans. Appl. Supercond.* **18** 882-6
[17] Yao W, Bascuñán J, Hahn S and Iwasa Y 2009 A superconducting joint technique for MgB_2 round wires *IEEE Trans. Appl. Supercond.* **19** 2261-4
[18] Yao W, Bascuñán J, Kim W S, Hahn S, Lee H and Iwasa Y 2008 A solid nitrogen cooled MgB_2 "demonstration" coil for MRI applications *IEEE Trans. Appl. Supercond.* **18** 912-5
[19] Glowacki B A, Majoros M, Vickers M, Evetts J E, Shi Y and McDougall I 2001 Superconductivity of powder-in-tube MgB_2 wires *Supercond. Sci. Technol.* **14** 193-9
[20] Canfield P C, Finnemore D K, Bud'ko S L, Ostenson J E, Lapertot G, Cunningham C E and Petrovic C 2001 Superconductivity in dense MgB_2 wires *Phys. Rev. Lett.* **86** 2423-6
[21] Larbalestier D, Gurevich A, Feldmann D M and Polyanski A 2001 High-T_c superconducting materials for electric power applications *Nature* **414** 368-77
[22] Bascuñán J, Lee H, Bobrov E S, Hahn S, Iwasa Y, Tomsic M and Rindfleisch M 2006 A 0.6 T/650 mm RT bore solid nitrogen cooled MgB_2 demonstration coil for MRI - A status report *IEEE Trans. Appl. Supercond.* **16** 1427-30
[23] Iwasa Y 2006 HTS and NMR/MRI magnets: Unique features, opportunities, and challenges *Physica C* **445-448** 1088-94
[24] Iwasa Y, Bascuñán J, Hahn S and Park D K 2012 Solid-cryogen cooling technique for superconducting magnets of NMR and MRI *Phys. Proc.* **36** 1348-53
[25] Yao W, Bascuñán J, Hahn S and Iwasa Y 2010 MgB_2 coils for MRI applications *IEEE Trans. Appl. Supercond.* **20** 756-9
[26] Iwasa Y 2009 *Case studies in superconducting magnets, design and operation issues* (New York: Springer)
[27] Patel D, Md Shahriar Al H, Khay Wai S, Qiu W, Kobayashi H, Zongqing M, Seong Jun K, Hong J, Jin Yong P, Choi S, Maeda M, Shahabuddin M, Rindfleisch M, Tomsic M, Dou S X and Kim J H 2016 Evaluation of persistent-mode operation in a superconducting MgB_2 coil in solid nitrogen *Supercond. Sci. Technol.* **29** 4LT02-9
[28] Wilson M N 1983 *Superconducting magnets* (Oxford University Press)
[29] www.kaptontape.com
[30] www.apiezon.com
[31] Patel D, Hossain M S A, See K W, Xu X, Barua S, Ma Z, Choi S, Tomsic M and Kim J H 2015 MgB_2 superconducting joints for persistent current operation *Supercond. Sci. Technol.* **28** 065017
[32] www.temati-uk.com
[33] www.lakeshore.com
[34] www.cryocon.com
[35] Nakamura T, Muta I, Okude K, Fujio A and Hoshino T 2002 Solidification of nitrogen refrigerant and its effect on thermal stability of HTSC tape *Physica C* **372-376** 1434-7
[36] Song J B, Kim K L, Kim K J, Lee J H, Kim H M, Kim W S, Yim S W, Kim H R, Hyun O B and Lee H G 2008 The design, fabrication and testing of a

cooling system using solid nitrogen for a resistive high-T_c superconducting fault current limiter *Supercond. Sci. Technol.* **21** 115023

[37] Kim H S, Kovacs C, Rindfleisch M, Yue J, Doll D, Tomsic M, Sumption M D and Collings E W 2016 Demonstration of a conduction cooled react and wind MgB_2 coil segment for MRI applications *IEEE Trans. Appl. Supercond.* **26** 1-5

[38] Kim J H, Dou S X, Matsumoto A, Choi S, Kiyoshi T and Kumakura H 2010 Correlation between critical current density and n-value in MgB_2/Nb/Monel superconductor wires *Physica C* **470** 1207-10

[39] Kara D C 2013 Production of a viable product in magnetic resonance imaging using MgB_2. (Master's Thesis, Case Western Reserve University)

8.6. Note: Chapter Publication and Text Usage Detail.

This Chapter is under preparation with the design portion of Chapter 4 for the submission to the Scientific Reports as a below paper. The written text in this Chapter has been taken from my paper (under preparation), as shown below.

[1] **Patel D**, Md Shahriar Al H, Khay Wai S, Qiu W, Jie H, Seong Jun K, Choi S, Maeda M, Shahabuddin M, Tomsic M and Kim J H 2016 Solid cryogen for MgB_2 superconducting MRI magnet (Under Preparation)

Chapter 9

9. Conclusions and Future Prospects

9.1. Conclusions

The ultimate aim of this thesis was to demonstrate a magnesium diboride (MgB_2) based persistent magnet in solid nitrogen (SN_2), which meets the technical requirements for applicability in magnetic resonance imaging (MRI). The aim was successfully achieved by demonstrating the first MgB_2 based persistent magnet in the SN_2 environment. In the course of this thesis, the SN_2 cooling system, the superconducting joining processes for the MgB_2 conductors, the MgB_2 persistent magnet, and the MgB_2 solenoid coils were studied and methodically developed.

First, the conduction cooled SN_2 cooling system with the option to operate in mixed cooling mode was designed, fabricated, installed, and tested. The design of the cooling system was conducted using the optimal combination of analytical, empirical, and FE analysis. The unique approach for achieving a uniform temperature in the low thermal conductivity stainless steel cooling chamber by using a copper (Cu) flange was developed, simulated, and experimentally verified. The cooling system was designed such that the total estimated thermal heat load on the radiation shield and SN_2 chamber was about 33.505 W and 0.482 W, respectively. These heat loads were ~16% and ~52% less than the available cooling power at the 1^{st} and 2^{nd} stages of the cryocooler, respectively. During the actual cool down, however, it was observed that the SN_2 level was as high as the radiation shield top flange. Thus, the SN_2 was delivering an additional conductive heat load onto the SN_2 chamber, which prevented the SN_2 chamber from reaching the temperature of the 2^{nd} stage of the cryocooler, so that it remained at 8 K.

The detailed installation procedure for the cooling system was presented. The high-temperature superconductor (HTS) modules of the current leads were fabricated using two samarium barium copper oxide tapes instead of the designed single, drastically innovative bismuth strontium copper oxide tape. Furthermore, the current leads were tested and used at 200 A current despite being designed for 150 A current.

No leaks in the system were observed, which means that the indium seal mechanism worked very well. The system cool down was smooth. The thermal contact of the 1st stage and the 2nd stage with the radiation shield and the SN_2 chamber, respectively, appeared to be excellent. Poor thermal contact between the transition region of the current leads and the 1st stage of the cryocooler was observed, however. Thus, liquid nitrogen cooling was necessary for the brass section of the current lead. A premature quench in the MgB_2 solenoid coil was observed. After the system warmed up, it was observed that the HTS links had been damaged during cool down. This might have played a role in the premature quench. Thus, in subsequent experiments, Cu links were used instead of HTS. In all, the system operation was well within the operation requirements for subsequent experiments.

In the next step, superconducting joints using unreacted *in situ* undoped monofilament MgB_2 wire were fabricated and evaluated. The critical current (I_c) results for the joined wires demonstrated consistent performance, which is promising from the viewpoint of "wind and react" magnets. Despite the performance consistency in the joint performance, about 60 to 66% of the current was retained after the joint was installed. A field-decay measurement of the closed-loop coil was also conducted to estimate the joint resistance, which was about 1.4×10^{-12} Ω. Optimization of the wire cutting, the heat-treatment conditions, and the powder density in the joint was required, however, for further performance enhancement. The scanning electron microscope observations showed very good MgB_2 core to core contact in the joint, but some cracks were also induced in this region. These should be avoided for reliable joint processing.

Moreover, a new approach to a superconducting joining process for an unreacted *in situ* C-doped monofilament MgB_2 wire was developed. The joints were evaluated for their joint resistance through a field-decay measurement. The new joining approach for C-doped MgB_2 conductor showed significantly enhanced performance compared to the reported results to date. According to the literature, the joint fabricated using the unreacted *in situ* C-doped MgB_2 monofilament wire was the first to achieve an I_c value >200 A in self-field at 20 K. The joint demonstrated current retention of up to 72% in different magnetic fields at 20 K. The results were

preliminary results, so still there is room to further improve the joint performance. The X-ray diffraction analysis showed no diffusion or reaction of the sealing material with the MgB_2 powder inside the joint. The solenoid closed-loop coil showed very reliable persistent-mode operation for a period of 48 h at temperatures up to 21.4 K in self-field. The estimated total circuit resistance was $<1.8 \times 10^{-13}\ \Omega$ at 16.7 ± 4.7 K temperature. These superconducting joint performance results demonstrate the potential of MgB_2 conductors for MRI application based on an LHe-free system.

To achieve the ultimate aim of this thesis, the MgB_2 coil, and the persistent-current switch was successfully fabricated through the superconducting joining technique, and the persistent-current mode of the magnet system was evaluated with SN_2 cooling and a 100 A operating current. The total circuit resistance was estimated to be $<7.4 \times 10^{-14}\ \Omega$ at 19.5 K ± 1.5 K, in the coil during reasonably long-term persistent-mode operation for 4.75 days. This performance is comparable to the technical requirements for practical MRI application.

In the end, the high current operation of an MgB_2 based solenoid coil in the SN_2 environment was successfully achieved for the first time. The multifilament MgB_2-conductor-based solenoid coil showed a high current carrying capacity of 200 A at 28 K in SN_2 with enhanced thermal stability. Furthermore, upon turning-off the cryocooler at ~28 K, it took about 21 h for the coil to reach 35 K (critical temperature of the coil) in SN_2. Such a slow warming up of the SN_2 can offer longer maintenance time, less re-cooling time, or even cooling-source-free operation of the MRI magnet in the event of power failure.

In summary, the research and development carried out in this thesis work will certainly pave the way to the development of the advanced technology of a next generation LHe-free MRI magnet system based on the MgB_2 conductor.

9.2. Future Prospects

MgB_2 has very good potential for application in MRI systems in the near future. Further work needs to be done, however, on the applicability of *in situ* monofilament MgB_2 wire for MRI magnet winding via a wind and react method. If the monofilament conductor doesn't meet the stability criterion for commercial MRI

application, then the joining process needs to be optimized for *in situ* multifilament MgB_2 wire. Moreover, if the wind and react approach is not viable for commercial MRI application, then a joining process for reacted mono- and multifilament *in situ* wire has to be developed. During this thesis work, however, reacted *in situ* wire showed significant degradation after the second heat-treatment, which is mandatory for joining MgB_2 conductors. In contrast, Hyper Tech Research Inc. observed no degradation in *in situ* wire after a second heat-treatment [1]. This result, however, needs to be verified.

In the case of commercial *ex situ* multifilament MgB_2 tape, a joint carrying >300 A current at 20 K has been reported [2]. This is a very promising result if the joining process reported in [2] can be applied to commercial MRI magnets via the react and wind method. For reacted conductor joining, *ex situ* conductor seems better compared to *in situ* conductor, in term of performance retention (i.e., *ex situ* wire retained good performance after the second heat-treatment as per literature).

React and wind MgB_2 magnets are obviously more suitable for commercial MRI application. Nevertheless, it should be noted that any fully reacted MgB_2 conductor (*in situ* or *ex situ*) has strain tolerance up to 0.4% [3, 4]. This means that, while joint fabrication of any fully reacted MgB_2 conductor, the strain limit has to be kept less than 0.4%, which seems very challenging, especially where there are requirements for pressing and heat-treatment. Thus, probably due to the strain sensitivity of MgB_2 conductor, the wind and react approach also has to consider for commercial application as in the case of niobium-tin.

9.3. References

[1] Rindfleisch M Hyper Tech Research Inc. (Personal communication).
[2] Nardelli D, Angius S, Capelluto A, Damiani D, Marabotto R, Modica M, Perrella M and Tassisto M 2010 Persistent mode MgB_2 short windings *IEEE Trans. Appl. Supercond.* **20** 1998-2001
[3] Kováč P, Kopera L, Melišek T, Sarmiento G, Castillo S S, Brisigotti S, Nardelli D and Tropeano M 2015 Tensile and bending strain tolerance of *ex situ* MgB_2/Ni/Cu superconductor tape *IEEE Trans. Appl. Supercond.* **25** 1-7
[4] Sumption M D, Bohnenstiehl S, Buta F, Majoros M, Kawabata S, Tomsic M, Rindfleisch M, Phillips J, Yue J and Collings E W 2007 Wind and react and react and wind MgB_2 solenoid, racetrack and pancake coils *IEEE Trans. Appl. Supercond.* **17** 2286-90

Appendix A: Publications

1. **D. Patel**, M. S. A. Hossain, K. W. See, W. Qiu, H. Jie, M. Maeda, *et al*., "Solid nitrogen for MgB_2 superconducting MRI magnet " Under preparation, 2016.
2. **D. Patel**, H. Md Shahriar Al, M. Shahabuddin, E. Yanmaz, S. Pradhan, M. Tomsic, *et al.*, "A new approach to a superconducting joining process for carbon-doped MgB_2 conductor," *Supercond. Sci. Technol.* vol. 29, p. 095001, 2016.
3. **D. Patel**, H. Md Shahriar Al, S. Khay Wai, W. Qiu, H. Kobayashi, M. Zongqing, *et al.*, "Evaluation of persistent-mode operation in a superconducting MgB_2 coil in solid nitrogen," *Supercond. Sci. Technol.*, vol. 29, pp. 4LT02-9, 2016. (Fast track communication)
4. **D. Patel**, M. S. A. Hossain, K. W. See, X. Xu, S. Barua, Z. Ma, *et al.*, "MgB_2 superconducting joints for persistent current operation," *Supercond. Sci. Technol.*, vol. 28, p. 065017, 2015.
5. S. Barua, **D. Patel**, N. Alzayed, M. Shahabuddin, J. M. Parakkandy, M. S. Shah, *et al.*, "Correlation between in-field Jc enhancement and grain connectivity in co-doped MgB2 superconductor," *Mat. Lett.*, vol. 139, pp. 333-335, 2015.
6. S. Barua, M. S. A. Hossain, Z. Ma, **D. Patel**, M. Mustapic, M. Somer, *et al.*, "Superior critical current density obtained in MgB2 bulks through low-cost carbon-encapsulated boron powder," *Scr. Mater.*, vol. 104, pp. 37-40, 2015.
7. **D. Patel**, M. S. A. Hossain, A. Motaman, S. Barua, M. Shahabuddin, and J. H. Kim, "Rational design of MgB_2 conductors toward practical applications," *Cryogenics*, vol. 63, pp. 160-165, 2014.
8. **D. Patel**, M. Maeda, S. Choi, S. J. Kim, M. Shahabuddin, J. M. Parakandy, *et al.*, "Multiwalled carbon nanotube-derived superior electrical, mechanical and thermal properties in MgB_2 wires," *Scr. Mater.*, vol. 88, pp. 13-16, 2014.
9. M. S. A. Hossain, A. A. Gazder, S. Barua, A. Motaman, **D. Patel**, J. H. Kim, *et al.*, "Development of high current capacity mono- and 18-filament MgB_2 cables by varying the twist pitch," *IEEE Trans. Appl. Supercond.*, vol. 24, pp. 1-4, 2014.

10. Motaman, S. Barua, **D. Patel**, M. Maeda, K. Cheong, J. H. Kim, *et al.*, "Power-law relationship between critical current density, microstructure, and the n-value in MgB_2 superconductor wires," *J. Supercond. Nov. Magne.*, vol. 27, pp. 1643-1645, 2014.
11. M. S. A. Hossain, A. Motaman, S. Barua, **D. Patel**, M. Mustapic, J. H. Kim, *et al.*, "The roles of CHPD: superior critical current density and n-value obtained in binary in situ MgB_2 cables," *Supercond. Sci. Technol.*, vol. 27, p. 095016, 2014.

Appendix B: Presentations

Oral

1. Development of new high performance persistent joining technique for MgB_2 wires, Applied Superconducting Conference **(ASC)**, 2014, Charlotte, NC, USA – 1953222
2. Fabrication and evaluation of MgB_2 superconducting joint in closed-loop coils, Magnet Technology **(MT)** Conference, 2015, Seoul, Korea - 0202OP0602

Poster

1. Persistent joints of MgB_2 wires for persistent-mode operation in MRI, 5^{th} Australia China Material Science **(ACMS)** Conference (2014), University of Wollongong, Australia.

Appendix C: Awards, Scholarships, Financial Supports, Participations, and Courses

Awards

1. Excellence Student Award (2015), Institute for Superconducting and Electronic Materials (ISEM), University of Wollongong.
2. Runner-up Award in Post-Graduate Student Category, Pitch Competition – 2013, University of Wollongong.
3. Encouragement Award in Post-Graduate Student Category, Pitch Competition – 2014, University of Wollongong.
4. Winner, Three Minute Thesis Competition (2013), Australian Institute of Innovative Materials (AIIM), University of Wollongong.

Scholarships

1. Career Launcher Scholarship, University of Wollongong.
2. University Post Graduate Award (UPA), University of Wollongong.
3. Global Challenge Travel Scholarship (2015), Global Challenge Travel Program, University of Wollongong.
4. International Postgraduate Tuition Fee Award (IPTA), University of Wollongong.
5. Matching Scholarship, University of Wollongong.

Financial Supports

1. Conference Registration Waiver, Magnet Technology (MT) Conference – 2015, IEEE Council on Superconductivity.
2. Travel Stipend, Magnet Technology (MT) Conference – 2015, IEEE Council on Superconductivity.
3. Travel and Living Allowance (2015), Korean Basic Science Institute (KBSI), Korea.
4. AIIM HDR Student Conference and International Travel Grants (2014), University of Wollongong.

5. Conference Registration Waiver, Applied Superconductivity Conference (ASC) – 2014, IEEE Council on Superconductivity.
6. Travel Stipend, Applied Superconductivity Conference (ASC) – 2014, IEEE Council on Superconductivity.

Participations

1. AMP Bright Spark Competition (2015), Amplify Festival, AMP, Sydney, Australia.
2. Pitch Competition (2014), University of Wollongong.
3. AIIM HDR Seminar Competition (2014), University of Wollongong.
4. AIIM Three Minute Thesis Competition (2013), University of Wollongong.
5. Pitch Competition (2013), University of Wollongong.
6. Finalist, Three Minute Thesis Competition (2013), University of Wollongong.
7. Poster Presentation Competition, IEEE Technologies of Future (2013), University of New South Wales (UNSW), NSW, Australia.

Courses

1. Introduction to COMSOL Multiphysics (Thermal, Structural, Joule Heating, Electromagnetic) – COMSOL Software
2. Introduction to SolidWorks, SolidWorks Software
3. Superconducting Magnet Design Course (During Applied Superconductivity Conference - 2014, Charlotte, USA). Electromagnetic, thermal and structural aspects.
4. Introduction ANSYS Mechanical (Online Full Course ANSYS)